An Examination of the Response of East Asian Lacquer Films to Changes in Environmental Conditions

By

Adel E. Elmahdy

A Doctoral Thesis

Submitted in partial fulfilment of the requirements for the award of Doctor of Philosophy of Loughborough University

2010

CERTIFICATE OF ORIGINALITY

This is to certify that I am responsible for the work submitted in this thesis, that is the original work is my own except as specified in acknowledgements or in footnotes, and that neither the thesis nor the work contained therein has been submitted to this or any other institution for a degree.

…… (Signed)

…….... (Date)

Abstract

This work addresses the material properties and behaviour of Japanese lacquers (*urushi*) coatings similar to those found on the Mazarin Chest, an important Japanese lacquerware artefact currently displayed in the Toshiba Gallery of Japanese Art at the Victoria and Albert Museum (V&A) in London. For almost four centuries, the Mazarin Chest has been displayed in uncontrolled environmental conditions and has been exposed to a range of lighting conditions. As a result, the Mazarin Chest has deteriorated and started to suffer from different kinds of damage. However, the optimal conservation approach to repairing this damage is not known and as a consequence, research on *urushi* and related materials is of great interest.

For the first time, the effect of changing relative humidity (RH) on the response of *urushi* is investigated by examining the deflection of a glass substrate coated with a thin film of *urushi.* Phase shifting interferometry was employed to measure this deflection, from which the in-plane stress developed in the system due to the expansion mismatch in the bilayer was calculated. This was performed for aged (exposed to ultra-violet radiation) and non- aged *urushi* films. The film stress was observed over 66 hrs under 30%, 36% and 42% RH, while the stress response was observed over 7 hrs during exposure to 60%, 54% and 48% RH.

During exposure to 30%, 36% and 42% RH and for both non-aged and aged *urushi* films, tensile in-plane stress was observed. It was seen to reach a peak value then relax over a longer time scale. The stresses develop in the non-aged *urushi* films were found to be higher than the stresses developed in the aged *urushi* films. The peak stress values for non-aged and aged *urushi* films were found to increase when increasing the difference between the storage RH (75%) and the target RH.

When the non-aged and aged *urushi* films were subjected to a step change from low RH (30%, 36% and 42%) to high RH (60%, 54% and 48% RH), a compression in-plane stress was observed and in this case, the aged *urushi* films exhibited higher stresses than those developed in non-aged *urushi* films.

To predict the behaviour of the *urushi* films, a simple 1D model of stress has been proposed. It shows reasonable agreement against the experimental stress measurements when the RH changes from 75% to 30%, 36% and 42% respectively, for both non-aged and aged *urushi* films. Furthermore, the model is extended to predict the stress response as a function of depth for non-aged *urushi* layers above an aged layer. For both the upper *urushi* layer (non-aged) and the lower *urushi* layer (aged), the model suggests that decreasing the layer depth results in an increase in the stress levels.

In addition to the stress response measurements and in order to fully characterise the mechanics of *urushi*, mechanical properties were determined for non-aged and aged *urushi* films under different RH levels. These including the moisture diffusion coefficients, the elastic modulus, the tensile strength at break, the elongation at break, and the viscoelastic properties.

The moisture diffusion coefficients were determined from the sorption and desorption curves when *urushi* films, non-aged and aged, subjected to step changes in RH. The results showed that the moisture diffusion coefficients were independent of the moisture content for non-aged and aged *urushi*.

A strong dependence of the elastic modulus and the elongation at failure on the RH has been observed for non-aged and aged *urushi* films. At all strain rates used and as the RH increases, a significant reduction in tensile elastic modulus and an increase in the elongation at failure were observed. As a result of the UV ageing, no plastic deformation was observed in the stress-strain curves at any RH or tensile speeds.

Creep recovery behaviours of non-aged and aged *urushi* under 30%, 50% and 75% RH and different stress levels were studied. The overall deformation levels at 75% RH for non-aged films were found to be higher than that at 30% RH and the aged films exhibited less stiffness. This trend reflects the strong influence of water, as a plasticizer, on *urushi* films.

The variation of the elastic recovery with the applied stress and the RH for non-aged and aged *urushi* films were determined from the recovery behaviour. The results showed that the amount of elastic recovery at 30% RH for non-aged *urushi* was higher

than that for aged *urushi* films at all stress values. At 50% RH and 75% RH, the aged *urushi* films recovered to a greater degree than non-aged *urushi* films.

The 4-element Burger's model was used for quantitative characterisation of the creep recovery curves to determine the viscoelastic properties for *urushi* films and their dependence on the RH and UV ageing. It was found that the RH has a strong effect on the viscoelastic properties for both non-aged and aged *urushi* films. A significant decrease in these parameters has been observed when the RH has been increased suggesting that the films tend to become soft as a result of the high mobility of the molecular chains under elevated RH.

We have proposed a methodology to identify the effectiveness of the Japanese traditional consolidation processes that are used to consolidate the formation of micro-cracks on lacquerware surfaces. A rectangular aluminium substrate, covered with a thin film of aged *urushi*, was mechanically loaded using three point bending device and the in-plane *urushi* surface displacement profile was obtained through phase shifting digital speckle pattern interferometry (DSPI). A comparison of the displacement profiles before and after creating a 'v' notch along the film showed an anomalous profile around the notch. While after consolidate the notch, no anomaly in the displacement profiles were observed. The potential for DSPI to play a key role in investigating consolidation mechanics has been demonstrated with the detection of the surface displacement around a notch before and after consolidation.

Key words: East Asian lacquer film, *urushi*, UV aging, moisture diffusion coefficient, phase shifting interferometer, stress in coating, mechanical viscoelastic properties, phase shifting digital speckle pattern interferometer, in-plane displacement.

Acknowledgement

Firstly, I kneel humbly to ALLAH thanking HIM for showing me the right path, without HIS help my efforts would have gone astray.

I am heartily thankful to my supervisors, Dr. R. D. Wildman, Dr. P. D. Ruiz and Prof. J. M. Huntley for their invaluable help, patience, guidance, modifications and comments on my thesis and papers published.

I am also very grateful to the Victoria and Albert Museum (V&A), the Toshiba International Foundation (TIFO) and Loughborough University for their financial support. Special thanks to Dr. Brenda Keneghan and Shayne River for their help and advice.

I would like to express my thanks to Dr. Russell Coggrave for his help on phase unwrapping evaluation by Matlab software.

I would like to express my highest appreciation and gratitude to my parents and my wife, Dr. Afaf Mahmoud, for their encouragement and support throughout my study.

Lastly, I offer my regards to all of those who supported me in any respect during the completion of this project.

Adel E. Elmahdy

Loughborough University

Table of Contents

List of Figures

List of Tables

Nomenclature

Chapter 1: Introduction

V&A	The Victoria and Albert museum.
RH	Relative humidity.

Chapter 2: *Urushi* and Mazarin Chest

E_t	Relaxation modulus.
UV	Ultar-violet radiation.
HALS	Hindered amine light stabilizer.
PL	Purified urushi.
Q-UV	Q-Pandel Accelerated Weathering Tester.
SEM	Scanning electron micrographs.
FTIR/ATR	Fourier Transform Infrared–Attenuated Total Reflectance.

Chapter 3: Development of a methodology for preparing *urushi* films

BK-7	Borosilicate glass Schott.
Al	Aluminium.
$NiCrO_4$	Nickel Chromate.
DC	Direct current.
BX-60	Olympus microscope.
DIC	Differential interference contrast microscopy.

Chapter 4: Development of a methodology to measure stresses in *urushi* thin films

PSI	Phase stepping interferometry.
E_s	Young's modulus of the substrate.
ν_s	Poisson's ratio of the substrate.
t_s	Thickness of the substrate.
t_f	Thickness of the film.
x, y	Spatial co-ordinates.
σ	Average stress.
δ	Substrate deflection field.

r, θ	Polar coordinates.
I	Interference intensity distribution.
I_o	Background intensity.
I_M	Modulation intensity.
ϕ	Phase difference between the interfering beams.
ϕ_w	Wrapped phase distribution.
ϕ_r	Phase of the reference state.
ϕ_d	Phase of the deformed state.
$\Delta\phi$	Unwrapped phase change distribution.
λ	Wavelength.
a, b, c, d, e, f	Quadratic and linear coefficients of second order surface.
θ_M, θ_m	Orientation angles of the major and minor axes respectively.
HWP	Half-wave plate.
PBS	Polarizing beam splitter.
RB	Reference beam.
OB	Object beam.
PZT	Open loop piezoelectric lead zirconate titanate.
NPBS	Non-polarizing beam splitter.
EC	Environmental loading chamber.
C	8 bits, 1024 × 1024 pixels CMOS camera.
L_1, L_2, L_3	Convex lens.
L_4	Imaging lens.
AS	Aperture stop.
RF	Reference fibre.
OF	Object fibre.
FDS	Fibre Delivery System.
V_1, V_2, V_3, V_4	Stepped voltage staircase
TTL	Transistor-transistor logic circuit.
I_r	Reference intensity distribution during PZT calibration.
S	Average of the squared differences between a reference intensity distribution I_r and an intensity distribution I obtained after an unknown phase difference.

V_r, V	Applied voltage to the PZT corresponding to I_r and I respectively.
$\alpha(V)$	Voltage function.
a_1, a_2, a_3	Constants.
PID	Proportional with integral and derivative control.
δ_{rms}	Root mean square error of the displacement distributions.
δ_{exp}	Measured displacement map.
δ_{fit}	Second order polynomial fit of the displacement map.
N, M	Number of pixels in x and y respectively.
u_σ	Uncertainty in the average film stress.
u_{t_s}	Uncertainties in the substrate thickness.
u_{t_f}	Uncertainties in the film thickness.
u_δ	Uncertainties in the displacement.
u_r	Uncertainties in the distance from the centre to where the displacement is measured.
$u_{\sigma t_s}$	Uncertainties in the average film stress due to the substrate thickness.
$u_{\sigma t_f}$	Uncertainties in the average film stress due to the film thickness.
$u_{\sigma \delta}$	Uncertainties in the average film stress due to the displacement.
$u_{\sigma r}$	Uncertainties in the average film stress due to the distance from the centre to where the displacement is measured.

Chapter 5: Measurements of moisture diffusion coefficient for non-aged and aged *urushi*

C	Moisture concentration.
D	Moisture diffusion coefficient.
C_o	Initial moisture concentration.
h	Thickness of the sheet.
C_s	Surface moisture concentration.
A_n, B_n, λ_n	Constants.
A_o	Average concentration.
M_t	Moisture content at time t.

M_∞	Moisture content at equilibrium.
m_t	Mass of the specimen at time *t*.
m_{dry}	Mass of the dry specimen.
P	Permeability.

Chapter 6: Stress response of *urushi* films under changes of environmental conditions

RH_C	Curing relative humidity.
RH_1	Lower relative humidity.
RH_2	Higher relative humidity.
t_{C1}, t_{12}	Times at which relative humidity changes from RH_C to RH_1 and from RH_1 to RH_2.
K	Substrate curvature.
R	Radius of curvature.
σ_∞	Asymptotic stress value.
σ_B, τ	Constants.
ΔRH	Relative humidity changes.
ΔC	Moisture change.
ΔT	Temperature change.
ε_1, ε_2	Strain components.
α	Thermal expansion coefficient.
β	Hygroscopic expansion coefficient.
ε_1^H, ε_2^H	Hygral strains.
σ_1^H, σ_2^H	Hygral stresses.
R	Effective relaxation function.
k_1, k_2	Viscoelastic model parameters.

Chapter 7: Mechanical properties of aged and non-aged *urushi* layers

E	The elastic modulus.
σ_B	Tensile strength at break.
ε_B	Elongation at break.
ε_R	Elastic recovery.

$\varepsilon(t)$	Creep strain at time *t*.
E_1	Instantaneous elastic modulus of the spring in the Maxwell unit.
η_1	Viscosity of the dashpot in the Maxwell unit.
E_2	Elastic modulus of the spring in the Kelvin unit.
η_2	Viscosity of the dashpot in the Kelvin unit.
η_1^r	Recovery viscosity.
ε_2^r	Unrecoverable strain during recovery.

Chapter 8: Feasibility study on the experimental assessment of the mechanical effects of traditional Japanese consolidation on aged urushi films

CHE	Coefficient of hygroscopic expansion.
$u(x)$	Displacement field in *x* direction.
DSPI	Digital Speckle Pattern Interferometry.
ESPI	Electronic speckle pattern interferometry.
G	Holographic diffraction grating.
M_{x1}, M_{x2}	Mirrors in *x* directions.
M_{y1}, M_{y2}	Mirrors in *y* directions.
BD	Three point bending device.
PS	Positioning stage.
g	Grating pitch.
RG	Reflection diffraction grating.
$< \varepsilon_{st.gauge} >$	Strain as measured with a strain gauge.
ε_p	Peak strain.
L	Gauge length.

Chapter 1
Introduction

1.1 Introduction

The Victoria and Albert museum (V&A) in London has a substantial collection of lacquer artefacts including those of Asian, Islamic and European origin. In particular it has one of the most important collections of Japanese lacquer artefacts outside of Japan, numbering around 2,500 pieces. The majority of objects in the collection date from the Edo period (1615-1868), which bore witness to an enormously creative outpouring in the craft of lacquering. The pieces exhibit an extremely high quality of workmanship and only a very small number of such objects were produced. The V&A has four items of this period, together with parts of a fifth: the Van Diemen Box, a casket in renaissance form, a small wedding casket, the Mazarin Chest, and panels from what is thought to have been another chest of comparable size and quality. The star item in Japanese lacquer work art collection is the Mazarin Chest and it is this item from which we draw our inspiration.

1.2 Overview of the Mazarin Chest

The Mazarin Chest is an extraordinary object of major cross-cultural significance, being renowned as one of the finest pieces of Japanese export lacquer to have survived from the late 1630s or early 1640. Its name is derived from having once been in the possession of the Mazarin–La Meilleraye family, whose coat of arms is carried on the chest's French steel key. It measures 59 cm high, 101.5 cm wide and 63.9 cm deep (Figure 1.1) [1].

Figure 1.1: The Mazarin Chest.

It is constructed from straight grain wood and cross grain pinewood. Each side of the chest is composed of several boards joined together which are additionally connected with several butterfly joints (Figure 1.2). There are wooden *hashibami* boards roughly 3 cm wide on the left and right ends of the lid to prevent the boards from becoming distorted, and a frame surrounds the entire periphery. All side boards are joined with five interlocking joints and nailed with wooden pegs. The bottom board is composed of two boards with no *hashibami*. Butterfly joints are used to reinforce the cracks on the bottom board. All side boards are fixed in place with wooden pegs through the bottom board. Four round wooden legs are attached to the bottom board. Part of the lid hinge is attached with copper nails before applying *makie* (sprinkled picture decoration) while the part that is attached to the body is inserted into a slot in the wood of the body and nailed from the outside after finishing the lid and the body with *makie*. Once the wooden boards are assembled, the chest was coated with numerous

foundation layers that consist of oriental lacquer mixed with other materials such as wheat flour paste and water mixed with clay. Finally the chest has been coated with multiple layers of coloured lacquer and decorated using a range of traditional Japanese techniques.

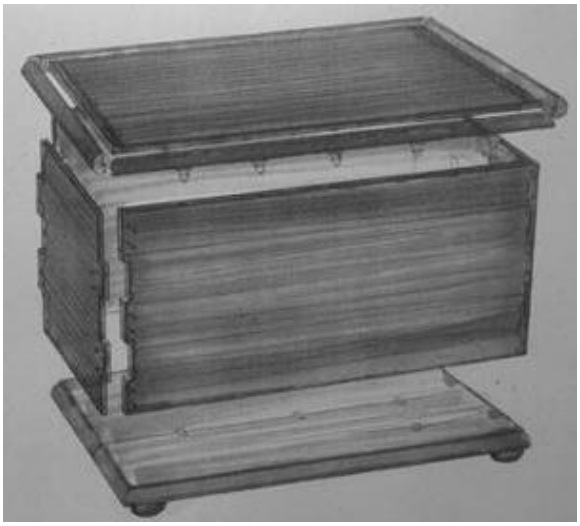

Figure 1.2: Wooden structure of the Mazarin Chest.

What makes the Mazarin Chest artistically and historical important is the wide range of lacquer decoration techniques and the extraordinarily fine workmanship. These include gold and silver *hiramakie* (flat sprinkled picture) and *takamakie* (raised sprinkled picture) decoration, *raden* (mother-of-pearl) and *hyomon* (metal foil) inlay, and embellishment with carved gold, silver and *shibuichi* alloy figures. Its corner plates, hinge plates and lock plate are made of gilded copper partially coloured with black *sumi* ink. The upper face of the lid and its reverse side are decorated with cartouches formed by phoenixes and dragons. Inside the cartouches are designs of a landscape with mountains, water and a pavilion and of a scene from court life (Figure 1.3). Designs of a similar scene are found at the front and on the right side of the chest (Figure 1.1). On the left side, there is design of a hunting scene taken from the Tale of *Genji* and the Tale of the *Soga* Brothers. The Tale of *Genji* is the supreme masterpiece of Japanese prose written in the early eleventh century by the court lady, *Murasaki Shikibu*. On the back, there is a design of bamboo and tiger. The sides of the lid and the bottom board are decorated with gold and silver *makie* powder sprinkled in gradation to create an effect of wood grain.

Figure 1.3: Photograph of the interior part of the lid of the Mazarin Chest.

1.3 *Urushi* lacquer degradation

The main material used during coating and decoration of the Mazarin Chest is a natural lacquer known as *urushi*, which is characterized by its smooth and gloss surface, its durability and water and solvent resistance.

In the years since its manufacture, the Mazarin Chest has suffered from different kinds of damage as a result of storage and display in fluctuating environmental conditions, particularly the relative humidity (RH), which is high in Japan compared to relative humidity in Europe. It has also been exposed to potentially harmful lighting conditions for long periods and it has also suffered from previously applied Western coatings that were used in an attempt to restore the original appearance and the lustre of the lacquer.

As a result of this exposure to fluctuating environmental conditions micro-cracks have appeared in the lacquer, leading to significant discoloration and fading of the originally glossy surface. In addition, there is also damage to the structure, in the form of cracks, due to the expansion and contraction of the wooden substrate. Because of this the lacquer film around the cracks have lifted, there has been a loss of lacquer coating with extensive loosening and wrinkling of adhered decorative elements, including silver and gold foils. There has also been extensive lifting of the mother-of-pearl decoration.

As a consequence of the damage suffered by the Mazarin Chest, it is not stable enough for display or transport and is at some risk of further deterioration. Even if it simply remains in storage without conservation, access to the chest within the V&A will be severely limited. In addition any requests for the loan of this object could not be

supported, preventing the chest from playing a wider role in the international field of art history. Every loss to the original decoration represents a loss of meaning and cultural value of the object and as a result, conservation is urgently needed. Therefore, the V&A with the support of the Toshiba Foundation and other charitable bodies has initiated a project to consider the most appropriate methodologies for conserving this object for future generations.

At the point of initiation of this project, the traditionally favoured method for the conservation of natural lacquer objects is to apply another layer of lacquer (usually diluted) to the damaged surface. This has the effect of filling any holes or micro-cracks. This contrasts with the Western approach of preserving the object in its current state. Conservators do not know for sure, however, which method is the most effective in minimising the negative long term impact.

1.4 The Mazarin Chest conservation project

The Mazarin Chest conservation project is a combination of art, historical and scientific research. The stated aims of the Mazarin Chest conservation project are to develop a comprehensive interdisciplinary methodology for the conservation of Japanese lacquer objects held in Japan and Western collections and develop a theoretical framework for the collaborative conservation treatment of the V&A Mazarin Chest and similar lacquer objects in Japan and in the West.

Achieving this aim will require the meeting of the following objectives:

- Consolidate the micro-cracks in the lacquer surface and stabilize, re-adhere, the poorly adhered lacquer and loose decoration in which much of the artistic, aesthetic, historical and technical value of the object is located.

- Remove restoration coatings where possible.

- Minimize further deterioration as much as possible, for example by improving the conditions in which the chest is stored or displayed.

- Allow future display, storage and transport without risk of further loss of original decoration.

The Mazarin Chest conservation project consists of a network of partnerships between universities and specialist institutions and the V&A. The partners include Loughborough University, the Polish Academy of Sciences, Imperial College and the Dresden Academy of Fine Arts.

The Institute of Catalysis and Surface Chemistry, within the Polish Academy of Sciences, will investigate the amount and the way that moisture is absorbed by wood and lacquer, the dimensional response (swelling isotherm) of wood and lacquer due to fluctuations in relative humidity, the rate at which moisture moves through each of these materials, and the effects of the moisture distribution in the wood and lacquer on cracks, as they respond to fluctuations in relative humidity [2].

The Chemistry Department at Imperial College will study the effect of Western varnishes on the chest's lacquer. Western varnishes have been applied in an attempt to restore the original colour and gloss of the aged lacquer. Unfortunately, they do not replicate the original appearance of lacquer. Further, Western varnishes can damage the original lacquer as they age and degrade in turn. The more aged the lacquer surface and the more degraded and oxidised the Western coating, the more difficult it is to remove the varnish without damaging the original lacquer. The problem of removing degraded Western varnishes from oriental lacquer affects a substantial proportion of such objects held in public collections in the West. Analysing the interpretation and presentation of Japanese lacquer in Western collections, identifying the aesthetic criteria applied to Japanese lacquer in Japan and the West, and understanding the cultural belief systems that define conservation ethics in Japan and the West will provide a framework for proposing experimental methodology [2].

Dresden Academy of Fine Arts in Germany will investigate problems encountered by conservators in their working practice when consolidating degraded oriental lacquer surfaces/structures. The main research strands are identification and characterisation of the typical problems/different types of deterioration/modes of failure of the lacquer layer structure and review the materials used for consolidation in conservation (i.e. collagen glues, PVAs, acrylics, traditional Japanese consolidation materials used on lacquer) [2].

The Wolfson School of Mechanical and Manufacturing Engineering at Loughborough University will focus on developing an understanding of the basic mechanics of *urushi* layers. Our aim is to understand and be able to predict the effect of ageing on the ability of *urushi* layers to support stresses that are generated through interaction with typical environments. To meet this aim we will

1- measure the development of stresses within *urushi* as a result of changes in environmental conditions.

2- determine the effect of environmental conditions and exposure to light on the mechanical properties of *urushi*.

3- observe the effect of consolidation on strain evolution in a deformed *urushi* layer.

This work will result in two major advances in this area. First, we will for first time have a complete view of the mechanical properties of *urushi* and its response to changing environmental conditions. Secondly, the research outcomes will support the V&A conservators in making informed decisions about conservation treatments options.

To achieve these objectives we will take a primarily experimental approach. After first reviewing the available literature on the effect of the environmental conditions on the properties of *urushi*, we will investigate traditional Japanese techniques for manufacturing *urushi* samples such as filtration and the *kurome* processes. Then, we will develop an experimental methodology that first establishes techniques for producing *urushi* samples with consistent properties and appearance to be used in the subsequent stages of the experimental programme. We then go on to develop an experimental procedure that will enable us to determine the stresses that arise within a thin layer applied on a glass substrate when exposed to changes in environmental conditions. Having obtained a general view of the response of the material, we will use this as a basis to examine the rheological properties of layers exposed to different accelerated ageing regimes. Other more traditional techniques will be used to determine the material properties of *urushi* such as elastic modulus, tensile strength and elongation at break and their dependence on the moisture content and ageing.

Finally, we will outline designs for simulating ageing, cracking, filling, ageing cycle that in situ conserved layers will be exposed to.

The Chapters of the thesis are structured as follows:

Chapter 2 gives an introduction to the nature of *urushi* material as a natural polymer. The chemical structure and the *kurome* process of *urushi* have been discussed. It also describes analysis of the published literature on *urushi* with special emphasis on the effect of the environmental conditions (temperature, humidity and exposure to UV radiation) on the properties of *urushi*.

Chapter 3 discusses the methodologies and the procedures for the controlled manufacture of *urushi* samples (Stage 1 in Figure 1.4) for the measurements of stress response of *urushi* as it subjected to different humidity levels. The artificial ageing process using UV radiation and thickness measurements of *urushi* films have been described.

Chapter 4 discusses (Stage 2 in Figure 1.4) the curvature method and the stress evaluation from deflection measurements. The principles of the phase stepping interferometry, the experimental setup and calibration are described. A description of the environmental load chamber has been presented.

Chapter 5 discusses the measurements of moisture diffusion coefficient (Stage 3 in Figure 1.4) for non-aged and aged *urushi* under different humidity levels.

Chapter 6 describes the measurements of the stress response of non-aged and aged *urushi* films under different humidity levels (Stage 2 in Figure 1.4). Also, a 1D model will be developed and tested against the experimental observation. We will demonstrate the potential of our model by investigating the stress response in layers of *urushi* of different ages.

Chapter 7 describes the effect of the moisture content and ageing on the rheological behaviour of *urushi* material through tensile, tensile creep and recovery tests (Stage 4 in Figure 1.4). It also discusses the experimental results which describes the effect of moisture content and ageing on the mechanical properties of *urushi* films.

Chapter 8 describes the traditional Japanese process used to consolidate micro-cracks which appear on degraded *urushi* surfaces and its effectiveness in minimising the long term impact (Stage 5 in Figure 1.4).

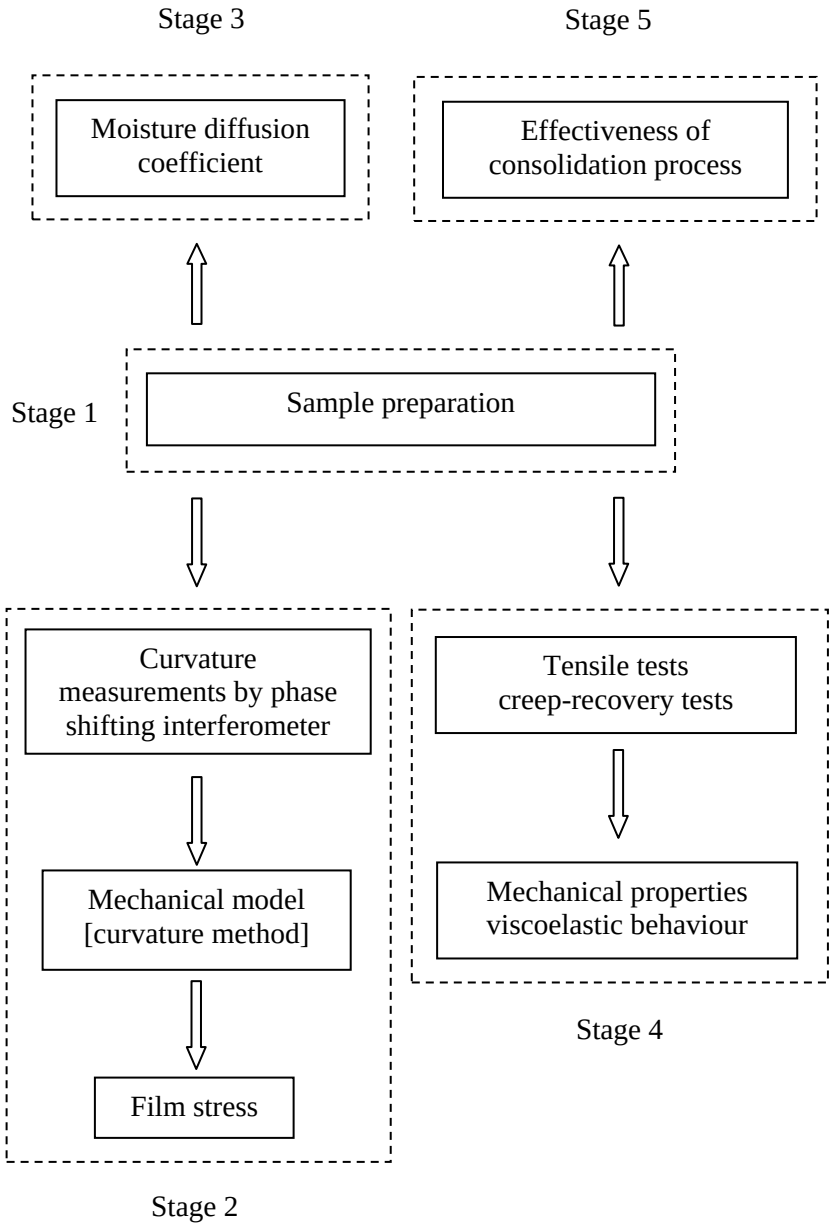

Figure 1.4: The work flow chart for the experimental programme.

1.5 Conclusion

The Mazarin Chest is one of the finest pieces of Japanese export lacquer to have survived from the late 1630's in the V&A's collection. The high quality of this piece is clearly evident in its lavish decoration, which is executed to an astonishing level of detail using a wide range of traditional Japanese decoration lacquer techniques. It also has a great scientific importance in the field of conservation science. This makes the research on Mazarin Chest and its relative subjects of great interest. The Mazarin Chest deteriorated over the centuries as a result of exposure to light, changes in temperature and relative humidity and previous western restorations. The result of this deterioration can be seen in terms of splits in the wood substrate, lifting metal foil, gold and silver, decoration, lifting mother-of-pearl decoration and degradation of the lacquer surface due to exposure to light. The Mazarin Chest project has been proposed and carried out, combining a comprehensive research on art, history and science and engineering, involving conservators, curators and scientists from the UK, Japan, Germany and Poland.

Chapter 2

Urushi and Mazarin Chest

2.1 Introduction

In order to be able to predict and control the behaviour of *urushi* under common environment conditions it is necessary to understand the mechanical behaviour of the material, not only under static conditions, but also in time varying states of relative humidity and ageing. Some work has been done in this area, and we look to exploring the state of the art before discussing the gap in the knowledge and our proposed programme of work.

2.2 East Asian lacquer overview

East Asian lacquer or *urushi*, is a natural polymeric material obtained from the sap of lacquer trees, *Rhus vernicifera* [3, 4] in China, Korea and Japan, *Rhus Succedanea* in Vietnam and Taiwan and *Melanorrhoea Usitate* in Thailand and Burma [5]. The plant is in the family that includes sumac, poison ivy, poison oak, mango and cashew. The

raw lacquer is a skin irritant, to which workers must develop a tolerance [6]. *Urushi* does not cure in the same way as other natural resins, which are usually dissolved in a solvent. When resin mixture is applied as a coating, the resin hardens into a solid film as the solvent evaporates. On the other hand, *urushi* cures as a result of a complex internal chemical crosslinking and, uniquely, does so only in the presence of high relative humidity. The resulting material is polymerized (like a plastic), it is very hard, lustrous and durable, resistant to water, acids, scratches, heat and exhibits excellent resistance to weathering indoors. These properties of *urushi* led to it being used as a protective, decorative and adhesive material in Japan and other oriental countries from ancient times. Examples include surfaces in shrines and temples, wooden bowls (lacquerware) and chests. Many of these objects are exhibited in museums in Japan, USA and Europe [6-10].

In Japan, sap is collected at the moment of oozing out from the cut trunk after removal of the outer bark of lacquer trees (Figure 2.1) [11] of age of about 7-10 years, at a 4-5 days interval from early June to late October. Each yield of sap is 120-200 g per tree. This scarce production makes *urushi* a very precious commodity. *Urushi* is graded according to the season it was collected and the age of the tree. Different grades of *urushi* are appropriate for various specific tasks [6].

Figure 2.1: Collection of *urushi* sap oozing out from cuts in the trunk of *urushi* tree [11].

2.3 Chemistry of *urushi*

The variety of sap *Rhus vernicifera* [12-14] is a very common natural product. Commercially available sap is a blend collected at different times. The constituents materials are water (20-30%), *urushiol* (60-65%) and an acetone insoluble powder, a mixture of water insoluble glycoprotein (3-5%), water soluble plant gum (6.5-10%) and enzymes (<1%). The plant gum contains mono-, oligo- and polysaccharides (5-7%), and the enzymes are laccase, lactase (a copper-glycoprotein enzyme having 4 atoms of copper in a molecule), stellacyanin, and peroxides. In sap, a water-in-oil type emulsion, a major part of the gum and the enzymes may be dissolved in the water phase, and the glycoproteins are in the oil (*urushiol*) phase [5, 15, 16].

The main component of the sap of the *urushi* tree is *urushiol*, whose chemical structure is shown in Figure 2.2 [7, 9, 17-19].

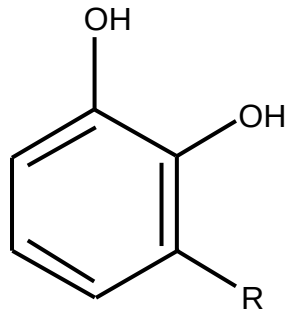

R : $(CH_2)_{14}$-CH_3	4 wt %
: $(CH_2)_7$-CH=CH-$(CH_2)_5$-CH_3	21 wt %
: $(CH_2)_7$-CH=CH-CH_2-CH=CH-$(CH_2)_2$	4 wt %
: $(CH_2)_7$-CH=CH-CH_2-CH=CH-CH=CH-CH_3	70 wt %
other constituent compounds with a C_{17}- side chain	1 wt %

Figure 2.2: Typical chemical structure and composition of *urushiol* [7].

2.4 *Urushi* process and treatment (*kurome*)

Raw *urushi* sap is a non stable water-in-oil type emulsion. As a result of the naturally high moisture content, the water soluble polysaccharides in the sap can aggregate to form large irregular islands during drying [20] (Figure 2.3(b)). It is therefore stirred and homogenized in an open vessel at room temperature for 30 minutes and then for 2 hrs at a temperature below 45 °C so as not to lose the activity of laccase, until the water content is reduced to 2-4% [5, 21]. The process of stirring and heating of the sap is known as *kurome* and leads to evaporation of water, polymerization of *urushiol* and reaction of glycoproteins with *urushiol*. The *urushi* constituents are homogenized and polysaccharides disappear into the oil phase in which the *urushiol*-glycoproteins complex is formed. Spherical grains of polymerized *urushiol* are surrounded by a thin wall of polysaccharides in the *urushi* film. Such a fine "core-shell" structure is believed to be responsible for the excellent durability of the *urushi* film owing to the high barrier of polysaccharides wall toward oxygen [4, 11, 20, 22] (Figure 2.3(a)). High humidity is essential for the crosslinking reaction to take place, explaining the need for the elevated RH required for curing. Figure 2.4 shows an electron micrograph of *urushi* film demonstrating a densely packed grain structure with the same diameter [ca. 0.1 μm], contaminated with polysaccharide particles (ca. 1-2 μm in diameter) deposited from water droplets [11].

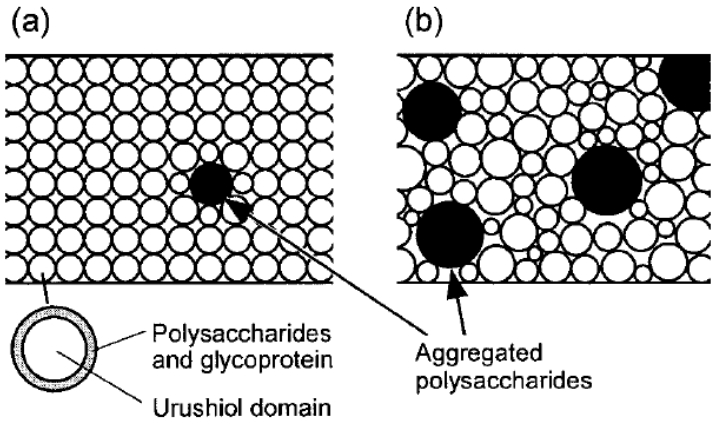

Figure 2.3: Schematic illustration of the structure of (a) *kurome*-treated *urushi* film and (b) sap [20].

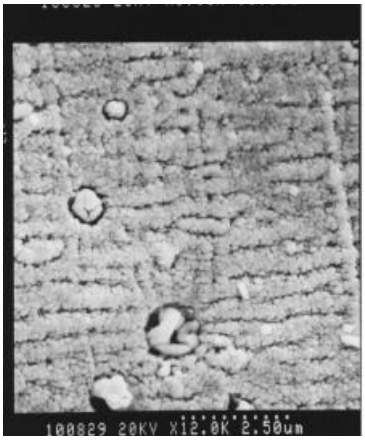

Figure 2.4: Scanning electron micrograph of *urushi* film [11].

The details of the *kurome* process are a closely guarded secret and differ from manufacturer to manufacturer [21].

A clear viscous *urushi* is composed of 3% water, *urushiol*, oligo-*urushiol*, enzymes, aggregates of polysaccharides and glycoproteins. The variation of viscosity and water content as a function of the stirring (cooking) time of sap is shown in Figure 2.5 [5]. We can see from this figure that the viscosity of sap decreases with stirring time, reaching a minimum, after which it rapidly increases again.

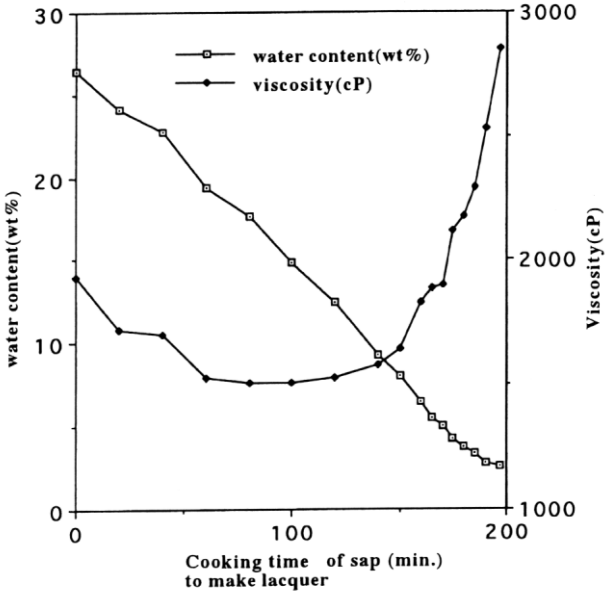

Figure 2.5: Variation of viscosity and water content in cooking sap to make *urushi* [5].

2.5 The effect of environmental conditions on the properties of *urushi*

2.5.1 Temperature

Obataya et al [20] investigated the effect of ageing on the dynamic viscoelastic properties, tensile storage modulus E and loss tangent $\tan\delta$ by using an Orientec DDV-25FP viscoelastometer. Three different kinds of *urushi* films were used, virgin (V), clear (C) and black (B) oriental *urushi*. These were made from the sap of *Rhus vernicifera* harvested at Iwate (Japan). The films were cast on a Teflon plate and dried at 20 °C and 85% relative humidity (RH) for 3-10 days and aged over 1000 days at room temperature. The virgin *urushi* was a neat filtered sap that has a naturally high moisture content of more than 20% and a low degree of polymerization. The clear and the black *urushi* had lower moisture content of about 3% and higher degree of polymerization as a result of *kurome* treatment. The black *urushi* was coloured with 1% (w/w) of iron powder.

The temperature variation of the storage modulus E and loss tangent $\tan\delta$ at 11 Hz within the range of -150-300 °C for the clear *urushi* film is shown in Figure 2.6. With respect to $\tan\delta$ peaks, three relaxation processes labelled α, β, and γ were detected. These were attributed to the glass-transition of polymerized *urushiol*, the motions of water molecules remaining in the film, and the molecular motions of methylene groups in the side-chains of *urushiol*, respectively.

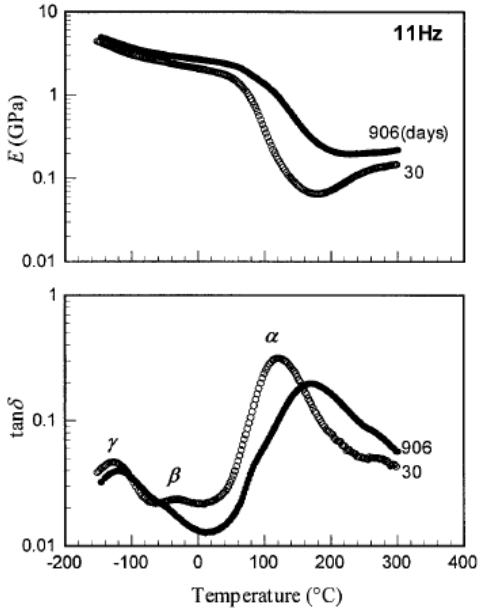

Figure 2.6: The temperature variation of the storage modulus E and loss tangent at 11 Hz for the clear *urushi* films aged for 30 days (○) and 906 days (●) [20].

Figure 2.7 shows the temperature location of the α loss peak T_α and its peak value $\tan\delta_\alpha$ plotted against the ageing duration, t. The glass transition temperature of the *urushi* films T_α shifted to higher temperatures and its loss peak $\tan\delta_\alpha$ decreased with an increase of ageing duration. These changes reflected the oxidative polymerization of *urushiol* and formation of crosslinking between their side chains. The B and V *urushi* films showed lower T_α and higher $\tan\delta_\alpha$ values than the C *urushi* films at the same time t. As the chemical components of these three *urushi* films were the almost identical, the variation in T_α and $\tan\delta_\alpha$ can be attributed to the effect of the *kurome* process and the addition of trace iron.

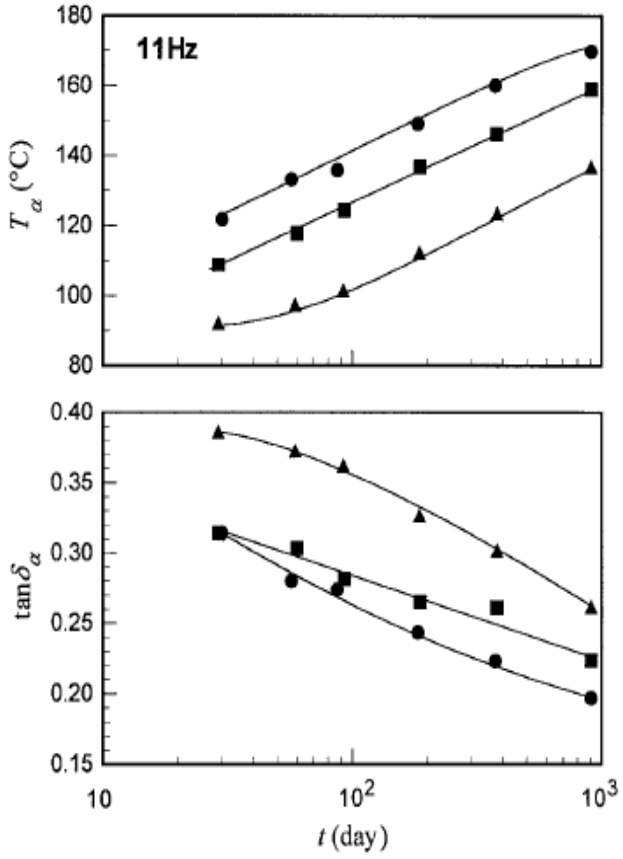

Figure 2.7: Changes in the peak temperature T_α and peak value $\tan\delta_\alpha$ of the α relaxation process detected in the clear (•), black (▲), and virgin (■) *urushi* films with the elapse of time (days) [20].

The storage modulus E at 20 °C increased and the loss tangent at 20 °C decreased as shown in Figure 2.8.

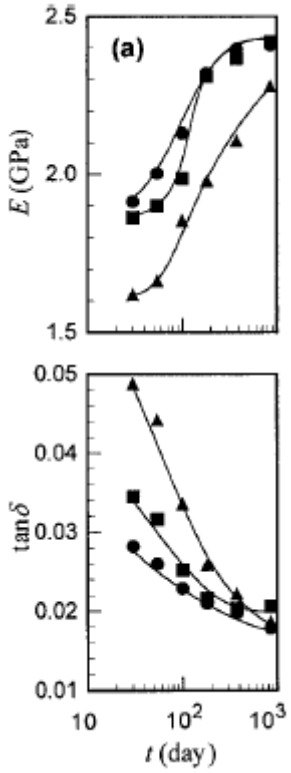

Figure 2.8: The storage modulus E and loss tangent at 20 °C and 11 Hz for *urushi* films plotted against the ageing duration t in the clear (•), black (▲), and virgin (■) [20].

2.5.2 Humidity

Lacquerware is susceptible to damage from very dry conditions or fluctuating humidity. Relative humidity (RH) fluctuation causes the wooden substrate to shrink and expand thus causing the *urushi* to crack to relieve the stress and to lose adherence to the substrate. For this reason, cracks most often appear along seams and joints, and usually in the direction of the grain of the underlying wood substrate. If the shrinkage becomes permanent then the *urushi* surface will no longer lie flat [23, 24]. In low RH, water, an essential part of *urushi* structure is lost and as a result *urushi* becomes more brittle, less strong and susceptible to attack by water and oxygen. If *urushi* is exposed to cycles of low and high humidity it will eventually start to flake off its wooden core. It is important not to let the humidity drop too low or fluctuate wildly to keep lacquerware in prime condition. In museums, a constant humidity of 50% to 60% is usually recommended during storage, treatment and display. In Japan the most valuable pieces of lacquerware are stored in silk bags or wooden boxes and brought

out for special occasions. The box serves a number of functions: it keeps the item from exposure to light, protects it from structural damage and buffers any changes in humidity [23].

Obataya et al [20] also investigated the effect of moisture on the viscoelastic properties of *urushi* films. Figure 2.9 shows the water sorption of C and V *urushi* films aged over a thousand days. The equilibrium moisture content (MC) of the V *urushi* film was higher than that of the C *urushi* film over the RH range (10%-90%). Obataya et al found that the hygroscopicity of polysaccharides is higher than that of the polymerized *urushiol*. Furthermore, the hygroscopicity of polysaccharides in the V *urushi* film must be higher than that in the C *urushi* film because the former is held more loosely among the *urushiol* domains. Thus, the higher moisture content of the V *urushi* film is attributable to the hygroscopicity of polysaccharide aggregated during drying. Figure 2.10 shows the changes in E and $\tan\delta$ for C and V *urushi* films at 30 °C and 0.5 Hz with increasing the moisture content (MC). As shown in Figure 2.10, E decreased and $\tan\delta$ for C and V *urushi* films increased with increasing moisture content of *urushi* film, showing that *urushi* films soften with increasing moisture content.

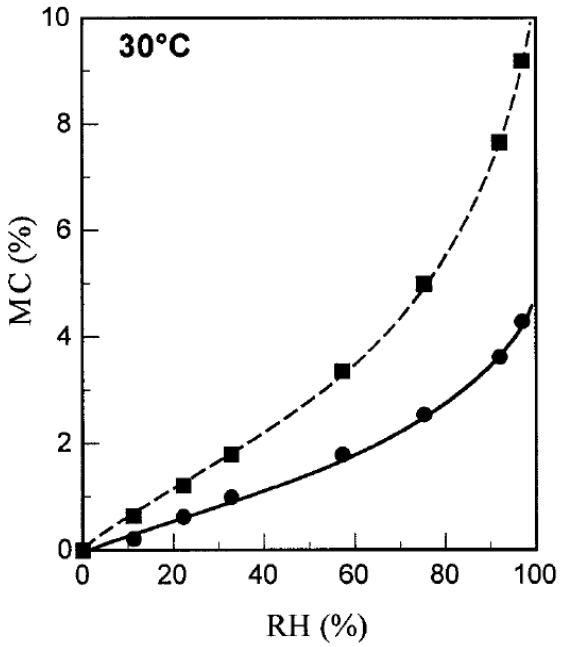

Figure 2.9: Equilibrium moisture contents (MC) of the clear (•), and virgin (▪) *urushi* films aged over 1000 days [20].

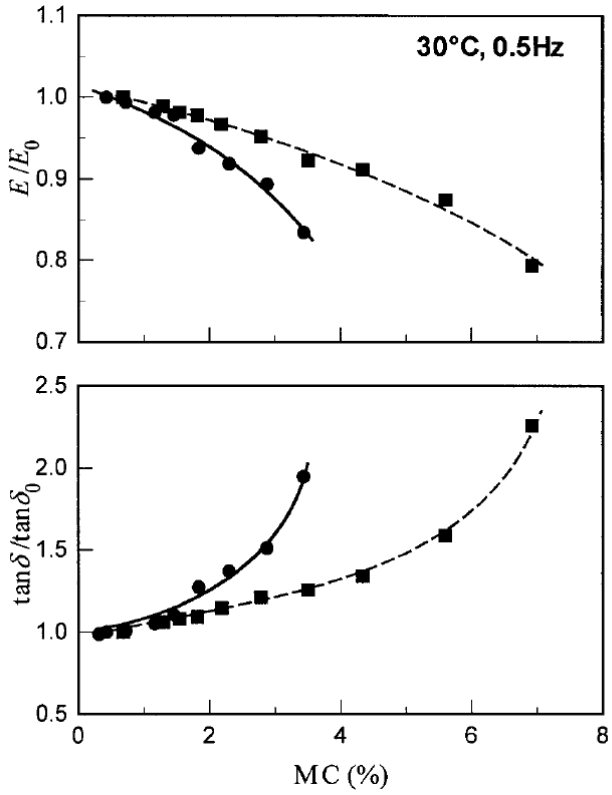

Figure 2.10: Changes in E and $\tan\delta$ at 30 °C for clear (•), and virgin (▪) *urushi* films [20].

Urushi properties are also affected by the moisture levels within the material. Ogawa et al [10] investigated the effect of water on mechanical properties of *urushi* film of constant thickness. Curing was achieved through three steps: at 60% RH for 4 hrs, 70% RH for 18 hrs and 80% RH for 24 hrs. A tensile test was carried out using a AGS-1000B tensile tester (Simadzu Co., Ltd., Japan) with a load cell of 981 N at a test speed of 2 mm/min. Test samples were 4 mm × 35 mm × 50 μm. The tensile stress-strain tests were conducted under various degrees of humidity (15%-100%) as shown in Figure 2.11 and the relation between tensile properties and humidity are shown in Figure 2.12. In general, *urushi* films become flexible by water absorption, leading to an increase in the strain at break and a decrease in the elastic modulus, demonstrating that the water serves as a plasticizer.

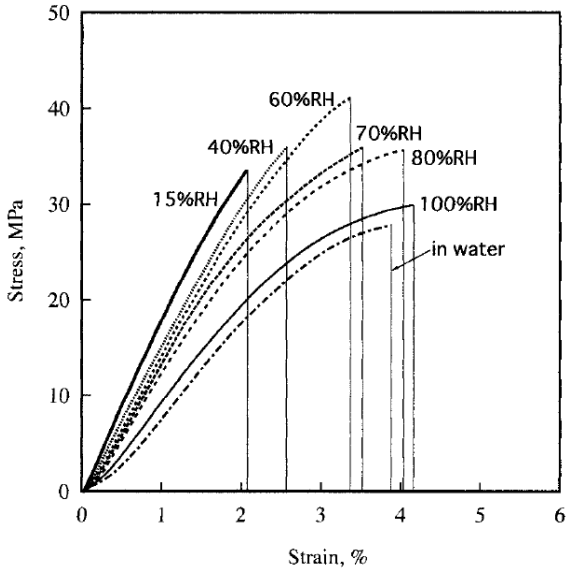

Figure 2.11: Effect of humidity on the tensile stress-strain curves for *urushi* film [10].

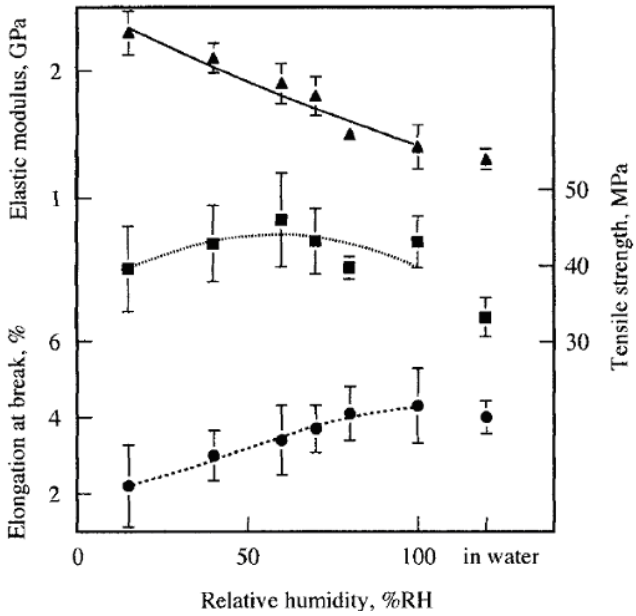

Figure 2.12: Relation between stress-strain properties and RH: (▲) elastic modulus, (■) tensile strength, and (●) strain at break [10].

Ogawa et al also investigated the changes of the relaxation modulus, $E(t)$ over 100hrs. The stress relaxation test was conducted using a dynamic viscoelastometer Rheovibron DDV-II-C (Orientec Co., Ltd., Japan). The experiments were carried out under a set temperature and humidity. Figure 2.13, on the left side, shows the relaxation moduli $E(t)$ at 60% RH. The master curve under this condition was obtained by applying the

principle of time–temperature superposition where a reference temperature was adopted as 293 ^{o}K (20 °C). The result is shown on the right side of Figure 2.13, where the long term region above the temperature of 333 ^{o}K was neglected because the chemical structure of the film changed during the experiment. The relaxation modulus for long or short term can be predicted from Figure 2.13. Figure 2.14, shows the relaxation modulus under dry and wet conditions, where the modulus of the film in a wet condition decreases with time at a high rate.

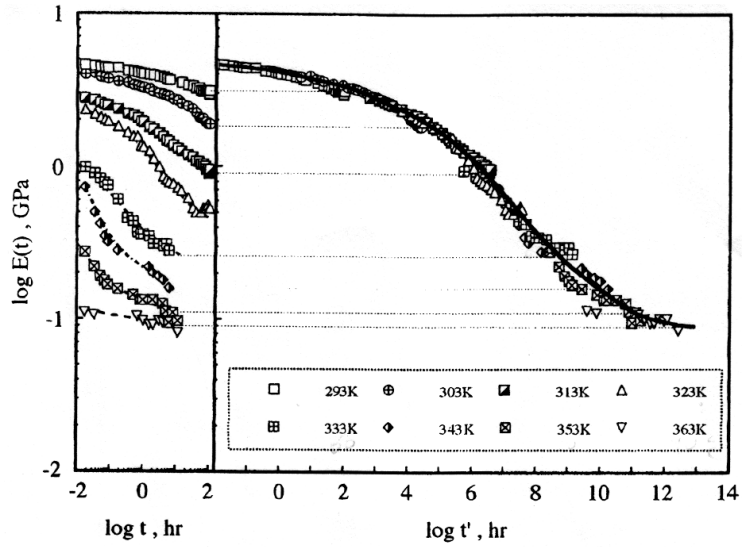

Figure 2.13: Relaxation modulus of *urushi* film and master curve for *urushi* film at 60% RH [10].

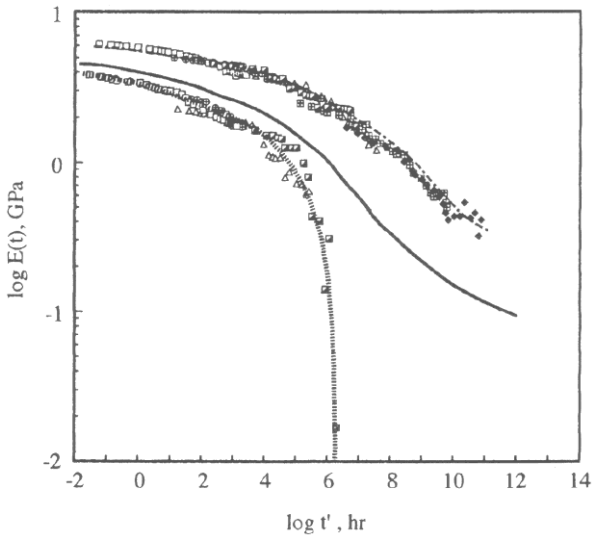

Figure 2.14: Relaxation modulus of *urushi* film under various humidity levels: (---) 20%, (__) 60%, and (_ _ _) 100% RH; (□) 293, (⊕) 303, (◆) 308, (◪) 313, (△) 323, (⊞) 333, (♦) 343 K [10].

Urushi film has a tendency to become brittle under dry conditions and toughens under wet conditions. On the other hand, the film becomes sticky and soft under high humidity or in water. When lacquerwares are used under these conditions, stress builds up between *urushi* and the substrate, which is usually wood. This stress makes bonding strength decrease in between *urushi* and adherent. The bonding strength is the unit load applied in tension, compression, flexure, cleavage, or shear, required to break an adhesive assembly, with failure occurring in or near the plane of the bond.

As a result of these stresses, *urushi* will eventually peel off from the substrate. It was concluded by Ogawa et al that water is one of the most important influences on the durability of lacquerware.

2.5.3 UV exposure

It is believed that the main cause of fading and loss of gloss in *urushi* is exposure to ultra-violet light [23, 25, 26]. The surface of the lacquerware fades and becomes dull as the *urushi* molecular structure during sustained exposure. Some black lacquer pieces, for example, eventually turn a mottled brown and also lose their sheen. Under magnification, one can see that the dull appearance is actually a network of very fine cracks (micro-cracks) that have formed on the surface of the lacquerware. The traditional consolidation technique, *urushi gatame*, is based on the impregnation of micro-cracks with diluted *urushi*. However, once the micro-cracks have formed they can penetrate through the decorative *urushi* layers and into the foundation layers causing further damage by trapping the solvents being used to clean the lacquer, leaving the lacquer vulnerable to further damage [26].

Lacquer damaged by light loses its durability, it lacks its normal resistance to water and other solvents and becomes brittle [23, 27, 28]. It is known that the damage increases with the length of exposure and the intensity of the illumination [6].

Ogawa et al [9] investigated the effect of exposure to fluorescent lamps on the mechanical properties of East Asian *urushi* films. The films were exposed to light under three different conditions: uncovered, in a box of acrylic plates, and in a box of glass plates. Hardness was obtained using a hardness meter (MVK-E; Akashi Seisakusho, Japan) with a load of 25 g under a pressing time of 15 s and tensile tests

were carried out using a AGS-1000B tensile tester (Simadzu Co., Ltd., Japan) with a load cell of 100 kg at a test speed of 1 mm/min. The test samples were prepared in a rectangular size of 35 × 5 mm. They found that the hardness and the elastic modulus increased with exposure time, while the tensile strength and the elongation at break decreased with exposure time. They concluded that the increased hardness is related to a crosslinking reaction by the enzyme laccase over the whole region of the films. Other studies have shown that following exposure to UV radiation, the surface of *urushi* fades and becomes dull as light breaks down the molecular structure [26].

Mee-Young Park et al [25], investigated the effect of UV-degradation chemistry of *urushi*, the effect of photostabilization on the physical properties of *urushi* coating and the effect of weathering exposure on *urushi*. Hindered amine light stabilizer (HALS) and benzotriazole UV absorber were added to *urushi* to improve the weatherbility (resistance to light degradation) of *urushi*. Three different mixtures were prepared: 1) unstabilized purified *urushi* (PL); 2) PL plus 2% HALS and 3) PL plus 2% weight benzotriazole UV absorber. Each mixture was coated on glass substrate slides, 60 μm thick, and dried for one week at room temperature and at 75±5% RH. The samples were exposed for 300 hrs at 50 °C to continuous irradiation with a UVB–313 lamp in a Q-Pandel Accelerated Weathering Tester (Q-UV). Figure 2.15 shows the Fourier Transform Infrared–Attenuated Total Reflectance, FTIR/ATR, spectra of unexposed and exposed PL. The effect of weathering exposure is shown in the difference of the spectra. The difference spectrum was obtained by using Spectra-Cal software after baseline correction.

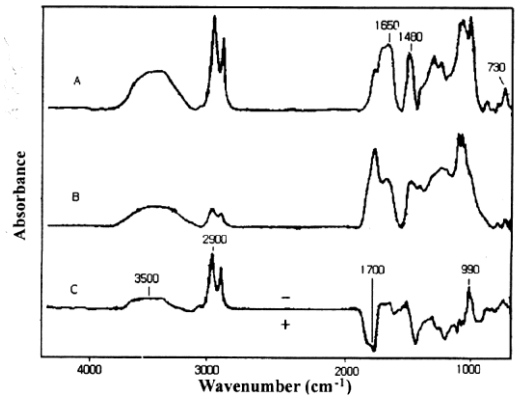

Figure 2.15:FTIR-ATR spectra of *urushi* film: (a) Original; (b) after 100 hrs exposure; (c) difference between spectra in a and b [25].

The presence of negative and positive intensity bands in the difference spectra can be regarded as resulting from the chemical changes due to photo-gradation. The negative absorbance in the difference spectrum reflects the structures that were formed during the photo-degradation, and the positive absorbance reflects the structures that were lost.

The difference spectrum is dominated by strong bands near 3500, 2900, 1700, 1650, 1480, 990 and 730 cm^{-1}. The broad band near 3500 cm^{-1} was associated with OH stretching in *urushiol*. The strong bands related to C-H stretching in the *urushiol* side chain were observed near 2900 cm^{-1}. The strong bands near 1650 cm^{-1} and 990 cm^{-1} may be related to the C-H out-of-plane bending in the quinone group and in conjugated triene, respectively.

The four sets of bands decrease in intensity when the *urushi* films are exposed to UV. The band near 1480 cm^{-1} is characteristic of CH_2 bending; its observed decrease in intensity is partly related to decomposition of *urushiol* side chains. Presumably, the weak peak at 730 cm^{-1} also decreased due to degradation of the aromatic substitute of *urushiol*. In contrast, the very strong peak near 1700 cm^{-1} increased and was attributed to C=O stretching in the various carbonyl functional groups formed by photo-oxidation. These results are consistent with the hypothesis that *urushi* network degrades mostly in the unsaturated side chains. A small number of photosensitive groups had already been formed in *urushi* film during the photo-degradation processing. The photolysis of these groups gives rise to carbonyl products. Carbonyl

absorbance starts increasing immediately for the unstabilized *urushi* film during UV exposure. Figure 2.16 shows the IR carbonyl intensity near 1700 cm^{-1} as a function of UV exposure time. The rate of increase of carbonyl intensity for photostabilized mixtures is lower than that for unstabilized mixture.

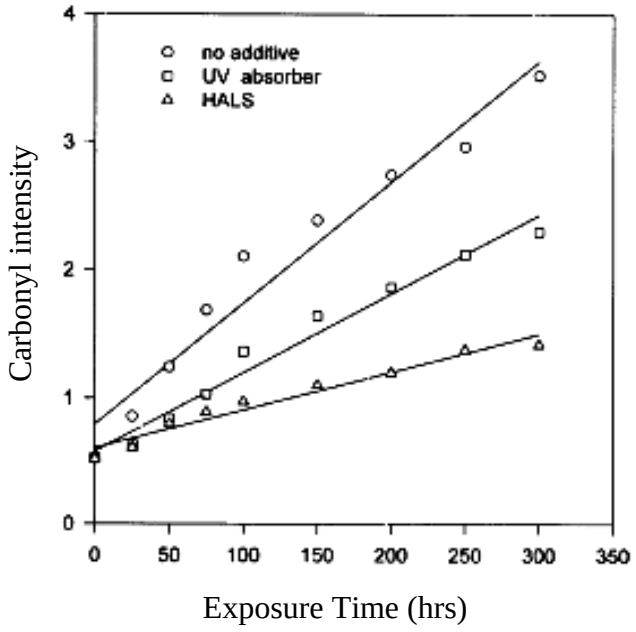

Figure 2.16: Increase in carbonyl intensity with UV exposure time [25].

Scanning electron micrographs of the surface of *urushi* are shown in Figure 2.17. As shown in Figure 2.17(a) the surface of unexposed *urushi* film has small regions 0.1-2 μm diameter, due to polysaccharide particles composed of polymerized *urushiol* and glycoproteins, (Figure 2.3(a)). After exposure to UV light, Figure 2.17(b), large black regions of 10-80 micron in diameter appear together with small regions of 0.1-3 μm diameter. The large black regions may be being formed due to deterioration of the polysaccharide walls and polymerized *urushiol*. After exposure to UV light, the small regions become larger and more numerous.

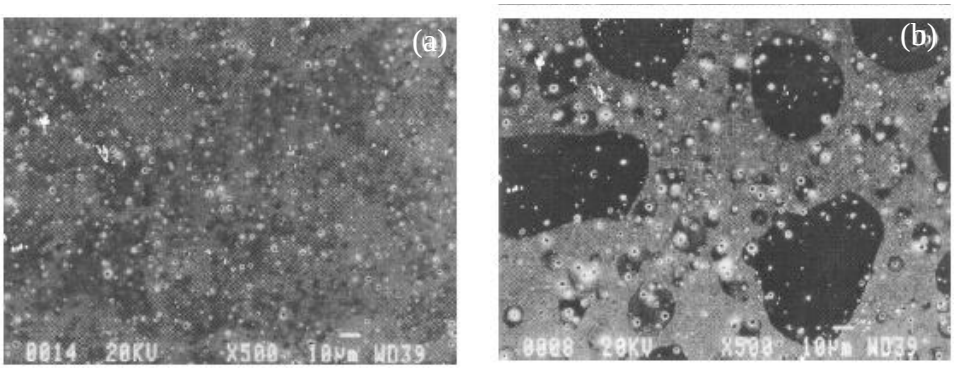

Figure 2.17: SEM of (a) unexposed *urushi* film and (b) *urushi* film exposed to UVB-313 lamp for 100 hrs [25].

In case of *urushi* containing 2% weight HALS, photo-degradation is significantly inhibited as shown in Figure 2.18.

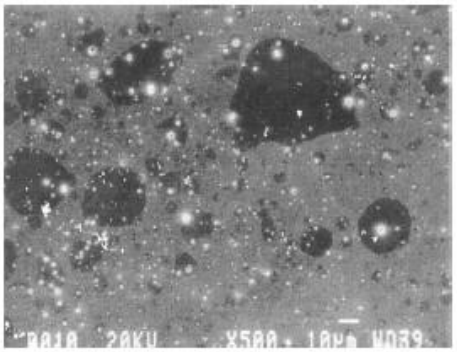

Figure 2.18:SEM of *urushi* film containing 2% wt HALS exposed to UVB-313 lamp for 100 hrs [25].

To confirm this result they also measured the weight loss of *urushi* film during photo-degradation as shown in Figure 2.19. All *urushi* films lost weight as a result of photo-degradation. This may be due to evaporation of water in the film. The same result was obtained by Toyoshima [29], where *urushi* film lost weight as a result of photo-degradation with UVA.

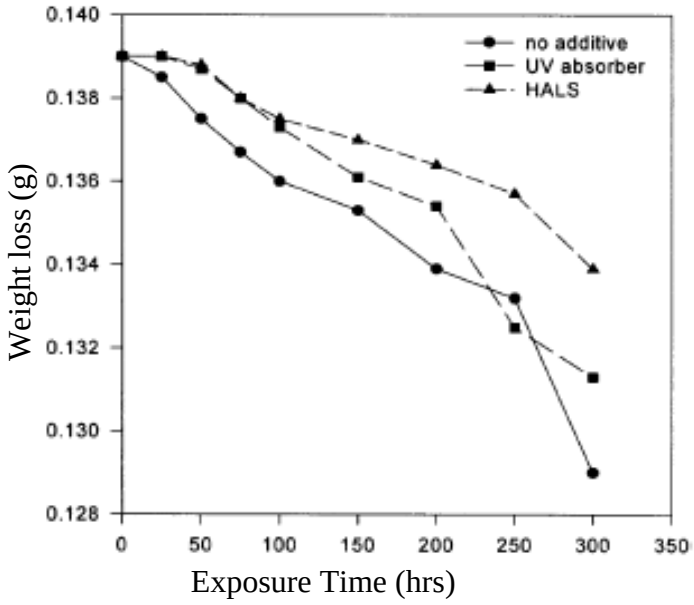

Figure 2.19:Weight loss of *urushi* film with UV exposure time [25].

FTIR/ATR analysis of an accelerated weathering test (Q-UV) showed that the addition of 2 wt% HALS into *urushi* enhanced photostabilization up to three times, which was supported by the results of weight loss measurements and SEM analysis [25].

Miyakoshi et al [28] developed a mixer capable of repeated *kurome* that make *urushi* dry fast in the natural environmental. The repeated *kurome* process (Section 2.4) is based on stirring raw *urushi* at room temperature for 1.5 hrs, then at 20-40 °C for 2 hrs until the concentration of water is reduced to 3-5% for the first *kurome* process (K-0). Water is added to K-0 to increase the moisture about 20-25%, comparable to the water concentration of the raw *urushi*, and the *kurome* process is repeated by adding water and reducing it, the second (K-1), the third (K-2), the fourth (K-3), the fifth (K-4) *kurome* process were obtained. The moisture concentration of raw and repeated *kurome urushi* are shown in Table 2.1. The moisture concentrations of the raw and repeated *kurome urushi* were estimated using an MX-50 moisture meter (A&D Co. Ltd., Japan). The water concentration of raw *urushi* was 24.5% and at least 3% moisture is required for the laccase oxidation of *urushiol*.

Table 2.1: The moisture concentration of raw and repeated *kurome urushi*.

urushi sap	Moisture (%)
Raw	24.5
K-0	3.55
K-1	3.49
K-2	3.48
K-3	3.34
K-4	3.47

Figure 2.20 shows SEM and SPM images of a cross section and the surface of raw and K-0 *urushi* films after drying at 20 °C 70% RH for 1 month. The images revealed that the holes in K-0 film are smaller than in the raw film. The holes are the marks of water drops in *urushi* sap. The holes were 2.08 μm in the raw *urushi* film and 0.97 μm in the K-0 *urushi* film. Also as a result of repeated *kurome* process, the drying time decreases.

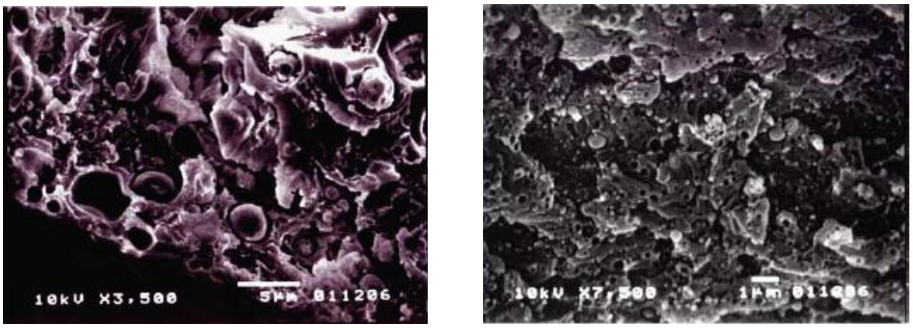

(a) (b)

SEM images of cross section of (a) raw, and (b) K-0 *urushi* film.

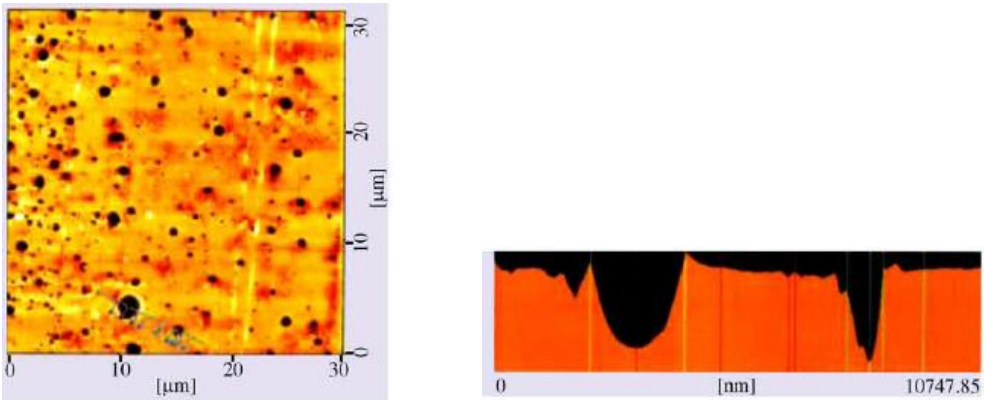

(c) (d)

SPM images of (c) surface, and (d) cross section of raw *urushi* film. The diameter of the biggest hole is about 2.08 μm.

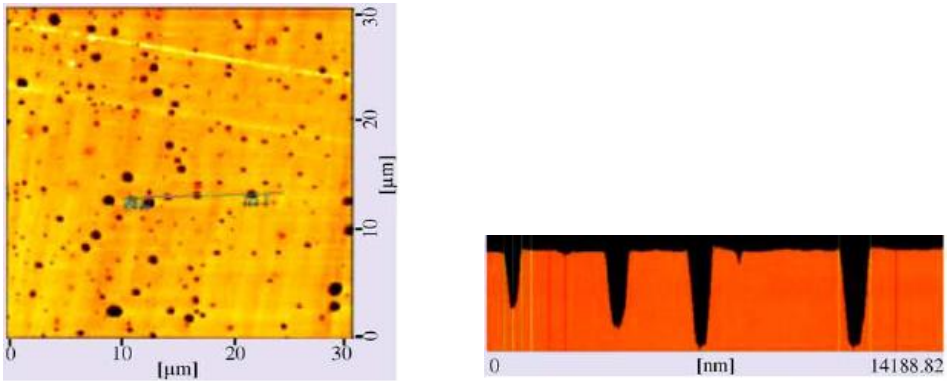

(e) (f)

SPM images of (e) surface and (f) cross section surface of K-0 *urushi* film. The diameter of the biggest hole is about 0.97 μm.

Figure 2.20: SEM and SPM photographs of the raw *urushi* and K-0 *urushi*.

2.6 The structure of lacquerware objects

Structurally, lacquerware objects are composed of substrate, foundation, coating and decoration. While wood is the most commonly substrate material for lacquer objects, there are two kinds of foundation. In one of them, *kokuso* (mixture of *urushi*, sawdust and hemp fibres), *nonokise* or *kamikise* (adhering of hemp cloth or paper, respectively, to the substrate) are applied to reinforce the substrate. In the other one, *jinoko* (coarse powder earth), *tonoko* (fine powdered earth) or *gofun* (calcium carbonate) are used to smooth the surface of the substrate. *Urushi*, wheat flour paste or animal glue is used in making these foundations. Normally several layers of foundation are applied. Over the foundation, several thin layers of *urushi* are applied. After each layer, the substrate is cured in a chamber with a relative humidity of 70-80% at 20-25 °C. The surface of *urushi* is polished with hard and then soft charcoals with water or oil, then sap is rubbed into the polished surface and cured to obtain a high gloss and durable coating surface. Coating-curing-polishing-rubbing-curing is repeated 10-20 times to obtain a lacquerware finish ready for decoration. This process is called *Roiro Siage*. There are various types of decoration applied on lacquerware objects, the most widely used being [27]:

- *Hiramakie* (flat sprinkled picture).
- *Takamakie* (raised sprinkled picture).
- *Raden* (mother-of-pearl) and *hyomon* (metal foil) inlay.

2.7 Nature of damage in Mazarin Chest

In the years since the Mazarin Chest was made, it suffered significant damage due to fluctuations in RH and exposure to light. The following section summarizes different types of damage [26]:

2.7.1 Structural damage

Expansion and contraction of the wooden substrate of the lid, in response to fluctuation in RH, lead to:

- Shrinkage across the centre of the lid, preventing the lid from closing. This warps it approximately 4 mm.
- Movement of the metal catch of the lock to inward.
- Hairline splits along the corner joints as show in Figure 2.21.
- Cracks are found in parts where the lid and the body join, along parts where the board and frame of the lid join and also on the reverse side of the lid [26, 30].

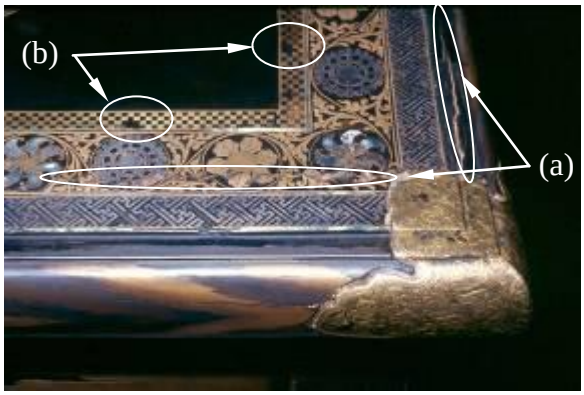

Figure 2.21: Detail of the right corner of the lid showing: (a) Stress fracture of the lacquer along the cleated joint line with associated loss and tenting (up to 3 mm high) of lacquer and decoration; (b) Exposed foundation layers in the inner square gold foil and losses of gold squares, silver and mother of pearl.

2.7.2 *Urushi* damage

As a result of structural damage mentioned before, *urushi* surface and foundation layers around the cracks are poorly adhered (Figure 2.21) and there are losses of *urushi* in approximately ten places, ranging in size from 1 mm ×1 mm to 10 mm ×15 mm. Additionally, exposure to light has caused photo-degradation of *urushi* with loss of lustre as micro-cracks have formed on the surface of *urushi* as shown in Figure 2.22(b). Previous applications of black Western natural resin to the *urushi* surface, in an attempt to restore its shine, resulted in changing the original decorative scheme from the original silver *makie*. In addition, the black varnish layer has been lost from some areas, leaving the original surface partially visible in many areas.

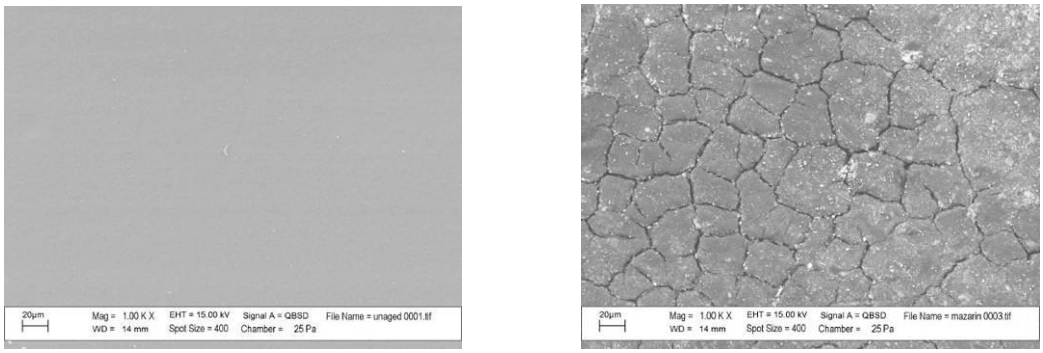

(a) (b)

Figure 2.22: SEM image showing the surface of (a) Freshly made *urushi* and (b) Mazarin Chest surface [2].

2.7.3 Decoration damage

Passive abrasive cleaning combined with photo-degradation of *urushi* coating has disfigured some areas of the black background and has exposed parts of the foundation (*shitaji*) layers (Figure 2.23(a)). Polishing the silver decoration and the applied elements in the past has resulted in loss of detail (e.g. *tsukegaki* decoration on the silver *hyomon*), damage to adjacent lacquer, and loss of poorly adhered decorative silver foil (Figure 2.23(b)). All silver decorative elements are tarnished. There is extensive lifting and wrinkling of gold and silver foil decoration (Figure 2.23(b, c)). There is also extensive lifting of the mother-of-pearl decoration (Figure 2.23(d)) where the shell is broken and has been lost in five places.

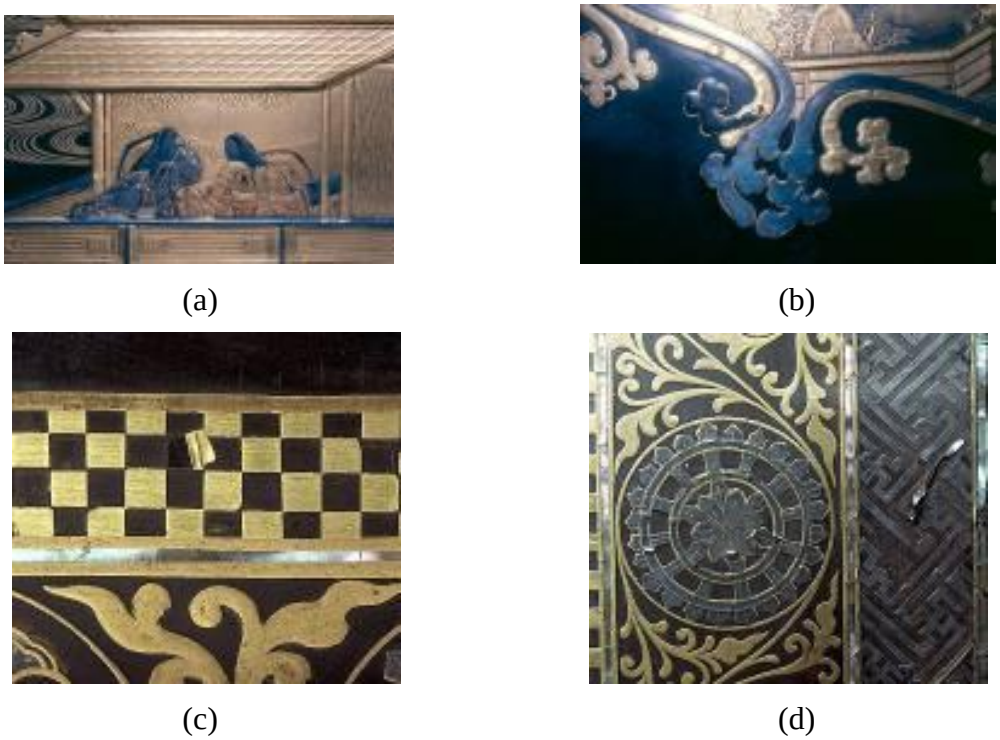

(a) (b)

(c) (d)

Figure 2.23: Examples of decoration damage: (a) Loss of facial detail as a result of corrosion and cleaning; (b) lifting and losses of silver and gold foil decoration; (c) wrinkling of gold foil decoration; (d) poorly adhesion and lifting of silver decoration and mother-of-pearl.

2.8 Record of past storage and display

It is likely that the Mazarin Chest has been on display for long periods since it was acquired by the V&A in 1882. For example, it was on continuous display at the V&A since the early 1960s. From 1986 to 1998 the Mazarin Chest was displayed in the Toshiba Gallery of Art and Design located at the V&A, under light levels of 80 lux and UV levels of less than 5 μW/lumen. The RH in the Toshiba Gallery ranges from 38% to 53% (15% annual variation) as shown in Figure 2.24. In October 1998 the chest was rotated off display and into an acrylic box as shown in Figure 2.25, located at the V&A main storage repository in Olympia, London. The stores are dark and unlit except when museum staff visit. The annual RH in storage ranges from 35% to 54% (19% annual variation) as shown in Figure 2.26.

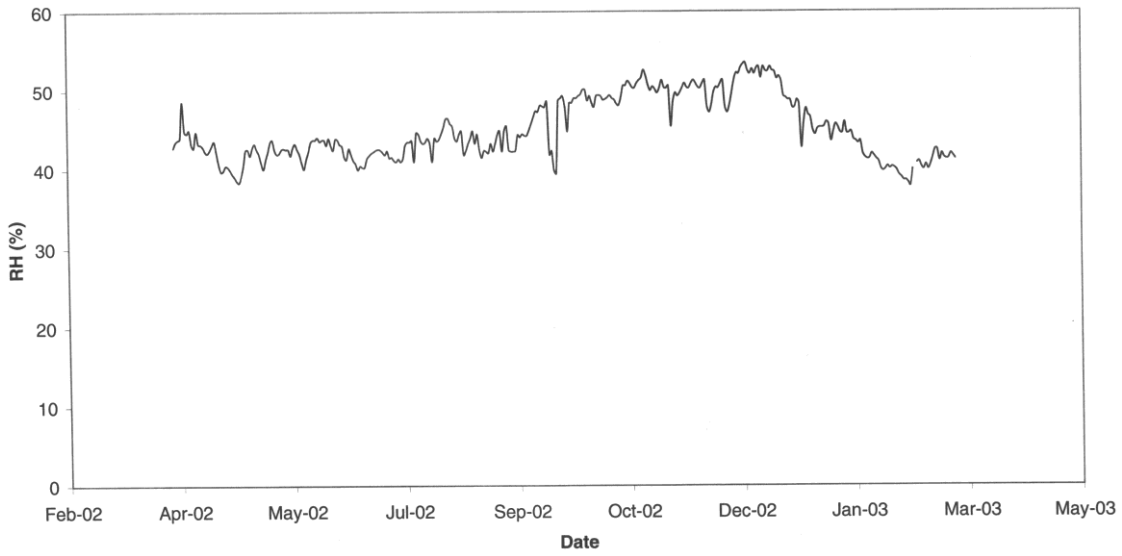

Figure 2.24: The RH variation in the Toshiba Gallery of Art and Design located at the V&A April 2002 – March 2003.

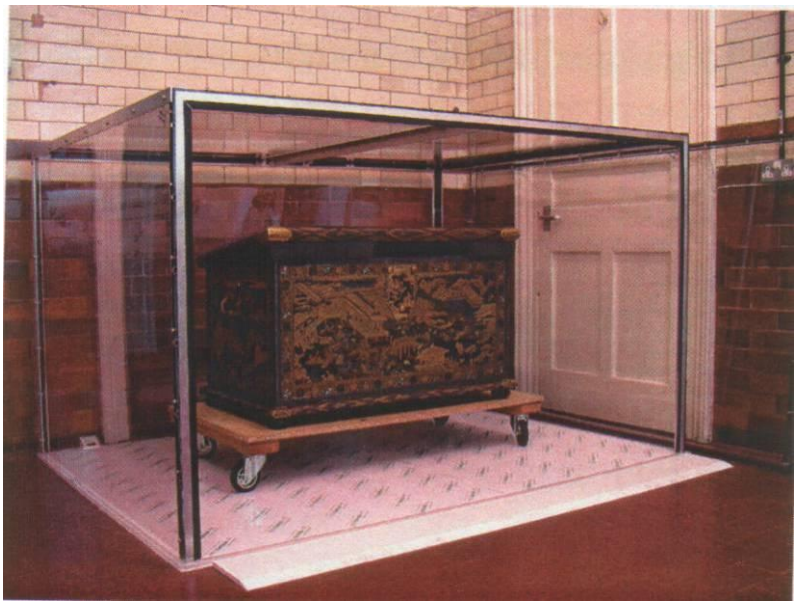

Figure 2.25: Acrylic box for storage and conservation treatment. Located at the V&A main storage repository in Olympia, London.

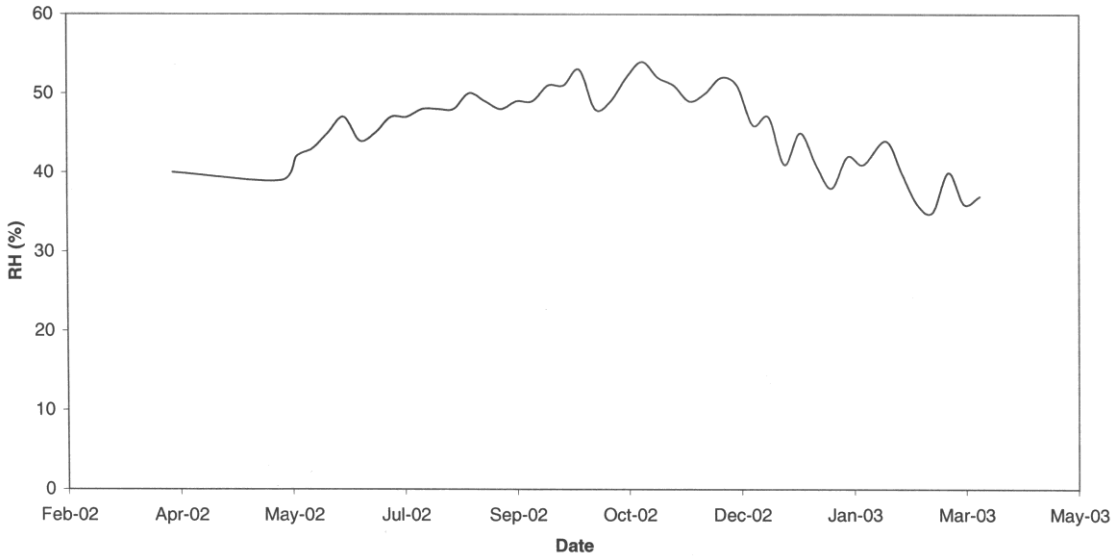

Figure 2.26:.The RH variation in the storage April 2002 – March 2003.

2.9 Conclusion

It is clear that the behaviour of *urushi* is highly complex, with strong changes in its mechanical behaviour when subjected to changes in moisture content and UV illumination. Many studies have been done on the chemical structure and reaction of *urushiol* (main component of *urushi*), but articles on the mechanical properties and responses of *urushi* film are of a comparatively small number. In order to formulate a predictive mechanical model for *urushi* that includes its constitutive relations, a comprehensive analysis of the response of *urushi* to changes in environmental conditions is still required in order to determine the precise nature of the relationship between stress, strain, moisture content and thermal and UV conditioning. Moreover, as the ultimate cause for the formation of surface micro-cracks is the surface stress, detailed measurements of the dependence of film stress with environmental conditions are required.

Chapter 3
Development of a Methodology for Preparing *Urushi* Films

3.1 Introduction

Stresses can develop within coatings during film formation through temperature changes and relative humidity fluctuations and these stresses have an effect on coating degradation. They may influence characteristics such as the resistance of the coating to wear and fatigue crack propagation. Furthermore, there is often a danger that the presence of stresses may promote debonding and palliation of the coating [31-34]. Therefore measuring stresses in coatings is of great significance.

In Chapters 1 and 2 we have discussed the importance of determining the response of *urushi* to environment changes. In this work the curvature method (described in 4.2) was used to determine the average plane stress developed in a thin *urushi* films. It can be measured by comparing the deflection of a substrate covered with a thin *urushi* film

relative to a reference state. However, in order to be able to achieve this, a standardised method for sample preparation must be developed. In this Chapter we lay out the methodologies and procedures that we used to produce consistent *urushi* samples. To prepare *urushi* samples, we followed some traditional Japanese processes such as the filtration, mixing and curing processes and spin coating was used to spread a thin layer of *urushi* on glass substrate.

3.2 *Urushi* preparation

The preparation of *urushi* samples involved several stages, each with the end point in mind of producing consistent thin layers. The stages are as follows:

1. Filtration.
2. Mixing process.
3. Glass substrate.
4. Coating process.
5. Curing condition.

In the follow sections we will describe these processes in detail.

3.2.1 Filtration

The *urushi* lacquer used in this study is *Kijiro urushi*, product of Wantanabe Syoten Co., Japan. As *urushi* is a natural product, it can often contain unwanted objects and particles. The first stage, therefore, in *urushi* preparation is the filtering to eliminate all impurities. We followed the traditional Japanese filtration process of using Rayon sheets to filter *urushi* by wrapping and twisting it as shown in Figure 3.1, repeating seven times with three Rayon sheets each time.

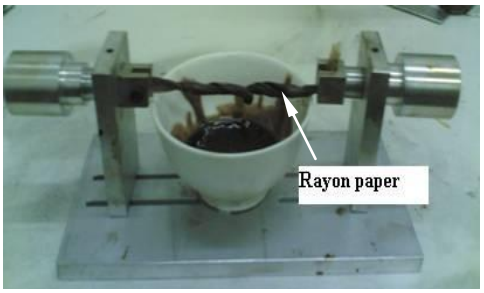

Figure 3.1: Traditional Japanese filtration method.

3.2.2 Mixing process

Raw *urushi* is a non-stable water-in-oil type emulsion. The water soluble polysaccharides in the raw *urushi* can often aggregate during drying [20] and therefore, *urushi* is mixed and homogenized for about 3 minutes to avoid aggregate formation. Gentle manual mixing is required to avoid bubble production.

3.2.3 Glass substrate

In order to measure depth averaged stresses using the curvature measurement method, it is necessary to deposit layers of known thickness onto a substrate. We obtained these *urushi*-substrate samples by casting a small amount of *urushi* onto the top surface of a BK-7 glass substrate of thickness 190±5 μm and 22 mm in diameter. Prior to applying *urushi*, the bottom surface of the substrate is coated with a thin film of a metallic coating using a thermal evaporation technique (Edward E 306 Vacuum Evaporator) to increase its reflectivity and thus obtain high visibility interference fringes. The metallic coating prevents interference fringes due to multi-reflections within the glass substrate thickness and within the *urushi* film. Two different types of metallic coating were used, Aluminium (Al) and Nickel Chromate ($NiCrO_4$). We found that the bonding between Nickel Chromate and the glass substrate is stronger than the bonding between Al and the glass substrate and consequently employed that in our work.

3.2.4 Coating process

Generally, in lacquerware artefacts, plastic or wooden spatulas are used to spread a thin layer of *urushi* over a wooden object. We found that it is difficult to obtain a homogenously thin layer of *urushi* on a small size glass substrate in a controlled fashion using this technique and opted to use the more reliable spin coating technique instead.

3.2.4.1 Spin coater theory

The spin coating process involves depositing small drop of liquid onto the centre of a substrate and then spinning the substrate at high speed [35-41]. Centripetal acceleration causes the liquid to spread out in the direction of the substrate edge

leaving a thin film on the substrate. The film properties depend on different factors such as liquid viscosity, particle content in the liquid, spinning speed and spin time.

The spin coater used in the preparation of *urushi* films is shown in Figure 3.2, and consists of a high speed DC motor and speed controller unit. A substrate holder, fixed on the chuck, is provided with three pins to hold the substrate down (Figure 3.3).

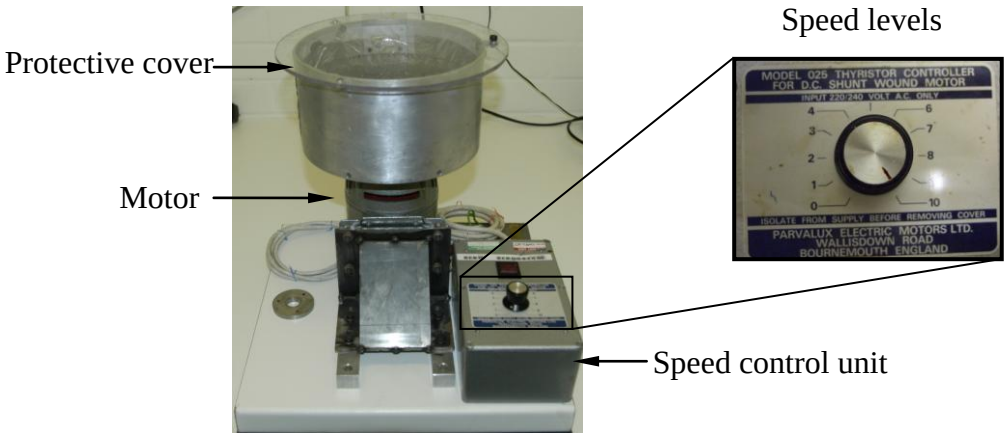

Figure 3.2: Image showing the spin coater with component parts labelled.

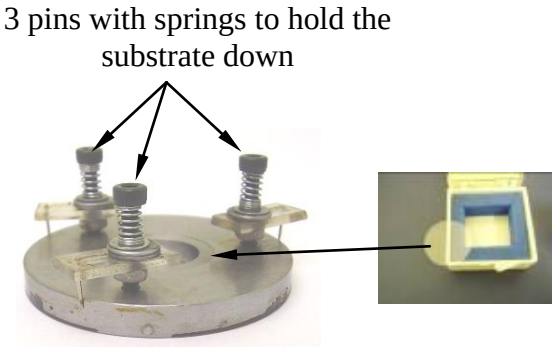

Figure 3.3: Substrate holder showing the three pins used to fix the substrate securely.

During the film preparation, a number of issues were encountered and overcome. We present the problems and solutions below.

Problem	Cause	Solution
Film too thin	Spin speed too high Spin time too long	Select lower speed Decrease spin time
Film too thick	Spin speed too low Spin time too short	Select higher speed Increase spin time
Air bubbles on substrate	Air bubbles in dispensed fluid (Figure 3.4a)	De-gas the fluid
Uncoated area	Insufficient dispense fluid (Figure 3.4b)	Increase amount of material dispensed
Pin holes	Air bubbles Particles in fluid Particles exist on substrate before dispense (Figure 3.4c)	De-gas the fluid Filter the fluid Clean the substrate

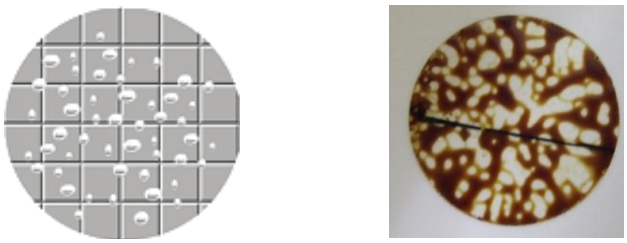

(a)

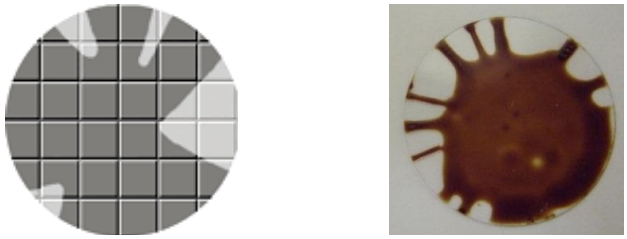

(b)

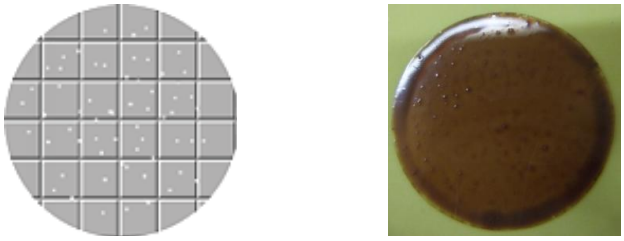

(c)

Figure 3.4: Some problems during film preparation (a) air bubbles in dispensed fluid, (b) uncoated area and (c) particles in fluid and exist on substrate before dispensing.

3.2.4.2 Spin coater calibration

The spin coater calibration was achieved by measuring the thickness of different *urushi* films coated at constant speed at different speed times. The amount of *urushi* per film was 0.1 gm and the spin times were 30 s, 90 s and 150 s. The spin coater speed used during the calibration was 3000 rpm. The samples used during calibration were cured in 78%-80% RH at 24 °C for 17 hrs. As expected, we observed that a longer spin time resulted in a thinner film (Figure 3.5).

At a spinning speed of 3000 rpm and spinning time of 150 s, a thin film of thickness of 10 μm was obtained. This could be increased to 25 μm by reducing the spinning time to 30 s.

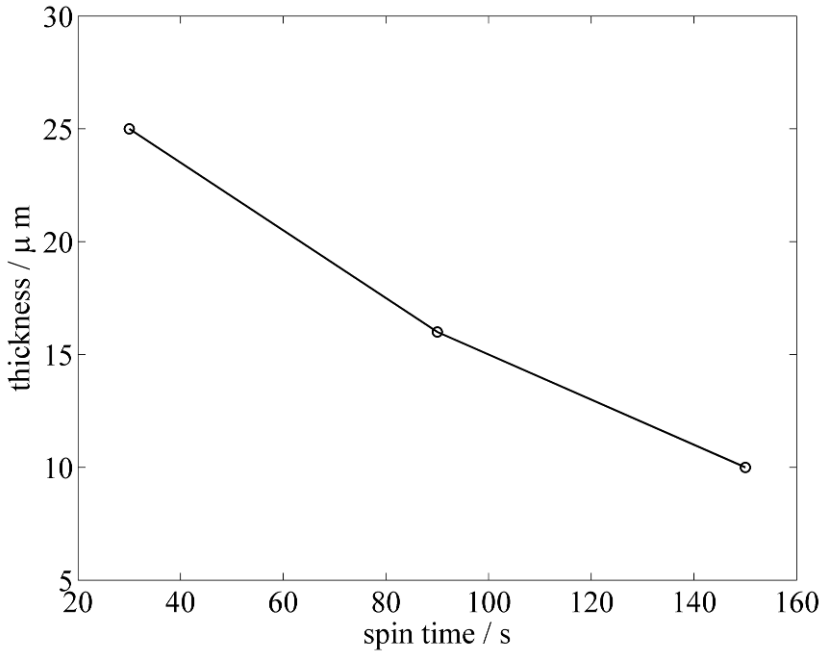

Figure 3.5: The relation between spin time and thickness at constant spin speed.

3.2.5 Curing conditions

As *Urushi* cures only in the presence of air and high relative humidity, a controlled humidity chamber was constructed for curing purposes (Figure 3.6). The appropriate RH can be maintained at a constant RH level in the chamber by increasing the moisture content of a stream of air blown through the chamber. The air moisture content can be increased by using an air-cooler which consists of a small fan forcing

air through a wet pad. The air-cooler is connected to an on/off Relative Humidity Controller which switches off the cooler each time the RH exceeds the desired RH value and switches on the cooler when the RH moves below the desired RH value. With this configuration, the tolerance in the RH was found to be less than ±2%.

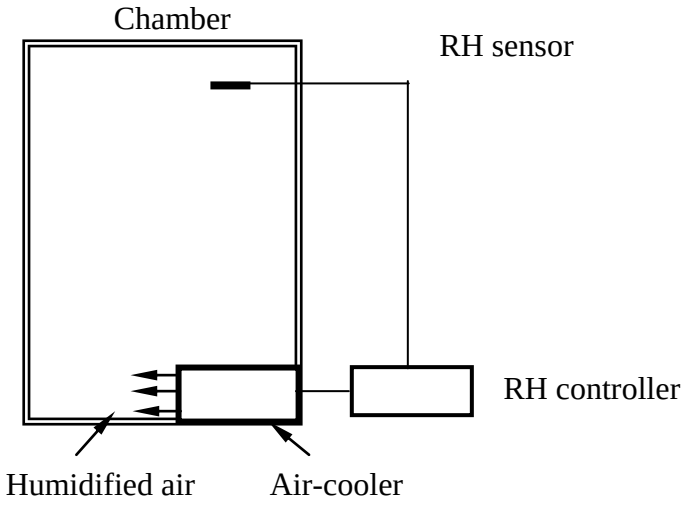

Figure 3.6: Schematic illustration of the chamber used to cure *urushi* thin films.

Immediately after spin coating, the films were cured at 75±2% RH. For films of around 20 μm, it takes at least 3 days for them to fully cured. The film thickness was measured by focusing a microscope (BX-60 Olympus with 50× objective) on the glass/*air* and the *urushi*/air interfaces and measuring the distance required to refocus.

3.3 Ageing process and conditions

In order to produce films that were aged we exposed a subset of the samples to UV radiation. The UV radiation exposure history of the Mazarin Chest is unknown and therefore any attempt to try to replicate its accumulated ageing will be flawed, and as such rather than replicating the damage to the lacquer exactly, we attempt to produce damage of a more general kind to understand the broad changes in behaviour that occur during UV ageing. To induce UV damage, we used a Q-Sun environmental test chamber, equipped with a Xenon arc source, into which the film was exposed to 340 nm, 0.7 $W.m^{-2}$ UV radiation for 400 hrs. The only clear data on the exposure of the chest to light is that during the period between 1986 to 1998 it was displayed at the Toshiba Gallery in the V&A, London, where the illuminance was 80 lux, with UV

levels less than 5 μW.lumen^{-1}, resulting in an energy density of 0.0004 W.m^{-2}. Considering 52 weeks per year, 5 days per week and 8 hrs per day display, this results in a total UV exposure of about 36 kJ.m^{-2}. As a comparison, one can estimate the average (accounting for seasonal and daily variations) exposure to 340 nm UV radiation due to sunlight as 0.08 W.m^{-2}. In order to place our tests into context, we can calculate that our test protocol is equivalent to an average daylight exposure of 0.4 years or an exposure within the Toshiba gallery of 80 years (assuming 80 lux at 340 nm, though the exposure at this wavelength is likely to be much lower in reality).

3.4 Thickness measurement

An Olympus microscope (BX-60) was used to measure the thickness of thin films of *urushi* on the circular glass substrate. It works by focussing on the *urushi's* upper surface and comparing this height to a reference plate, usually a substrate on which a film has been deposited and when the substrate is flat, a localized thickness can be measured. The BX-60 Olympus microscope is an optical microscope with features that include transmission/reflection illumination for different object types and filters. Differential interference contrast microscopy (DIC) tools are provided to enhance the contrast in unstained, transparent samples. In addition, the BX-60 Olympus microscope is characterized by a 1 μm fine focusing adjustment knob and a collecting lens unit with aperture diaphragm and field iris diaphragm adjustment knobs. The last two features are more helpful in thickness measurements, where the fine focusing knob can be used for precise adjustment.

Calibrating the Olympus fine focusing knob was done using standard gauge blocks. Figure 3.7 shows the relation between the microscope fine knob divisions and the block thickness.

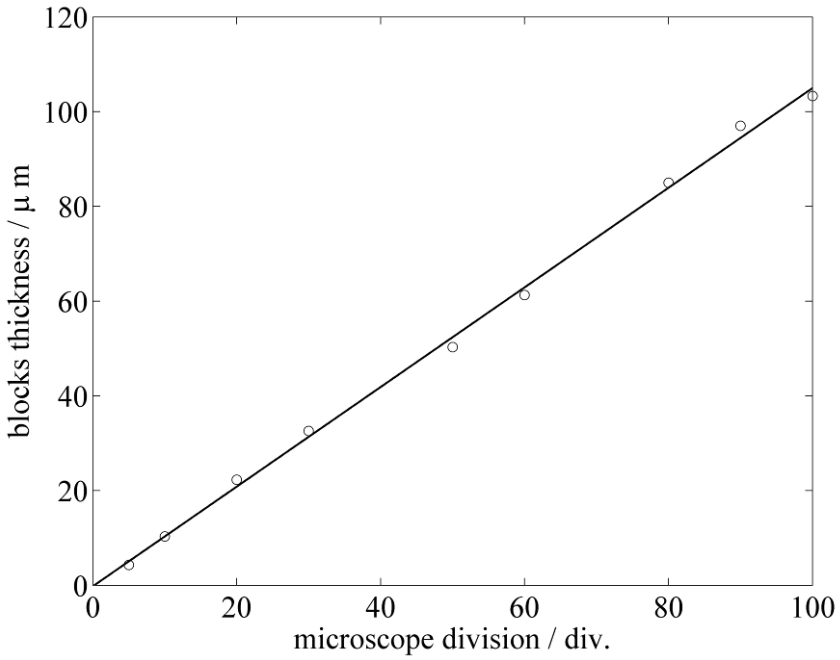

Figure 3.7: Relation between the microscope divinations and the block thickness.

3.5 Conclusion

In this Chapter, we have described the procedures for the controlled manufacture of *urushi* samples. We have developed a protocol that will enable us to reliably produce large batches of *urushi* films of calibrated thickness ready for the subsequent stages of the experimental programme. We have found that the traditional Japanese filtration method is appropriate providing we apply the filter several times. This filtration method offers the benefits of obtaining thin *urushi* film without bubbles and voids. Our preparation and calibration techniques provide for a controlled *urushi* thin layer to be produced of known thickness and ready for measurement of the developed stresses in *urushi*. The techniques for measurement of stresses and analysis will be described in the following Chapters.

Chapter 4
Development of a Methodology to Measure Stresses in *Urushi* Thin Films

4.1 Introduction

Loss of gloss in *urushi* is linked to the formation of micro-cracks [23, 42, 43]. These are caused as a consequence of ageing, mainly due to exposure to UV radiation and fluctuations in temperature, relative humidity (RH) and mechanical strain due to expansion and shrinkage of the substrate, which is generally wood. Due to the multilayer fabrication process, *urushi* can be thought of as a superposition of thin films one on top of another, each with properties that will depend on their composition, deposition and curing history.

As mentioned in Section 2.5.2, *urushi* film is strongly affected by water. It has the tendency to become brittle by water desorption and to be toughened with absorption of water [10]. However, few studies have been done on the effect of relative humidity

changes on the mechanical responses of *urushi*. The approach followed in this work to understand the micro-crack formation was, first, to study the stress levels that develop in a thin *urushi* film as it is subjected to humidity variations and second, to do it on fresh (recently cured) and aged *urushi*.

Many other techniques have been used to observe and measure the response of coatings to changes in the environmental conditions [44, 45]. These techniques make use of relations between the physical or crystallographic parameters and the stress developed in the coatings. These techniques include X-ray diffraction, neutron diffraction, ultrasound, curvature measurements, nano-indentation and Raman/Fourier-Transform Infrared Spectroscopy. The physical principle of stress measurement by neutron diffraction is similar to those for the X-ray diffraction method. The greatest advantage that neutrons have over X-rays is the very large penetration depths that neutrons can achieve [46, 47]. Ultrasonic methods are based on the variation of the velocity of ultrasound waves travelling through a solid where this variation can be related to the stress state [46, 47]. Raman scattered light conveys information about a sample's physical state and chemical structure. Raman spectral lines shift linearly with hydrostatic stress and can be used to measure stresses [48, 49]. However, it relies on spectral signatures of narrow bandwidth which are unfortunately absent in *urushi*. A number of authors have used the curvature method to determine stresses in thin films and the wide applicability and accuracy of this approach has shown it to be a very powerful method [31, 34, 50-53].

The average plane stress developed in a thin *urushi* film under constant temperature and changing RH can be obtained by comparing the deflection of the substrate to which the film is adhered to, relative to a reference state at a known temperature and RH. As long as the substrate mechanical properties remain stable under changing environmental conditions, the substrate thickness and the film stress will ultimately determine the deflections, which will be in the sub-micrometer range. For constant temperature and changing RH, glass possesses the mechanical stability required and constitutes a suitable substrate material. For the range of environmental conditions covered in this study small stress levels are expected on *urushi* films onto glass substrates. Phase stepping interferometry (PSI) [54-59] is a well known optical

technique that allows full-field non-contact measurements of deformations in the nm range without sign ambiguities and is therefore an ideal candidate to measure small substrate deflections due to film stress.

The purpose of this Chapter is to describe Stage 2 in Figure 1.4. The curvature method and the stress evaluation from deflection measurements are described in 4.2. The principles behind phase stepping interferometry, the relationship between the measured spatial distribution of optical phase difference and the deflections that cause it are described in Section 4.3. In Section 4.4, average principal stresses in the film are evaluated from measured displacement fields. The experimental setup is presented in Section 4.5, a discussion on the experimental errors in Section 4.6 and conclusions in Section 4.7.

4.2 The curvature method

The curvature method, widely used for the determination of residual stresses in thin films [60, 61], consists of measuring the deflection of a substrate plate due to stress build up in the film after this is deposited on the substrate. The deformation is usually a change in the curvature of the substrate depending on the tensile or compressive nature of the film stress. Under certain conditions, the substrate deflection field $\delta(x, y)$ and the average stress σ in the film are related by the following approximation, known as the Atkinson's formula [31, 34, 50-53, 62]:

$$\sigma = \frac{t_s^3}{3t_f^2(1+t_s/t_f)}\frac{E_s}{(1-\nu_s)}\frac{\delta(r,\theta)}{r^2}, \tag{4.1}$$

where E_s, ν_s and t_s are the Young's modulus, Poisson's ratio and thickness of the substrate respectively. t_f is the film thickness, assumed constant all over the substrate, whilst $r = (x^2 + y^2)^{1/2}$ and $\theta = \tan^{-1}(y/x)$ are the polar coordinates of point (x, y) as shown in Figure 4.1. It is worth noting that, provided certain conditions are satisfied, σ is independent of the Young's modulus and the Poisson's ratio for the film, which makes this method appealing for our purposes as these are unknown. Equation (4.1) is derived under the following assumptions [63-65]:

1- Strains and rotations are infinitesimally small (i.e. all displacement gradients << 1).

2- The film/substrate thickness ratio $t_f / t_s < 0.4$. When the thickness ratio $t_f / t_s << 0.1$, however, a simpler approximation can be used, known as the Stoney's equation [51-53, 62-64, 66].

3- Substrate material is homogeneous, isotropic and linearly elastic, and the film material is isotropic.

4- The film is in plane stress.

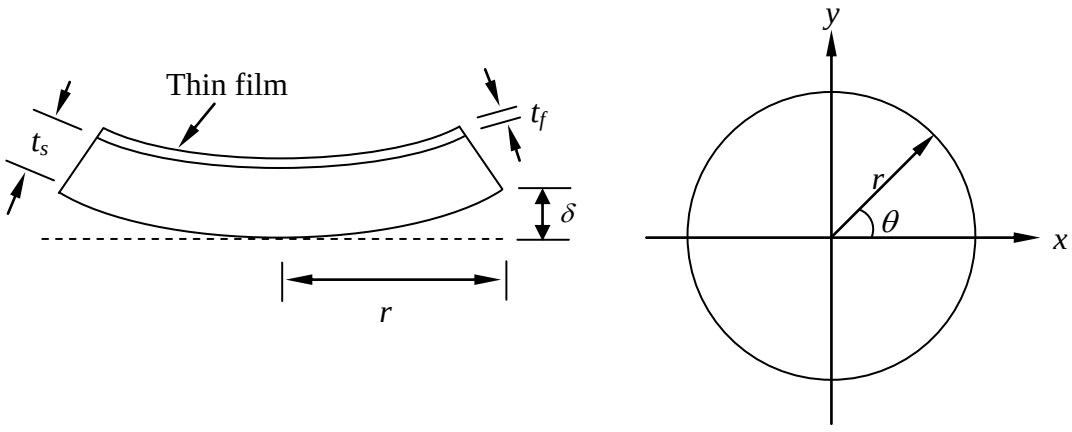

(a) (b)

Figure 4.1: (a) Deflection of an initially flat substrate due to tensile stress following film shrinkage. (b) A schematic showing the top view of the substrate geometry with Cartesian and polar pixel coordinates.

For our thin films, these assumptions are generally true. It is worth noting that although this technique was developed with the aim of measuring residual stresses, our concern in this work is to measure the response of the average stress in *urushi* thin films due to changes in relative humidity. In order to achieve this with the curvature method, several requirements needed to be addressed. First, an appropriate film and substrate system has to be designed so that assumptions 1-4 are all met. Secondly, a highly sensitive method is required to measure the small deflections expected of the substrate. Finally, a chamber had to be built to enable full control over the system environment.

4.3 Phase stepping interferometry

Phase-stepping interferometry has been shown to be a powerful method for measuring small displacements. Well known advantages of phase stepping interferometry over conventional interferometers include: (1) high measurement accuracy, (2) rapid measurements, (3) good results even with low contrast fringes, (4) phase obtained at a grid of data points, and (5) the sign of the displacement field is automatically obtained [67]. When two beams that originate from a common light source are recombined after they have travelled optical paths that differ by no more than the coherence length of the source, they interfere and form a fringe pattern. This is usually recorded with a 2D detector array and can be described by the following intensity distribution,

$$I(x,y) = I_0(x,y) + I_M(x,y)\cos\left[\phi(x,y)\right] \tag{4.2}$$

where $I_0(x,y)$, $I_M(x,y)$ and $\phi(x,y)$ are three unknown distributions referred to as the background intensity, the modulation intensity and the phase difference between the interfering beams at point (x,y), respectively.

In order to evaluate the phase, $\phi(x,y)$, having been given three unknown parameters, $I_0(x,y)$, $I_M(x,y)$ and $\phi(x,y)$, it is necessary to have at least three independent measurements of the intensity $I(x,y)$. A simple and widely used phase evaluation algorithm [68, 69] is based on four intensity measurements where a $\frac{\pi}{2}$ phase shift is introduced between the interfering beams between consecutive interferograms. The intensity for each interferogram is thus given by

$$\begin{aligned}
I_1(x,y) &= I_0(x,y) + I_M(x,y)\cos\left[\phi(x,y)\right], \\
I_2(x,y) &= I_0(x,y) + I_M(x,y)\cos\left[\phi(x,y) + \frac{\pi}{2}\right], \\
I_3(x,y) &= I_0(x,y) + I_M(x,y)\cos\left[\phi(x,y) + \pi\right], \\
I_4(x,y) &= I_0(x,y) + I_M(x,y)\cos\left[\phi(x,y) + \frac{3\pi}{2}\right].
\end{aligned} \tag{4.3}$$

By solving this set of equations, under the assumption that $\phi(x,y)$ does not change during the acquisition of I_1 to I_4, it can be shown that

$$\phi_w(x,y) = \tan^{-1}\left(\frac{I_4(x,y) - I_2(x,y)}{I_1(x,y) - I_3(x,y)}\right). \tag{4.4}$$

The arctangent function, $\phi_w(x,y)$ lies in the range $[-\pi,+\pi)$ and is referred to as the wrapped phase, thus the subscript 'w'. The process of recovering the continuous phase distribution $\phi(x,y)$ that extends beyond the $[-\pi,+\pi)$ range is known as phase unwrapping, and consists of adding an appropriate integer multiple of 2π at each point in the wrapped phase distribution [68, 70-73]. When the interferometer is set up to measure object deformations, two unwrapped phase distributions $\phi_r(x,y)$ (phase of the reference state) and $\phi_d(x,y)$ (phase of the deformed state) are required to evaluate the unwrapped phase change distribution, $\Delta\phi(x,y)$. An alternative method consists in a direct evaluation of the wrapped phase change distribution as

$$\Delta\phi_w(x,y) = \tan^{-1}\left(\frac{N_d D_r - D_d N_r}{D_d D_r + N_d N_r}\right), \tag{4.5}$$

where N_r, D_r, N_d and D_d are defined in terms of the phase shifted interferograms recorded for the reference state, I_{r1} to I_{r4}, and those for the deformed state, I_{d1} to I_{d4}:

$$\begin{aligned} N_r &= I_{r4}(x,y) - I_{r2}(x,y), \\ D_r &= I_{r1}(x,y) - I_{r3}(x,y), \\ N_d &= I_{d4}(x,y) - I_{d2}(x,y), \\ D_d &= I_{d1}(x,y) - I_{d3}(x,y). \end{aligned} \tag{4.6}$$

The advantage of this approach is that the numerator and denominator in the argument of the arctangent function in Eq. (4.5) can be low-pass filtered to reduce phase noise [68]. In the case when the interferometer has pure out-of-plane sensitivity, i.e. parallel to the observation direction, the relationship between the measured unwrapped phase change $\Delta\phi(x,y)$ and the displacement (or deflection) distribution $\delta(x,y)$ is given by

$$\delta(x,y) = \frac{\lambda}{4\pi}\Delta\phi(x,y), \tag{4.7}$$

where λ is the wavelength of the coherent light source used. Equation (4.7) assumes that the object and the interferometer are immersed in a medium of unit refractive index.

4.4 Evaluation of film stress from displacement fields measurements

Ideally, a film and substrate system such as the one described in Section 4.2 will respond to a uniform stress field in the film by deforming with axial symmetry so that the deflection perpendicular to the plane $x-y$ has circular contour lines. However, slight heterogeneities in the stress field lead to elliptical contour lines, as shown in Figure 4.2. The principal axes of the elliptical contour lines correspond to the directions of the principal in-plane stress components in the film plane.

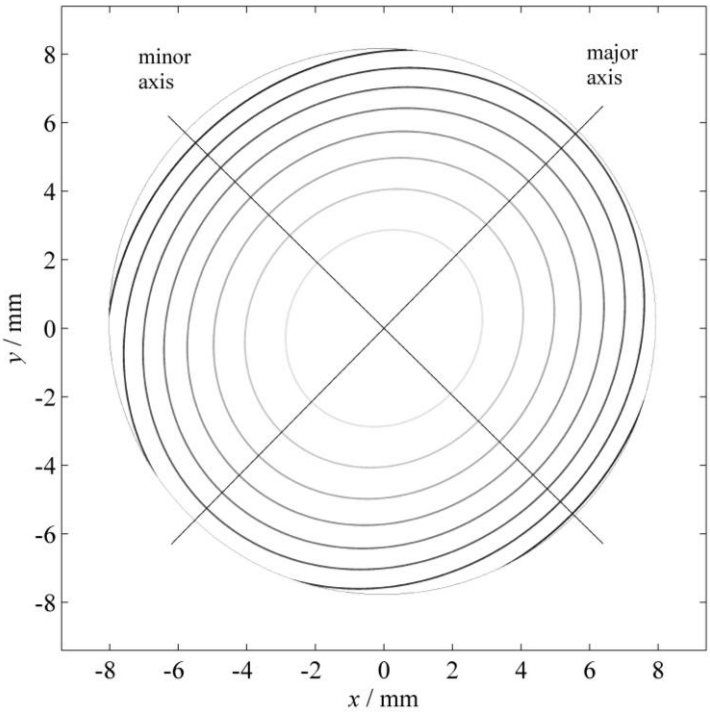

Figure 4.2: Deflection distribution contour for non-aged *urushi* film when exposed to a humidity change from 75% to 30% for 4080 minutes.

The deflection distribution $\delta(x,y)$ can conveniently be approximated by a second order surface as follows

$$\delta(x,y) \cong ax^2 + by^2 + cxy + dx + ey + f\,, \tag{4.8}$$

where the quadratic coefficients a, b and c reflect the curvature characteristics of the paraboloid, while coefficients d and e describe a linear tilt and f the displacement of the centre of mass of the film/substrate system perpendicular to the $x-y$ plane. The linear and constant terms in Eq. (4.8) can be ignored as they do not contribute to the curvature and therefore are not linked to the film stress. After a convenient change to polar coordinates, Eq. (4.8) reduces to

$$\delta(r,\theta) \cong r^2\left[a\cos^2\theta + b\sin^2\theta + c\cos\theta\sin\theta\right]. \tag{4.9}$$

The benefit of this is that once the orientation of the ellipse is determined, the problem is reduced to the determination of δ along the major and minor axes of the ellipse corresponding to θ_M and θ_m respectively. θ_M and θ_m are the orientation angles of the major and minor axes respectively, where

$$\theta_M = \theta_m + \frac{\pi}{2}. \tag{4.10}$$

Substitution of Eq. (4.9) into Eq. (4.1) for θ_M and θ_m finally leads to the film principal stresses

$$\begin{aligned}
\sigma_1 &= \frac{t_s^3}{3t_f^2(1+t_s/t_f)}\frac{E_s}{(1-\nu_s)}(a\cos^2\theta_m + b\sin^2\theta_m + c\cos\theta_m\sin\theta_m),\\
\sigma_2 &= \frac{t_s^3}{3t_f^2(1+t_s/t_f)}\frac{E_s}{(1-\nu_s)}(a\cos^2\theta_M + b\sin^2\theta_M + c\cos\theta_M\sin\theta_M)\ .
\end{aligned} \tag{4.11}$$

Due to the fact that a higher film stress would be responsible for the curvature of the substrate on the plane that contains the minor axis of the ellipse and the z axis, σ_1 and σ_2 have been defined here following the usual convention in which $\sigma_1 > \sigma_2$.

If $\delta(x,y)$ is available as a full-field measured deflection distribution, then coefficients a, b and c can be found by least squares fitting of the measured distribution to an elliptical paraboloid. Equation (4.9) is used to find the orientation θ_m of the minor axis by minimizing the radius at a contour of constant deflection. The orientation θ_M of the

major axes is found from Eq. (4.10) and finally Eq. (4.11) leads to the film principal stresses along θ_m and θ_M .

4.5 Experimental setup

4.5.1 Layout

Figure 4.3 shows a schematic of the interferometer used to measure changes in the curvature of a film/substrate sample due to variations of relative humidity. A He-Ne laser (Melles Griot model) is used as the coherent light source, providing a vertically polarized 30 mW beam with wavelength λ =632.8 nm. The beam goes through a half-wave plate (HWP) that rotates the plane of polarization before entering a polarizing beam splitter (PBS) that splits the incoming beam into reference beam (RB) and object beam (OB) with orthogonal polarizations, the intensities of which can be easily adjusted by rotating the HWP. These beams are then launched into single mode polarization preserving optical fibres, reference fibre (RF) and object fibre (OF). The reference beam (RB) goes through a pair of opposing glass wedges, one of which is fixed and the other is moved across the beam with an open loop piezoelectric lead zirconate titanate (PZT) transducer to increase the optical path and introduce controlled phase steps. The fibres then deliver both beams with the same polarization to the recombination head of the interferometer. The object beam, OB, is transmitted through a non-polarizing beam splitter (NPBS) and propagates towards the film/substrate sample, where it is reflected back from the specular bottom surface of the substrate. On its way back, the object beam is recombined with the reference beam so that the optical path difference remains within the coherence length of the laser. The sample is mounted inside an environmental loading chamber (EC). A CMOS camera (C) (HCC-1000 Vosskühler, 8 bits, 1024×1024 pixels) records the interference fringe patterns that encode the shape of the substrate relative to the reference wavefront. The purpose of lens L_1, shown in the side view inserted in Figure 4.3 is to illuminate the sample with a collimated beam, and thus the distance from the output end of the object optical fibre is equal to the focal length of L_1. L_2 collimates the beam launched by the reference fibre and lens L_3 focuses it at the aperture stop plane (AS) of imaging lens L_4. This results in a reference beam that covers the CMOS detector with a Gaussian distribution that is typical of the TEM_{00} mode.

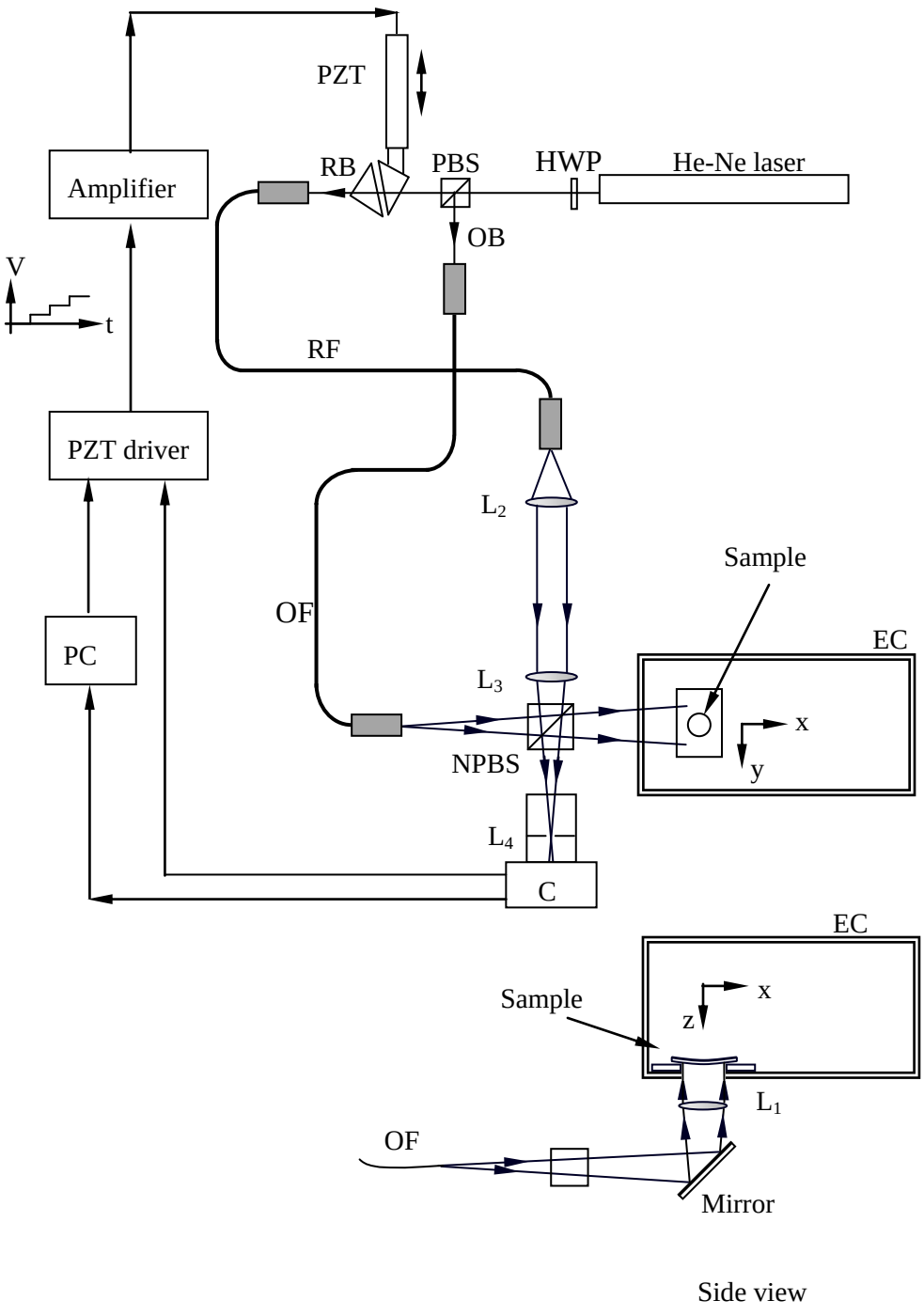

Figure 4.3: Schematic of phase shifting interferometer and side view of the object beam and the environmental chamber EC: HWP, half-wave plate; PBS, polarizing beam splitter; PZT, open loop piezoelectric transducer; RB, reference beam; OB, object beam; NPBS, non polarizing beam splitter; L_1, L_2 and L_3 convex lenses; L_4, imaging lens; C, CMOS camera.

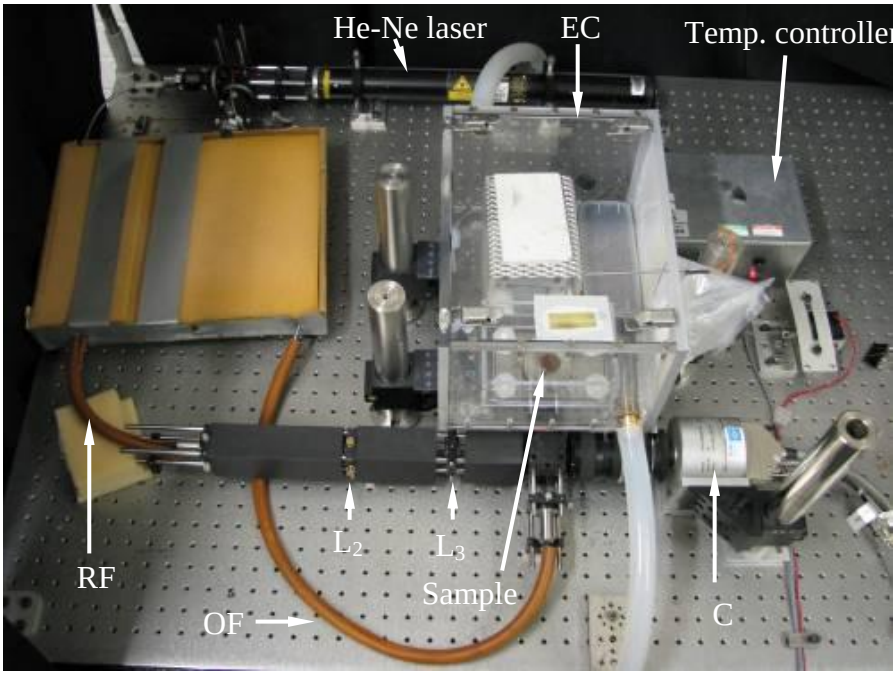

Figure 4.4: Photograph of the phase stepping interferometer: EC, environmental chamber; RF, reference fibre; OF, object fibre; C, CMOS camera.

4.5.2 Alignment of polarisation preserving optical fibre

Single mode fibre optic delivery allows flexible remote delivery with a near pure Gaussian output which removes the need of spatial filters. Flexibility in the fibre optic delivery system offers the benefit of allowing infinite adjustment of the emission direction. The fibre-launch optics system consists of two precision 4-axis Manipulated (Point Source FDS-4X-2) and two Fibre Delivery Systems (FDS) (see Figure 4.5).

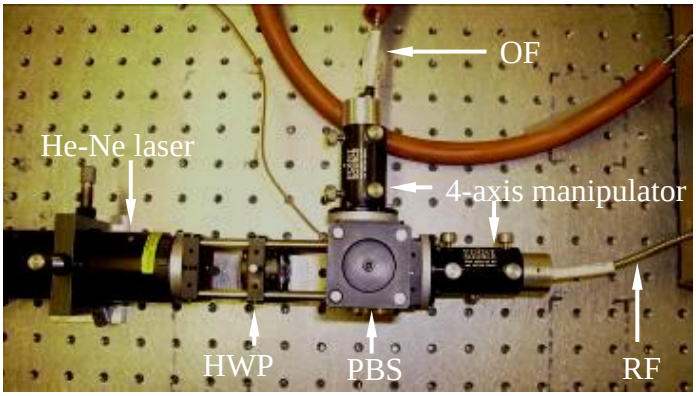

Figure 4.5: Optical fibre launch setup, showing He-Ne laser, half wave plate (HWP), polarizing beam splitter (PBS) and 4-axis fibre alignment mounts for the object (OF) and the reference (RF) fibre.

The FDS-4X-2 is a kinematics manipulator for FDS optical assemblies which allows four axes of adjustment to achieve perfect launch conditions. Each unit is designed to mount directly onto the direct and the right angle directions of the Microbench holder as shown in Figure 4.5. The FDS is designed to efficiently couple light into the core of a single mode fibre via a focusing lens (FL) as shown in Figure 4.6. The focal length of FL is chosen firstly to suit the desired input beam diameter and secondly to produce a focus that matches the mode field diameter of the fibre.

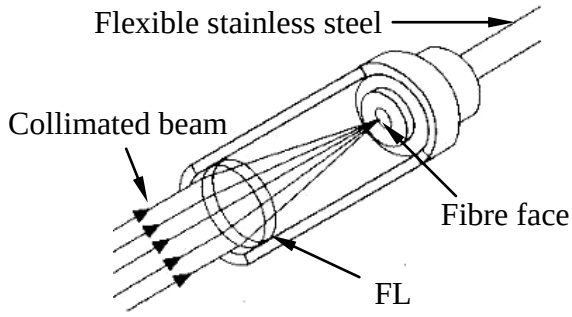

Figure 4.6: The input optics of a Fibre Delivery System.

4.5.3 Fibre delivery system alignment

The alignment tool consists of a 60 mm long, 12 mm outer diameter and 2 mm inner diameter metal cylinder, shown in Figure 4.7, is used to align the FDS as follows:

1. The tool is inserted into the manipulator with the small aperture nearest to the laser, where the tool is tightened using the tension screw.

2. Screws A and A` are adjusted to gain maximum optical transmission, Figure 4.8(a).

3. The tool is inserted into the manipulator with the small aperture farthest from the laser, where the tool is tightened using the tension screw.

4. Screws B and B` are adjusted to gain maximum optical transmission, (Figure 4.8(a)).

5. The FDS input is inserted into the manipulator and again screws A, A`, B and B` are adjusted to gain maximum optical transmission at the FDS output (Figure 4.8(b)).

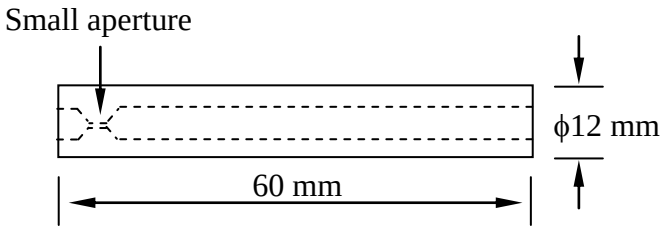

Figure 4.7: Tool used for the coarse alignment of FDS with a collimated beam.

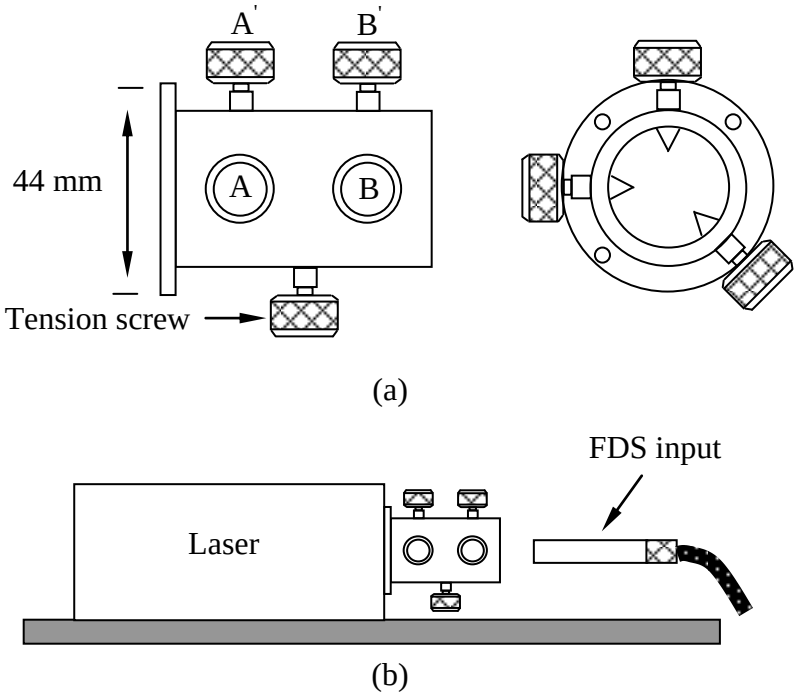

Figure 4.8: Precision 4-Axis Manipulator.

4.5.4 Polarisation alignment

To satisfy the interference condition between two beams and to get high intensity modulation the state of polarisation should be the same and stable at the detector plane. The fibre transmits a linear and stable state of polarisation when two main conditions have been satisfied. Firstly, the input state of polarisation must be linear and stable and secondly, the input state of polarisation must be aligned to either the fast or the slow axis of the fibre. Therefore it is necessary to make sure that the light is polarised in one

direction (say vertical) both at the fibre inputs and output ends. Figure 4.9 shows a typical arrangement that can be use to align the state of polarisation.

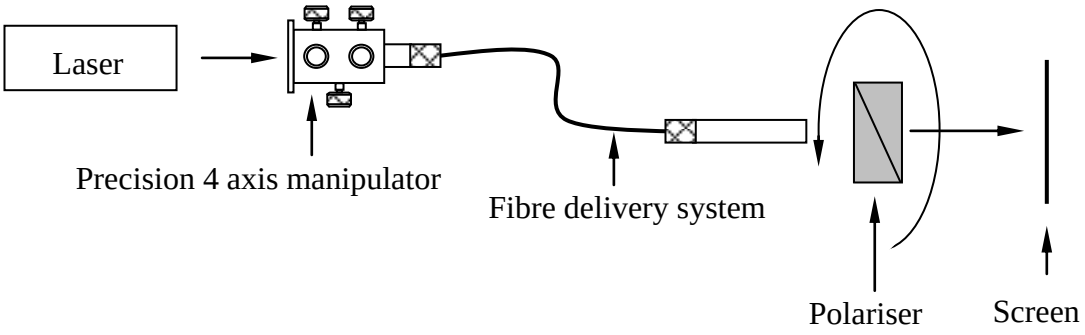

Figure 4.9: Setup for polarisation alignment.

The alignment is achieved in the following way [74]:

1- The polariser is placed on the output fibre end such as to give vertically polarised light.

2- The input end is rotated to get maximum stable beam of light on a screen.

3- Put the polariser again such as to give vertically polarised light.

4- The output end is rotated while maintaining the orientation of the polariser so as to get maximum optical transmission, which indicates that the light is vertically polarised at the fibre output end.

4.5.5 Phase stepping control and synchronization

As mentioned in Section 4.3 the four-frame algorithm requires, for each deformation state, the acquisition of four interferograms with $\frac{\pi}{2}$ phase shifts between successive ones. A PZT driver, manufactured at Loughborough University, is used to generate a calibrated stepped voltage staircase profile $V_1 = 0 < V_2 < V_3 < V_4$ which is encoded and stored in a look-up table in the driver's internal microprocessor. During synchronisation, the camera is used as master and the PZT driver as slave. Once triggered from a PC-based application to start the acquisition of four frames (see Figure 4.10(a)) each time the camera records a frame it outputs a train of pulses

separated a few microseconds which are conditioned to a single pulse of longer duration (Figure 4.10(b)). This pulse is input and detected by the PZT driver. The driver then moves to the next voltage level in the look-up table and holds it until it receives another TTL rising edge from the camera. Once four steps V_1, V_2, V_3 and V_4 are scanned, it resets to $V_1 = 0$ V ready for the next voltage profile (Figure 4.10(c)).

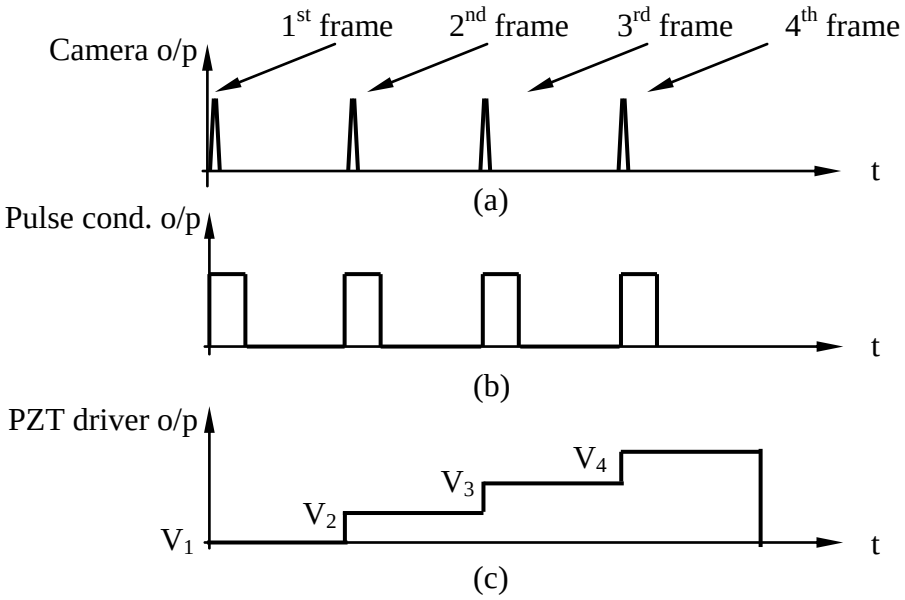

Figure 4.10: Camera output of frame pulses (a), Pulses conditioned for PZT driver (b) and PZT driver output voltage (c).

The sign of the phase change distribution evaluated through the four-frame algorithm as expressed in Eq. (4.5) was checked for consistency by simply moving a test object towards the camera, and defining the *z*-axis accordingly. A calculated positive phase change, corresponding to a positive displacement with the *z*-axis so defined, is obtained when the object moves towards the camera along the observation direction. The microbench construction shown in Figure 4.5 includes also the phase stepping optics, shown in Figure 4.11 in detail. Phase stepping is achieved by mounting and translating a 45^o glass wedge w_1 placed in one of the interfering beams RB with a PZT. The PZT actuator used in this work was a Physik Instrument type P-820.10 PZT which is a low voltage device with a maximum displacement of 15 μm for 100 V of applied voltage. A second identical wedge, w_2, brings the beam parallel to its original direction. This phase stepping method has several advantages over the conventional approach of reflecting the beam from a PZT-mounted mirror: (a) no beam tilt is

produced if the PZT tilts during translation, and (b) extension of the PZT does not introduce lateral beam translation provided the wedge is angled correctly in the beam.

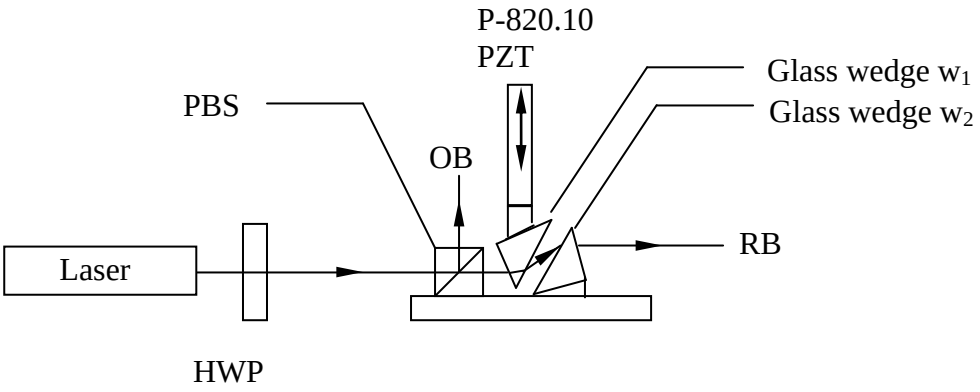

Figure 4.11: Layout of phase stepping optics.

4.5.6 PZT calibration

The displacement/voltage response of PZT actuators is sensitive to changes in humidity and temperature. For this reason, they need to be calibrated before each measurement. We followed the procedure described by Ochoa et al [73] to calibrate our PZT phase shifting actuator. The procedure is only suitable for calibrating phase modulators that can produce a full 2π phase shift and for which the phase changes monotonically with applied voltage, but is relatively simple to implement and can be performed *in situ.* The aim of the PZT calibration is to determine the voltage values that are required to introduce known phase steps. The basic principle of the calibration process depends on the evaluation of the average of the squared differences (S) between a reference intensity distribution (I_r) and an intensity distribution (I) obtained after an unknown phase difference, which is produced by a known voltage applied to the PZT. The intensity distributions are given by [73]

$$I_r(x,y) = I_0(x,y) + I_M(x,y)\cos\left[\phi(x,y) + \alpha_r(V_r)\right], \tag{4.12}$$

$$I(x,y) = I_0(x,y) + I_M(x,y)\cos\left[\phi(x,y) + \alpha(V)\right], \tag{4.13}$$

where (x, y) are the pixel coordinates of an arbitrary point in the interference pattern, V_r and V are the applied voltage corresponding to I_r and I respectively. $I_0(x, y)$ and $I_M(x, y)$ are the background and visibility functions, which are presumed to be voltage independent; $\phi(x, y)$ is the phase difference between the interfering beams and $\alpha(V)$ is the voltage function. Assuming it is a second order polynomial then

$$\alpha(V) = a_1 + a_2 V + a_3 V^2, \tag{4.14}$$

$$\Delta\alpha(V) = a_2(V - V_r) + a_3(V^2 - V_r^2). \tag{4.15}$$

From Eq. (4.12) and Eq. (4.13), the average of the squared difference is given by

$$S = \left\langle (I_r - I)^2 \right\rangle = \left\langle I_M^2 \right\rangle \left\langle \left[1 - \cos(2\phi + \alpha + \alpha_r)\right] \right\rangle \left[1 - \cos(\alpha - \alpha_r)\right]. \tag{4.16}$$

Using a conventional trigonometric identity we obtain

$$S = \left\langle I_M^2 \right\rangle \left[1 - \left\langle \cos(2\phi) \right\rangle \cos(\alpha + \alpha_r) + \left\langle \sin(2\phi) \right\rangle \sin(\alpha + \alpha_r)\right]\left[1 - \cos(\alpha - \alpha_r)\right]. \tag{4.17}$$

Both $\left\langle \cos(2\phi) \right\rangle$ and $\left\langle \sin(2\phi) \right\rangle$ tend to zero if the interference pattern contains sufficient fringes or speckle noise and therefore Eq. (4.17) can be simplified to

$$S = \left\langle I_M^2 \right\rangle \left[1 - \cos(\alpha - \alpha_r)\right]. \tag{4.18}$$

Substituting Eq. (4.15) into Eq. (4.18), we get

$$S = \left\langle I_M^2 \right\rangle \left[1 - \cos\left\{a_2(V - V_r) + a_3(V^2 - V_r^2)\right\}\right]. \tag{4.19}$$

Equation (4.19) is used to fit the measured values $S(V_i)$, the average of the squared differences between the reference intensity distribution I_r and the intensity distributions I obtained after applying a known voltage. 125 steps were used in the calibration process with a 0.4 V / step. An example of the calibration results is shown in Figure 4.12 with the fitting of the first three cycles.

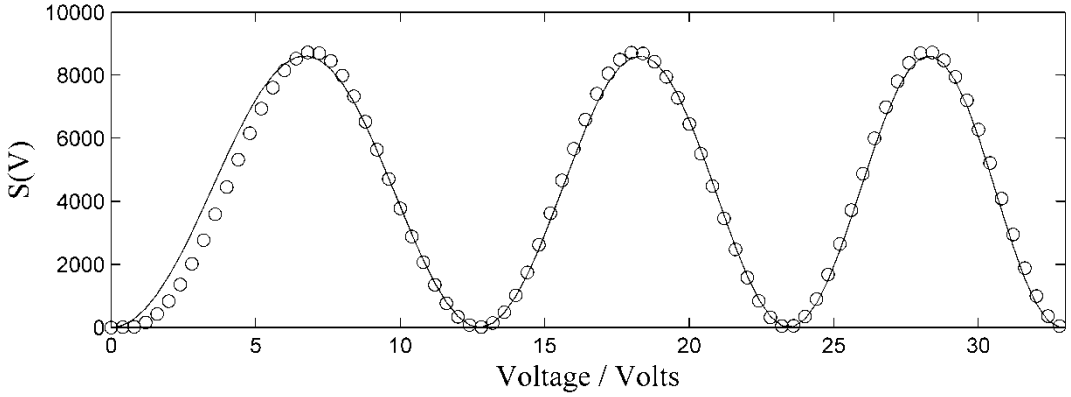

Figure 4.12: Second order polynomial fitting of $S(V)$. The open circles represent the experimental data and the line is the fitting.

The fitting coefficients a_2 and a_3 are used to find the dependence of the phase shift on the applied voltage, Eq. (4.15), shown in Figure 4.13. The coefficients, a_2 = 0.44 rad./volt (linear coefficient) and a_3 = 0.004 rad./volt^2 (quadratic coefficient), were obtained. In general, even good quality PZTs have non-linear relationship between the displacement and the applied voltage [67, 75, 76]. The dependence of the phase shift on the applied voltage can be used to extract the voltage values required to introduce an incremental phase shift of $\frac{\pi}{2}$, as shown in Figure 4.14, by using a one-dimensional data interpolation function.

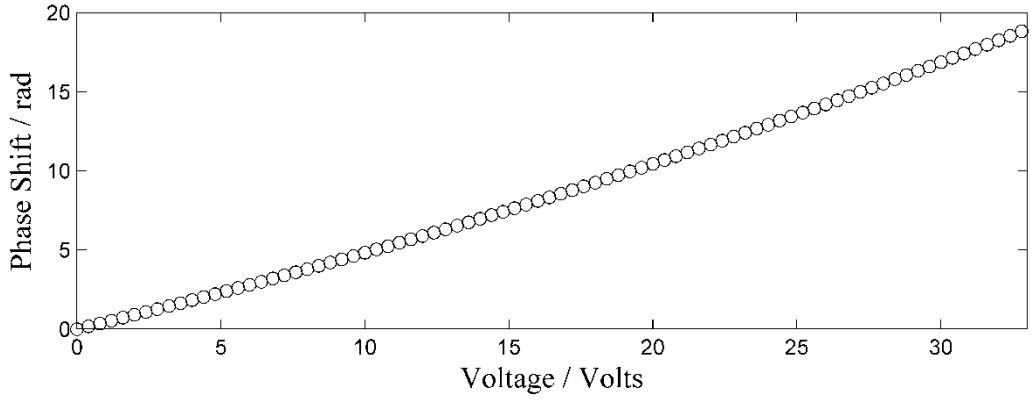

Figure 4.13: The dependence of phase change on the applied voltage

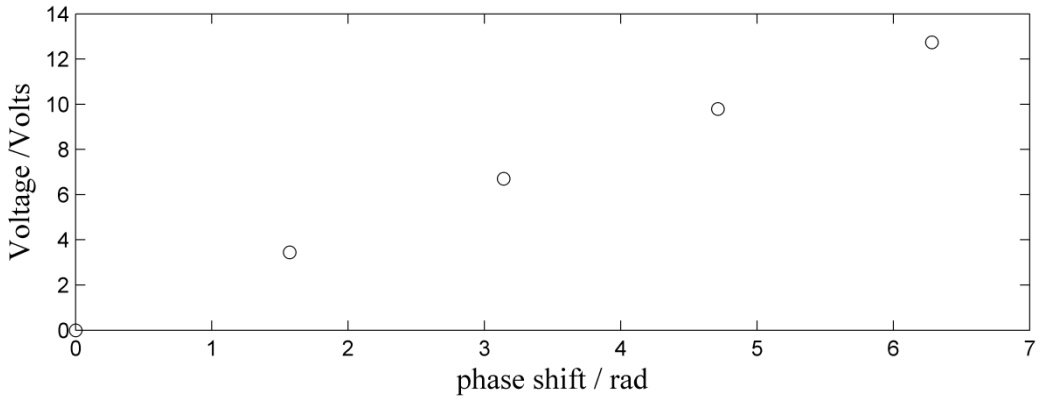

Figure 4.14: The voltage values required for phase shifts 0, $\frac{\pi}{2}$, π, $\frac{3\pi}{2}$ and 2π rad.

4.5.7 Environmental chamber

Triggering the response of *urushi* films to changes in relative humidity and measuring it with the interferometer requires a fine control over the environmental conditions. An environmental chamber (EC) with thermal and humidity control systems was built and is shown in Figure 4.15. It was made from sealed acrylic sheets of thickness 10 mm and its dimensions are 300 mm × 220 mm × 170 mm. The sample holder, RH sensor, heating element and temperature sensor are all placed within the chamber.

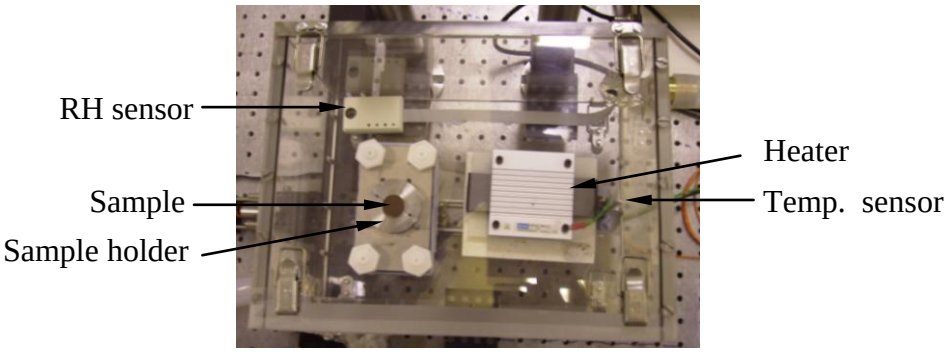

Figure 4.15: Top view of the environmental load chamber.

4.5.7.1 Humidity control

After some trial and error, humidity control was obtained by using Calcium Chloride and water reservoirs within the chamber. The water reservoir was open or closed to the chamber according to the humidity detected by a capacitive sensor. Opening the water reservoir leads to an increase in moisture within the chamber whereas Calcium

Chloride is used to decrease the moisture content within the chamber. The film/substrate test sample sat horizontally on a recessed holder by its own weight.

4.5.7.2 Temperature control

The temperature controlling system has three main components:

1- Input:

The input is a platinum thermo-couple (PT100) to measure the temperature inside the chamber.

2- Controller:

The controller, see Figure 4.16, monitors the input from the PT100 and compares it with the setting point or the desired temperature setting. As required, it increases the temperature by switching on the heating element. It is provided with an on/off and proportional with integral and derivative control (PID), where PID is used when precise control is required.

3- Output:

The output is a part of the controller that is used for turning the heating element on and off. The output inside the controller is a Solid State Relay.

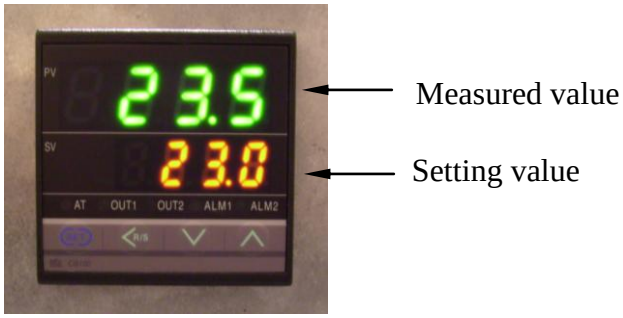

Figure 4.16: Temperature controller.

This approach allowed us to control RH and temperature to within ±1% RH and ±1 °C, respectively.

4.6 Experimental errors

The greatest challenge in this experimental study was to maintain interference fringe stability during the long recording times required for the measurements. Environmental vibration and temperature variations introduce strain in the optical

fibres, which can result in relative phase shifts and induce slow fluctuations in the d.c. component of the measured phase change, $\Delta\phi$. Regular calibration of the system was performed to ensure that changes in room temperature and humidity did not affect the results. The interferometer was setup on a vibration isolated table, the room temperature was kept at 18 °C and the optical fibres were thermally insulated. Slight rigid body motion of the sample over the sample holder was dealt with in the data processing stage by following the procedure described in Section 4.4.

The measured optical phase difference maps have some spatial noise which is a combination of electronic noise sources in the camera, camera dynamic range (8 bits in this case), the phase shifting algorithm used, spurious diffraction patterns and also environmental stability. Noise directly affects the measured displacement field $\delta(x, y)$, which is proportional to the phase as expressed by Eq. (4.7). A common parameter that describes this noise is that the root mean square error (*rms*) of the displacement distributions, which is defined as

$$\delta_{rms} = \sqrt{\frac{\sum_{x=1}^{N}\sum_{y=1}^{M}\left(\delta_{\exp}(x,y) - \delta_{fit}(x,y)\right)^2}{N \times M}}, \tag{4.20}$$

where $\delta_{\exp}(x, y)$ is the measured displacement map, $\delta_{fit}(x, y)$ is its best second order polynomial fit, $N \times M$ is the total number of pixels in the region where *rms* is evaluated and x and y are pixel coordinates.

Using Eq. (4.1), the uncertainty in the average film stress σ due to the uncertainties in the substrate thickness $u_{\sigma t_s}$, in the film thickness $u_{\sigma t_f}$, in the displacement $u_{\sigma\delta}$ and in the distance from the centre to where the displacement is measured, $u_{\sigma r}$, can be calculated as

$$u_{\sigma t_s} = \left|\frac{\partial\sigma}{\partial t_s}\right| u_{t_s}, \tag{4.21}$$

$$u_{\sigma t_f} = \left|\frac{\partial\sigma}{\partial t_f}\right| u_{t_f}, \tag{4.22}$$

$$u_{\sigma\delta} = \left| \frac{\partial\sigma}{\partial\delta} \right| u_{\delta}, \tag{4.23}$$

$$u_{\sigma r} = \left| \frac{\partial\sigma}{\partial r} \right| u_{r}, \tag{4.24}$$

where u_{t_s}, u_{t_f}, u_{δ} and u_r are the uncertainties in t_s, t_f, δ and r, respectively. We neglected the uncertainty in the Young's modulus and Poisson's ratio of glass as these are not tabulated for our substrates. The total error in σ is obtained by combining the individual contributions in quadrature:

$$u_{\sigma} = \sqrt{u_{\sigma t_s}^2 + u_{\sigma t_f}^2 + u_{\sigma\delta}^2 + u_{\sigma r}^2}\ . \tag{4.25}$$

The results of the root mean square and the total error calculations will be presented in Chapter 6.

4.7 Conclusion

In this Chapter, we described the stress measurement process in thin *urushi* films which comprised of several steps. The first step is to alter the environment in which the sample resides in order to induce a change in curvature. We do this in a controlled manner by placing the sample within an environmental chamber with thermal and humidity control. We then change the relative humidity and observe the displacement of the sample using phase shifting interferometry which is a powerful full-field and non-contact technique for the measurements of sub-micron displacement. Having obtained the phase maps, we then employ regression methods to extract the curvature of the sample from the displacement field and thence the stresses. We found that the displacement distribution in polar coordinates is more appropriate where the stress associated with the minimum and maximum curvature can be evaluated. In the following Chapter the phase shifting interferometer will be employed to observe stress response of cured non-aged and aged *urushi* films to different humidity levels.

Chapter 5
Measurements of Moisture Diffusion Coefficient for Non-Aged and Aged *Urushi*

5.1 Introduction

The practical and aesthetic importance of *urushi* has meant that many studies have been carried out to investigate the chemical structure of *urushi*, but a comparatively small number of studies have looked to determine its mechanical properties and their dependence on the environmental conditions. This Chapter is motivated by the need to investigate the rheological properties of non-aged and aged *urushi* films as they are subjected to different RH levels so that ultimately, they can serve as an input to models to predict the hygroscopic contributions to stress.

Water sorption in polymers is related to the availability of free volume holes in polymer networks and polymer-water affinity. The availability of holes depends on the polymer structure, morphology and crosslink density [77, 78]. The polymer-water

affinity is related to the presence of hydrogen bonding sites along the polymer chains, which create attractive forces between the polymer and the water molecules.

In this Chapter we will measure the diffusion coefficient for *urushi*, as a function of moisture content and UV ageing. This will be done by applying the solution of the diffusion equation to moisture uptake experiments and extracting the diffusion coefficient through fitting.

5.2 Analytical solution of the diffusion equation

The diffusion of moisture in a flat sheet during absorption or desorption is assumed to be one dimensional. The simplest moisture diffusion model in this case is based on Fick's law, which is represented mathematically by [79-82]

$$\frac{\partial C(x,t)}{\partial t} = \frac{\partial}{\partial x}\left(D \frac{\partial C(x,t)}{\partial x} \right), \tag{5.1}$$

where $C(x,t)$ is the moisture concentration, t is the time, x is the spatial coordinate and D is the diffusion coefficient. For the case where D is independent of the moisture concentration, Eq. (5.1) can be written as:

$$\frac{\partial C(x,t)}{\partial t} = D \frac{\partial^2 C(x,t)}{\partial x^2}. \tag{5.2}$$

Initial conditions

In the case where the initial concentrations of the penetrant are uniform throughout the sheet, we take the initial conditions to be

$$C(x,0) = C_\circ \text{ at } t = 0 \text{ and } 0 \le x \le h, \tag{5.3}$$

where $C_\circ$ is the initial concentration and h is the thickness of the sheet.

Boundary conditions

If the sheet is exposed to different amount of penetrant than the one in which it was exposed, then the boundary conditions are

$$C(x,t) = C_s \text{ at } x = 0 \text{ and } x = h \text{ at } t > 0, \tag{5.4}$$

where C_s is the surface moisture concentration corresponding to the environmental relative humidity. The solution to Eq. (5.2) [81] is

$$C(x,t) = A_\circ + \sum_{n=1}^{\infty} (A_n \sin \lambda_n x + B_n \cos \lambda_n x) \exp(-\lambda_n^2 Dt) \quad , \tag{5.5}$$

where $A_\circ$ is the average concentration after the equilibrium has been reached following a step change in the relative humidity and A_n, B_n and λ_n are constants.

With the boundary condition given in Eq. (5.4), $C(x,t) = C_s$ at $x = 0$, and when $A_\circ \to C_s$ a solution can be obtained for Eq. (5.5) where

$$C_s = C_s + \sum_{n=1}^{\infty} (0 + B_n) \exp(-\lambda_n^2 Dt), \tag{5.6}$$

which implies that $B_n = 0$.

With the boundary condition given in Eq. (5.4), $C(x,t) = C_s$ at $x = h$ a solution can be obtained for Eq. (5.5) that gives

$$C_s = C_s + \sum_{n=1}^{\infty} (A_n \sin \lambda_n h + B_n \cos \lambda_n h) \exp(-\lambda_n^2 Dt). \tag{5.7}$$

Recalling that $B_n = 0$,

$$\sum_{n=1}^{\infty} (A_n \sin \lambda_n h) \exp(-\lambda_n^2 Dt) = 0. \tag{5.8}$$

Equation (5.8) can only be satisfied if $\lambda_n = \frac{n\pi}{h}$.

Applying the initial condition given in Eq. (5.3), $C(x,0) = C_\circ$ at $t = 0$, with $B_n = 0$ and $\lambda_n = \dfrac{n\pi}{h}$ to Eq. (5.5) one arrives at

$$C_\circ = C_s + \sum_{n=1}^{\infty} A_n \sin\left(\frac{xn\pi}{h}\right). \tag{5.9}$$

Multiplying Eq. (5.9) by $\sin\left(\dfrac{xp\pi}{h}\right)$ and integrating x over the range $0 \le x \le h$, gives

$$\int_0^h (C_\circ - C_s)\sin\left(\frac{xp\pi}{h}\right)dx = \sum_{n=1}^{\infty} A_n \int_0^h \sin\left(\frac{xn\pi}{h}\right)\sin\left(\frac{xp\pi}{h}\right)dx\,. \tag{5.10}$$

Integrations on the right hand side equals zero, except the one for which $n = p$, and by using standard trigonometry identities we arrive at

$$\int_0^h \sin^2\left(\frac{xp\pi}{h}\right)dx = \int_0^h \left(\frac{1-\cos\dfrac{2xp\pi}{h}}{2}\right)dx \tag{5.11}$$

leading to

$$\int_0^h \sin^2\left(\frac{xp\pi}{h}\right)dx = \frac{h}{2}. \tag{5.12}$$

Substituting Eq. (5.12) into Eq. (5.10) gives

$$\int_0^h (C_\circ - C_s)\sin\left(\frac{xp\pi}{h}\right)dx = A_n\left(\frac{h}{2}\right) \tag{5.13}$$

which finally leads to

$$A_n = \frac{2(C_\circ - C_s)}{n\pi}\left[1-\cos n\pi\right]. \tag{5.14}$$

From Eq. (5.14), it can be seen that $A_n = 0$ at n = even values and $A_n = \frac{4(C_\circ - C_s)}{n\pi}$ at n = odd values. Therefore we can change the summation index so that only odd values of n are summed

$$A_n = \frac{4(C_\circ - C_s)}{\pi(2j+1)} \text{ where } n = 2j+1. \tag{5.15}$$

Substituting the values of A_n, B_n and λ_n into Eq. (5.5) gives

$$C(x,t) = C_s + \sum_{j=0}^{\infty} \frac{4(C_\circ - C_s)}{\pi(2j+1)} \sin\left(\frac{(2j+1)\pi x}{h}\right) \exp\left(-\left(\frac{(2j+1)\pi}{h}\right)^2 Dt\right). \tag{5.16}$$

The total moisture content at time t, M_t, is then obtained by integrating Eq. (5.16) over the sheet thickness h i.e.

$$M_t = A\int_0^h C(x,t)dx \tag{5.17}$$

where A is the exposed surface area of the sheet. Then Eq. (5.17) becomes

$$M_t = C_s hA + \frac{8(C_\circ - C_s)hA}{\pi^2} \sum_{j=0}^{\infty} \frac{1}{(2j+1)^2} \exp\left(-\left(\frac{(2j+1)\pi}{h}\right)^2 Dt\right) \tag{5.18}$$

where $M_\infty = C_s hA$ is the moisture content at equilibrium when $t \to \infty$. Therefore finally we obtain for the mass uptake as a function of time,

$$M_t = M_\infty + \frac{8(C_\circ - C_s)hA}{\pi^2} \sum_{j=0}^{\infty} \frac{1}{(2j+1)^2} \exp\left(-\left(\frac{(2j+1)\pi}{h}\right)^2 Dt\right). \tag{5.19}$$

The determination of the water uptake can be carried out on free films and on supported coatings. For supported coatings, the denominator of the argument of the exponent in Eq. (5.19) is equal to $4h^2$ where h is the thickness of the coating (equal to one symmetrical half of the free film) [83].

5.3 Methodology

5.3.1 Material and sample preparation

Two groups of *urushi* samples have been used in this study. *Urushi* (*Kijiro* type) samples were prepared for the study of water absorption as follow: *urushi* was homogenously mixed and filtered as described in Chapter 3 (Section 3.2.1 and Section 3.2.2). *Urushi* was then cast, using the spin coater described in Section 3.2.4, onto 70 mm × 50 mm rectangular glass substrates. The curing procedures of the samples were same as described before in Chapter 3 (Section 3.2.5) in which they cured by storage at 75±2% RH for three weeks (to ensure that a full cure was achieved). A Q-Sun environmental weathering chamber was used to simulate UV ageing into which one subset of the non-aged *urushi* films was exposed to UV radiation. The films were exposed to 340 nm, 0.7 $W.m^{-2}$ UV radiation for 400 hrs (Section 3.3). The thickness of each *urushi* layer was measured in 25 locations to calculate the average thickness with a Mitutoyo digital micrometer of 0.001 mm resolution.

5.3.2 Gravimetric measurements

Diffusion of water in *urushi* films was studied by the gravimetric method in which the changes in weight of all the samples were monitored as a function of time using an electronic balance. A digital balance HA180 (A&D Instruments Ltd) that had a precision of 0.1 mg was used for all weight measurements. Care was taken to ensure that the balance was accurately calibrated and zeroed prior to each set of weighings and kept in the environmental chamber during the experiments.

5.3.3 Desorption and sorption measurements

Our desorption and sorption experiment involved four step changes in relative humidity for both non-aged and aged *urushi* films. Initially, aged and non-aged *urushi* samples were allowed to reach a uniform moisture distribution by storing them in the curing chamber at 75% until there was no change in mass of the sample. The samples were then put into 30% RH atmosphere, which was maintained for 20 hrs. After that the samples' environment was changed to 40%, 50% and 60% RH for 16 hrs, 20 hrs and 20 hrs, respectively, where the samples' mass was observed every 30 min. The

samples were dried at 100 °C for 27 hrs to remove any excess moisture, after which the dried samples were weighed.

During exposure to each relative humidity level, the moisture contents were measured gravimetrically and calculated with the following expression [84, 85]:

$$M_t(\%) = \frac{m_t - m_{dry}}{m_{dry}} \times 100\,, \tag{5.20}$$

where M_t is the moisture content at time t, weight percent of the specimen, m_t is the weight or mass of the specimen at time t in mg and m_{dry} is the weight or mass of the dry specimen in mg.

5.4 Results and discussion

Figure 5.1 and Figure 5.2 show the sorption and desorption curves for non-aged and aged *urushi*, respectively, at different RH levels. As expected the moisture contents of non-aged and aged *urushi*, during the desorption processes, decrease with time, while there is an increase during the sorption process. For non-aged and aged *urushi*, the initial moisture contents at 40%, 50% and 60% RH were found to be higher than the final moisture contents at 30%, 40% and 50% RH. These resulted as a result of the time taken to change the RH from lower to higher levels. Using the data shown in Figure 5.1 and Figure 5.2, the values of the diffusion parameters were obtained using the solution given in Eq. (5.19) fitted to the experimental data using regression techniques where the summation has been taken to the first 50^{th} terms. The resultant values for the diffusion coefficient D, the initial moisture content $M_\circ$, the moisture contents at equilibrium M_∞ and the permeability P for non-aged and aged *urushi* are given in Table 5.1 and Table 5.2, respectively. P is the permeability, calculated as the product of D and M_∞ [86]. A typical fit is shown in Figure 5.1 and Figure 5.2.

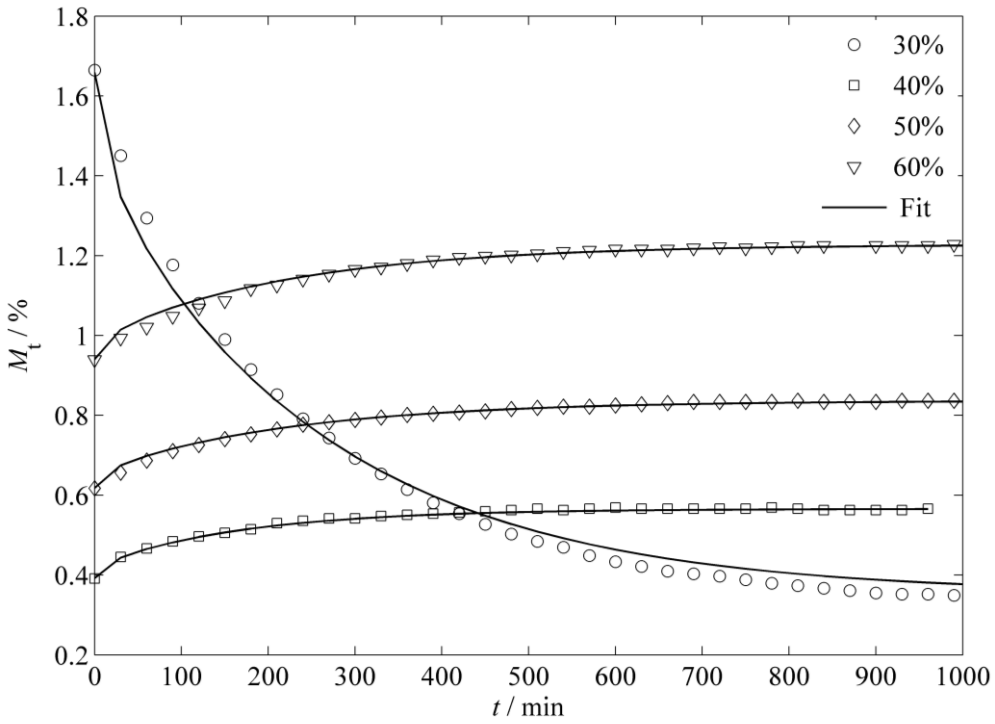

Figure 5.1: Sorption and desorption curves for non-aged *urushi* at different RH levels as a function of time. Solid lines represent the fitting from Eq. (5.19).

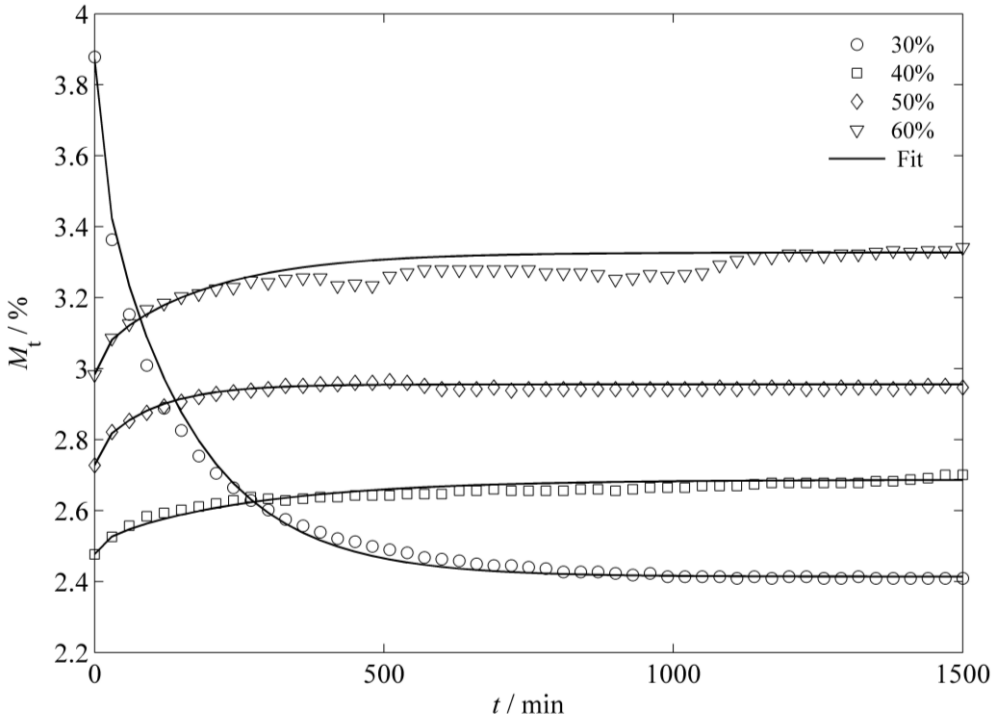

Figure 5.2: Sorption and desorption curves for aged *urushi* at different RH levels as a function of time. Solid lines represent the fitting from Eq. (5.19).

Figure 5.3 to Figure 5.6 show the variation of moisture contents M_t with time during desorption/sorption processes for non-aged and aged *urushi* film at 30%, 40%, 50% and 60%, respectively. As shown in all curves, the aged *urushi* films have higher M_t values than non-aged *urushi* films over the RH range (30%-60%).

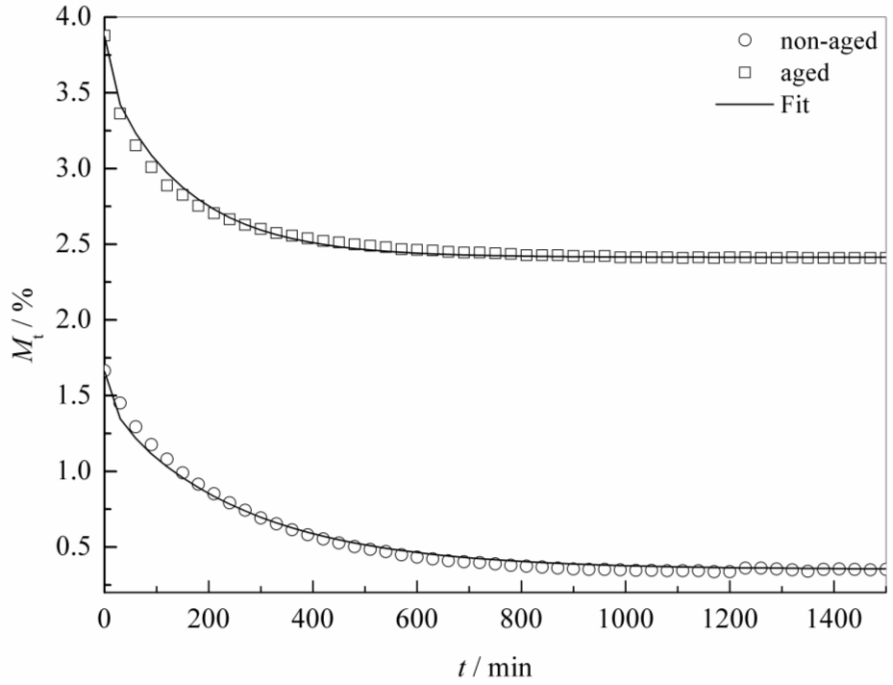

Figure 5.3: Desorption curves for non-aged and aged *urushi* at 30% RH.

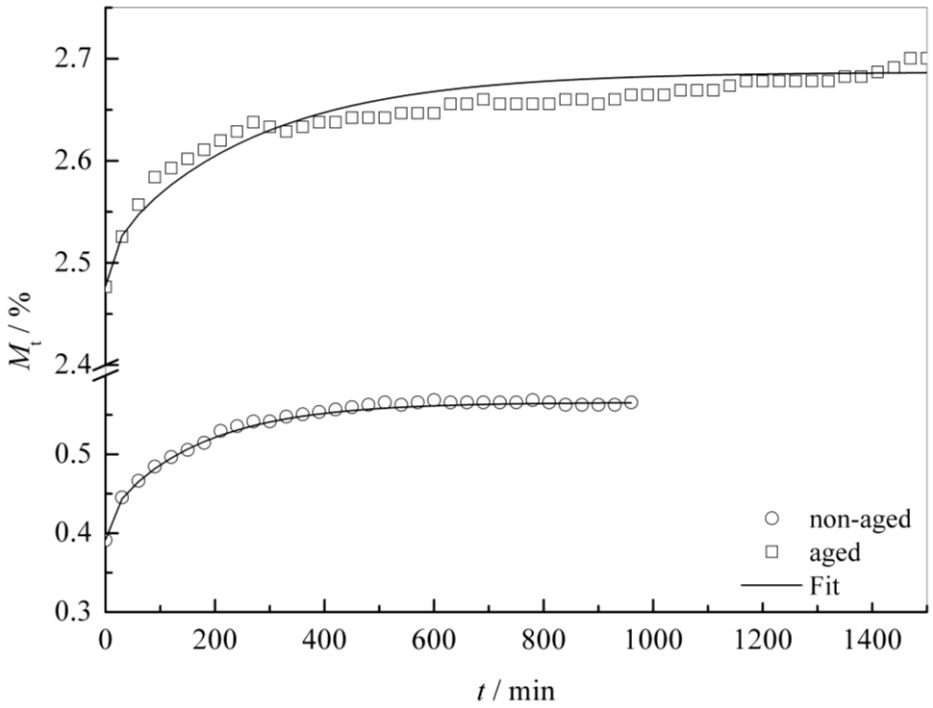

Figure 5.4: Sorption curves for non-aged and aged *urushi* at 40% RH.

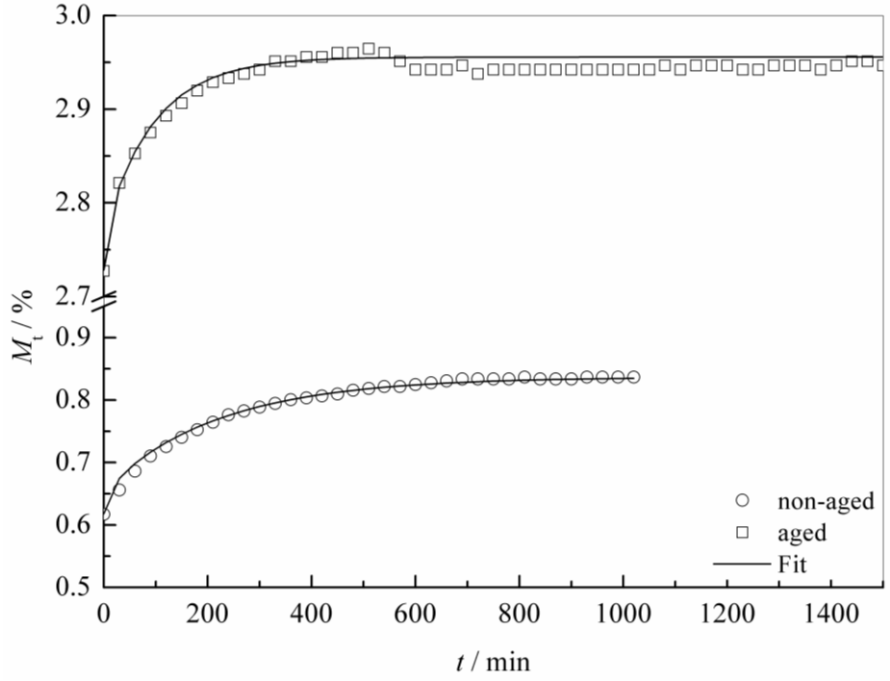

Figure 5.5: Sorption curves for non-aged and aged *urushi* at 50% RH.

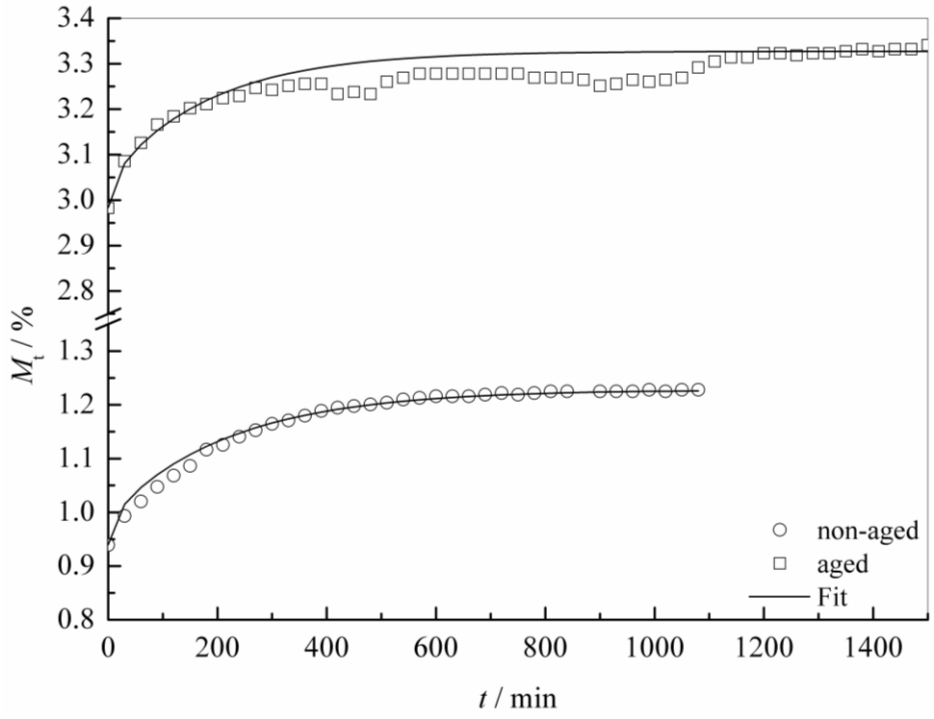

Figure 5.6: Sorption curves for non-aged and aged *urushi* at 60% RH.

Figure 5.7 shows the variation of the asymptotic moisture contents at equilibrium, M_∞, with the RH for non-aged and aged *urushi*. From the data obtained, we can see that the moisture content at equilibrium, M_∞, for both non-aged and aged *urushi*,

increased with RH. Also, the moisture contents at equilibrium, M_∞, values in aged *urushi* were significantly higher than those in non-aged over the RH range (30%-60%) which suggests that the ageing process has a significant influence on the mechanisms for mass transport at a microscopic level as a result of chemical changes due to UV exposure. These chemical changes would likely increase its water affinity and decrease the crosslink density and so increase the availability of free volume holes. Physically, micro-crack networks (Figure 5.8) have been observed on the aged *urushi*, which would facilitate the penetration of moisture into the aged films during the sorption process.

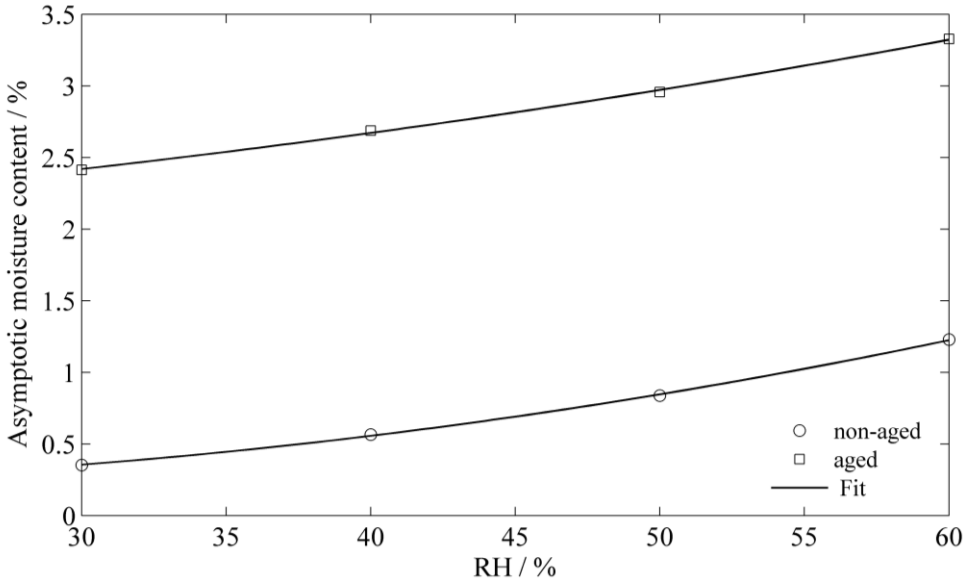

Figure 5.7: Asymptotic moisture contents, M_∞, as a function of RH for non-aged and aged *urushi*.

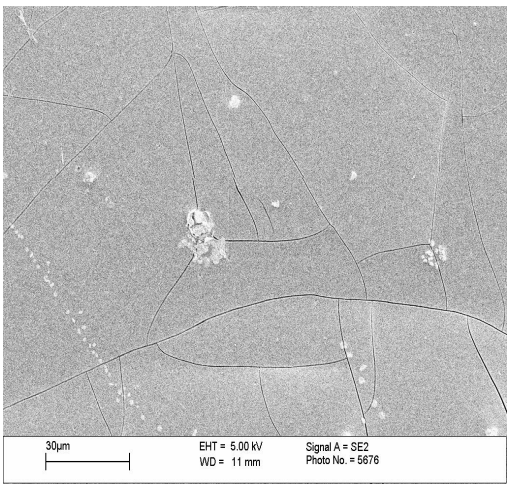

Figure 5.8: Micro-cracks observed on aged *urushi* film.

Table 5.1: Water diffusion parameters for non-aged *urushi*.

Humidity changes	$M_\circ$ (%)	M_∞ (%)	D (m^2/min)	P (m^2/min)
75% → 30%	1.66	0.35	1.1 E-11	3.87 E-12
30% → 40%	0.39	0.56	1.7 E-11	9.61 E-12
40% → 50%	0.62	0.84	1.3 E-11	1.08 E-11
50% → 60%	0.94	1.23	1.3 E-11	1.59 E-11

Table 5.2: Water diffusion parameters for aged *urushi*.

Humidity changes	$M_\circ$ (%)	M_∞ (%)	D (m^2/min)	P (m^2/min)
75% → 30%	3.89	2.41	1.55 E-11	3.74 E-11
30% → 40%	2.48	2.69	0.9 E-11	2.41 E-11
40% → 50%	2.73	2.95	2.5 E-11	7.38 E-11
50% → 60%	2.98	3.33	1.3 E-11	4.32 E-11

5.5 Conclusions

The desorption and sorption curves from the gravimetric experiments at different humidity levels were undertaken to investigate the characteristics of water diffusion in non-aged *urushi* films. In each case the effect of ageing on the water diffusion process was considered. The moisture diffusion coefficient was determined by fitting the solution of the diffusion equation to the experimental data. The results show that no significant dependence of the moisture diffusion coefficient on the moisture contents for non-aged and aged *urushi*. The higher values of the moisture contents at equilibrium, M_∞, in aged *urushi* would be contributed to chemical changes due to UV exposure where further spectroscopic measurements will be required to identify the effects of ageing on the chemical microstructure of *urushi*.

Chapter 6

Stress Response of *Urushi* Films under Changes of Environmental Conditions

6.1 Introduction

We investigated the response of *urushi* to changes in environment conditions by examining the deflection of a glass substrate coated with a thin film of *urushi* when it was subjected to different humidity levels. This deflection was measured using phase shifting interferometry and then related to the bending moment and in-plane stress developed in the system due to the expansion mismatch in the bilayer using Atkinson's formula (Section 4.2).

In Section 6.4, the results of the average stress measurements in *urushi* film are presented for aged and non-aged *urushi*. The stresses were measured when *urushi* films were subjected to three low RH (30%, 36% and 42%) and three high RH (60%, 54% and 48%). Comparison of the behaviour of the aged and non-aged *urushi* showed

that both have the same response to changes in the humidity. During desorption, stresses were higher for the non-aged *urushi* films while during adsorption stresses were higher for the aged *urushi* films. A discussion on the experimental errors analysis and conclusions are presented in Section 6.5 and Section 6.7. Upon changing the humidities we observed rapidly changing stresses in *urushi*, which then showed evidence of relaxation over much longer timescales. A simple 1D model of stress will be also proposed (Section 6.6) to predict the behaviour of the *urushi* thin layers to changes in environmental RH.

6.2 Experimental conditions

Two sets of *urushi* samples have been used in this study, in which a thin layer of *urushi* films of thickness 21 μm were deposited on a circular glass substrate of thickness 190 μm and cured at the same conditions. One subset has been exposed to UV radiation for 400 hrs. Full description of *urushi* films preparation and ageing condition has been described in Sections 3.2 and 3.3.

6.3 Environmental loading

The stress response of three non-aged and three UV-aged *urushi* films to changes in RH were measured in this work. Each of them was used for measuring its response to two changes in RH, rather than using the same sample to measure different RH changes, so as to avoid history dependent effects. The RH history of each of the samples is shown in Figure 6.1.

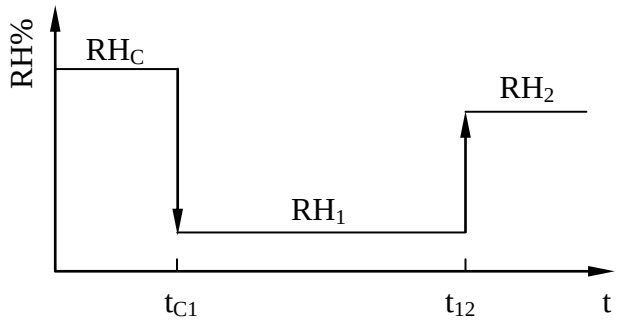

Figure 6.1: Schematic of step changes in relative humidity levels with time, where RH_C = 75% is the curing RH, RH_1 is the low RH = 30%, 36% and 42% and RH_2 is the high RH= 60%, 54% and 48%. t_{C1} and t_{12} are the times at which RH changes from RH_C to RH_1 and from RH_1 to RH_2, respectively.

Initially, all samples were kept at the relative humidity for curing, RH_C=75±2%, for 3 weeks to ensure equilibrium. Each sample was then exposed to a step reduction in RH, to one of three different low relative humidity levels, denoted as RH_1 in Figure 6.1. Under each low relative humidity level, the film stress was observed over 66 hrs, a time that corresponds to 95% of an approach to the asymptote. After that the samples' environment was changed to one of three different high relative humidity levels, denoted as RH_2 in Figure 6.1. During exposure to the high humidity levels, the stress response was observed for the following 7 hrs. The low relative humidity levels (RH_1) were 30%, 36% and 42% while the high relative humidity levels (RH_2) were 60%, 54% and 48%. The measurements were carried out every 5 minutes until the stress reached a maximum value and then every 1 hr. During all measurements the temperature was held constant at 23 °C.

6.4 Results and discussion

As mentioned in Chapter 4, to obtain wrapped phase of difference, four interferograms were recorded with $\frac{\pi}{2}$ phase shift introduced between the interfering beams. An example of four interferograms obtained with 0, $\frac{\pi}{2}$, π, $\frac{3\pi}{2}$ phase shifts is shown in Figure 6.2. Since there is a π phase shift between the first and the third interferograms, Figure 6.2 (a) and (c), they appear out of phase.

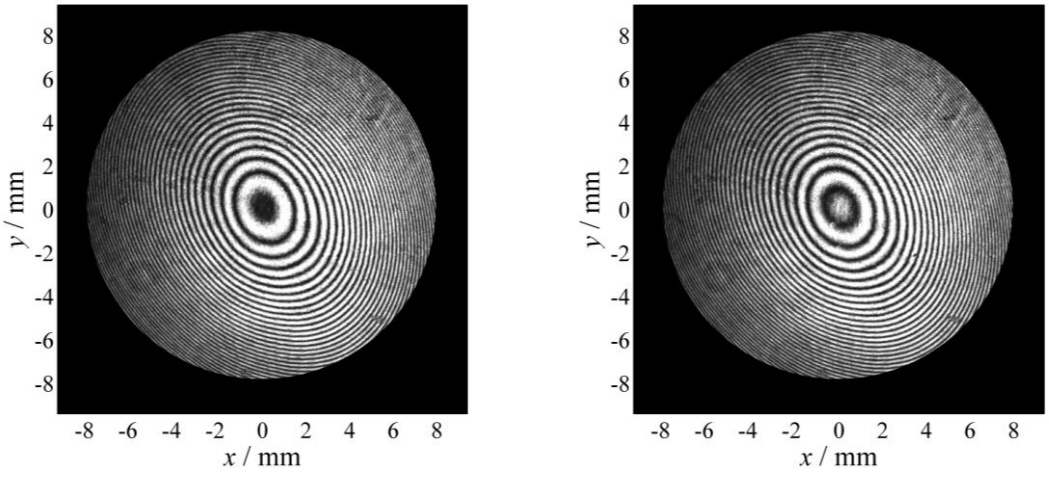

(a) (b)

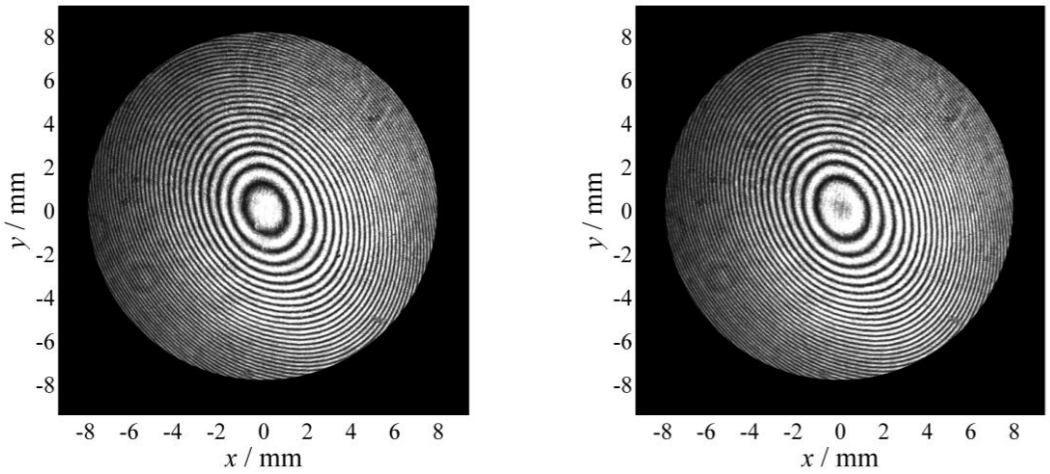

(c) (d)

Figure 6.2: Interferograms with (a) 0, (b) $\frac{\pi}{2}$, (c) π and (d) $\frac{3\pi}{2}$ phase difference.

Figure 6.3 shows typical results of wrapped phase of difference maps, $\Delta\phi_w(x,y)$, for non-aged *urushi* thin film during exposure to 30% RH for 5 min, 50 min, 100 min, 1080 min, 2280 min and 4080 min, respectively. As shown in Figure 6.3, the wrapped phase of difference maps lie in the range $(-\pi,\pi)$. The changing in colour discontinuously from white to black means there is a phase jump of 2π. It is shown that in Figure 6.3 that the fringe frequency increases with exposure time reaching a maximum value after exposure time 100 min (Figure 6.3 (c)) followed by a decrease in the fringe frequency over long exposure time. Increasing the fringe frequency indicates that more wrapped out-of plane deformation while a decrease in the fringe frequency indicates less wrapped deformation. Unwrapped phase of difference maps, $\Delta\phi(x,y)$, have been evaluated as shown in Figure 6.4. It can be seen that the 2π discontinuities have been removed by adding an appropriate integer multiple of 2π at each point in the wrapped phase of difference distribution.

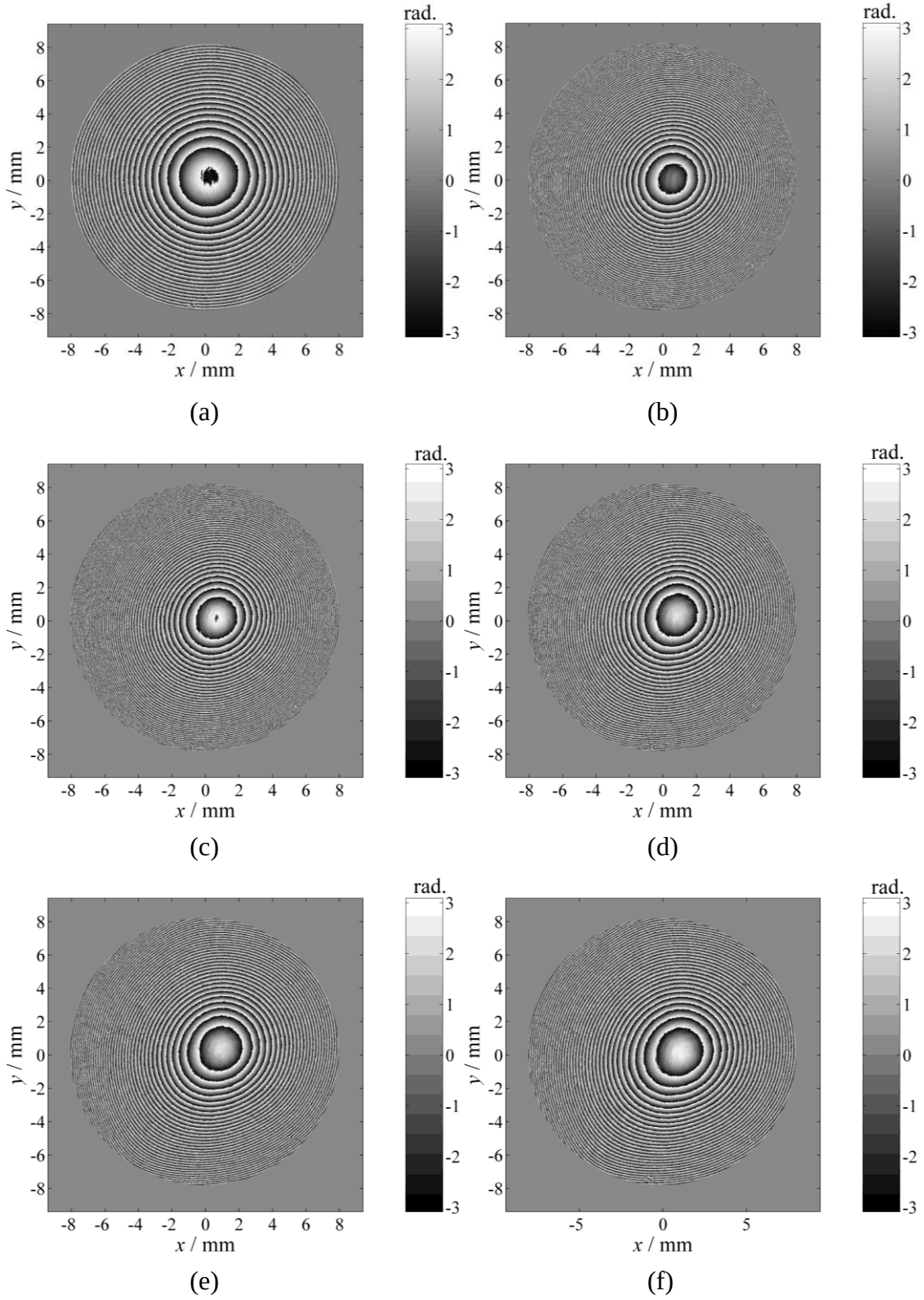

Figure 6.3: Wrapped phase of difference maps, $\Delta\phi_w(x, y)$, for non-aged *urushi* thin film when exposed to a humidity change from 75% to 30% for (a) 5 min, (b) 50 min, (c) 100 min, (d) 1080 min, (e) 2280 min and (f) 4080 min.

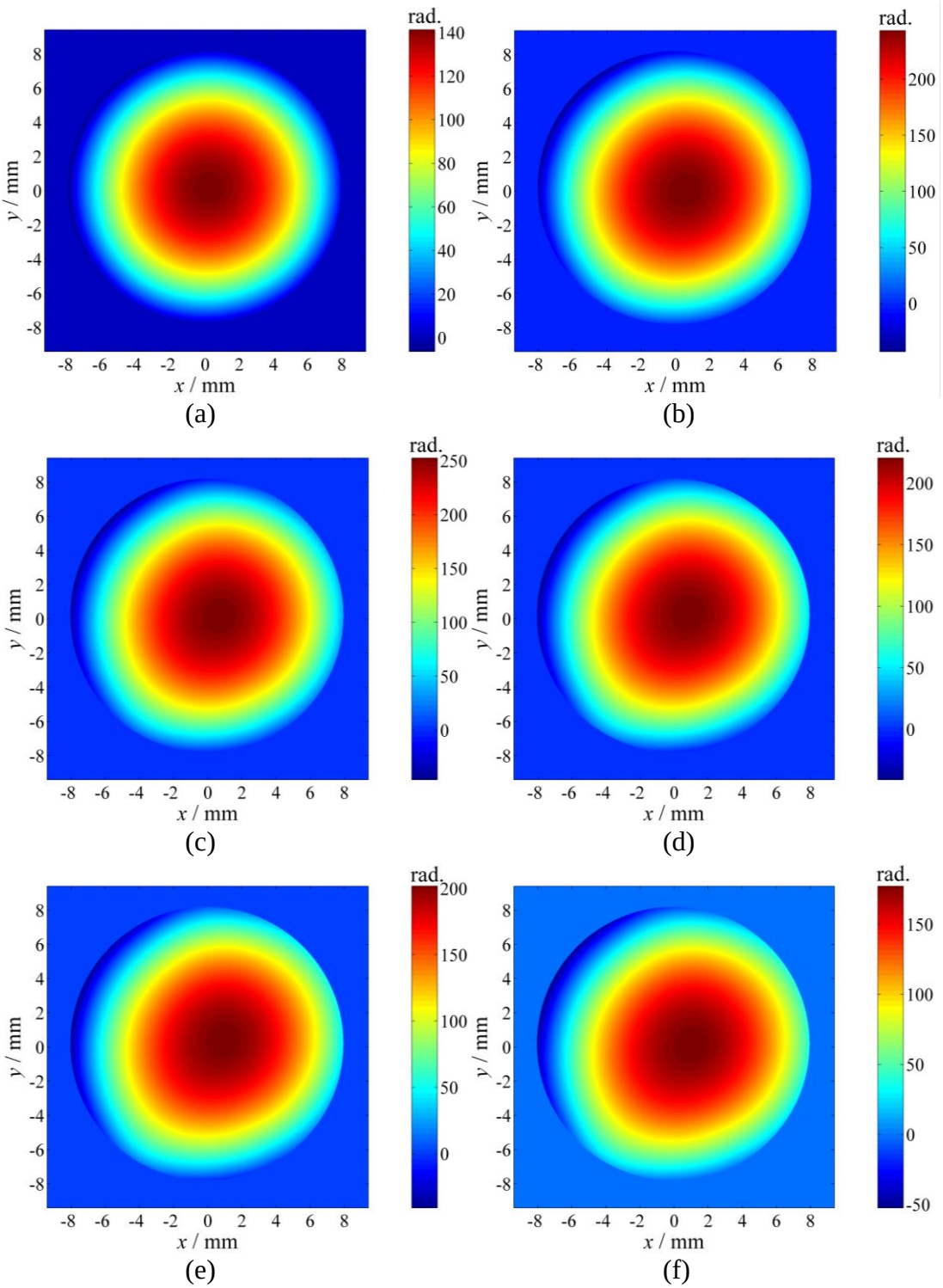

Figure 6.4: Unwrapped phase of difference maps, $\Delta\phi(x, y)$ for non-aged *urushi* thin film when exposed to a humidity change from 75% to 30% for (a) 5 min, (b) 50 min, (c) 100 min, (d) 1080 min, (e) 2280 min and (f) 4080 min.

Using Eq. (4.7), the displacement distribution maps, $\delta(x, y)$, can be extracted and is shown in Figure 6.5 for the same conditions in Figure 6.3 and Figure 6.4. Figure 6.6

shows the best fit of Eq. (4.8) to the experimental data, only showing the quadratic coefficients a, b and c.

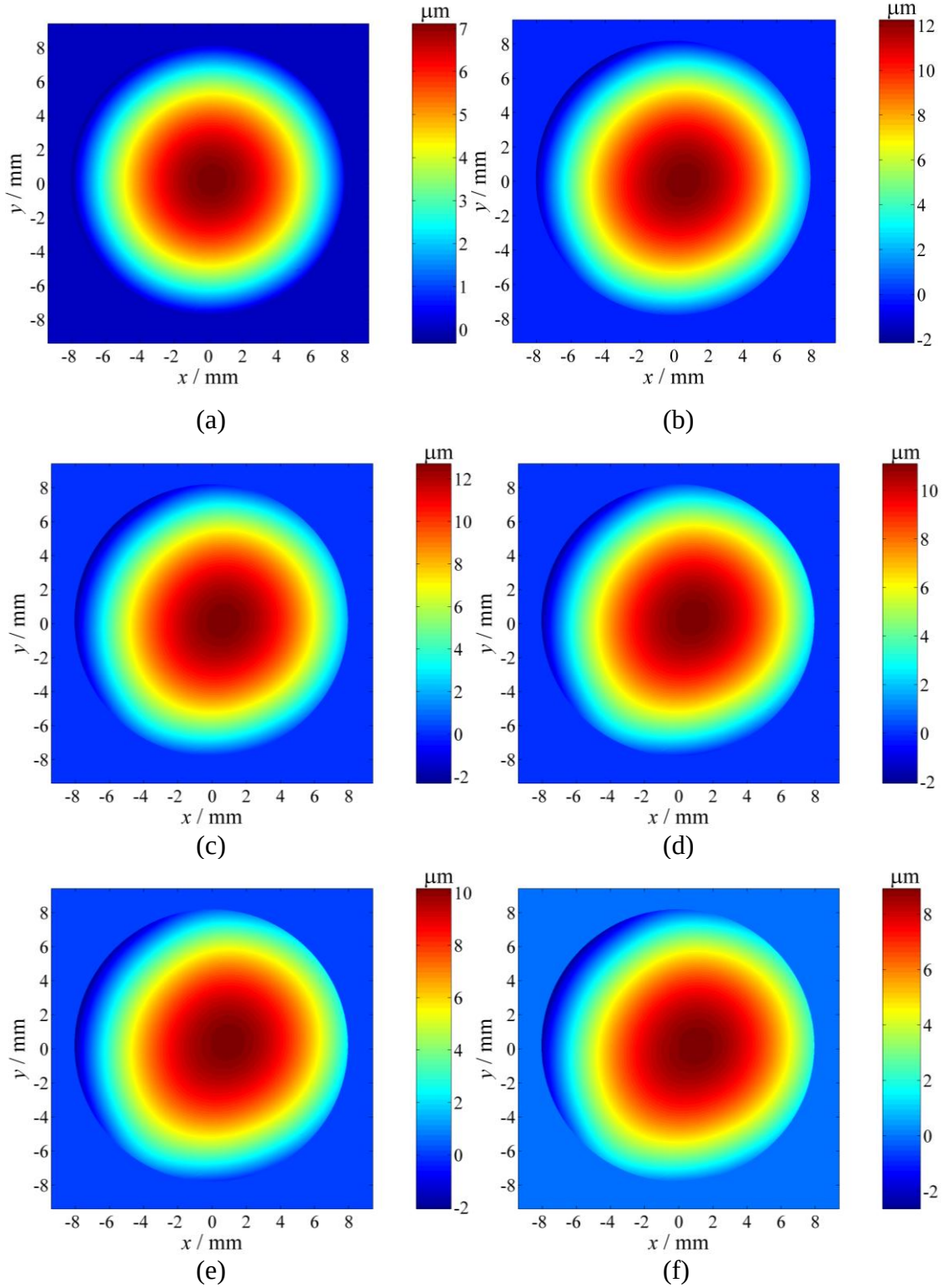

Figure 6.5: Displacement distributions maps, $\delta(x, y)$, for non-aged *urushi* thin film when exposed to a humidity change from 75% to 30% for (a) 5 min, (b) 50 min, (c) 100 min, (d) 1080 min, (e) 2280 min and (f) 4080 min.

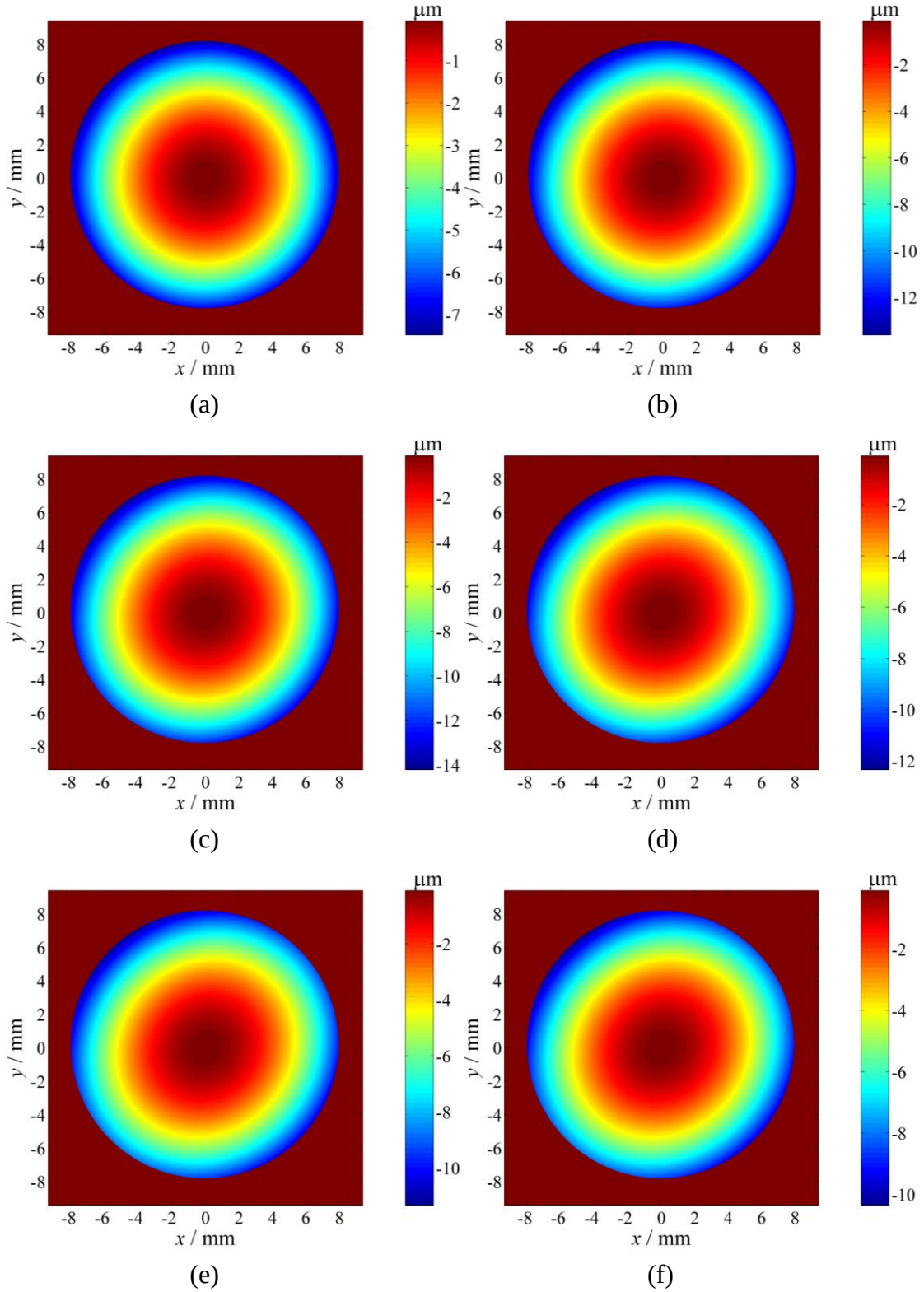

Figure 6.6: Least square fitting of the displacement distribution, $\delta(x, y)$, using the quadratic coefficients for non-aged *urushi* thin film when exposed to a humidity change from 75% to 30% for (a) 5 min, (b) 50 min, (c) 100 min, (d) 1080 min, (e) 2280 min and (f) 4080 min.

Figure 6.7 shows a contour representation of the displacement distribution shown in Figure 6.6(f). The orientation of the minor axis, θ_m, is 2.36 rad. and the orientation of the major axis, θ_M, is 3.93 rad. For this figure, the depth-averaged film stresses along the minor and the major axes, σ_1 and σ_2, are 9.14 MPa and 7.51 MPa respectively.

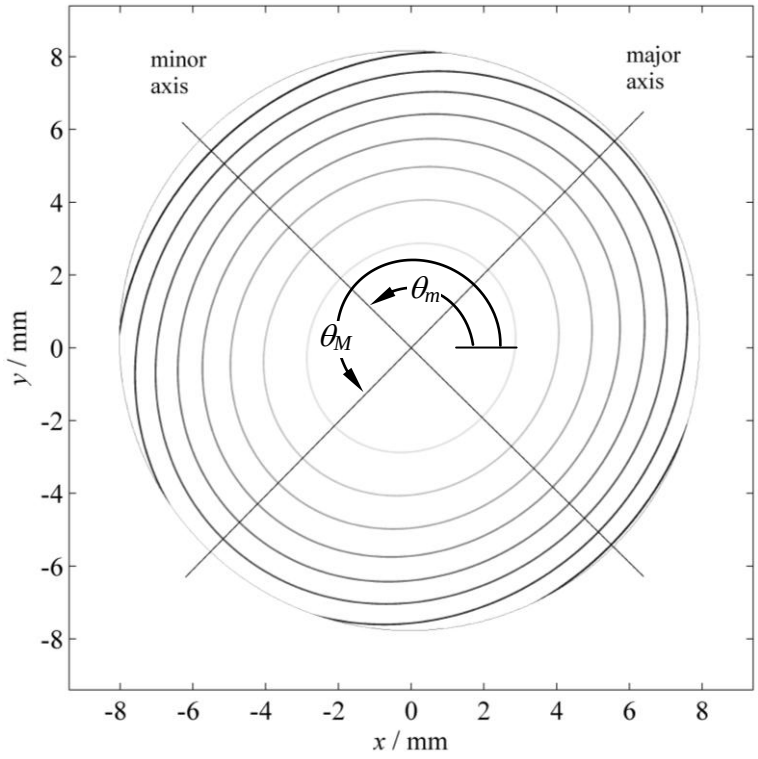

Figure 6.7: Displacement distribution contour for non-aged *urushi* film when exposed to a humidity change from 75% to 30% for 4080 min.

Figure 6.8 shows a further comparison of the out–of plane deflection for non-aged *urushi* thin film when exposed to a humidity change from 75% to 30% for (a) 5 min, (b) 50 min, (c) 100 min, (d) 1080 min, (e) 2280 min and (f) 4080 min. As shown in Figure 6.8, the bi-material system experiences stress relaxation after an exposure time of 100 min in 30% RH.

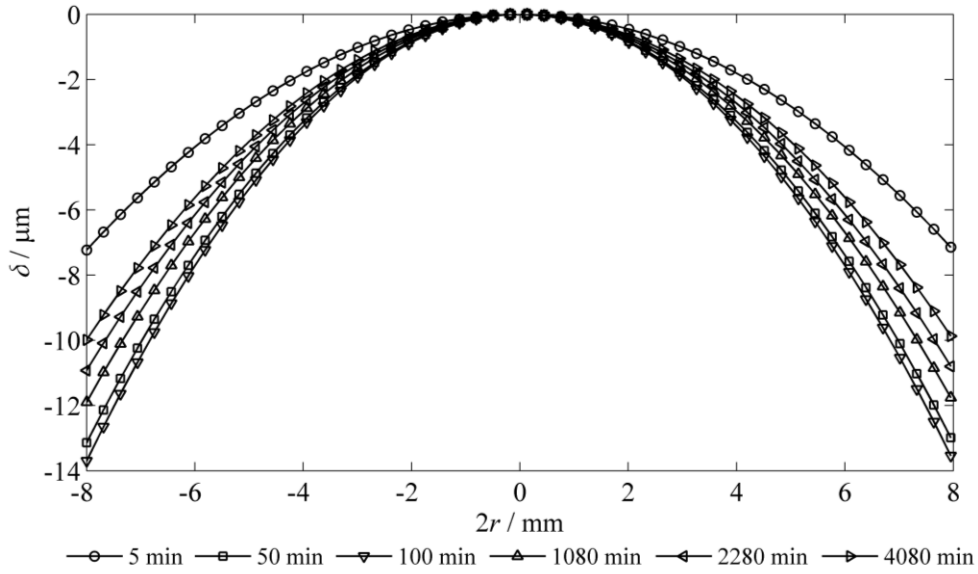

Figure 6.8: Surface topography along the minor axis for non-aged *urushi* thin film/substrate system during exposure to 30% RH for different exposure times.

As shown in Figure 6.9, the curvature (K) of a deformed substrate is related to the radius of curvature (R), based on the assumption of $\delta << R$, by

$$K = \frac{1}{R} = \frac{2\delta}{r^2}, \tag{6.1}$$

where r is the substrate radius.

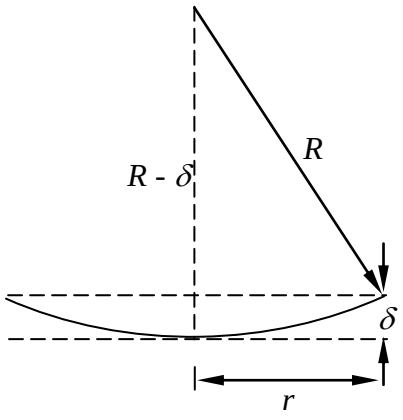

Figure 6.9: Relation between the radius of curvature and the deflection.

Figure 6.10(a-c) shows the development of film curvature along the minor axis of non-aged and aged *urushi* films exposed to a range of relative humidity levels, as a function

of time. The general behaviour of the *urushi* film subsequent to a reduction in humidity from 75% is a positive deflection of the substrate (cusp towards the camera) which corresponds to a tension in-plane stress developing in the film.

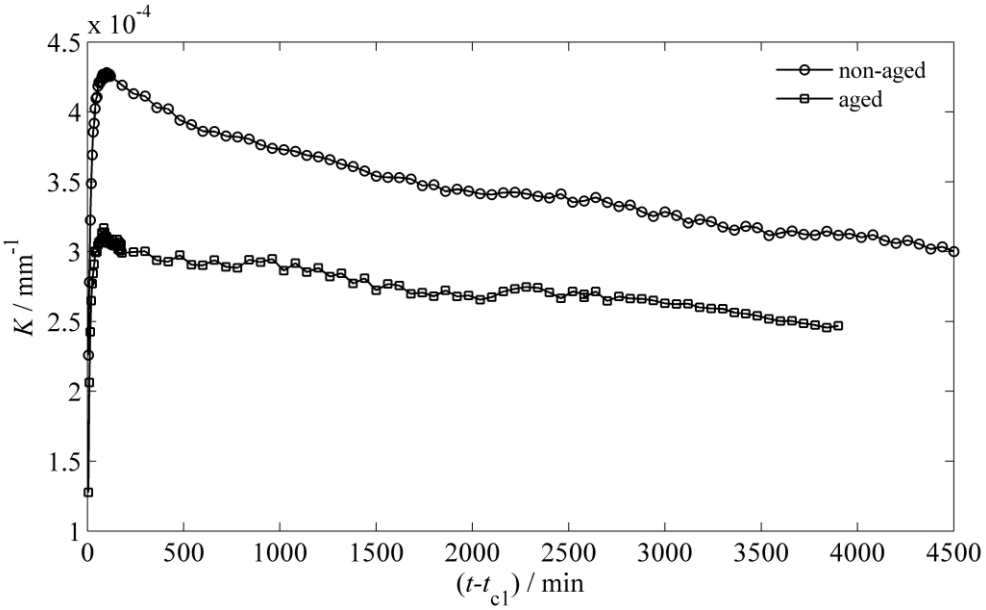

(a)

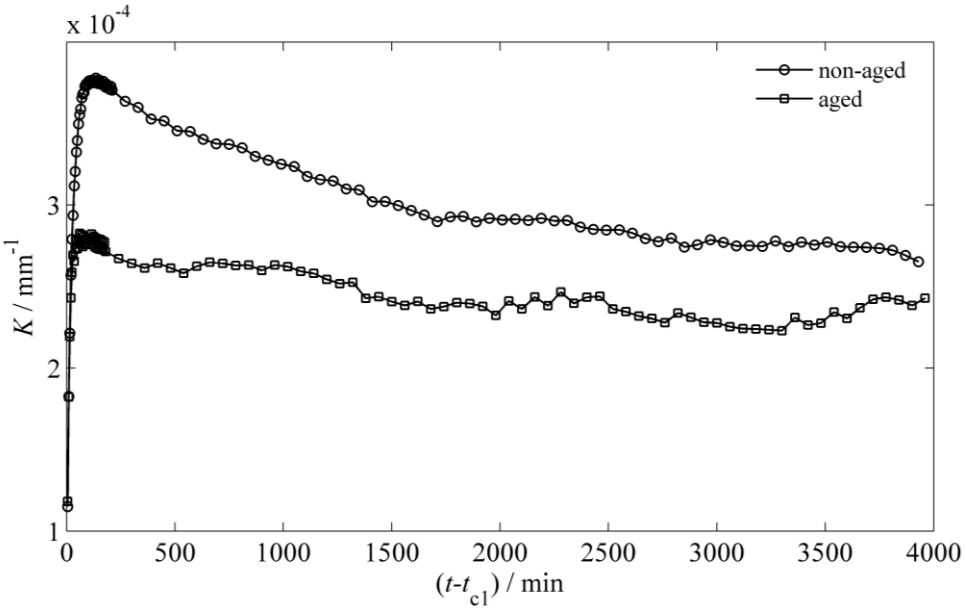

(b)

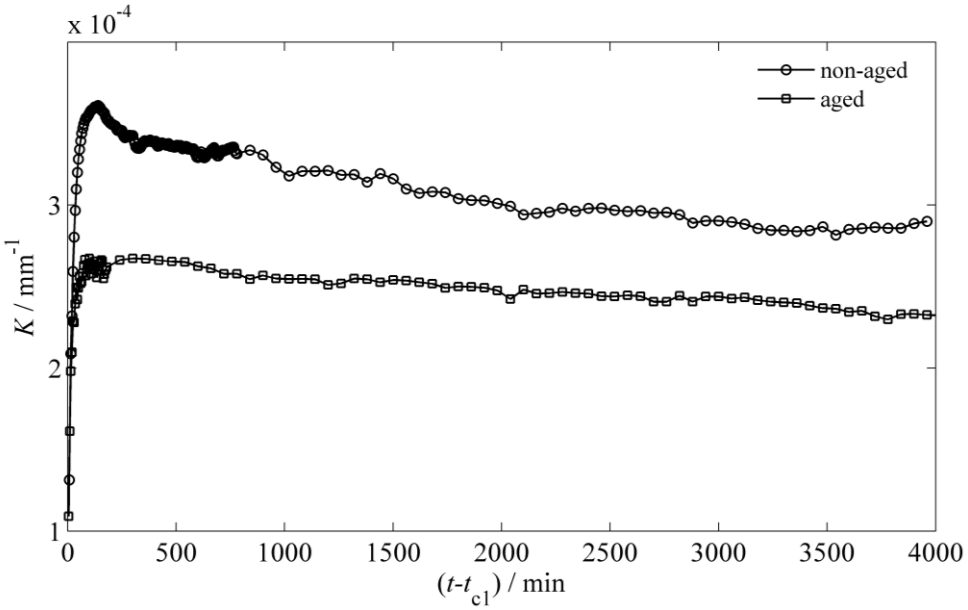

(c)

Figure 6.10: Curvature development as a function of time in non-aged and aged *urushi* films after changing the humidity from 75% to (a) 30%, (b) 36% and (c) 42%.

Figure 6.11(a-c) shows the development of film stress in three different non-aged and aged *urushi* films during exposure to the low relative humidity levels, as a function of time. The stress peaks within about 2 hrs then relaxes over a longer time scale with a slight reduction in the magnitude of the stress. Semi-log (line-log) plots have been inserted in Figure 6.11 to illustrate the stress behaviour during the first 2 hrs.

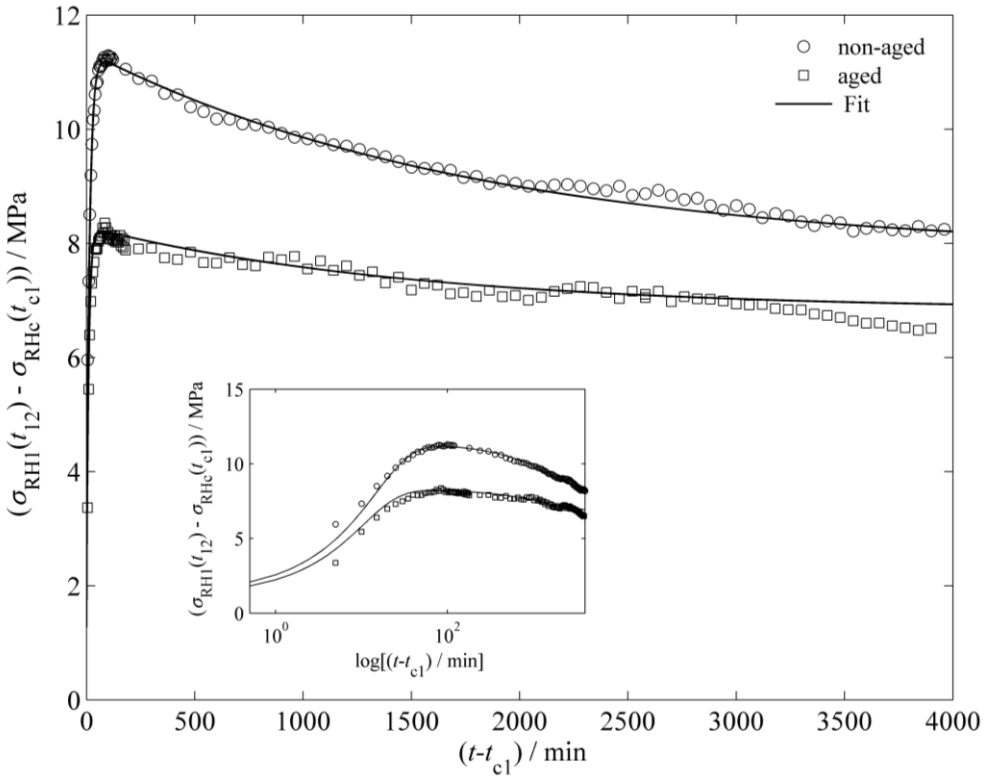
non-aged
aged
Fit
$(\sigma_{RH1}(t_{12}) - \sigma_{RHc}(t_{c1}))$ / MPa
$(t\text{-}t_{c1})$ / min
$\log[(t\text{-}t_{c1})$ / min]

(a)

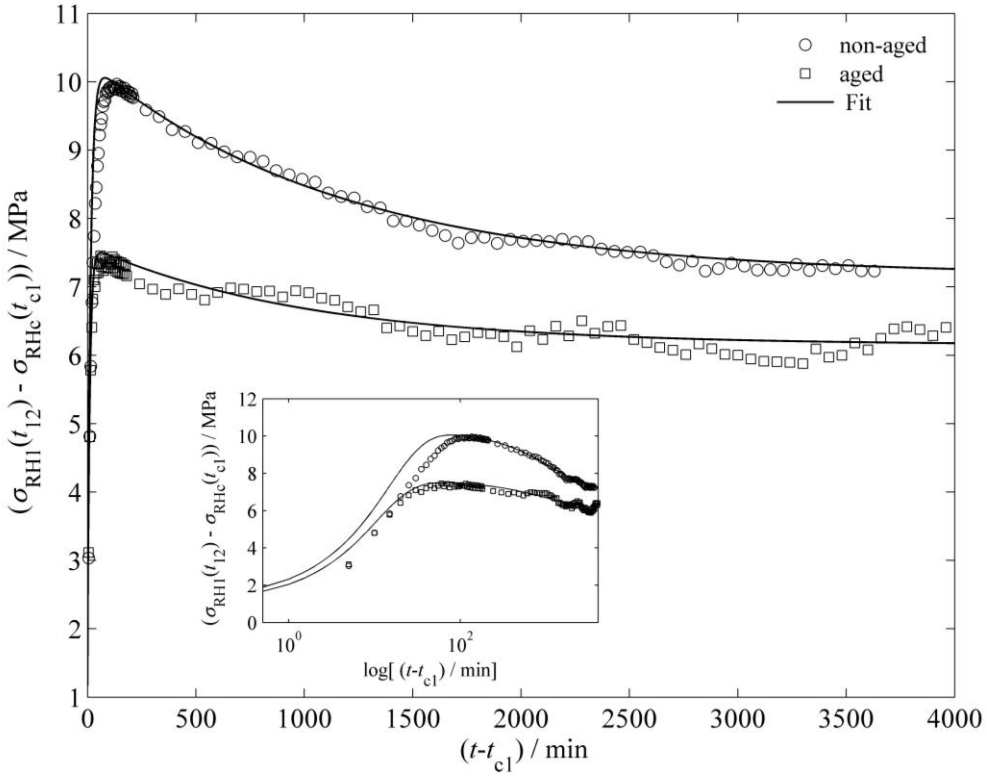
non-aged
aged
Fit
$(\sigma_{RH1}(t_{12}) - \sigma_{RHc}(t_{c1}))$ / MPa
$(t\text{-}t_{c1})$ / min
$\log[(t\text{-}t_{c1})$ / min]

(b)

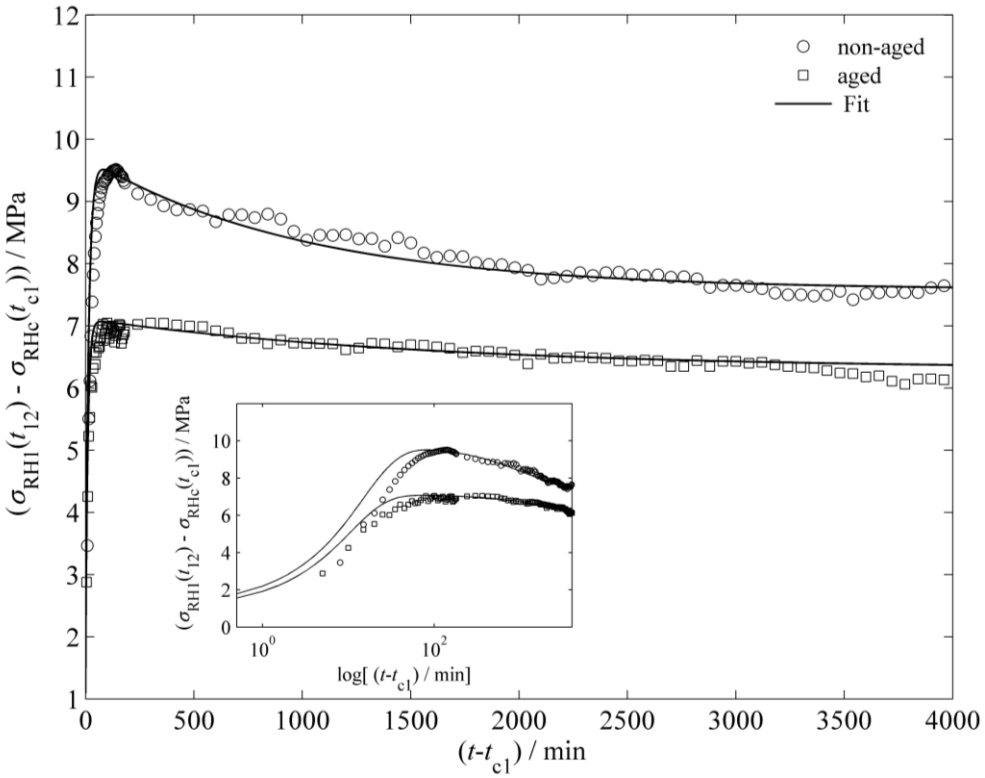

(c)

Figure 6.11: Film stress development along the minor axis in non-aged and aged *urushi* films after changing the humidity from 75% to (a) 30%, (b) 36% and (c) 42%. Inserted plots are semi-log plots to illustrate the stress behaviour during the first 2 hrs. Solid lines are the predicted film stress, further discussion in Section 6.6.1.

In order to compare the behaviour of the *urushi* to changes in humidity we plot three functions. Firstly we estimate the rate at which the stress develops in the period after the first step change in humidity occurs (Figure 6.12). Secondly, we note the peak tensile in-plane stress (Figure 6.13). Finally we determine the asymptotic stress values (σ_∞) reached in the film (Table 6.1 and Table 6.2) by assuming that at long times, the relaxation can be modelled by a single relaxation function and fitting an exponential approach to the long time behaviour, approximated by

$$\sigma = \sigma_\infty + \sigma_B e^{(-t/\tau)} \tag{6.2}$$

where σ_B and τ are fitting constants. We can attribute different physical mechanisms to the stages of deformation for the material when subjected to a reduction in relative

humidity. Shortly after the humidity is changed, the desorption of water leads to volume shrinkage and as a result of the adhesion to the glass substrate a compressive in plane stress (on the substrate) and its associated bending moment will be created. Because the substrate/film system is in equilibrium, a tensile stress develops in the film. Following this period we observe that tensile in-plane stress peaks after which there is a relaxation of the material. We believe that the most likely explanation for this behaviour is that the viscoelastic properties of the *urushi* lead to time dependent behaviour since the humidity and therefore hygral strain is maintained at a constant value once hydrothermal equilibrium is reached: we are observing stress relaxation in the material. In order to identify the physical processes, further investigation is required to quantify the moisture dependent material properties of *urushi*. The peak stress values and times for non-aged and aged *urushi* samples which were subjected to low relative humidity levels are shown in Table 6.1 and Table 6.2 and are plotted in Figure 6.13 as a function of the difference between storage (75%) and different low RH levels. This shows clearly that the absolute value of the in-plane stress scales with the size of the RH change. Figure 6.12 shows the rate at which the tensile stress develops in non-aged and aged *urushi* films as a function of the difference between storage (75%) and different low RH levels. As shown in Figure 6.12, the stress develops quickly with a change in humidity but it is not clear that the rate increases with increasing RH difference.

Table 6.1: Maximum stress, time of peak occurrence, stress rate and the asymptotic stress values obtained for non-aged *urushi* films in response to different amounts of decrease in relative humidity.

RH_C (%)	RH_1 (%)	non-aged *urushi*			
		σ_{max} (MPa)	t (min)	stress rate ($MPa.min^{-1}$)	asymptotic stress σ_∞ (MPa)
75	30	11.29	100	0.26	7.7454
75	36	9.964	135	0.28	7.0395
75	42	9.52	140	0.2	7.3016

Table 6.2: Maximum stress, time of peak occurrence, stress rate and the asymptotic stress values obtained for aged *urushi* films in response to different amounts of decrease in relative humidity.

RH_C (%)	RH_1 (%)	aged *urushi*			
		σ_{max} (MPa)	t (min)	stress rate ($MPa.min^{-1}$)	asymptotic stress σ_∞ (MPa)
75	30	8.357	85	0.3	6.026
75	36	7.454	60	0.27	6.0071
75	42	7.045	100	0.23	5.0982

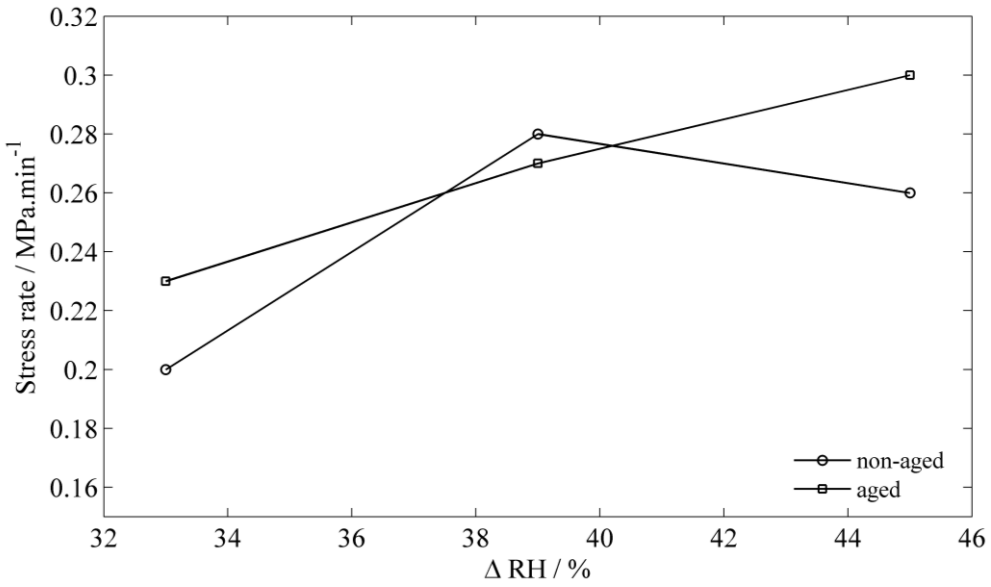

Figure 6.12: Stress rate in non-aged and aged *urushi* films as a function of the difference between storage (75%) and different low RH levels.

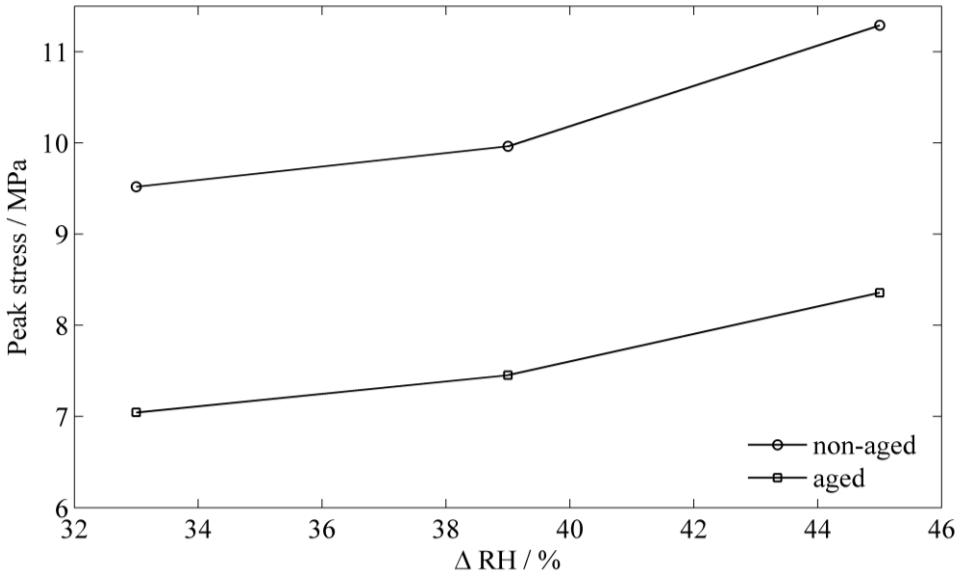

Figure 6.13: Effect of relative humidity changes ΔRH (RH_C to RH_1) on the peak film stress developed in non-aged and UV-aged *urushi* films.

6.5 Experimental errors analysis

It was observed that the *rms* error, Eq. (4.20), was below 0.17 μm for the time between t_{C1} and the time at which the stress peaked, corresponding to 1.2% of the maximum deflection at peak stress. For small deformations of the glass substrate, this error is mainly due to the high spatial frequency nature of the phase noise. For large deformations of the substrate, i.e. at peak stress, the *rms* error was at most 0.17 μm for the biggest RH step from 75% to 30%, and reflects not only the spatial variations of the measured displacements but the truncation error of the second order polynomial used to approximate what in reality is not exactly a parabolic displacement field. To obtain an estimate of the error associated with the calculated stress, an error propagation analysis was performed for non-aged *urushi* film when RH changes from 75% to 30% (the RH change which produced the maximum peak stress of 11.29 MPa as shown in Table 6.1). This used the experimental parameters u_{t_s} = 5 μm, u_{t_f} = 2 μm, u_δ = 0.1749 μm, u_r = 18 μm, t_s = 190 μm, t_f = 21 μm, δ = 14.32 μm and r = 8 mm. The individual contributions obtained from Eq. (4.21) to Eq. (4.24) to the overall uncertainty u_σ are shown in Table 6.3. It can be observed that the film thickness t_f has the greatest contribution on the error of the estimated average film stress while the

displacement δ and the distance from the centre to where the displacement is measured, r, have the lowest contributions. The overall uncertainty is then approximately 1.4 MPa, for the state described, resulting in an error of less than 13% of the absolute stress observed.

Table 6.3: The uncertainty in the average film stress σ due to the substrate thickness t_s, the film thickness t_f, the displacement δ and the distance from the centre to where the displacement is measured, r.

$u_{\sigma t_s}$ (MPa)	$u_{\sigma t_f}$ (MPa)	$u_{\sigma \delta}$ (MPa)	$u_{\sigma r}$ (MPa)	u_{σ} (MPa)
0.65	1.22	0.14	0.05	1.39

When the *urushi* films are subjected to an increase in relative humidity (RH_1 to RH_2), a similar behaviour to that seen during desorption is observed. Due to water ingress, we naturally anticipate that there will be a volume increase, and a compression in-plane stress is observed that supports this. Similar to that observed for desorption, we observe an initial region of rapid in-plane stress change, followed by a peak and relaxation to the asymptotic value. In this case however, the magnitude of the relative humidity changes is small and the behaviour is correspondingly weaker (Figure 6.14(a-c)).

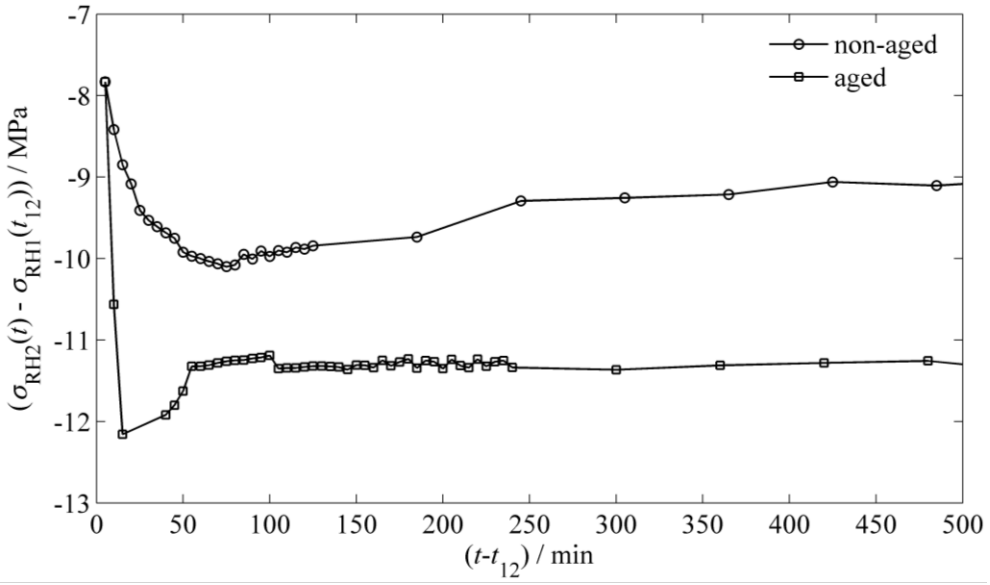

(a)

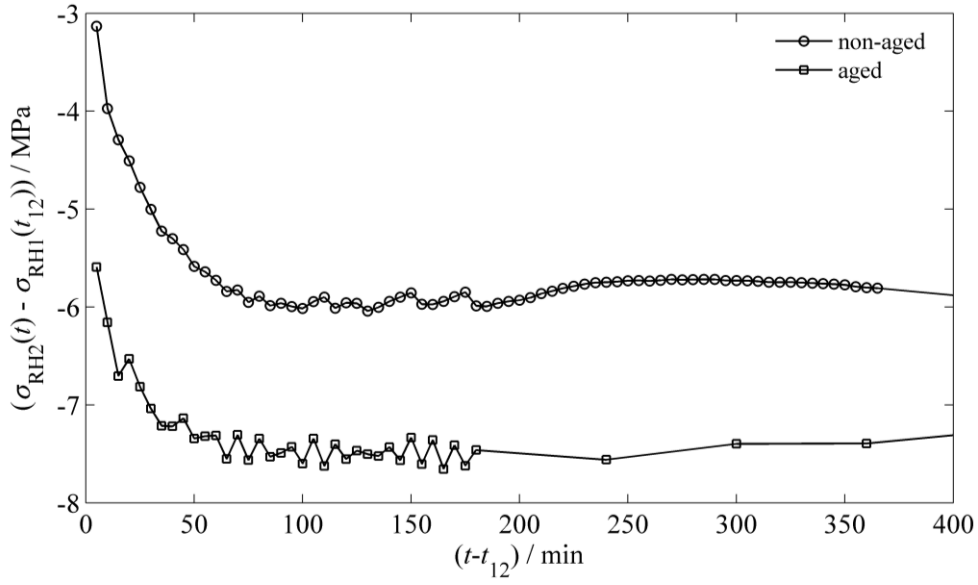

(b)

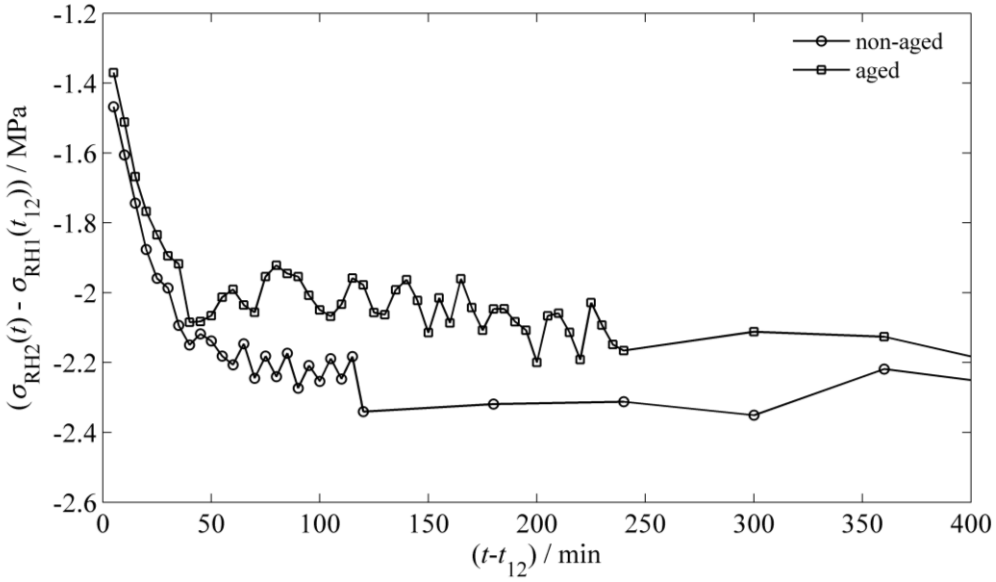

(c)

Figure 6.14: Film stress development along the minor axis in non-aged and aged *urushi* films after changing the humidity from (a) 30% to 60%, (b) 36% to 54% and (c) 42% to 48%.

The behaviour observed following a humidity change is broadly consistent regardless of whether the material has been aged or not. The patterns we observe are similar, but we do observe significant differences in the absolute values. In general, for large reductions in relative humidity, the aged films exhibit a smaller in-plane stress than the non-aged materials. For example, we observe a ~30% reduction in the peak tensile stress in Figure 6.11(c), which is replicated for other changes in relative humidity, and applies to the asymptotic stress as well. When RH changes from 30% to 60% and from

36% to 54%, the aged films exhibit a higher in-plane stress than the non-aged materials (Figure 6.14a-b). When RH changes from 42% to 48%, the picture for the rehydration is much less clear, and it is difficult to obtain good trend from simply looking at the comparisons (Figure 6.14 (c)). For the relaxation following the peak stress, similar behaviour was observed for the asymptotic stresses for the desorption part of the tests (Figure 6.11) however, for the rehydration the in-plane stress changes are much smaller in magnitude (Figure 6.14).

The peak stress values and times for non-aged and aged *urushi* films when going from RH_1 to RH_2 are shown in Table 6.4. To obtain a better view of the trends when we go from RH_1 to RH_2 we plot the peak stress values and the relative humidity differences for both the aged and the non-aged films in Figure 6.15.

Table 6.4: Maximum stress and time of peak occurrence obtained for non-aged and aged *urushi* films in response to different amounts of increase in relative humidity.

RH_1 (%)	RH_2 (%)	non-aged *urushi*		aged *urushi*	
		σ_{max} (MPa)	t (min)	σ_{max} (MPa)	t (min)
30	60	-10.1	75	-12.16	15
36	54	-6.041	130	-7.655	165
42	48	-2.341	120	-2.2	200

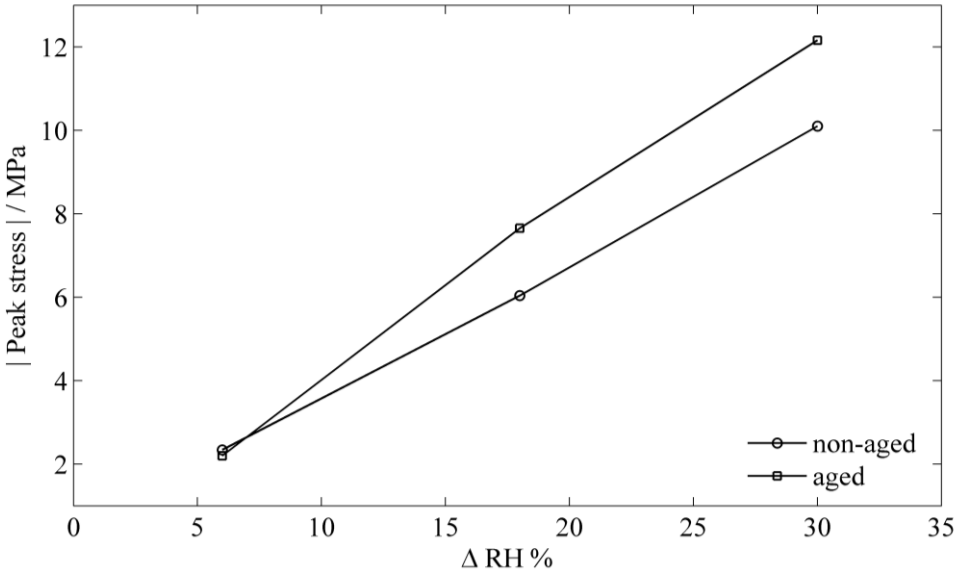

Figure 6.15: Effect of relative humidity changes ΔRH (from RH_1 to RH_2) on the peak film stress developed in non-aged and aged *urushi* films.

We observe different gradients to those observed in Figure 6.13, but at this stage, we are unable to determine the physical cause of this phenomenon since the in-plane stress states are different (compressive and tensile) and there is no overlap in the change of relative humidities in the figures. This suggests that in order to be able to fully describe the temporal and spatial evolution of the strain and stress fields, a complete assessment of *urushi* thin layer mechanical properties is required, but in subsequent sections we will show that a simplified model can reproduce some of the key features that we observed.

6.6 1D Model of stress development in *urushi* layers

Having observed the response of the material to changes in relative humidity (Section 6.4), we now propose a 1D model that will be used to characterise and predict *urushi* behaviour. We will show how this model can describe the observed behaviour of the *urushi* thin layers and then go on to demonstrate the model's potential for applications in this area.

6.6.1 Hygral stresses induced by absorption of moisture

The experimental observations of the stress response over time (Section 6.4) indicate that the system responds to both changes in moisture content and relaxation of the stresses in the material, with the moisture changes dominating initially, followed by a period in which the relaxation is stronger. Under these conditions, we can consider an isotropic plate in plane stress subject to the biaxial mechanical stresses σ_1 and σ_2, moisture change ΔM, in percentage, and temperature change ΔT. In this case the strain components ε_1 and ε_2 are given by

$$\begin{aligned} \varepsilon_1 &= \frac{\sigma_1}{E} - \frac{\nu\sigma_2}{E} + \beta\Delta M + \alpha\,\Delta T \\ \varepsilon_2 &= -\frac{\nu\sigma_1}{E} + \frac{\sigma_2}{E} + \beta\Delta M + \alpha\,\Delta T \end{aligned} \tag{6.3}$$

where α is the thermal expansion coefficient, β is the hygroscopic expansion coefficient, ν is Poisson's ratio and E is Young's modulus. For the case where σ_1, σ_2 and ΔT are all zero, we are left therefore with the hygral strains

$\varepsilon_1^H = \varepsilon_2^H = \beta\Delta M$ assuming the film is isotropic. The film is however unable to expand due to the underlying substrate, giving rise to hygral stresses $\sigma_1^H = \sigma_2^H$ where

$$\begin{aligned}\sigma_1^H &= \frac{E}{1-\nu}\varepsilon_1^H \\ &= \frac{E\beta}{1-\nu}\Delta M\end{aligned} \tag{6.4}$$

To describe the stress relaxation over time we employ a three-element viscoelastic material model given by the equation [87]

$$\sigma(t) = E_\infty \varepsilon_\circ \left[1 - \exp(-t/\lambda)\right] + E_\circ \varepsilon_\circ \exp(-t/\lambda)\,, \tag{6.5}$$

where λ is the time constant for the model, $\varepsilon_\circ$ is the magnitude of the imposed strain step, and E_∞ and $E_\circ$ are respectively the relaxed and instantaneous moduli [87]. The effective relaxation function, $R(t)$, is therefore

$$R(t) = E_\infty \left[1 - \exp(-t/\lambda)\right] + E_\circ \exp(-t/\lambda)\,. \tag{6.6}$$

The stress for a general strain history, $\sigma(t)$, is

$$\sigma(t) = \int_{-\infty}^{t} R(t-\tau)\dot{\varepsilon}(\tau)d\tau$$

which for the model considered here, with $\sigma(t) = 0$ for $t < 0$, can be written

$$\sigma(t) = \int_0^t \left\{ k_1 \left[1 - \exp\left(-\frac{(t-\tau)}{\lambda}\right)\right] + k_2 \exp\left(-\frac{(t-\tau)}{\lambda}\right)\right\} \frac{dM(\tau)}{d\tau} d\tau \tag{6.7}$$

where

$$k_1 = \frac{E_\infty \beta}{1-\nu} \tag{6.8}$$

and

$$k_2 = \frac{E_\circ \beta}{1-\nu}. \tag{6.9}$$

Thus, the material response to a change in moisture content is characterised by the three parameters k_1, k_2 and λ, which are themselves combinations of the material properties.

The values of k_1, k_2, and λ, for each combination of RH and ageing can be determined from the experimental data shown in Figure 6.11(a-c) by fitting Eq. (6.7) to the data. To do this, the moisture contents at equilibrium at 30%, 36% and 42% RH for non-aged and aged *urushi* were extracted from the asymptotic moisture content at equilibrium results shown in Figure 5.7. Having obtained the moisture contents at equilibrium (at 30%, 36% and 42% RH) and a single value of D and $M_\circ$ when RH changes from 75%→30% (Table 5.1 and Table 5.2), these were then inserted into the diffusion model (Eq.(5.19)) over the timescales used in Figure 6.11(a-c) to get a prediction of the moisture content as a function of time at 30%, 36% and 42% RH (Figure 6.16). As shown in Figure 6.16, the response is more rapid than in Figure 5.1 and Figure 5.2 because of the thinner film thickness (20 μm). The term $\frac{dM}{d\tau}$ (in Eq. (6.7)) is proportional to the strain gradient and was determined by calculating the gradient of the moisture contents versus time (Figure 6.16).

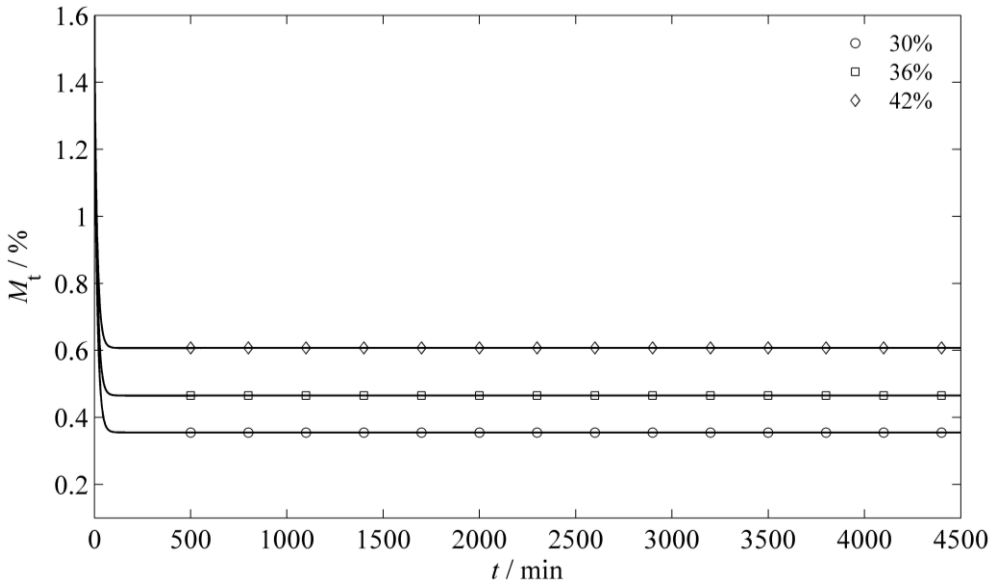

(a)

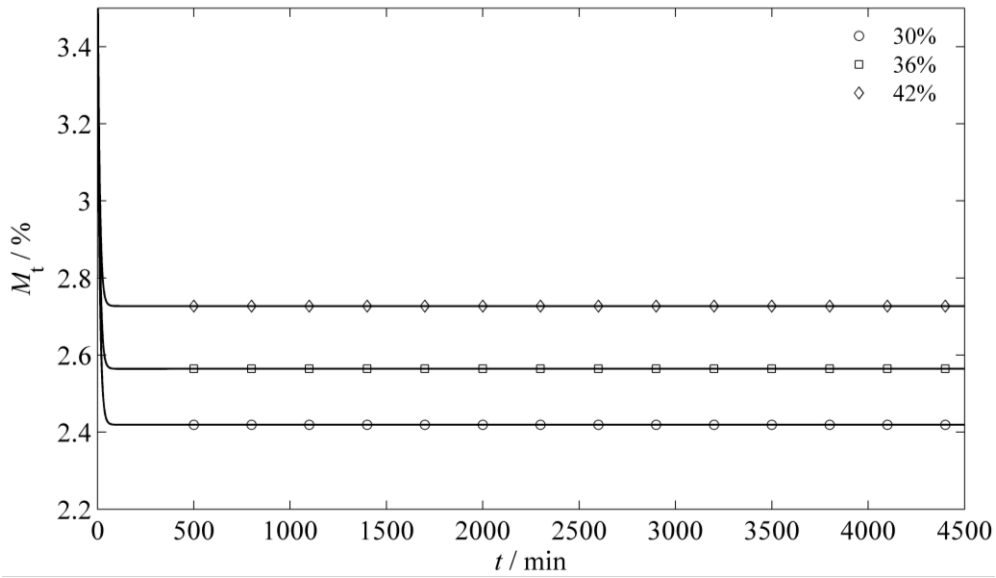

(b)

Figure 6.16: Predicted moisture contents for (a) non-aged *urushi* films and (b) aged *urushi* films when RH changes from 75% to 30%, 36% and 42%. Markers provide for clarity.

As shown in Figure 6.11(a-c), the fitting of Eq. (6.7) is reasonably good over the time ranges interrogated for all three curves and the rheological parameters k_1, k_2 and λ obtained for non-aged and aged *urushi* are shown in Table 6.5 and Table 6.6. The parameters show no obvious dependency on RH but there does, however, appear to be a systematic upward shift in relaxation time λ as the humidity level rises for the non-aged material. For the aged material, the picture is similar, although the data is somewhat confused for the shift from 75% to 42%.

Table 6.5: Summary of best-fit viscoelastic model parameters for non-aged *urushi*.

Humidity change	k_1 (MPa)	k_2 (MPa)	λ (min)
75%→30%	5.79	8.34	1.9E+3
75%→36%	5.36	7.94	2.0E+3
75%→42%	4.72	6.46	3.1E+3

Table 6.6: Summary of best-fit viscoelastic model parameters for aged *urushi*.

Humidity change	k_1 (MPa)	k_2 (MPa)	λ (min)
75%→30%	3.35	5.18	5.4E+3
75%→36%	3.85	4.73	1.4E+3
75%→42%	0	4.40	4.1E+4

6.6.2 A 1D model for multiple layers of *urushi* on a substrate

The agreement between the 1D model and the experimental observation (Figure 6.11 (solid lines)) suggests that the important behaviour is being captured by the model. In practice, *urushi* is most often found in multiple layers. A natural extension to the model, therefore, is to incorporate further layers of *urushi*. To demonstrate the possibility, we consider a domain consisting of two layers of *urushi*, constrained in the lateral direction by the presence of an infinitely stiff and impermeable substrate as the lower most boundary and a completely permeable interfacial layer. The moisture content at the upper most boundary is fixed by the relative humidity in the environment (Figure 6.17).

Figure 6.17: Schematic of the substrate and two *urushi* layers. The bottom layer is aged *urushi* layer, while the upper layer is non-aged *urushi* layer.

The problem is solved sequentially. First we solve the diffusion equation (Eq. (5.19)) using a finite-difference approximation to find the moisture content distribution within each layer. A time step of 0.01 min was employed throughout the analysis, and the number of spatial nodes varied until we obtained a mesh independent solution. The depth averaged moisture content in each layer was then calculated from the time-dependent moisture profile, and the gradient determined. The initial gradient was obtained by examining the short time behaviour at successively shorter time steps until

the initial gradient was independent of the time step. This gradient was then taken as the gradient of the depth averaged moisture content at $t = 0$. The boundary conditions were a fixed moisture content at the upper surface specified by the relationship in Figure 6.17, a zero flux condition at the base representing an impenetrable barrier at the base and we assume that the flux at the layer-layer interface is controlled by a diffusion coefficient that is an average of the two layers' diffusion coefficients. The model was validated by comparing against the numerical solution expected for a single layer of the same depth, and the analytical solution of a single layer, with agreement observed. The gradient of the depth averaged moisture content for each layer was then inserted into Eq. (6.7) and the stress calculated using the material properties k_1, k_2 and λ determined previously in Section 6.6.1.

This model was used to investigate the development of stress as a function of upper layer depth when placed upon a much thicker support layer. The bottom layer was set to be 500 μm, and represented an aged layer. We then envisage a scenario where there was a step change in RH (45% RH) resulting in a change of moisture content of -1.31% and then used our model to determine the stress evolution. Figure 6.18 shows the depth averaged stresses in the upper and bottom layers, respectively. We see that the stress developed in the upper layer is significantly larger than that in the lower layer, but that the form of the stress distribution is similar. This simple model suggests significant complexity in the stress development in lacquers where conservation may have occurred through the addition of new layers of material and the layers are of significantly different age and depth. In both cases we observe that reducing the depth of the upper will result in an increase in both the maximum and asymptotic stresses, which can be attributable to the quick uptake of moisture and the rapid passing of moisture through the upper layer to the lower, when using thin upper layers. This model has the benefit of simplicity and may in the future be modified to include time varying RH, multiple layers and the effect of changes in the substrate, and will be effective in guiding the type of layers that should be employed to reduce the magnitude of stresses that a conserved *urushi* lacquer might suffer in environments of rapidly changing moisture content.

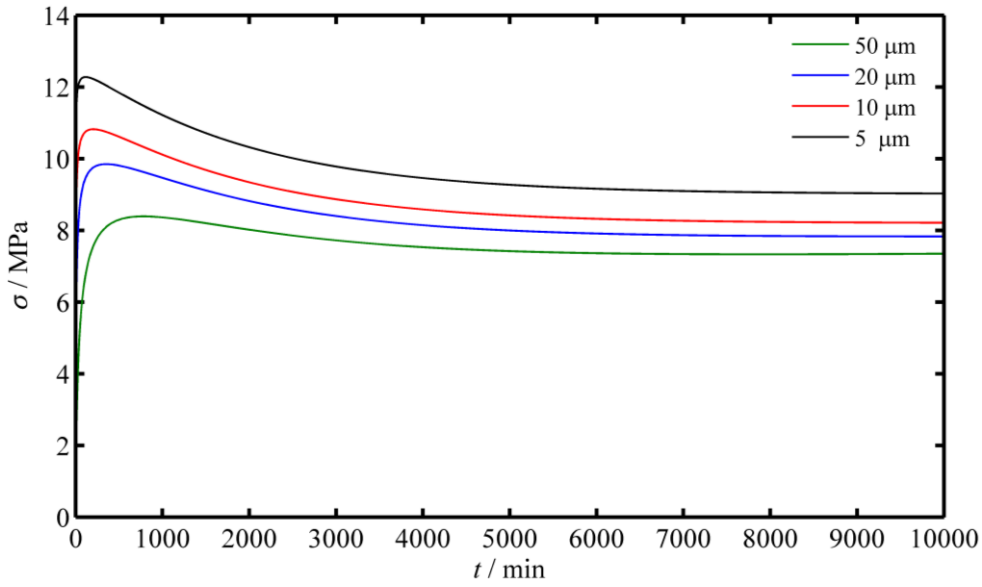

(a)

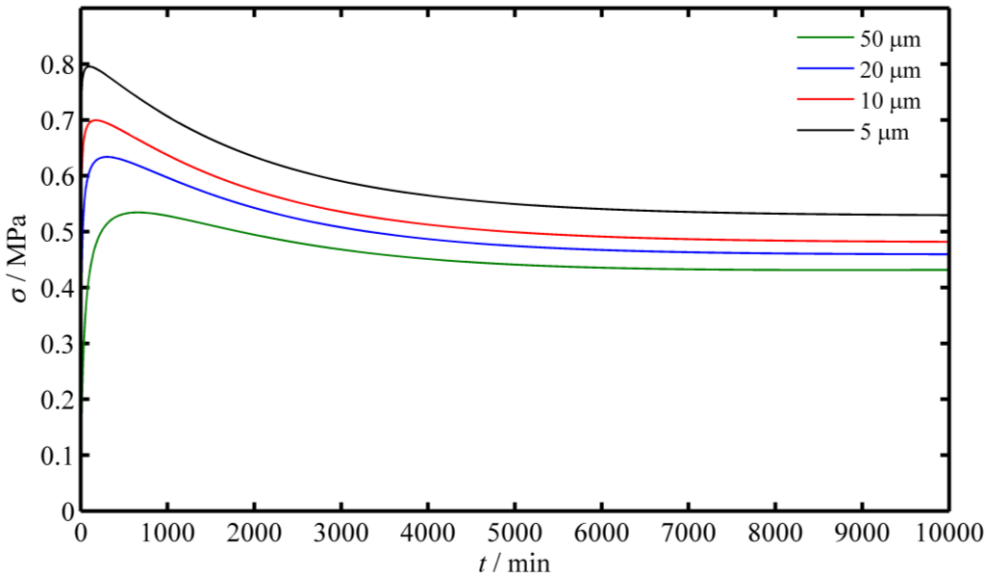

(b)

Figure 6.18: Predicted depth average stresses in *urushi* layers subjected to a change in moisture content of -1.31% at the upper surface for (a) the upper layer and (b) the bottom layer.

6.7 Conclusions

The stress response of cured non-aged and aged *urushi* films to different humidity levels has been measured using a phase shifting interferometer. This method has been shown to be able to resolve displacements in a bilayer to within 1.2% of the best

second order deflection approximation. We compared the behaviour of aged and non-aged *urushi* films when subjected to changes in the environmental relative humidity. We observed similar modes of behaviour, with a strong indication of time dependent behaviour and a coupling of the diffusion and relaxation of the material, but we also observed that the in-plane stresses during desorption were higher for the non-aged *urushi* films and during adsorption were higher for the aged *urushi* films. The results indicate that the material properties are likely to be strongly affected by the moisture ingress during variation of the RH, and this depends on the amount of ageing the material has been subjected to. A 1D model has been developed and tested against the experimental observation, showing reasonable agreement. The hygroscopic expansion can be incorporated into the parameters of this model, so that only three parameters are needed. Despite the relatively small number of parameters, the model was found to capture the behaviour of non-aged and aged *urushi* films over several days following a step change in humidity level. As *urushi* is applied on the object in the form of multiple layers, an extension to the model has been developed to investigate the stress response in *urushi* layers. The extension of this model was used to predict the development of stress as a function of depth for non-aged *urushi* layer covered an aged layer. The model suggests that a reduction in the layer depth leads to an increase in the stress levels for both the upper and lower layer. The model also suggests an increase in the stress levels in the upper non-aged layer more than that in the lower aged layer.

Chapter 7
Mechanical Properties of Aged and Non-aged *Urushi* Layers

7.1 Introduction

In order to fully characterise the mechanics of *urushi* layers it is necessary to determine the rheological behaviour of the material. In this Chapter, we will look to tensile, tensile creep and recovery tests of freestanding *urushi* films for this characterisation. We will present the results of experimental studies that investigated the effect of moisture content and ageing on the mechanical properties of *urushi* films. The elastic modulus (E), tensile strength at break (σ_B) and elongation at break (ε_B) were determined from the tensile stress–strain curves for non-aged and aged *urushi* samples under three different RH levels. The effects of strain rates [88-91] on the mechanical characteristics of non-aged and aged *urushi* films were also studied. Creep and recovery tests have been performed to study the influence of RH and UV ageing

on the long-term viscoelastic behaviour of non-aged and aged *urushi* films. Based on the creep and recovery measurements, we will describe the viscoelastic properties using a Burger's style model, show how the rheological characterisation depends upon the RH, UV ageing and the applied stress.

7.2 Methodology

7.2.1 Material and sample preparation

Urushi (*kijiro* type) samples were prepared for tensile and creep-recovery tests by using the preparation techniques described in Chapter 3 (Section 3.2.1 and Section 3.2.2). *Urushi* was then cast using a spin coater (Section 3.2.4) onto 70 mm × 50 mm rectangular glass substrates. The films were left to cure at room temperature at 75±2% RH for three weeks. After curing, the films were cut into rectangular strips of 60 mm × 5 mm. One subset of *urushi* samples was exposed to UV radiation for 400 hrs as per the method described in Section 3.3. The test pieces were then peeled from the glass substrate. The thickness of each *urushi* strip was measured with a Mitutoyo digital micrometer of 0.001 mm resolution.

7.2.2 Tensile test

Tensile tests [92-98] were performed on non-aged and aged *urushi* films up to failure with an Instron universal testing machine 5569 (100 N load cell), Figure 7.1. A relative humidity (RH) controllable chamber has been attached to the tester. The tensile tests were carried out under 30%, 50% and 75% RH. Prior to each test, the films were kept for 1 week under constant RH (30%, 50% and 75%) to be sure that the film reached equilibrium.

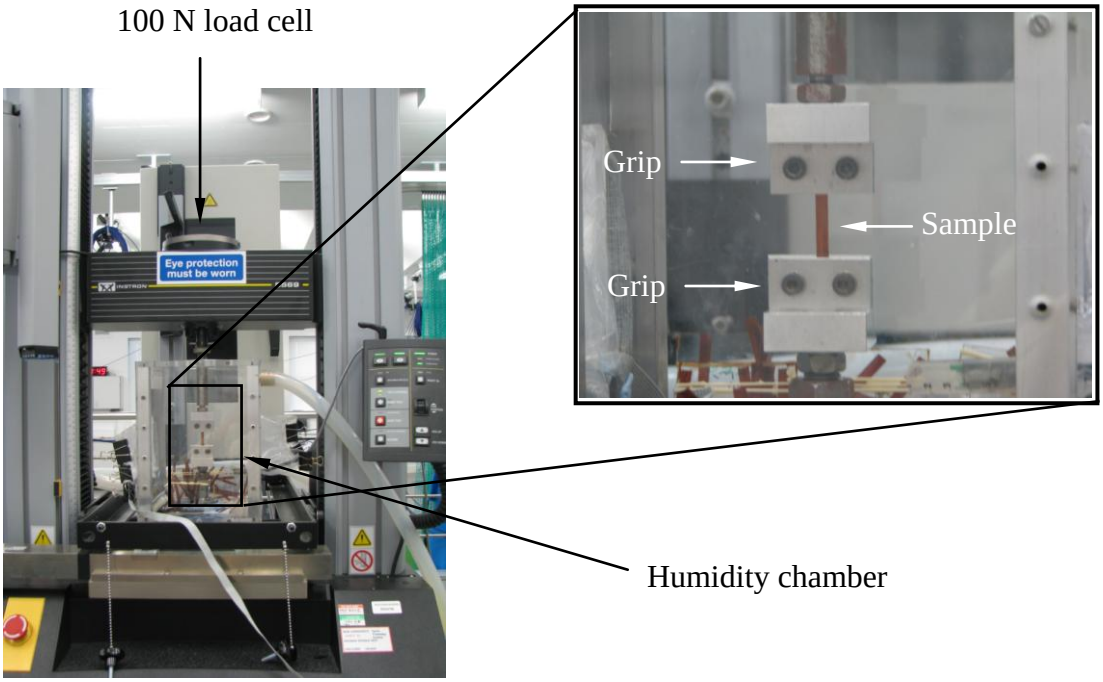

Figure 7.1: Instron tensile-test machine model 5569.

The tensile test consists of a non-aged and aged free *urushi* strip that is placed between 2 grips and then stretched at a constant rate until the film fractures. Under a given RH, samples were tested at tensile speeds of 0.002 mm/min, 0.02 mm/min and 0.2 mm/min which correspond to strain rates of 1.3×10^{-6} s^{-1}, 1.3×10^{-5} s^{-1} and 1.3×10^{-4} s^{-1}. These tensile speeds were chosen to be relatively low to reflect the long timescales of straining likely to be experienced by *urushi* films. The force and displacement values are recorded during the test and these data are converted to stress (σ) and stain (ε).

7.2.3 Creep and recovery

Creep recovery [87, 99-103] is one of the simplest tests for characterizing viscoelastic behaviour. The creep recovery behaviour is a rheological test method where a constant stress is applied to a material and its resulting deformation is recorded. The main objectives in these creep recovery tests were to measure how non-aged and aged *urushi* films will perform under different constant stresses [104-106] and different constant RHs [107, 108] and the effect of UV ageing on the rheological behaviour [109, 110]. During creep tests four different constant values of stress were used and the samples were maintained within an atmosphere of constant RH. The resulting strain is measured and plotted as a function of elapsed time. The tests were performed for non-

aged and aged *urushi* films under 30%, 50% and 75% RH with a uniaxial tensile Instron testing machine 5569 (100 N load cell) (Figure 7.1). Prior to each test, the samples were first kept for 1 week under constant RH (30%, 50% and 75%) to be sure that the film reached equilibrium. The applied stresses have been chosen based on the tensile strength at break values, for non-aged and aged films, established during the tensile tests that have been performed at a tensile speed of 0.002 mm/min. The applied stresses were 30%, 50%, 60% and 70% of their tensile strength at break (Table 7.1 and Table 7.2). The applied stress values are tabulated in Table 7.3. Under each stress value, the stress held for 12 hrs during creep and the strain was monitored. For the recovery test, the stress was removed and the strain was monitored for 12 hrs.

7.3 Results and discussion

7.3.1 Tensile tests

In order to investigate the effect of RH and UV ageing on the mechanical behaviour and properties of *urushi* films, the experimental results are represented in three ways. Firstly, the stress-strain curves as a function of RH for non-aged and aged *urushi* films are shown in Figure 7.2 and Figure 7.3 respectively. Secondly, the evaluated mechanical properties for both non-aged and age *urushi* films are plotted as a function of RH (Figure 7.5 and Figure 7.6) to find out the effect of RH on the mechanical properties of non-aged and aged *urushi* films. Finally, the stress-strain curves for both non-aged and aged *urushi* films as a function of the tensile speeds are represented in Figure 7.4 to evaluate the effect of the UV ageing and effect of the tensile speed on the tensile behaviour and properties.

7.3.1.1 Effect of Humidity

The stress versus strain curves for non-aged and aged *urushi* films under three different RHs and different tensile speeds (Figure 7.2 and Figure 7.3) were used to extract the tensile properties. The results of the tensile properties, tensile elastic modulus, tensile strength at break and elongation at break, are tabulated in Table 7.1 and Table 7.2. The tensile elastic modulus was calculated as the slope of the linear part of the $\sigma - \varepsilon$ curves (at $\varepsilon < 0.1\%$). As to be expected for non-aged *urushi* films, it has been observed that increasing the RH, from 30% to 75% RH, leads to a decrease in the

elastic modulus. This behaviour has been observed with tensile speeds 0.002 mm/min, 0.02 mm/min and 0.2 mm/min, Figure 7.2(a-c). This trend means that the non-aged *urushi* films become more flexible with increasing moisture content [10]. In aged *urushi* films, Figure 7.3(a-c), it is noticeable that brittle fracture took place instead of yielding and no plastic deformation was observed in the stress-strain curves at any RH or tensile speeds. Also, the stress levels, in comparison with the non-aged *urushi* films, seem to be less sensitive to RH changes. On the other hand, the elongation at break increases with increasing RH with tensile speeds 0.002 mm/min and 0.2 mm/min. It is likely that this can be related to a crosslinking reaction by the enzyme laccase over the whole region of the aged films [9].

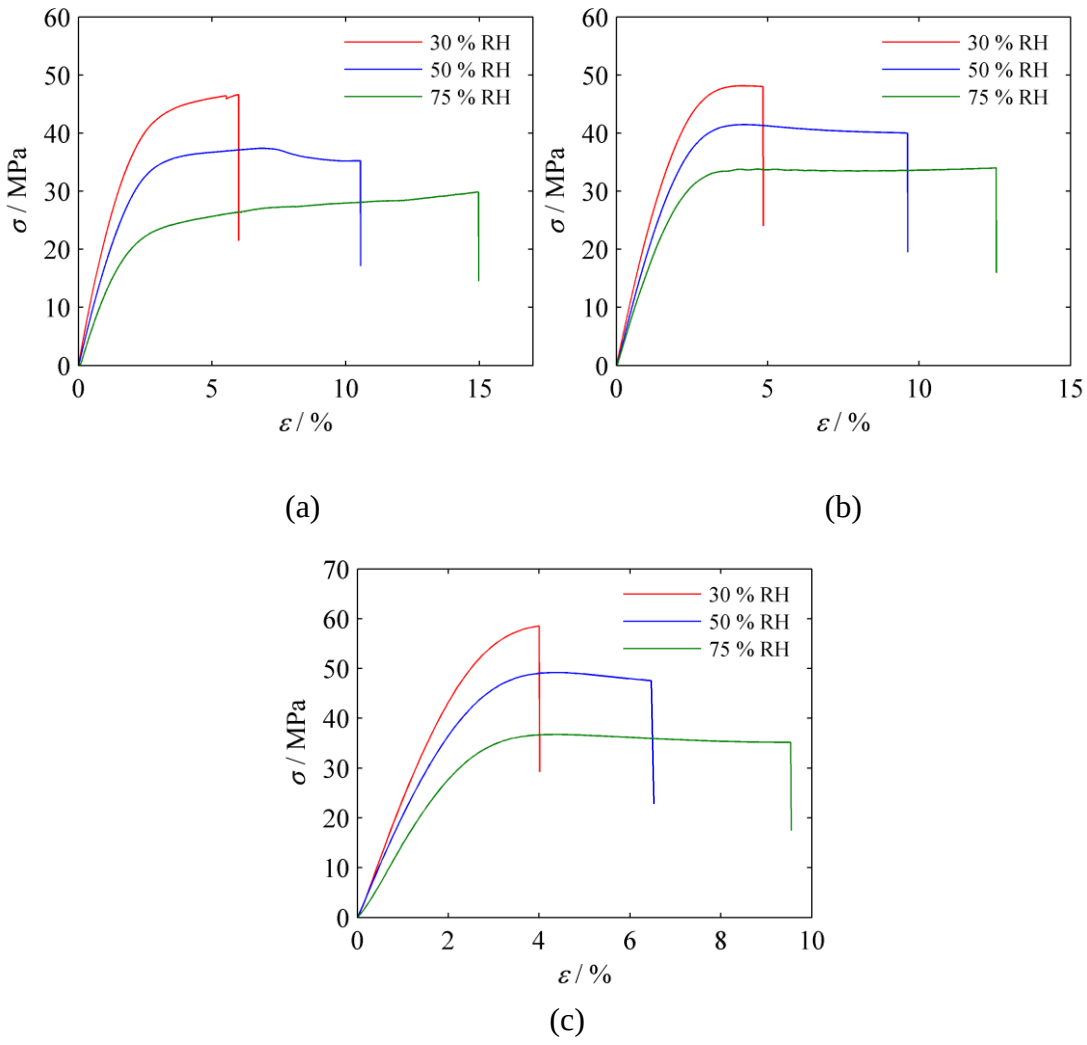

Figure 7.2: Stress versus strain for uniaxial extension for non-aged *urushi* films under different RH levels at (a) 0.002 mm/min, (b) 0.02 mm/min and (c) 0.2 mm/min.

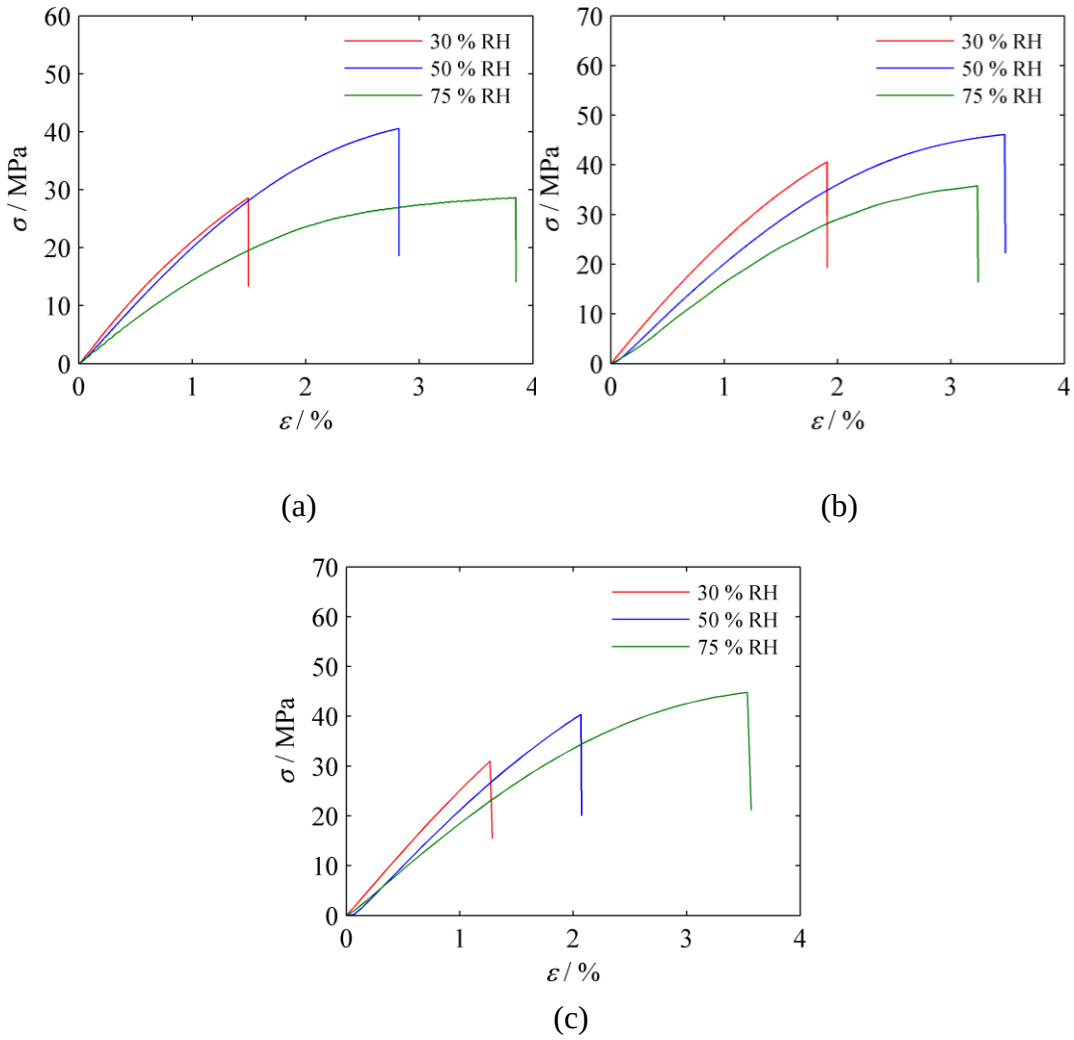

Figure 7.3: Stress versus strain for uniaxial extension for aged *urushi* films under different RH levels at (a) 0.002 mm/min, (b) 0.02 mm/min and (c) 0.2 mm/min.

7.3.1.2 Effect of UV ageing

To have a general view of the effect of the UV ageing and strain rate on the tensile behaviour of *urushi* film, the tensile behaviour for non-aged *urushi* together with the tensile behaviour of aged *urushi* films is plotted in Figure 7.4 under 30%, 50% and 75% RH respectively. As shown in Figure 7.4, the ageing treatment changes the stress-strain behaviour drastically in comparison with the non-aged *urushi* films. Importantly we see a substantial reduction in strain at failure, underlining that UV ageing is detrimental for *urushi*.

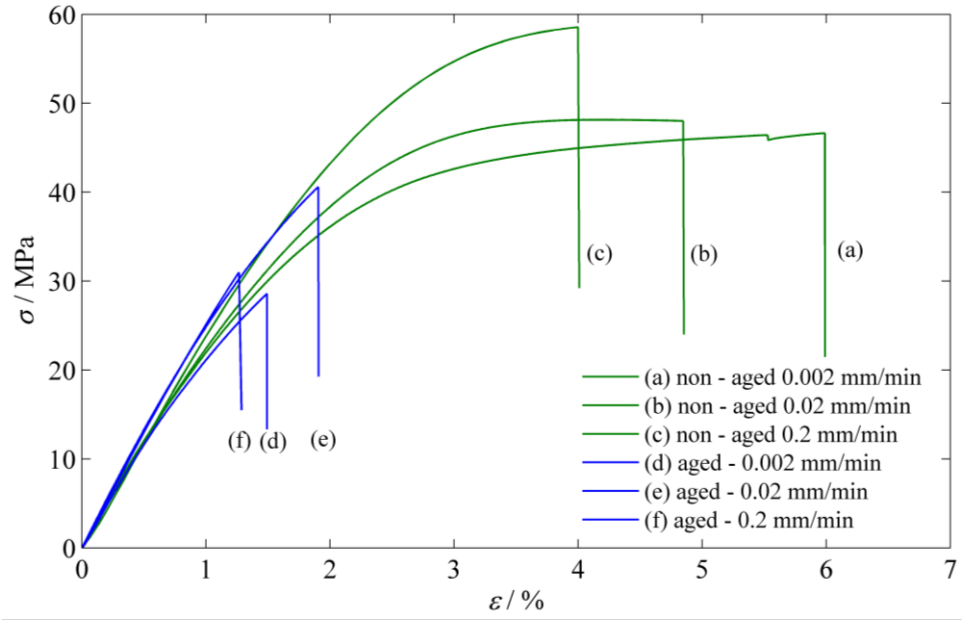
σ / MPa
ε / %
(a)
(b)
(c)
(d)
(e)
(f)
(a) non - aged 0.002 mm/min
(b) non - aged 0.02 mm/min
(c) non - aged 0.2 mm/min
(d) aged - 0.002 mm/min
(e) aged - 0.02 mm/min
(f) aged - 0.2 mm/min

(a)

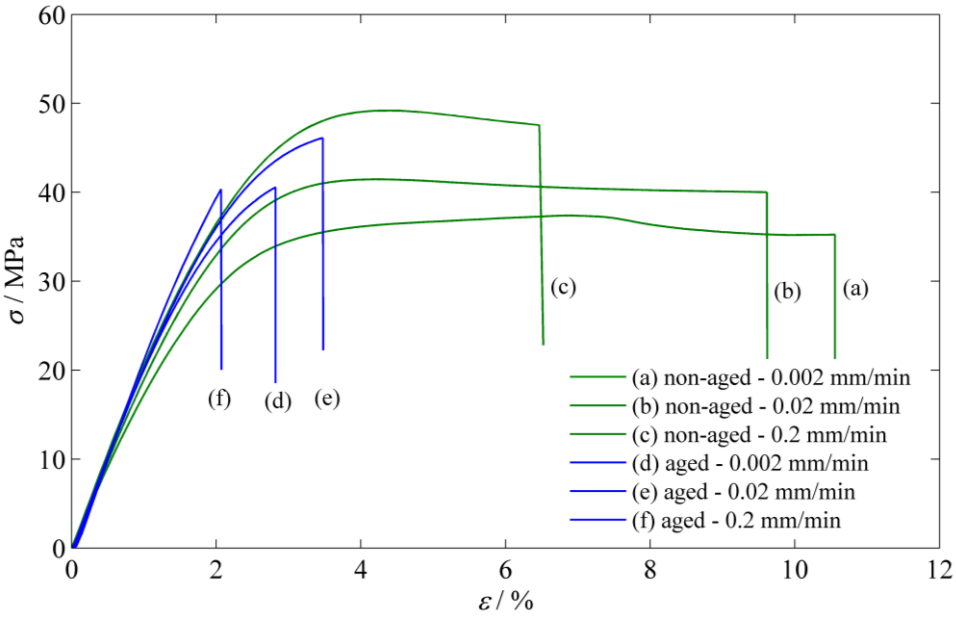
σ / MPa
ε / %
(a)
(b)
(c)
(d)
(e)
(f)
(a) non-aged - 0.002 mm/min
(b) non-aged - 0.02 mm/min
(c) non-aged - 0.2 mm/min
(d) aged - 0.002 mm/min
(e) aged - 0.02 mm/min
(f) aged - 0.2 mm/min

(b)

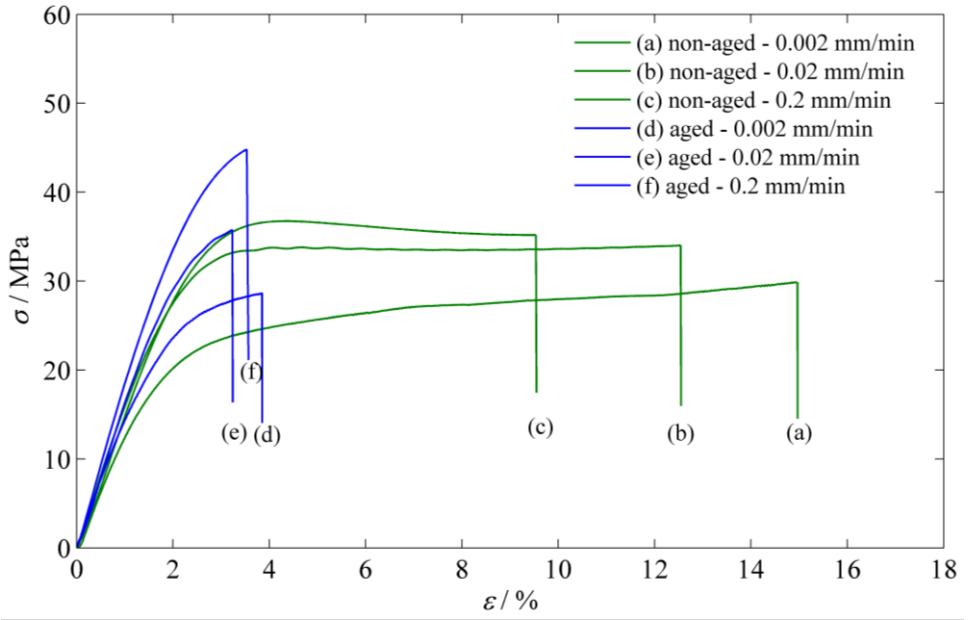

(c)

Figure 7.4: Stress versus strain for uniaxial extension of non-aged and aged *urushi* under (a) 30% RH, (b) 50% RH and (c) 75% RH at different tensile speeds.

Table 7.1: Tensile elastic modulus (E), tensile strength at break (σ_B) and elongation at break (ε_B) for non-aged *urushi* at different tensile speeds for RH = 30%, 50% and 75%.

tensile speed (mm/min)	30% RH			50% RH			75% RH		
	E (GPa)	σ_B (MPa)	ε_B (%)	E (GPa)	σ_B (MPa)	ε_B (%)	E (GPa)	σ_B (MPa)	ε_B (%)
0.002	2.2	46.63	5.989	1.7	35.23	10.56	1.3	30	15
0.02	2.3	48	4.847	1.9	40	9.613	1.6	34	12.5
0.2	2.3	58.56	4	2.1	47.55	6.467	1.5	35	9.5

Table 7.2: Tensile elastic modulus (E), tensile strength at break (σ_B) and elongation at break (ε_B) for aged *urushi* at different tensile speeds for RH = 30%, 50% and 75%.

tensile speed (mm/min)	30% RH			50% RH			75% RH		
	E (GPa)	σ_B (MPa)	ε_B (%)	E (GPa)	σ_B (MPa)	ε_B (%)	E (GPa)	σ_B (MPa)	ε_B (%)
0.002	2.2	28.59	1.494	2.1	40.55	2.821	1.5	28.7	3.8
0.02	2.6	40.6	1.906	2.1	46.11	3.473	1.7	35.8	3.2
0.2	2.6	31	1.267	2.2	40.35	2.067	1.9	44.8	3.5

7.3.1.3 Mechanical properties

The results of the tensile test experiments are summarized in Figure 7.5 and Figure 7.6. As shown in Figure 7.5(a-c), a significant reduction in tensile elastic modulus were observed with increasing the RH for non-aged and aged *urushi* films at all tensile speeds. For the highest RH, that is 75% RH, the average reduction in tensile elastic modulus was about 64.5% and 69% of the initial value (at 30% RH) for non-aged and aged *urushi* films, respectively. Also, the results show that the UV ageing resulted in an increase of the tensile elastic modulus and a decrease in the elongation at break for aged *urushi* film (Figure 7.6).

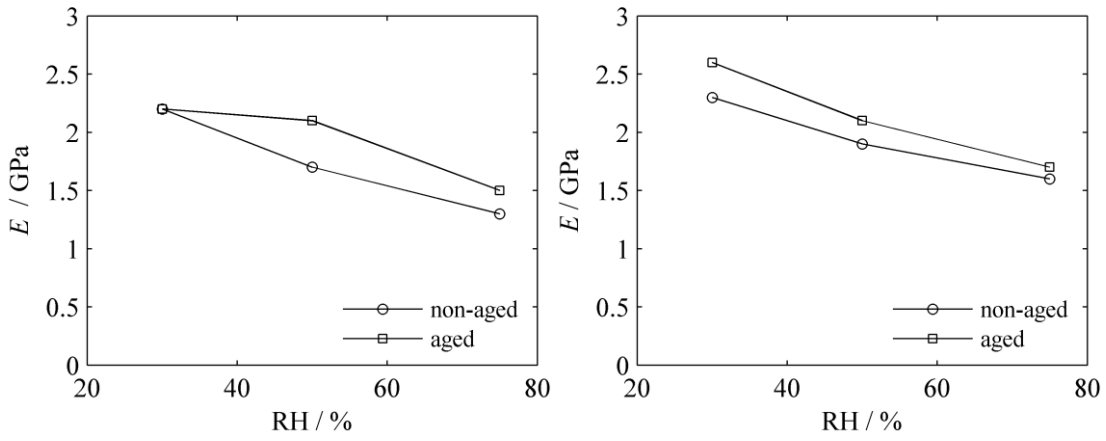

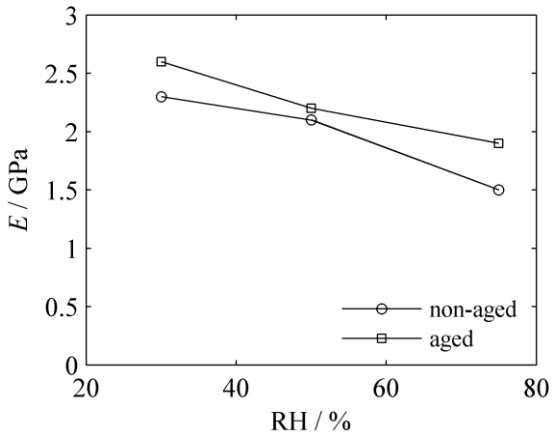

(c)

Figure 7.5: Dependence of elastic modulus on RH for non-aged and aged *urushi* at (a) 0.002 mm/min, (b) 0.02 mm/min and (c) 0.2 mm/min. Solid lines provide for clarity.

The tensile strength at break for non-aged *urushi* films shows a significant reduction with increasing the RH at all tensile speeds (Figure 7.6), while a relative increase in tensile strength at break, at 50% RH, has been observed for aged *urushi* films at all tensile speeds. At 75% RH, the average reduction in tensile strength at break for non-aged *urushi* films was about 65% relative to the initial values at 30% RH. For non-aged *urushi* films, when the RH was increased, the reduction in tensile elastic modulus and tensile strength at break was accompanied by a strong increase in the elongation at break at all tensile speeds (Figure 7.6). Aged *urushi* shows a relative increase in the elongation at break with increasing RH at all tensile speeds (Figure 7.6).

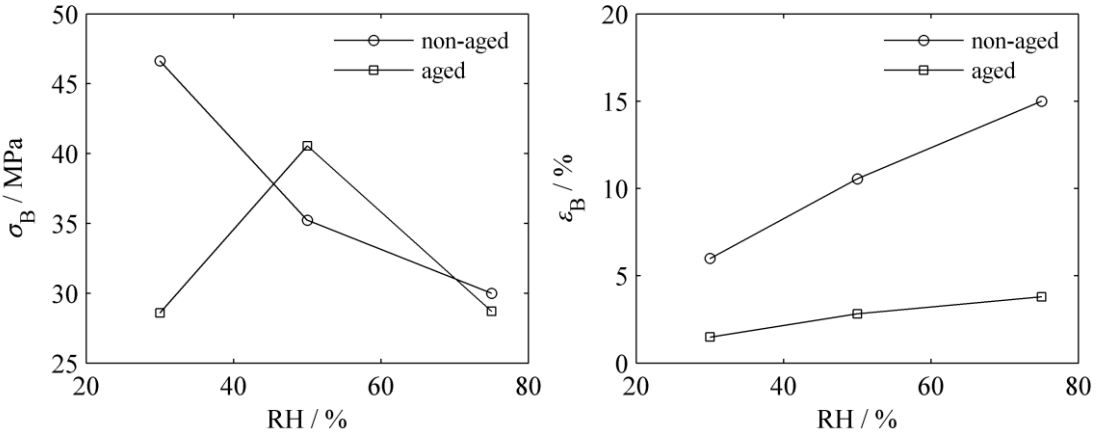

(a)

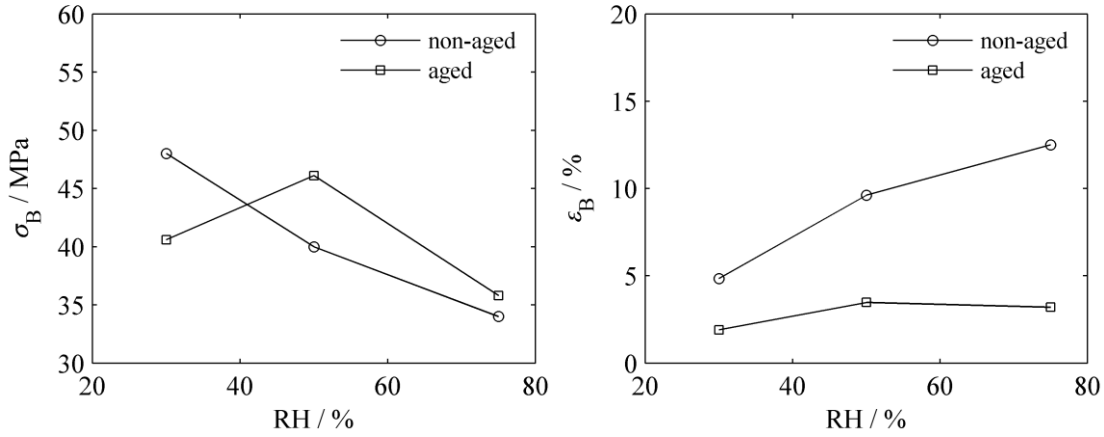

(b)

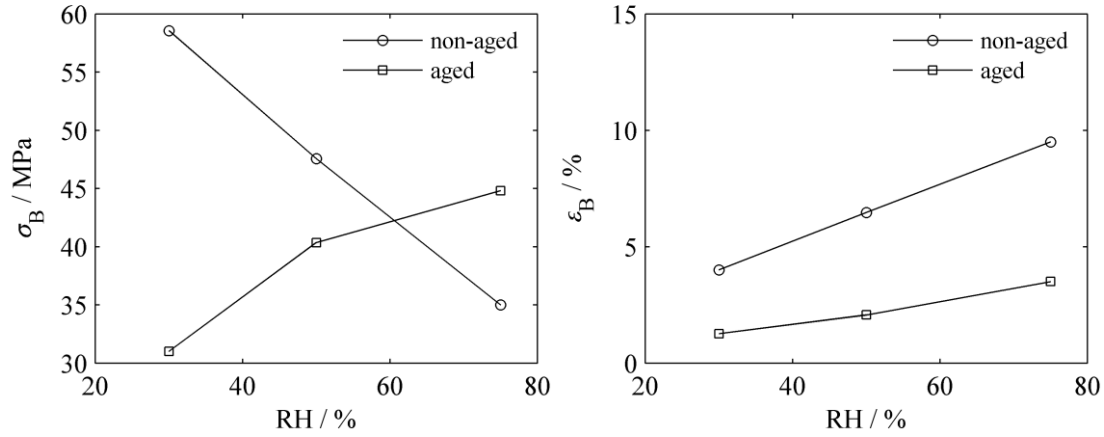

(c)

Figure 7.6: Dependence of tensile strength at break (left) and elongation at break (right) on RH for non-aged and aged *urushi* at (a) 0.002 mm/min, (b) 0.02 mm/min and (c) 0.2 mm/min cross-head speed. Solid lines provided for clarity.

The previous trends of the mechanical properties indicate that the compliance of non-aged *urushi* films increases with the amount of water absorbed. This behaviour can be attributed to the fact that water serves the film as a plasticizer. The evolution of mechanical properties for non-aged *urushi* films is in good agreement with results already reported in literature [9, 10].

7.3.1.4 Effect of Strain rate

It is important to characterize the effects of strain rate on the mechanical properties and tensile behaviour of *urushi* films. As shown in Figure 7.4(a-c), a strong strain rate dependency in non-aged and aged *urushi* has been observed under all RH levels. As the strain rate goes up (from 1.3×10^{-6} s^{-1} to 1.3×10^{-4} s^{-1}), the flow stress increases and the rupture strain decreases drastically. This has been observed for non-aged *urushi* films tensile tests that have been undertaken for the range 30%, 50% and 75% RH. The elastic modulus, the tensile strength at break and elongation at break are shown in Figure 7.7 and Figure 7.8 as a function of strain rate for non-aged and aged *urushi* films, respectively (Table 7.1 and Table 7.2).

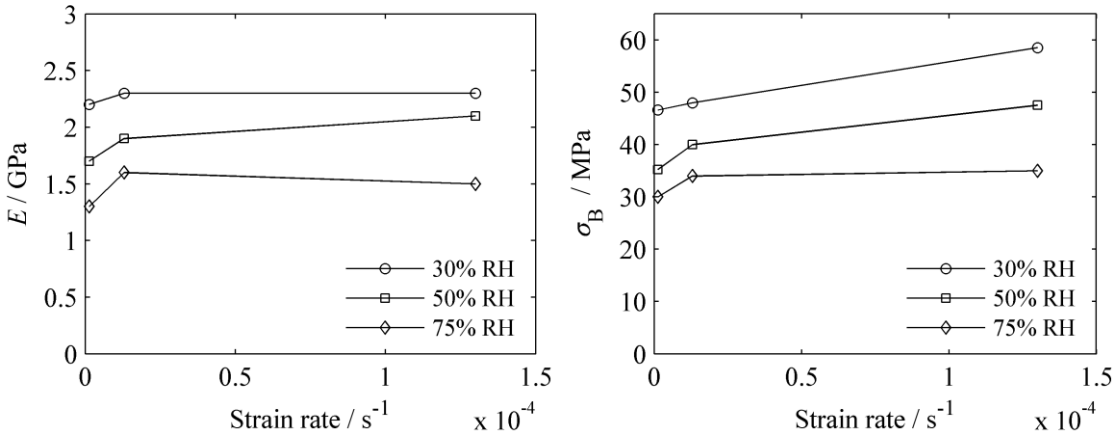

(a) (b)

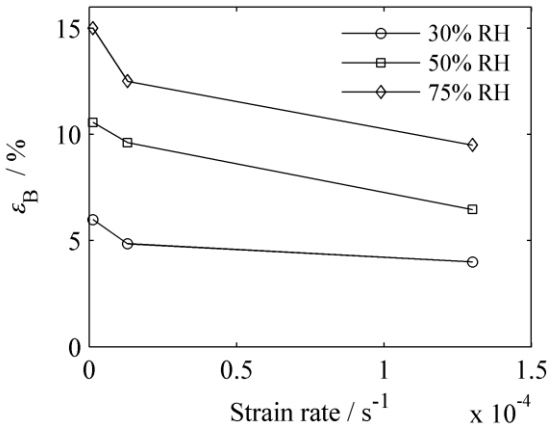

(c)

Figure 7.7: Mechanical properties as a function of strain rate for non-aged *urushi* films. (a) tensile elastic modulus, (b) tensile strength at break and (c) elongation at break. Solid lines provided for clarity.

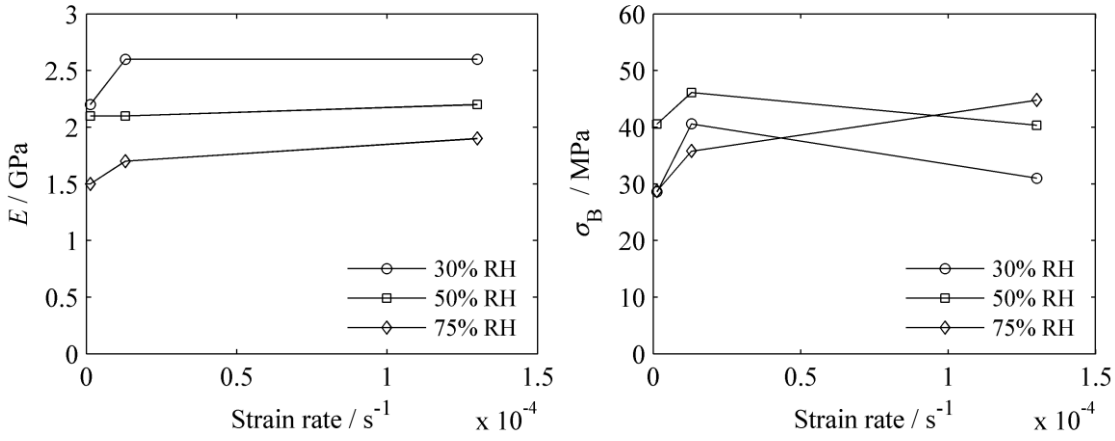

(a) (b)

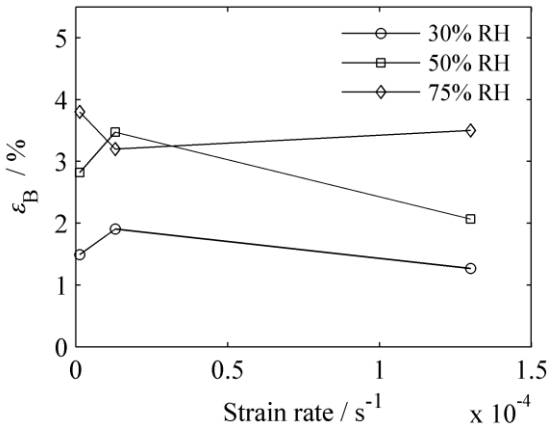

(c)

Figure 7.8: Mechanical properties as a function of strain rate for aged *urushi* films, (a) tensile elastic modulus, (b) tensile strength at break and (c) elongation at break. Solid lines provided for clarity.

For non-aged *urushi* films (Figure 7.7 (a)), the elastic modulus slightly increases at the strain rate ranging from 1.3×10^{-6} s^{-1} to 1.3×10^{-5} s^{-1}. Figure 7.7(b and c) shows the tensile strength at break and the elongation at break plotted against the strain rate. An increase in the tensile strength at break and a decrease in the elongation at break as the strain rate increases are observed for all RH. These results reveal that non-aged *urushi* is sensitive to the rate of the tensile testing. For aged *urushi* films, the strain rate does not show any influence on the elastic modulus under 50% RH, while under 30% and 75% RH The elastic modulus slightly increases with the strain rate (Figure 7.8(a)). As shown in Figure 7.8(b), under high RH (75%) a strong increase in the tensile strength with the strain rate is observed, while under 30% and 50% RH an increase and then a decrease in the tensile strength is observed with increasing the strain rate.

7.3.2 Creep recovery test

Figure 7.9 - Figure 7.14 show the creep and creep recovery curves for non-aged and aged *urushi* films under 30%, 50% and 75% RH at different stress values. The curves all show two stages of creep, primary followed by a stabilization period characteristic of secondary creep. The experiments were completed before the tertiary stage was observed here since it was unlikely to be experienced on the Mazarin Chest.

The creep curves form a consistent set at all stress levels for the non-aged and aged films at all RH levels, where increasing stress levels lead to an increase in the creep deformations. It was noticeable that the non-aged *urushi* films at 30% RH show less resistance to deformation than the aged films at the same RH (Figure 7.9 and Figure 7.10). The overall deformation levels of non-aged films at 30% RH were very close to the deformation levels at 50% RH, Figure 7.9 and Figure 7.11. While at 75% RH, Figure 7.13, the overall deformation levels of non-aged films were noticeably higher than those at 30% (Figure 7.9) and 50% RH (Figure 7.11) suggesting that the films tend to be more flexible at 75% RH. On the other hand, as shown in Figure 7.10, Figure 7.12 and Figure 7.14, increasing the RH in aged films leads to a significant effect in lowering their stiffness.

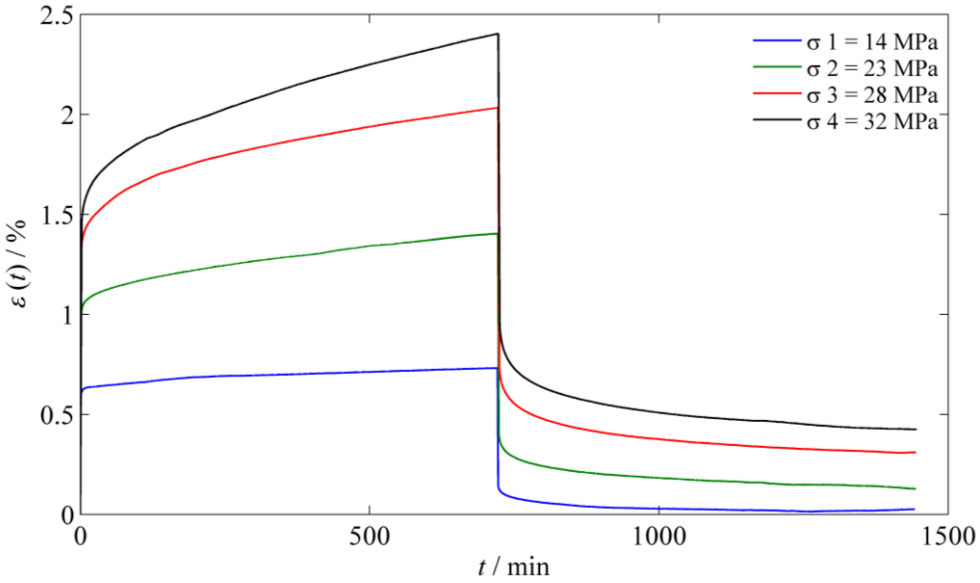

Figure 7.9: Creep recovery curves for non-aged *urushi* films under 30% RH at different stress values.

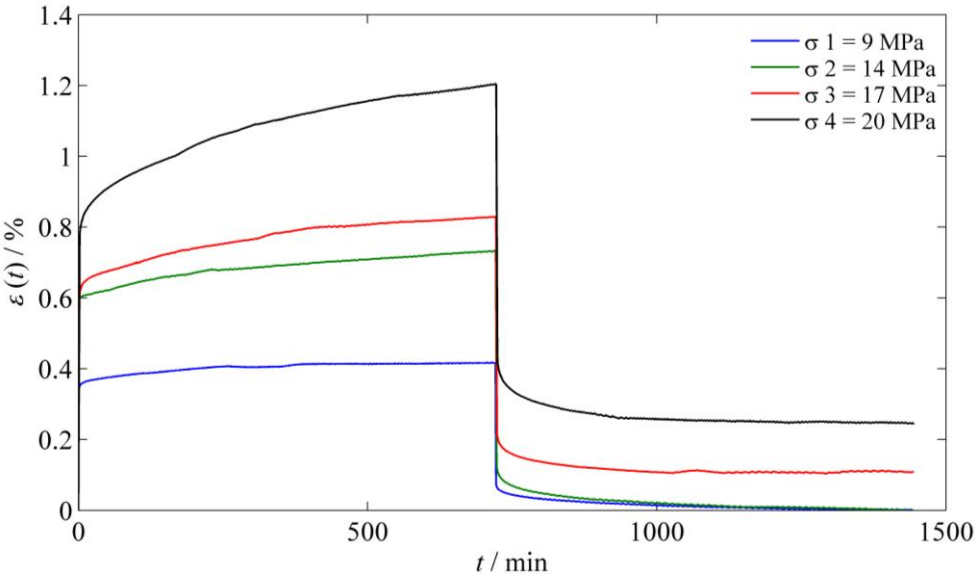

Figure 7.10: Creep recovery curves for aged *urushi* films under 30% RH at different stress values.

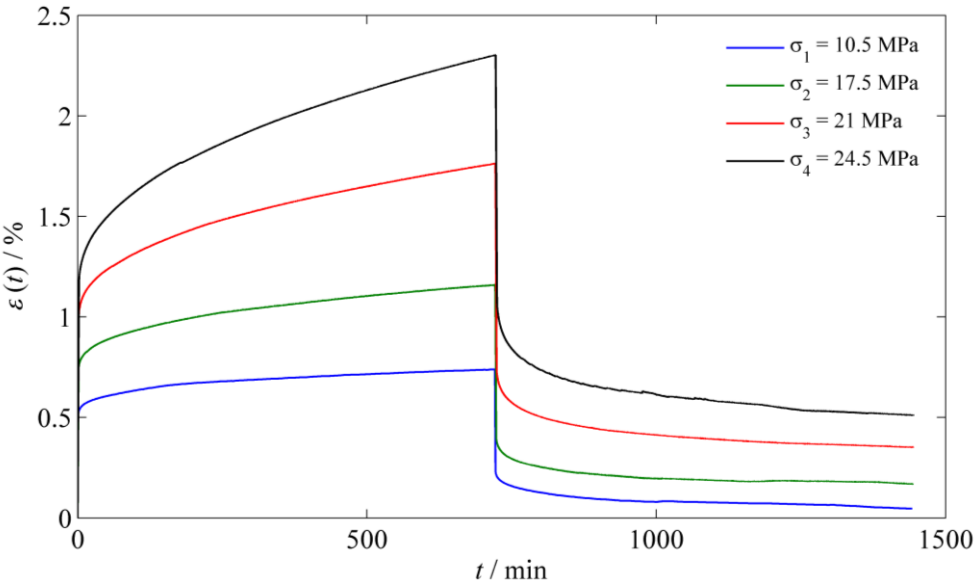

Figure 7.11: Creep recovery curves for non-aged *urushi* films under 50% RH at different stress values.

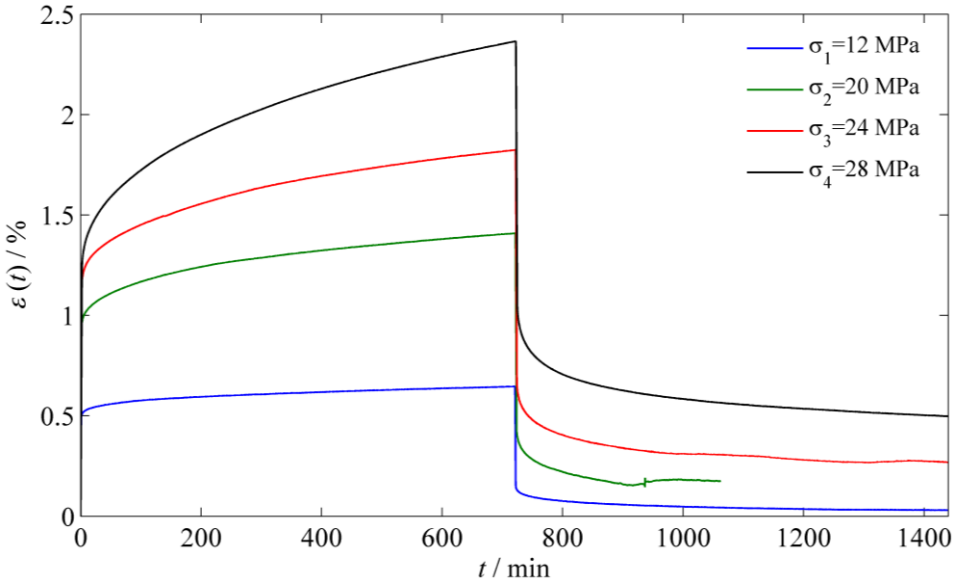

Figure 7.12: Creep recovery curves for aged *urushi* films under 50% RH at different stress values.

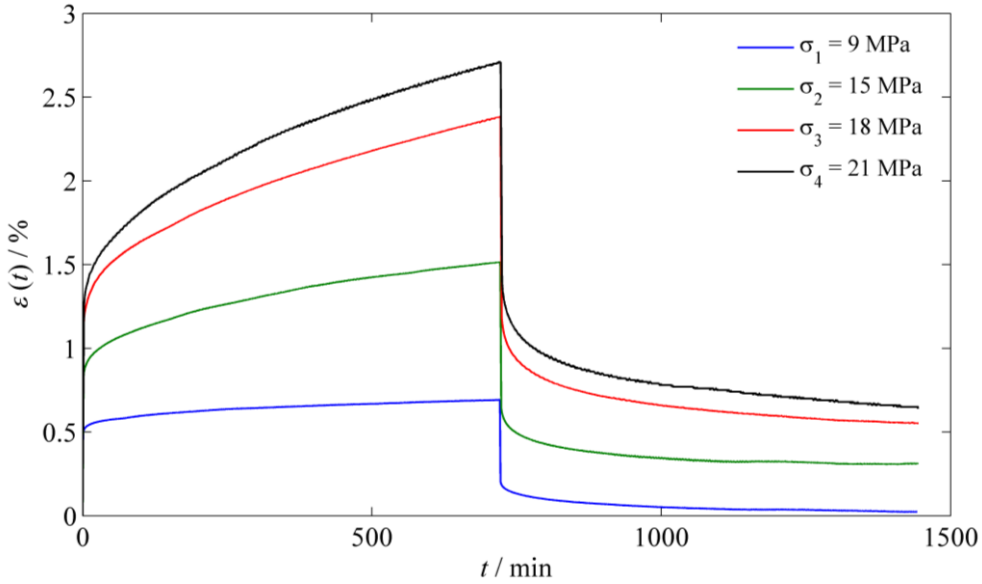

Figure 7.13: Creep recovery curves for non-aged *urushi* films under 75% RH at different stress values.

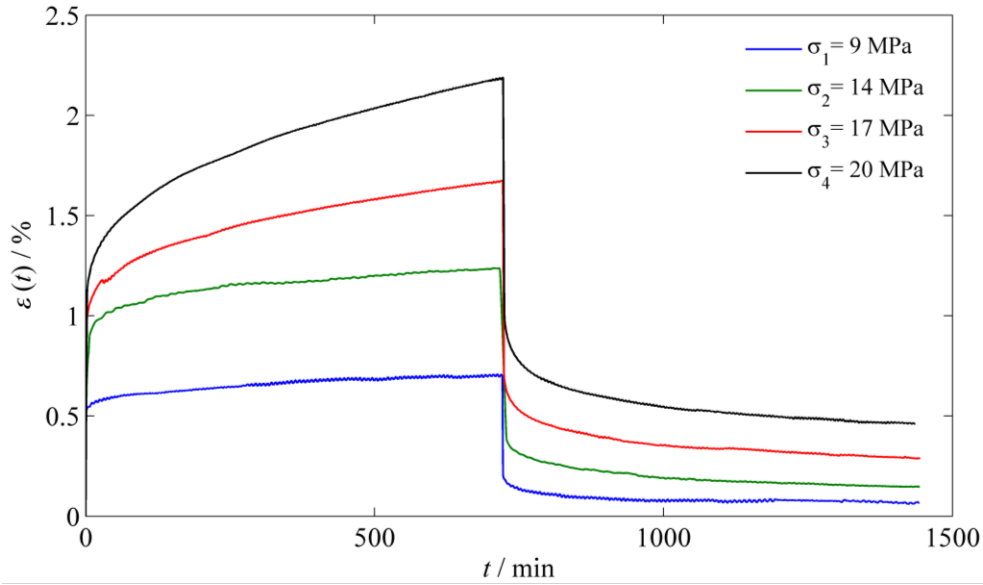

Figure 7.14: Creep recovery curves for aged *urushi* films under 75% RH at different stress values.

7.3.3 Isochronous stress-strain

In order to know whether the material is linear or non-linear viscoelastic, it is more convenient to construct a series of isochronous stress-strain curves [111, 112]. An isochronous stress-strain curve is a plot showing how the strain depends on the applied load at a specific point in time after application of the load. On the basis of experimental creep curves presented in Figure 7.9 to Figure 7.14, isochronous creep curves were obtained and presented in Figure 7.15 to Figure 7.17 for non-aged and aged *urushi* samples under 30%, 50% and 75% RH, respectively. Seven curves are plotted in each figure, corresponding to times 15 min, 30 min, 45 min, 60 min, 120 min, 180 min and 240 min. To obtain an isochronous stress-strain curve for previous times (say 15 min), we read off the strain at 15 min from each creep curve and plot these strain values against the corresponding stress values. This process was repeated for other times to obtain a series of isochronous curves.

As shown in Figure 7.15 to Figure 7.17, the total strains all increase with the increase of applied stresses over the whole range of testing times with different degrees. The higher the level of stress is, the greater the degree of strains increases.

Isochronous stress-strain curves (Figure 7.15 to Figure 7.17) show that the behaviour approximates linear viscoelasticity for non-aged and aged *urushi* films in the range of stresses which were used in the investigations. The average coefficients of determination (R^2) were found to be about 0.98, 0.98 and 0.97 for non-aged *urushi* films under 30%, 50% and 75% RH respectively. In aged *urushi* films, R^2 were found to be about 0.98, 0.99 and 0.99 under 30%, 50% and 75% RH respectively. However, non-liner viscoelasticity has been observed for non-aged *urushi* films at 75% RH (Figure 7.17(a)).

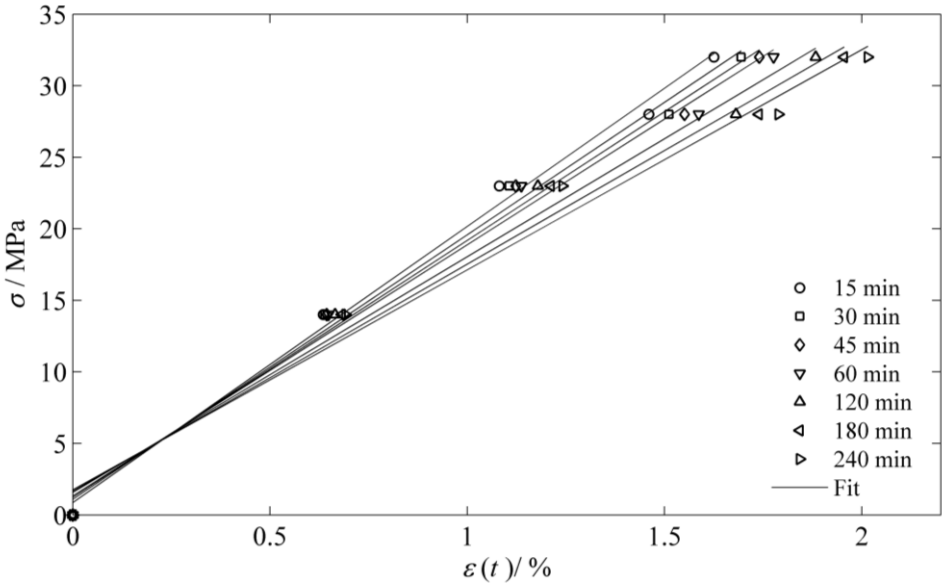

(a)

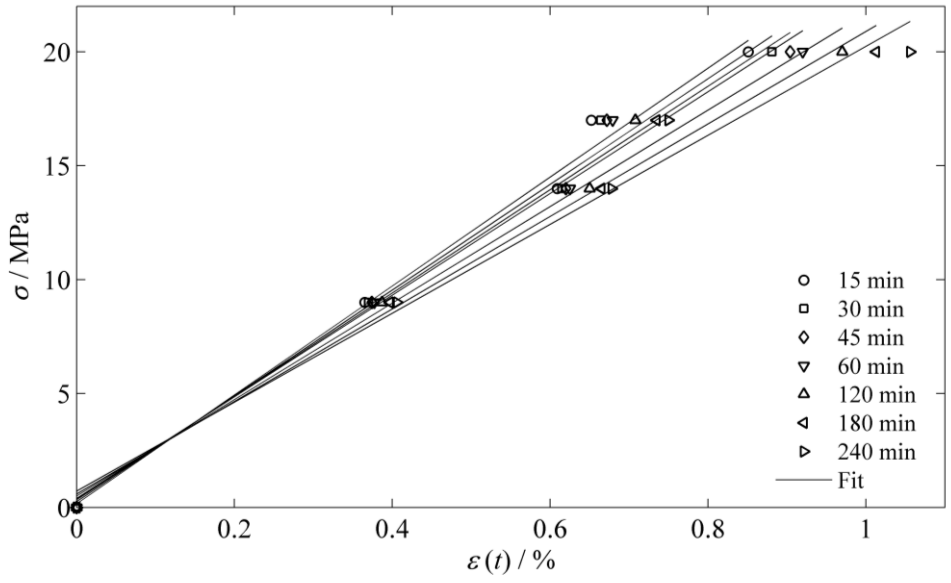

(b)

Figure 7.15: Isochronous creep curves of (a) non-aged and (b) aged *urushi* films under 30% RH.

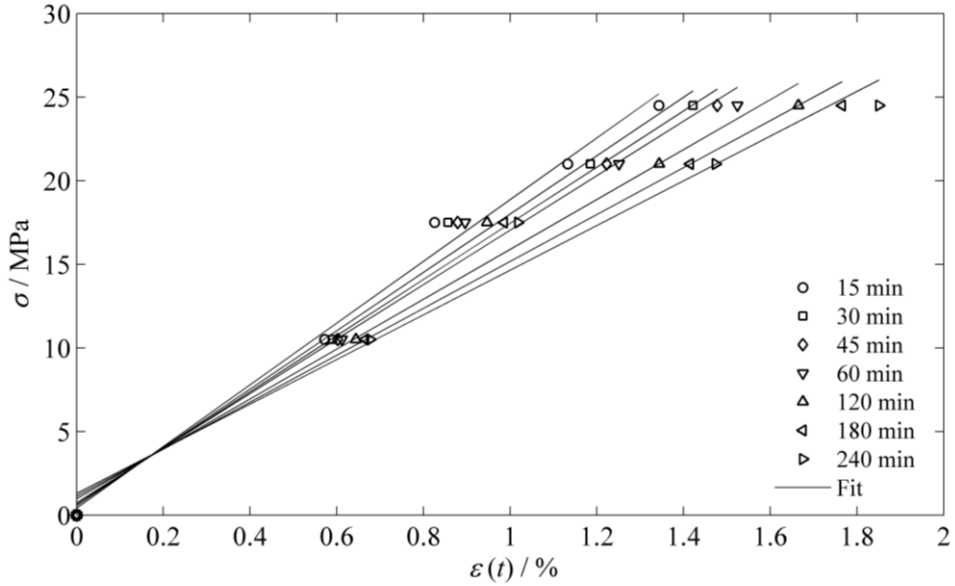

(a)

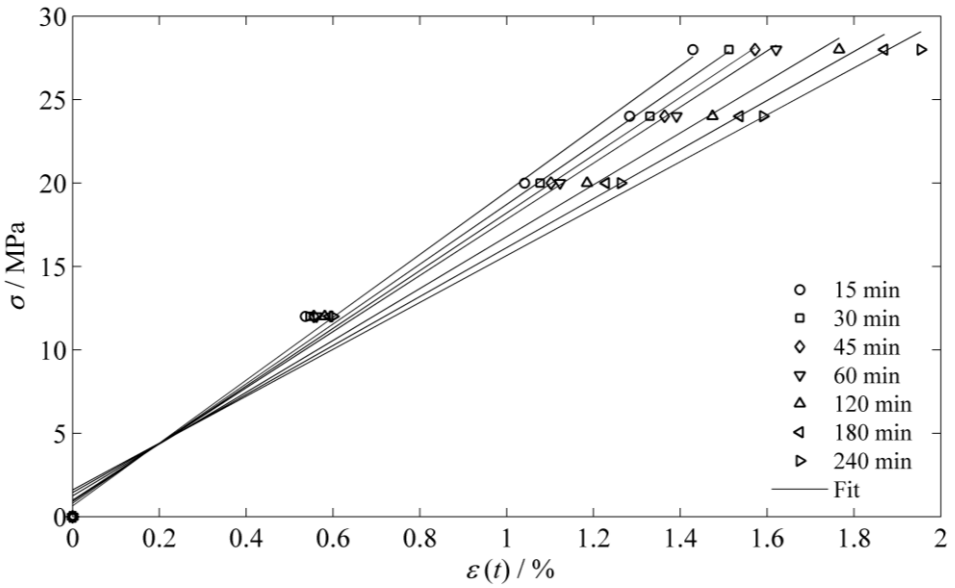

(b)

Figure 7.16: Isochronous creep curves of (a) non-aged and (b) aged *urushi* films under 50% RH.

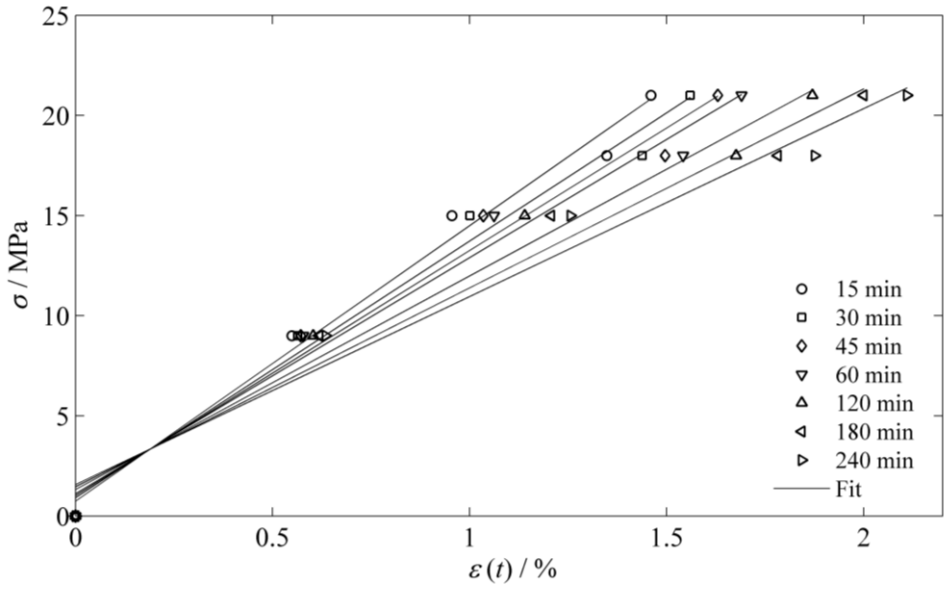

(a)

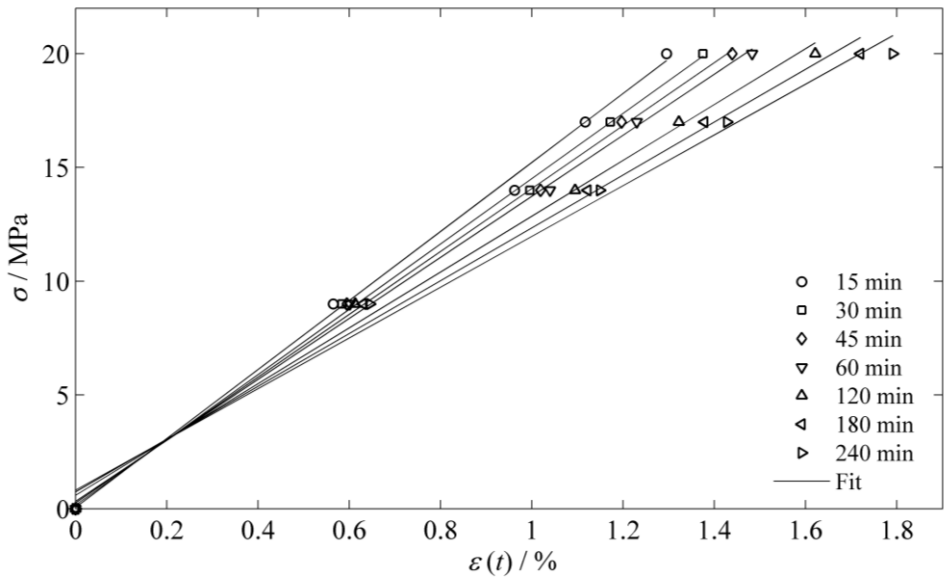

(b)

Figure 7.17: Isochronous creep curves of (a) non-aged and (b) aged *urushi* films under 75% RH.

Based on the experimental creep recovery curves, the applied stress values (σ) and the percent of elastic recovery (ε_R) for non-aged and aged *urushi* films under 30%, 50% and 75% RH are presented in Table 7.3. The variation of the elastic recovery with the applied stress is presented in Figure 7.18. As was expected, it has been observed that the percentage recovery decreases as we increase the applied stress for both non-aged and aged *urushi* films at all relative humidities (Figure 7.18). The non-aged *urushi* films exhibited higher amount of elastic recovery with increasing the stress than the aged films at 30% RH (Figure 7.18a). At elevated RH, 50% and 75% RH (Figure 7.18b,c), the aged *urushi* films recovered with higher amount than that of non-aged *urushi* films which indicate the strong influence of UV ageing on the films. Figure 7.19 shows the variation in elastic recovery for aged *urushi* films with stress at the lower and the higher RH, 30% and 75%. At σ = 20 MPa the amount of elastic recovery is almost the same at 30% and 75% RH. While at lower stress, σ = 9 MPa, the amount of elastic recovery at 30% RH was higher than that at 75% RH.

Table 7.3: Stress values and elastic recovery values for non-aged and aged *urushi* films used during creep test under 30%, 50% and 75% RH.

urushi	30% RH		50% RH		75% RH	
	σ (MPa)	ε_R (%)	σ (MPa)	ε_R (%)	σ (MPa)	ε_R (%)
non-aged	14	96.44	10.5	93.64	9	96.6
	23	90.94	17.5	85.43	15	79.39
	28	84.75	21	80	18	76.82
	32	82.31	24.5	77.85	21	76.01
aged	9	99.76	12	95.35	9	90.43
	14	100	20	90.33	14	88.37
	17	86.73	24	85.31	17	82.81
	20	79.65	28	78.98	20	78.95

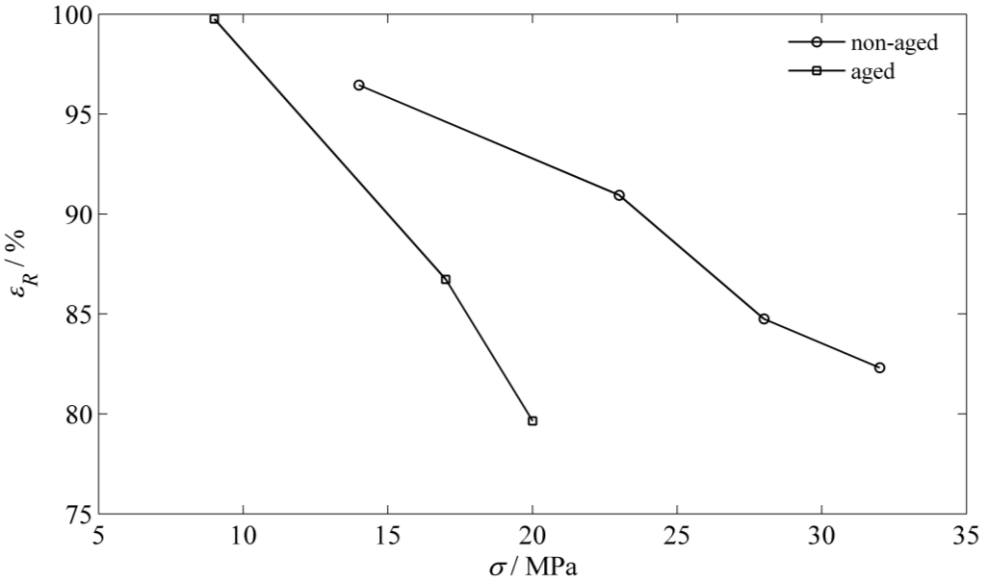
non-aged
aged
100
95
90
85
80
75
5
10
15
20
25
30
35
ε_R / %
σ / MPa

(a)

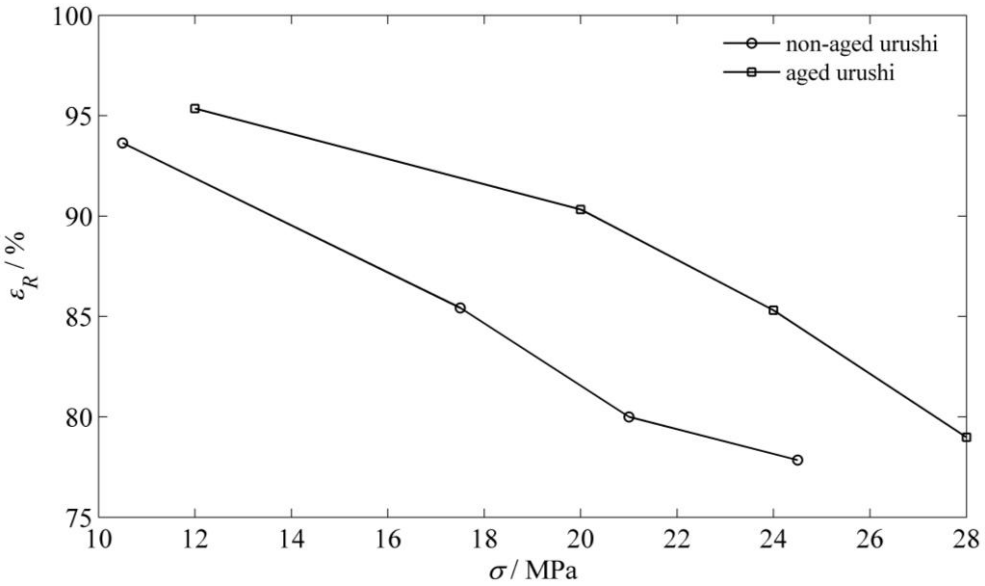
non-aged urushi
aged urushi
100
95
90
85
80
75
10
12
14
16
18
20
22
24
26
28
ε_R / %
σ / MPa

(b)

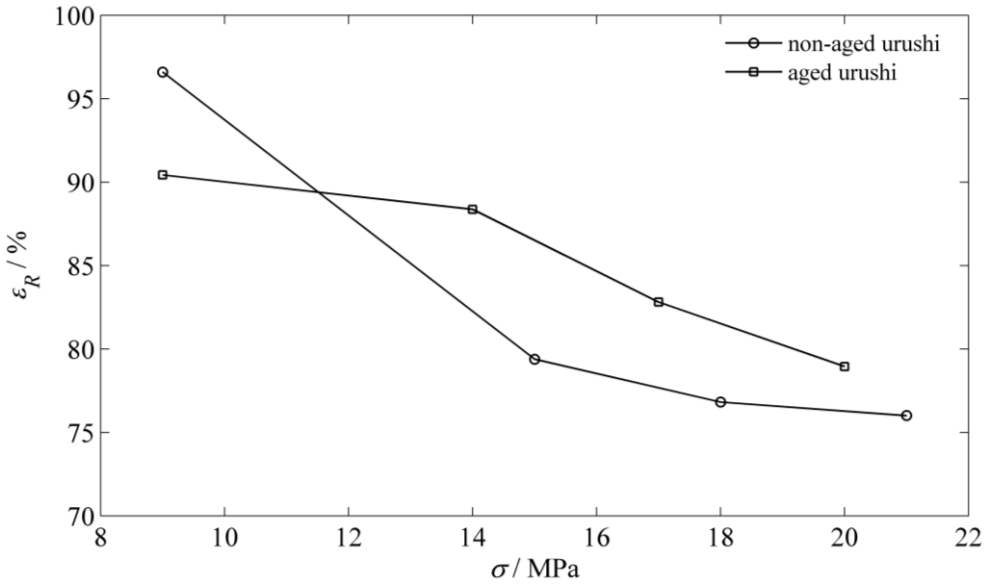

(c)

Figure 7.18: Variation of elastic recovery with the applied initial stresses for non-aged and aged *urushi* under (a) 30%, (b) 50% and (c) 75% RH.

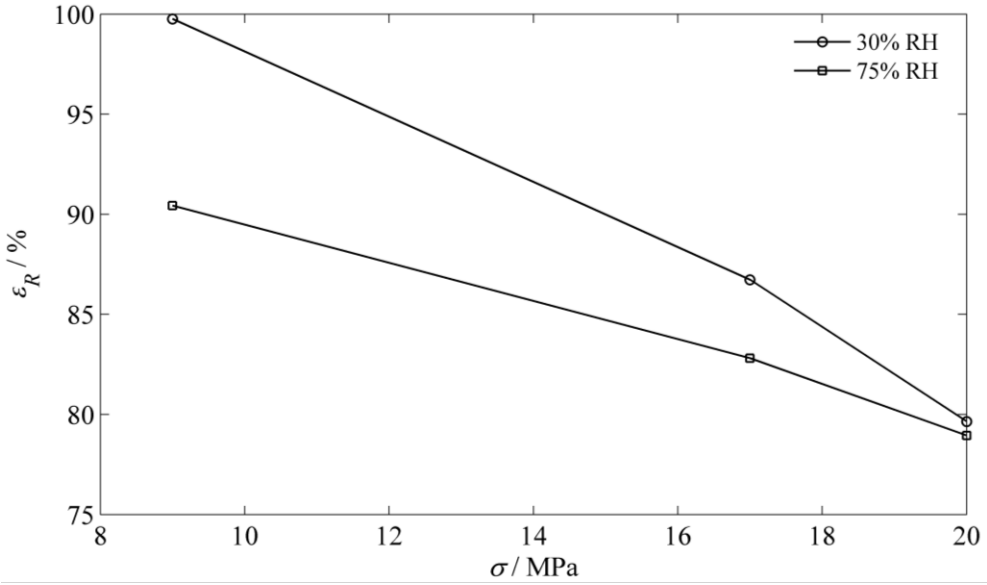

Figure 7.19: Variation of elastic recovery with the applied initial stresses for aged *urushi* under 30% and 75% RH.

7.3.4 Viscoelastic properties of *urushi*

Creep modelling is of considerable interest in creep analysis for viscoelastic materials. Different models have been reported in the literature [99, 101, 112] for viscoelastic polymeric materials. These models can be classified into physical models and empirical models based on the interpretation of the parameters. Among these models, Burger's model is the most commonly used physical model. A generalized Burger's model has one Maxwell unit and one or multiple Kelvin units connected in series. It divides the creep strain of a polymeric material into three parts: instantaneous deformation resulting from the Maxwell spring, viscous deformation resulting from the Maxwell dashpot and viscoelastic deformation resulting from Kelvin units.

In this work, a four-element Burger's model (one Kelvin unit) was used to characterize the creep curves of non-aged and aged *urushi* films (Figure 7.20(a)). The parameters from the 4-element Burger's model were easily interpretable due to their physical meanings. According to Burger's model, the creep behaviour is described as the sum of the instantaneous elastic strain ε_1, steady creep strain ε_2 and transient creep strain ε_3, controlled by Maxwell spring, Maxwell dashpot and Kelvin unit respectively as shown in Figure 7.20(b). During recovery, the instantaneous strain is reversible and recovers immediately on removal of the stress at t_1 due to Maxwell spring effect. ε_3 recovers gradually with time, while ε_2 is unrecoverable deformation due to the viscous flow (denoted as ε_3^r and ε_2^r in Figure 7.20(b)). The system deformation ε (t) is given by [112]

$$\varepsilon(t) = \varepsilon_1 + \varepsilon_2 + \varepsilon_3 = \sigma\left[\frac{1}{E_1} + \frac{t}{\eta_1} + \frac{1}{E_2}\left(1 - \exp\left(\frac{-E_2}{\eta_2}t\right)\right)\right], \qquad (7.1)$$

where $\varepsilon(t)$ is the creep strain at time t, σ is the stress, E_1 and η_1 are the instantaneous elastic modulus of the spring and viscosity of the dashpot in the Maxwell unit, and E_2 and η_2 are elastic modulus of the spring and viscosity of the dashpot in Kelvin unit.

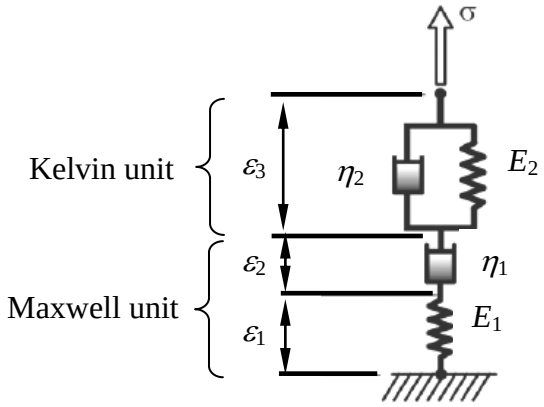

(a)

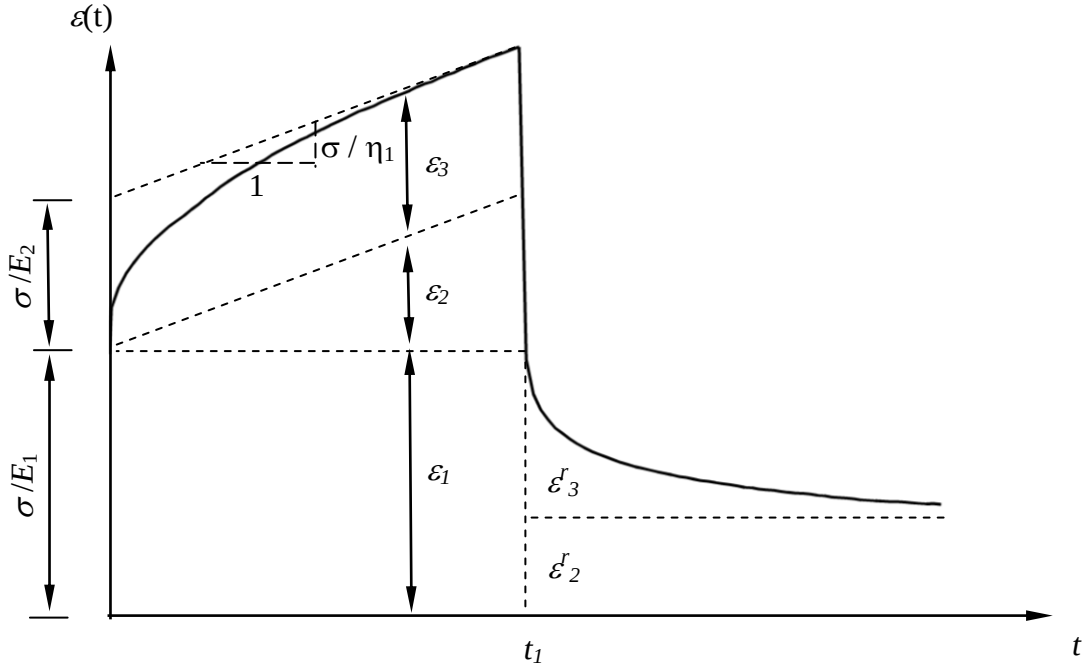

(b)

Figure 7.20: A diagram of generalized Burger's model.

In this work, E_1, E_2 and η_1 were separately calculated for each of the four levels of stress for non-aged and aged *urushi* films (presented in Figure 7.9 to Figure 7.14). The value of measured strain at $t = 0$ was taken as instantaneous elastic strain ε_1, allowing us to calculate E_1 from

$$\varepsilon_1 = \frac{\sigma}{E_1}. \tag{7.2}$$

The tangent of each creep curve at t_1 was evaluated where its rate of change ($\frac{\sigma}{\eta_1}$) was used to calculate η_1 and its value at $t = 0$ was used to calculate E_2 (Figure 7.20(b)). Having obtained E_1, E_2, η_1 we are then able to determine η_2 by inserting the known elements into Eq. (7.1) leaving η_2 as the only unknown, i.e.,

$$\exp\left(\frac{-E_2}{\eta_2}t\right) = 1 - E_2\left[\frac{\varepsilon(t)}{\sigma} - \frac{1}{E_1} - \frac{t}{\eta_1}\right]. \tag{7.3}$$

η_2 can then be obtained from Eq. (7.3) using regression. The recovery viscosity η_1^r was calculated using

$$\eta_1^r = \frac{\sigma\, t_1}{\varepsilon_2^r}, \tag{7.4}$$

where ε_2^r is the unrecoverable strain during recovery.

The parameters of Burger's model, E_1, E_2, η_1 and η_2, during creep and the recovery viscosity, η_1^r, were calculated for each stress for non-aged and aged *urushi* (Appendix A1 and Appendix A2). Figure 7.21 and Figure 7.22 show the variations of the average of these parameters, $< E_1 >$, $< E_2 >$, $< \eta_1 >$, $< \eta_2 >$ and $< \eta_1^r >$ with RH. For both non-aged and aged *urushi* films, increasing RH leads to a decrease in $< E_1 >$, $< E_2 >$, $< \eta_1 >$, $< \eta_2 >$ and $< \eta_1^r >$ (Figure 7.21 and Figure 7.22). The decrease in $< E_1 >$ and $< E_2 >$ under elevated RH indicates that *urushi* films, non-aged and aged, become soft [10] leading to increase the instantaneous and the viscoelastic deformations. The decrease in $< \eta_1 >$ and $< \eta_2 >$ with RH is evidence of the effects of the higher mobility of molecular chains and lower glass transition temperature at higher RH. This is consistent with the previous discussion that increasing plasticizer concentration increases the molecular mobility (Section 7.3.1.3). It has been found that $< \eta_1 >$ and

$<\eta_2>$ for aged *urushi* film are higher than those for non-aged films at all RH values (Figure 7.21(c-d) and Figure 7.22(c-d)) indicating that the ageing treatment results in slowing down of the rheological processes and can be related to the shift in the glass transition temperature and increases in the cross-links density as reported by Obataya et al [20].

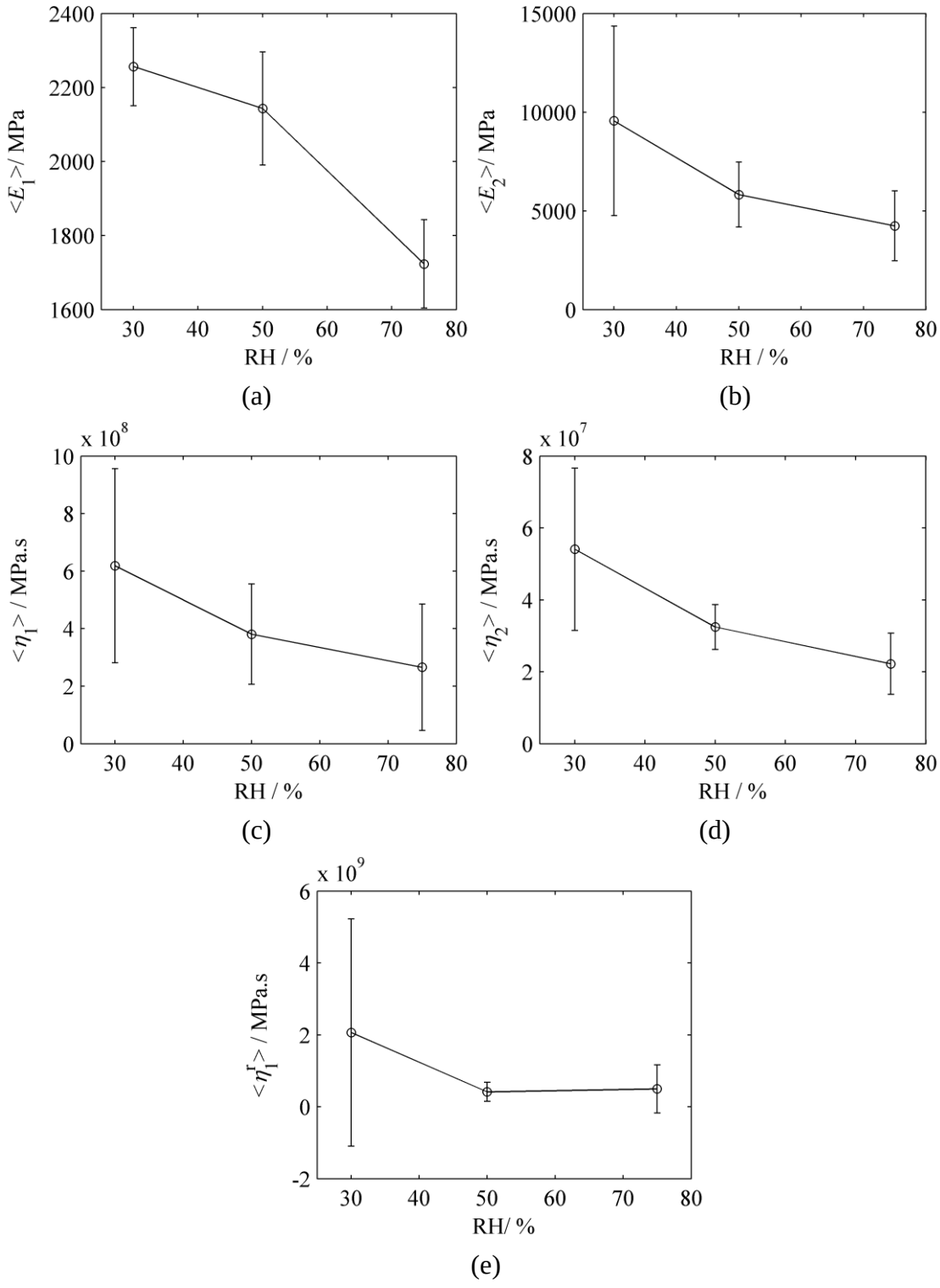

Figure 7.21: Variation of parameters in a Burger's model with RH for non-aged *urushi* films.

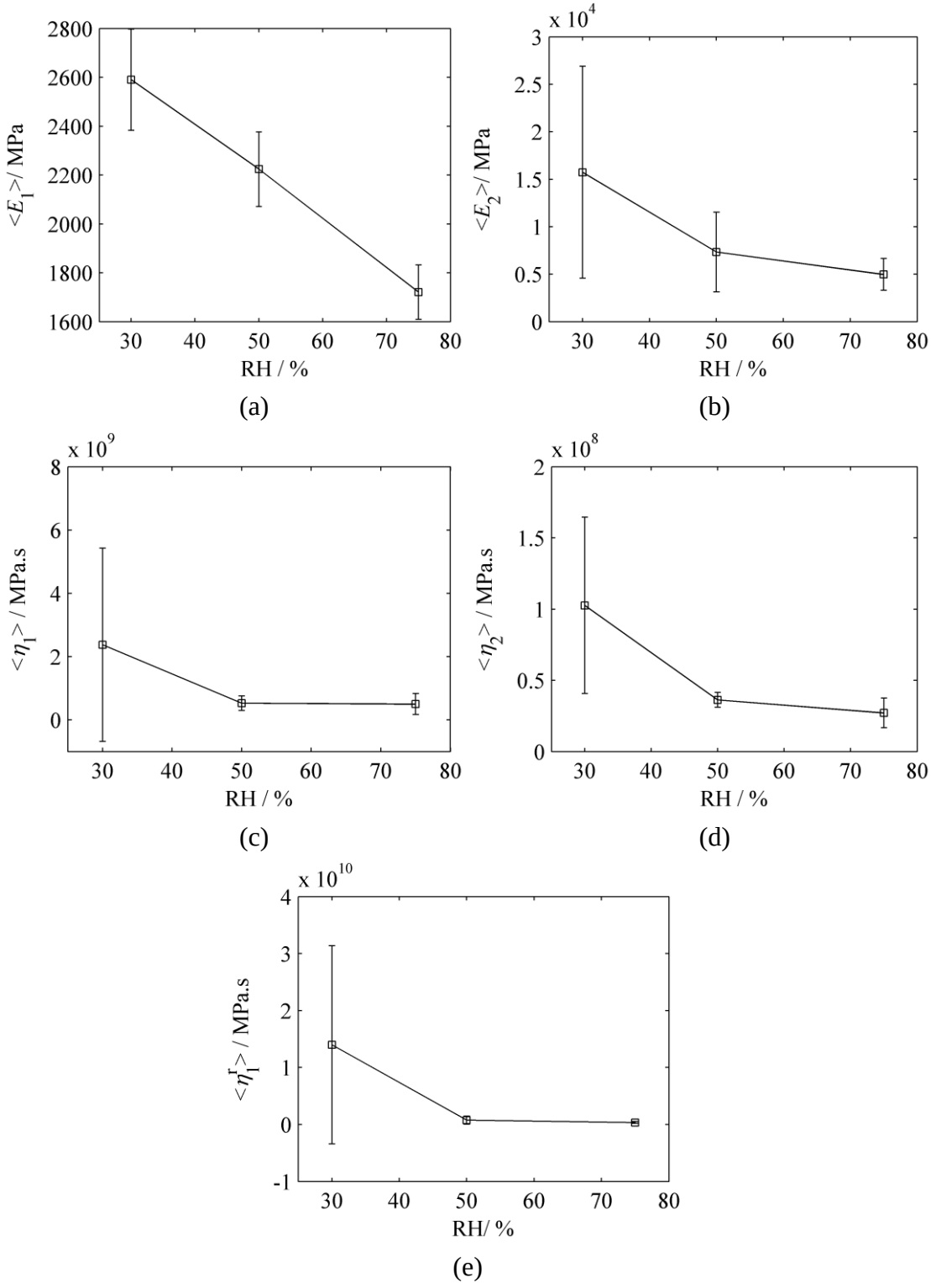

Figure 7.22: Variation of parameters in Burger's model with RH for aged *urushi* films.

7.4 Conclusions

Tensile stress-strain and creep recovery tests were conducted to investigate the effects of humidity on the mechanical properties and the viscoelastic behaviour of non-aged and aged *urushi* films. A strong dependence of the stress-strain behaviour on the strain rate and RH has been observed for non-aged *urushi* films, while the aged films showed less sensitivity to the strain rate and RH variation in comparison to the non-aged films. The effects of strain rate and RH on the mechanical properties of non-aged and aged *urushi* films at different strain rates were characterized.

The elastic modulus, tensile strength and elongation at break of non-aged *urushi* films are found to be strongly dependent on the strain rate. As the strain rate increases, these films show a decrease in elongation and an increase in the elastic modulus and tensile strength at break. The aged films show that the elastic modulus increases as the strain rate increases.

The UV ageing resulted in a strong decrease of elongation at break under the RH levels used in this study. At all strain rates used, a significant reduction in tensile elastic modulus and an increase in the elongation at break were observed with increasing the RH for non-aged and aged *urushi* films. As a result of the ageing process, the UV ageing films showed higher tensile elastic modulus and lower elongation at break than the non-aged films with increasing the RH. The creep tests show that the overall deformation levels of non-aged and aged films increase with increasing the RH. This behaviour can be explained considering that high humidity plays the role of a plasticizer, allowing more chain movement.

The creep and recovery tests results were used to calculate the viscoelastic properties represented by Burger's model parameters, for non-aged and aged *urushi* film, under 30%, 50% and 75% RH. Increasing the humidity showed a strong effect on all parameters in Burger's model, where increasing RH leads to a significant decrease in these parameters. It is found that dry environment, at 30% RH, hinders the molecular chains mobility in non-aged and aged *urushi* materials. UV ageing treatment showed a large impact on the viscoelastic properties leading to increase $< E_2 >$, $< \eta_1 >$ and $< \eta_2 >$ under the same RH. This change suggests that UV ageing resulted in an increase in the cross-linked density.

Chapter 8
Feasibility Study on the Experimental Assessment of the Mechanical Effects of Traditional Japanese Consolidation on Aged *Urushi* Films

8.1 Introduction

Over 4 centuries of fluctuating environmental conditions have led to the formation of micro-cracks on the main *urushi*-covered surfaces in the Mazarin Chest. The traditional Japanese consolidation method of lacquerware objects, known as *urushi-gatame,* consists in applying a diluted layer of fresh *urushi* to the damaged (aged) surface in order to fill any micro-cracks and restore its original gloss [113]. It is unknown, however, whether this procedure is effective in arresting crack propagation in the long term or whether it would accelerate damage mechanisms leading to

propagation of pre-existing micro-cracks. This poses a dilemma to Western museum curators and restorers, whose approach to conservation is based on minimum impact on the art piece, as opposed to their Japanese counterparts, who would apply the traditional methods used in the creation of the art piece to bring it back to its original appearance, even if this means adding or removing substantial parts of it.

Consolidated *urushi* can be effectively seen as a mechanical system consisting of a stack of thin films with dissimilar mechanical properties ($E_{non\text{-}aged}$ = 1.9 GPa; E_{aged}= 2.13 GPa; $CHE_{non\text{-}aged}$=0.00266 wt %; CHE_{aged}=0.00113 wt %). Whilst a protective layer of new non-aged *urushi* may reduce the surface area through which moisture is absorbed and delay the response of the aged film as a result, it is still uncertain how the different properties would compound to arrest or alternatively to promote crack growth.

The displacement or strain fields around the crack tip on a plane along which the crack propagates (cross section of the crack) can be used to evaluate the stress intensity factors with which the maximum stress can be estimated [114]. In the case of the micro-cracks in *urushi* films, which would be classed as Mode I fractures, this means that measurements of the strain field on a plane "through the thickness" of the films would be required. We are not aware of any technology able to provide such information for polymeric materials at the spatial scale required (field of view of ~100 μm^2), in a non contact way, with the required strain sensitivity and in a plane transverse to the plane of the film. We have access, however, to the surface of the film.

In order to assess the effect of the traditional Japanese *urushi gatame* consolidation, an experiment was designed to measure displacement fields around a controlled groove (representing a crack) on an aged *urushi* film before and after the consolidation procedure. The basic idea, illustrated in Figure 8.1, is to measure the displacement field across a crack (or 'v' groove) in the plane of the film surface when the substrate expands and strains the film. We will assume that no residual stresses are present and that we have a long groove, i.e. it is not growing in length by propagating the crack on the plane of the film. Under uniform strain, a crack-free film as illustrated in Figure 8.1(a) will show a linear displacement field $u(x)$. Four points on the film surface, identified as A, B, C and D, will show displacements u_A, u_B, u_C and u_D,

respectively. Figure 8.1(b) shows these displacements relative to point A, and for this reason $u_A = 0$. The constant slope $\frac{\partial u_x}{\partial x}$ of the graph indicates a uniform longitudinal strain ε_x, shown in Figure 8.1(c). In the presence of a crack, however, it is expected that an anomaly would appear in the displacement field measured around the crack, indicated at x=0 in Figure 8.1(d), as either side of the crack would be unable to transmit surface stress as before, and for a deep crack they could even behave like de-coupled film surfaces. As a result, point B will lag behind point C in terms of horizontal displacement relative to A, and the displacement and strain profiles would resemble the ones shown in Figure 8.1(e) and (f). Measuring this displacement anomaly for thin, stiff films could be a challenge, as it would be effectively equivalent to measuring shear lag through the thickness of the film, and the expected displacements could be very small. As the consolidation treatment restores the film surface by filling the cracks with fresh *urushi*, see Figure 8.1(g), the question that remains is whether there are still localized strains (due to displacement anomalies) around the crack that could eventually activate the crack and propagate it towards the substrate, Figure 8.1(h) and (i). Finally, the same question would apply a long time after the consolidation treatment, after the restoring *urushi* has aged, see Figure 8.1(j)-(l). It is important to note that we limited this study to the case where the substrate deformation plays the dominant role as the loading mechanism. No changes in humidity or temperature were permitted in our experiment, but these cannot be ignored in a complete study, which is beyond the scope of this thesis. Even though no strain measurements have been performed on the Mazarin chest, museum curators have observed a shrinkage of about 2 cm across the centre of the lid (70 cm wide), corresponding to a strain level of 0.028, dominated by the shrinkage of the wood structure due to low relative humidity.

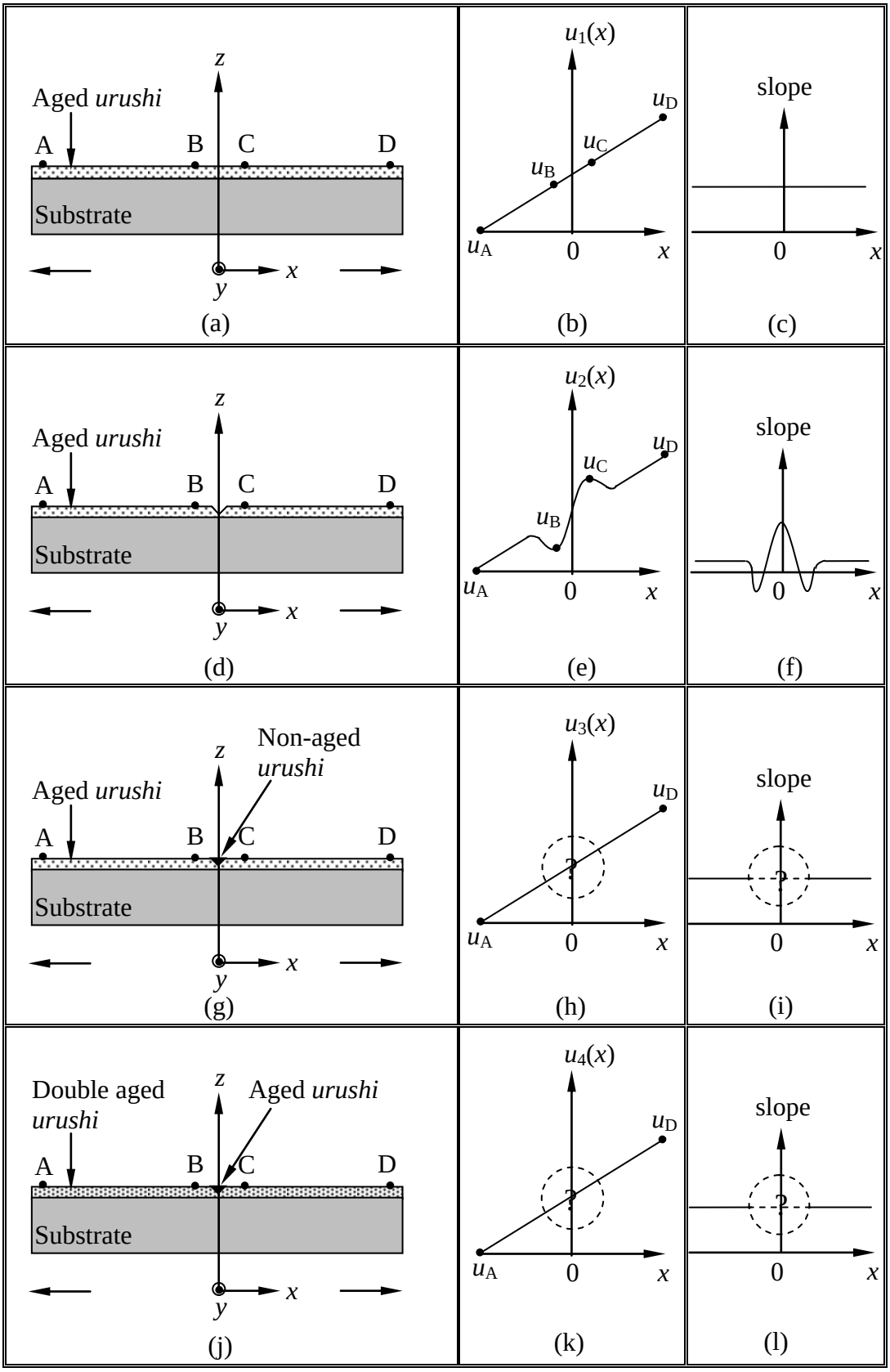

Figure 8.1: Schematic representation of the experimental stages.

In order to measure in-plane displacements around the crack, a high spatial resolution, high displacement sensitivity, non-contact method is required, all of these well known characteristics of Digital Speckle Pattern Interferometry (DSPI). In Section 8.2 some basic concepts of the speckle effect are presented, along with the fundamental principles of DSPI and the displacement sensitivity of the technique. Section 8.3 describes sample preparation and loading, Section 8.4 the physical implementation of the interferometer, Section 8.5 the measurement methodology and the results obtained, and finally Section 8.7 some concluding remarks.

8.2 Digital speckle pattern interferometry

8.2.1 The Speckle effect

When coherent light is reflected or scattered from a rough surface (Figure 8.2), the optical wave arriving at any point on the observation plane consists of the superposition of many waves, each arising from a different point in the illuminated surface. The path lengths travelled by these waves, from source to object point to the observation plane, can differ from zero to many wavelengths, depending on surface roughness and the geometry of the system. Interference of the de-phased waves arriving at the observation plane will cause the resultant irradiance varying from dark to fully bright. This variation in resultant irradiance from one receiving point to another is the cause of laser speckle. These speckles are normally observed to be randomly distributed in space in the form of bright and dark spots (Figure 8.3).

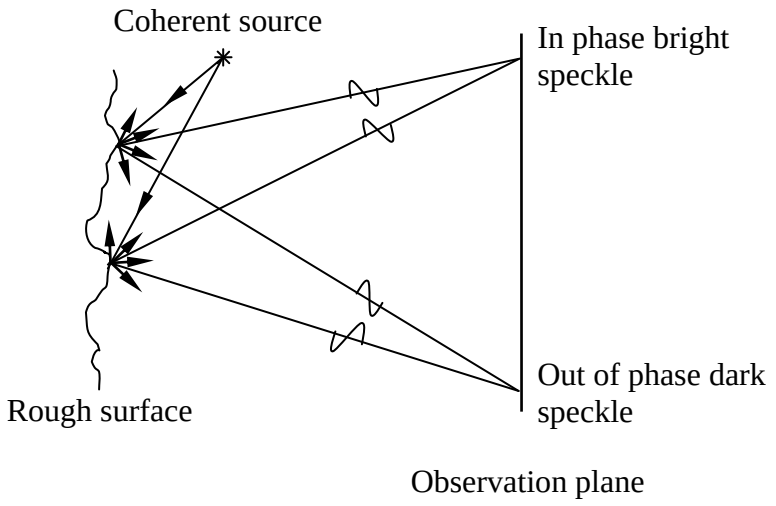

Figure 8.2: Speckle formed by interference of scattered coherent light.

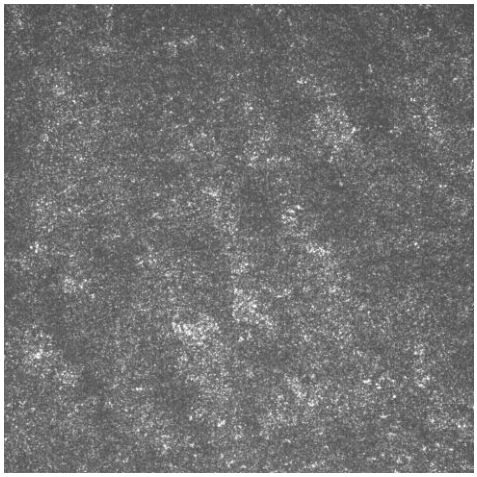

Figure 8.3: Speckle pattern resulting from interference of scattered waves.

Speckle techniques can be basically classified into two types: (1) those based on positional shift of the speckles, and (2) those based on irradiance changes of the speckles. Speckle photography includes all those methods where positional changes of speckles are monitored, whereas speckle interferometry includes methods that are based on the measurements of phase changes and hence irradiance changes [115].

8.2.2 Digital speckle pattern interferometry

The basic principles of speckle interferometry go back to the famous article of Leendertz [116]. This paper was the first to propose combining speckle interferometry with electronic detection and processing. With advances in digital recording and computing facilities, DSPI has evolved from electronic speckle pattern interferometry (ESPI) and was adopted to study a broad range of problems in applied mechanics. In DSPI, image subtraction, transforming, exporting, and various kinds of pre-processing can be performed flexibly and rapidly. It is an optical measuring technique that allows rapid and highly accurate measurement of deformations. Furthermore, in comparison with other techniques for strain measurement or calculation, DSPI enjoys the advantages of being non-contact, full-field, has a high spatial resolution, high sensitivity, delivers accurate displacement data and does not require any costly surface preparation. It can be applied to any material provided that the surface is sufficiently rough and the laser light is diffusely reflected [115]. An increased number of applications of DSPI for in-plane deformation and displacement measurements with one-dimensional sensitivity and two dimensional (2-D) sensitivities have been reported

[117-121]. The dual-beam optical arrangement of Leendertz [116] is normally used in these applications. 2-D in-plane deformation can be obtained using two orthogonal sets of Leendertz dual-beam systems by different means.

8.2.3 Dual-beam illumination arrangement for measuring in-plane displacements

Figure 8.4 shows a schematic representation of an optical configuration which is used for the measurement of the in-plane displacement component along the $x-$axis. In this case, the object surface is supposed to lie in the xy plane. The surface is illuminated by two collimated beams of coherent light propagating parallel to the xz plane and incident at equal angles θ to the observation direction on either side of the surface normal, which lies parallel to the observation direction. The two beams generate their own speckle patterns which are combined coherently and form a resulting speckle pattern at the detector of a CCD camera. The intensity distribution of the speckle pattern for a particular state of the object is given by:

$$I_1(x,y) = I_0(x,y) + I_M(x,y)\cos\left[\phi(x,y)\right], \tag{8.1}$$

where $I_0(x,y)$ is the background average intensity, $I_M(x,y)$ is the modulation intensity of the speckle interference pattern, $\phi(x,y)$ is the a random phase difference between both scattered beams and (x,y) are the spatial co-ordinates in the reference frame of the image.

Deformation of the object changes the relative phase $\phi(x,y)$ encoded in the interference pattern, thus another speckle pattern is formed and the intensity recorded in the deformed state becomes:

$$I_2(x,y) = I_0(x,y) + I_M(x,y)\cos\left[\phi(x,y) + \Delta\phi(x,y)\right], \tag{8.2}$$

where $\Delta\phi(x,y)$ is the phase change caused by the deformation.

The motion of the surface in the $z-$direction induces, as a consequence of the symmetrical illumination, an equal amount of phase change $\Delta\phi(x,y)$ in the two speckle patterns. The cancellation of these terms in the calculation in the relative phase

change renders the method insensitive to the movement in $z-$direction. Similarly, the arrangement has no sensitivity to the motion in the $y-$direction. The relative phase change $\Delta\phi(x, y)$ results from the motion of the surface in the $x-$direction.

With the ensuing phase change induced in the two speckle patterns being of equal magnitude and of opposite sign, namely $\frac{2\pi}{\lambda} n u \sin\theta$ for one and $-\frac{2\pi}{\lambda} n u \sin\theta$ for the other, with λ the wavelength of the light used and n being the refractive index of the medium ($n=1$ for air). The in-plane component of the displacement in the $x-$direction, u, relates to the phase change $\Delta\phi$:

$$\Delta\phi = \frac{4\pi}{\lambda} n u \sin\theta, \tag{8.3}$$

By the use of Eq. (8.3) we can therefore determine the extent of the in-plane displacement map on the sample surface by determining the wrapped phase difference $\Delta\phi_w$ using Eq. (4.5) and then unwrapping it as described in Section 4.3. It is seen from Eq. (8.3) that the sensitivity of the dual-beam interferometer is only dependent on the illumination angle and the wavelength.

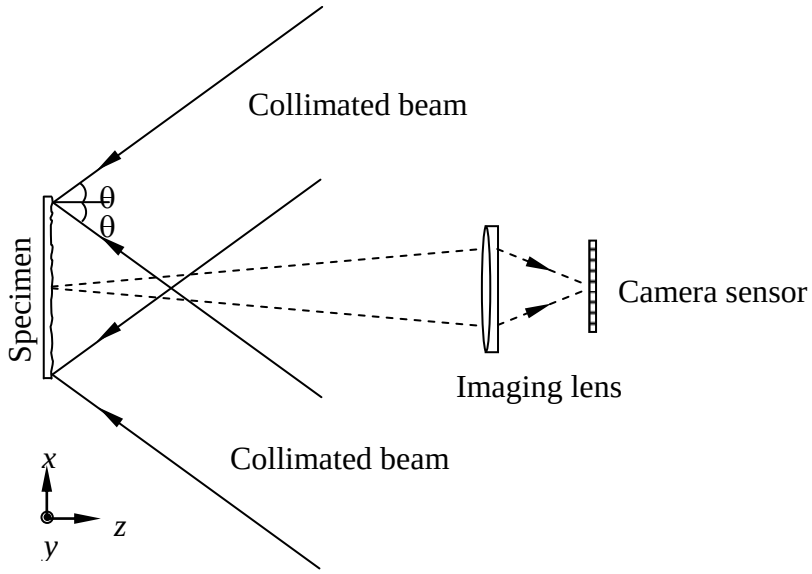

Figure 8.4: Basic configuration of a dual-beam speckle interferometer [122].

8.3 Sample preparation and loading

We followed the same preparation procedure described in Section 3.2.1 and Section 3.2.2 to prepare *urushi* (*kijiro* type) samples for notched tests. A spin coater (Section 3.2.4) was used to cast *urushi* films (60 µm thickness) onto 70 mm × 15 mm × 3 mm rectangular aluminium substrates. The films were left to cure at room temperature and 75±2% RH for three weeks. After curing, the films were cut into rectangular strips of 40 mm × 5 mm, and the excess removed from the substrate. The samples were aged with UV radiation during 400 hrs of exposure as described in Section 3.3. A 'v' groove was then created across the middle of the *urushi* film using a sharp blade (see Figure 8.5).

In order to strain the *urushi* film in a controlled and repeatable way, the aluminium substrates were mounted on a three-point-bending loading rig, with the *urushi* film facing the imaging system and the back face in contact with an edge that was positioned by a micrometer screw (Figure 8.8). Three point bending loading ensures a nearly uniform longitudinal strain field $\varepsilon_x = \frac{\partial u_x}{\partial x}$ around the midspan of the beam.

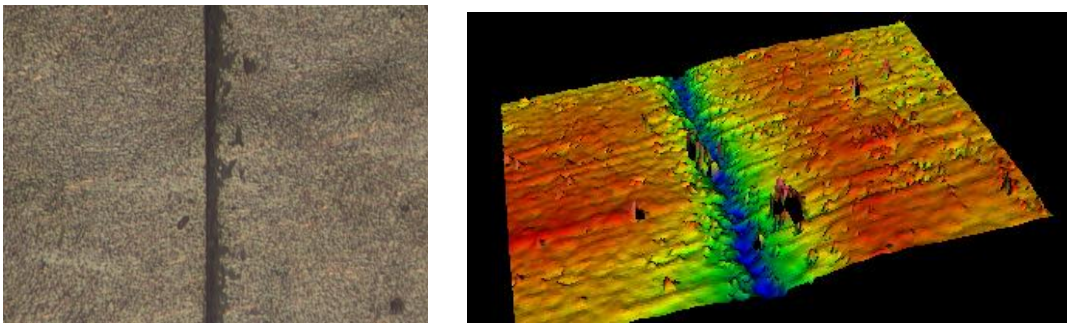

(a) (b)

Figure 8.5: A 'v' groove in aged *urushi* film as viewed through an optical microscope in reflection mode (a) and a 3D surface profile obtained with a Zygo White Light Scanning Interferometer.

8.4 Experimental setup

8.4.1 Layout

A dual sensitivity phase-shifting DSPI setup was used to measure 2-D in-plane displacement components in x and y directions (Figure 8.6). In the experiment,

however, we were only concerned with the horizontal x sensitivity. A beam from a 30mW He–Ne laser beam (Melles Griot model) with wavelength λ =632.8nm is used as the coherent light source. A single mode optical fibre (OF) is used to deliver the laser beam that is collimated by lens L_1 and then diffracted by two crossed transmission holographic diffraction gratings (G) (1200 lines/mm). The purpose of the gratings is twofold. Firstly, it splits the incident collimated beam into two pairs of beams (+1 and -1 orders of each of the diffraction gratings in the xz and yz planes. Four mirrors M_{x1}, M_{x2}, M_{y1} and M_{y2} (Figure 8.6) steer the collimated beams coming from the diffraction gratings towards the sample. M_{x1} and M_{x2} mirrors are arranged on the horizontal plane to form one set of dual-beam illumination to measure the displacement component in the x direction (u), while M_{y1} and M_{y2} are arranged on the vertical plane to measure the displacement component in the y direction (v). Each mirror is fixed on a holder with 3 degrees of freedom for ease of adjustment. The four coherent illumination fields should preferably be plane wavefronts, incident at equal angles θ on either side of the surface normal. The illumination angles are chosen to be 29° to the sample normal. The sample is mounted and mechanically loaded using a three point bending device (BD) with a micrometer head as shown in Figure 8.8. A CMOS camera (C) (HCC-1000 Vosskühler, 8 bits, 1024×1024 pixels) records the speckle patterns imaged with a long working distance microscope objective zoom lens $L_{2,}$ mounted 80 mm away from the sample surface. The imaged field of view was set to 2.6 mm × 2.6 mm by adjusting the zoom lens. A positioning stage (PS), Figure 8.9, has been designed by a project student to mount and translate the diffraction gratings (G) in an accurate and repeatable way [123].

The second role of the transmission crossed gratings is to enable controlled phase stepping by translating it with a positioning stage with an open loop piezoelectric lead zirconate titanate transducer (PZT). The PZT actuator used in this work was a Physik Instrument type P055.31 PZT which is a low voltage device with a maximum displacement of 2 μm for 100 V of applied voltage. In order to obtain a fringe pattern corresponding to the u displacement field, only the illumination beams lying on the horizontal plane were allowed to be incident on the surface (Figure 8.7) while the other beams were blocked.

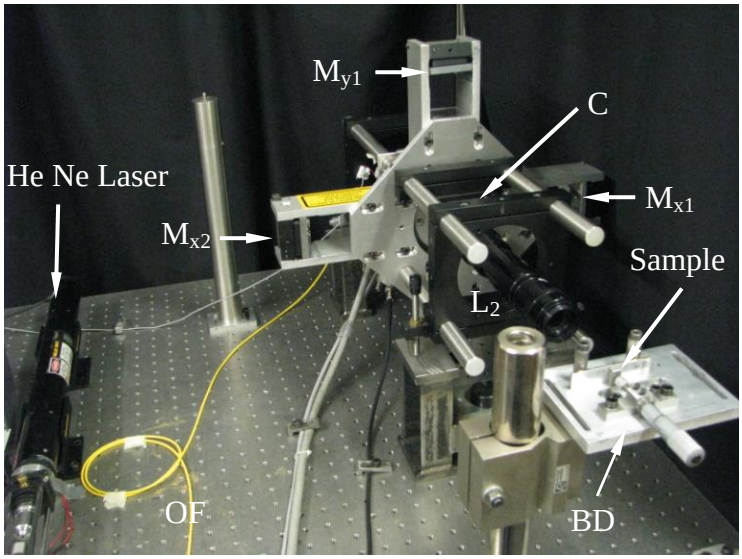

Figure 8.6: Photograph of the 2-D in-plane phase-shifting DSPI system: OF, optical fibre; M_{x1}, M_{x2} and M_{y1}, mirrors; BD, three point bending device; L_2, zoom lens; C, CMOS camera.

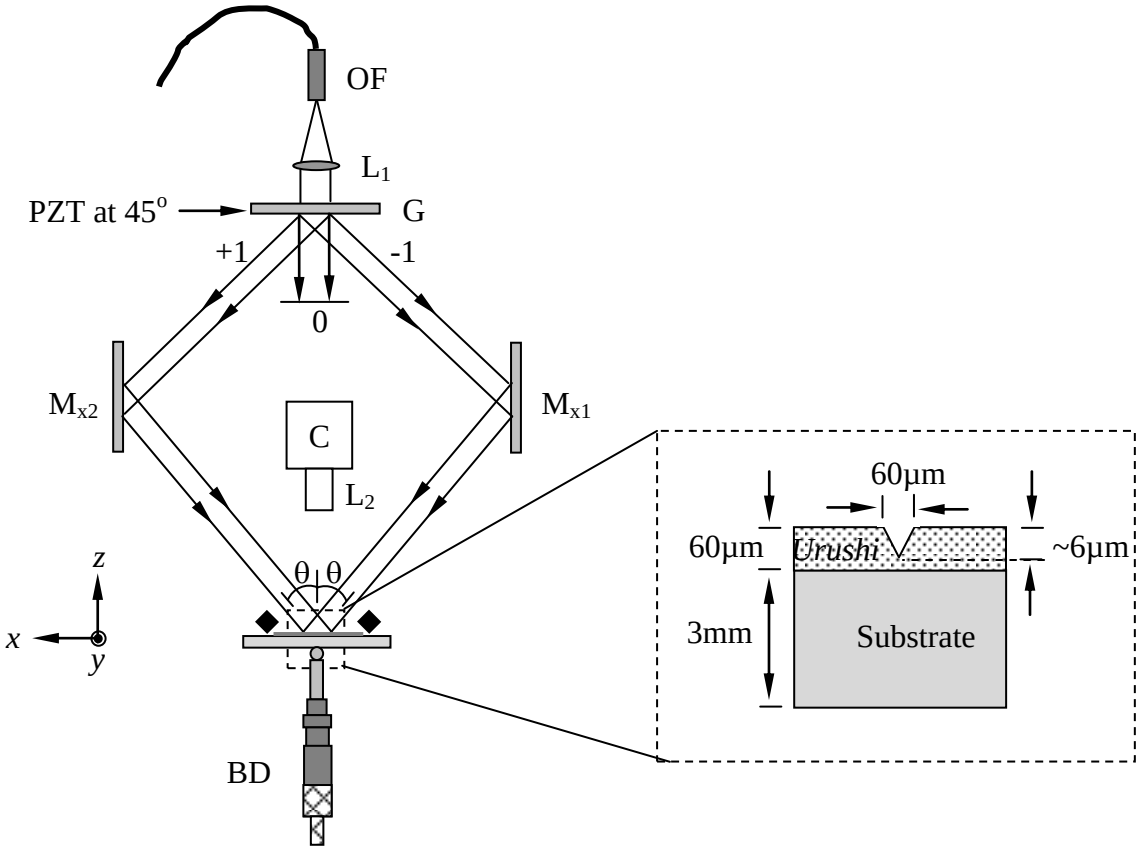

Figure 8.7: Optical arrangement for 1-D in-plane phase shifting digital speckle pattern interferometer: OF, optical fibre; L_1, collimating lens; G, crossed diffraction gratings; M_{x1} and M_{x2}, mirrors; BD, three point bending device; PZT, open loop piezoelectric transducer; L_2, zoom lens; C, CMOS camera.

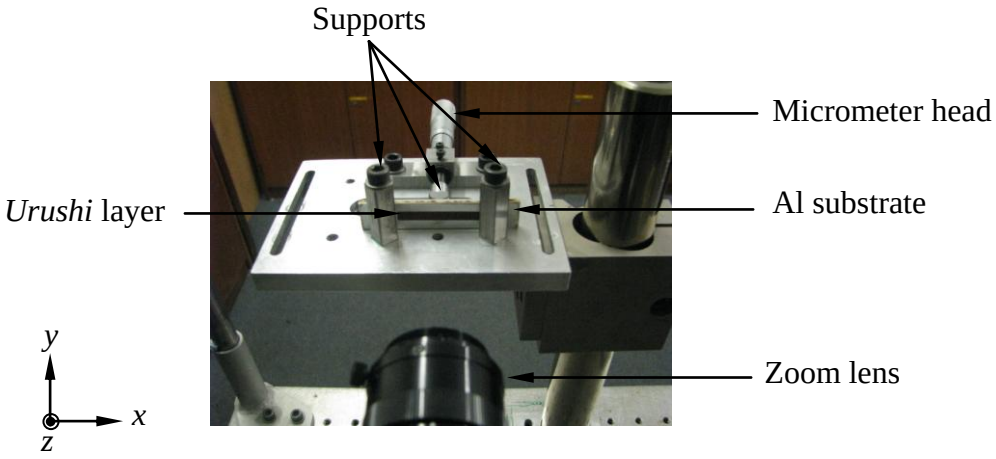

Figure 8.8: Three point bending device used to deform the sample mechanically.

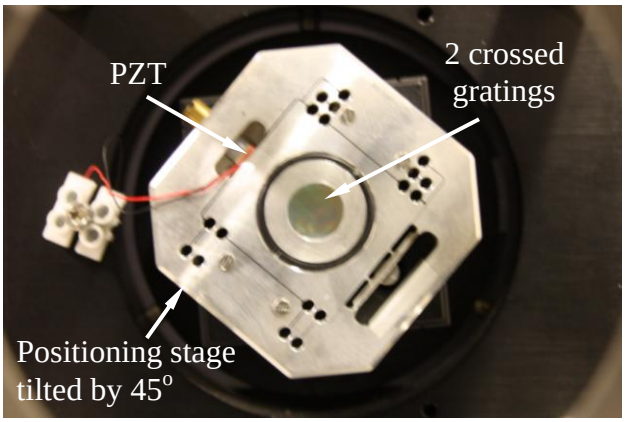

Figure 8.9: Positioning stage with PZT and grating holder.

8.4.2 Phase stepping and calibration

In order to measure the phase change $\Delta\phi$ in Eq. (8.2), one has to determine the three unknown values $I_0(x,y)$, $I_M(x,y)$ and $\Delta\phi(x,y)$ so that at least three acquisitions (interference images) are necessary. For a higher accuracy, a four-phase algorithm was chosen in order to get the phase value (Section 4.3). This is a process in which known phase shifts are introduced between the two interfering beams enabling the phase to be extracted by measuring the fringe or speckle intensity. In this work, the phase shifting was achieved by translating diffraction grating G onto its plane. A phase shift of $\frac{\pi}{2}$ between the +1 and -1 diffracted orders in the xz or yz planes is introduced when the

grating G moves a distance $g\frac{\sqrt{2}}{8}$ (with g the grating pitch) along an axis at 45° to the $x-$axis [124-126]. Accurate phase shifting requires calibration of the (usually non-linear) phase-shifting device in order to obtain equal phase shifts between interferograms. The calibration was performed using a Moiré Interferometry approach. A reflection diffraction grating (RG) (600 lines/mm) was illuminated by the collimated beams reflected from M_{x1} and M_{x2} at an angle of 23° (Figure 8.10). Each collimated beam generated its own diffraction pattern (Figure 8.10). Interference between the +1 order of the diffracted light coming from M_{x1} and -1 order of the diffracted light coming from M_{x2} gives rise to an interference pattern, whose spatial frequency encodes the angle between these diffracted beams –see Figure 8.11. A sequence of phase-shifted interferograms was recorded for the horizontal sensitivity. Subsequently the procedure described in Sections 4.5.5 and 4.5.6 [73] to control and calibrate another PZT was followed.

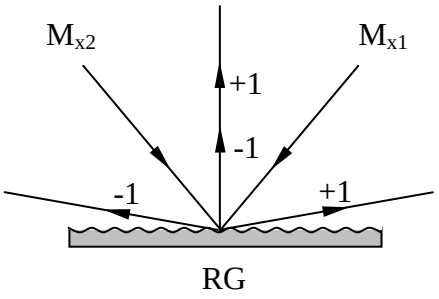

Figure 8.10: Diffraction orders of the grating used in calibration.

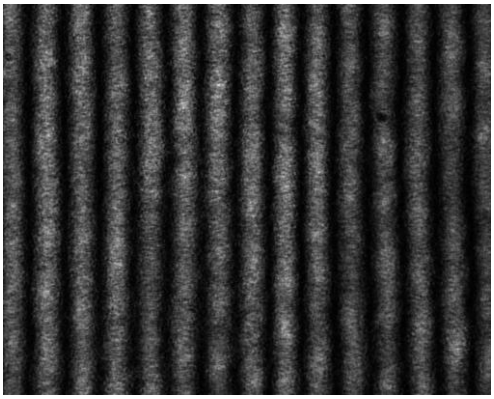

Figure 8.11: Interference pattern obtained during calibration process.

Figure 8.12 shows the average of the squared differences (S) versus the applied voltage to the PZT, and also the best fit for a little over the first cycle using Eq. (4.19). During the calibration process, 100 steps were used at 0.5 V / step.

The dependence of the phase shift on the applied voltage is shown in Figure 8.13. The amount of voltage required to introduce a $\frac{\pi}{2}$ phase shift was extracted from the dependence of the phase shift on the applied voltage (Figure 8.13) using a one-dimensional data interpolation function, (Figure 8.14).

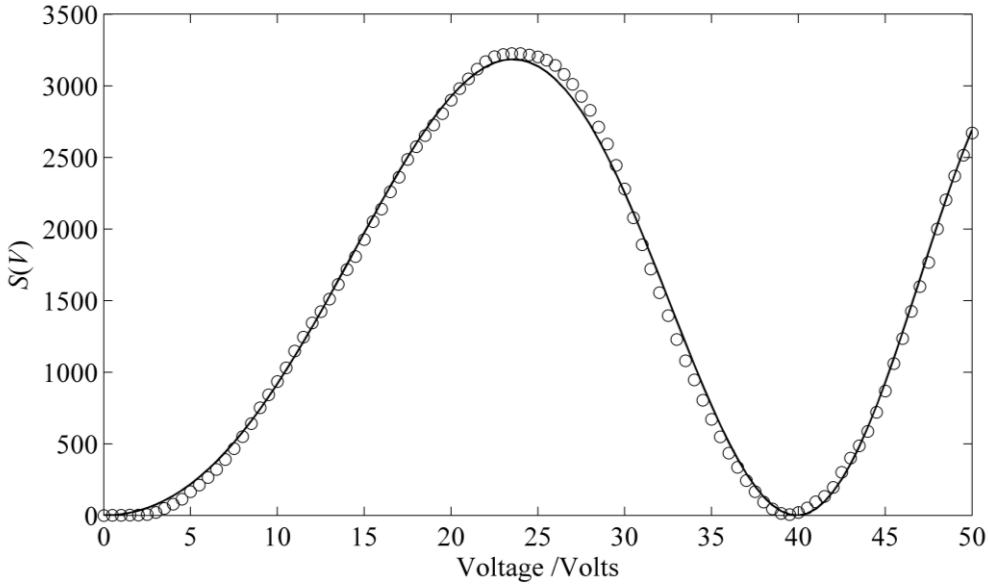

Figure 8.12: Second order polynomial fitting of $S(V)$. The open circles represent the experimental data and the line is the fitting.

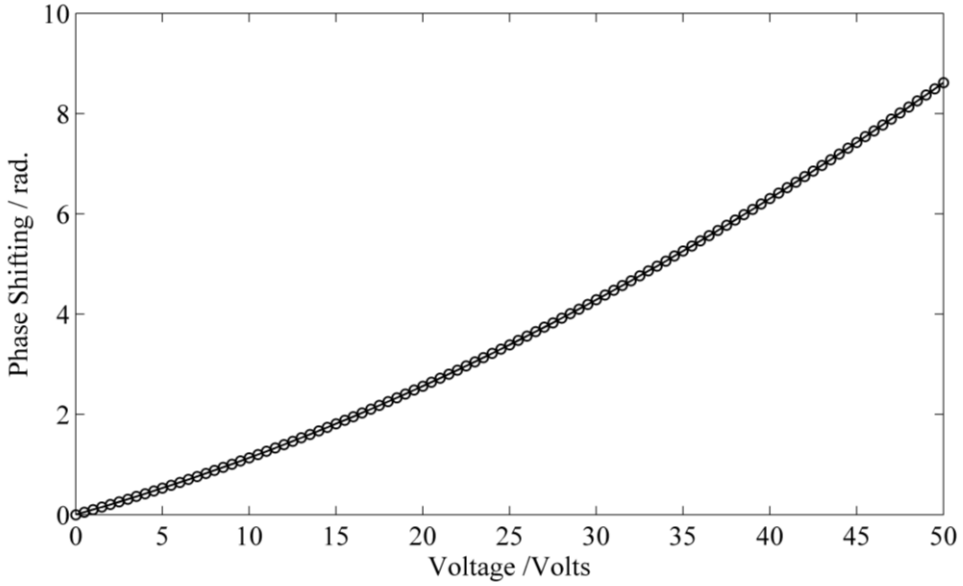

Figure 8.13: The dependence of phase shift on the applied voltage.

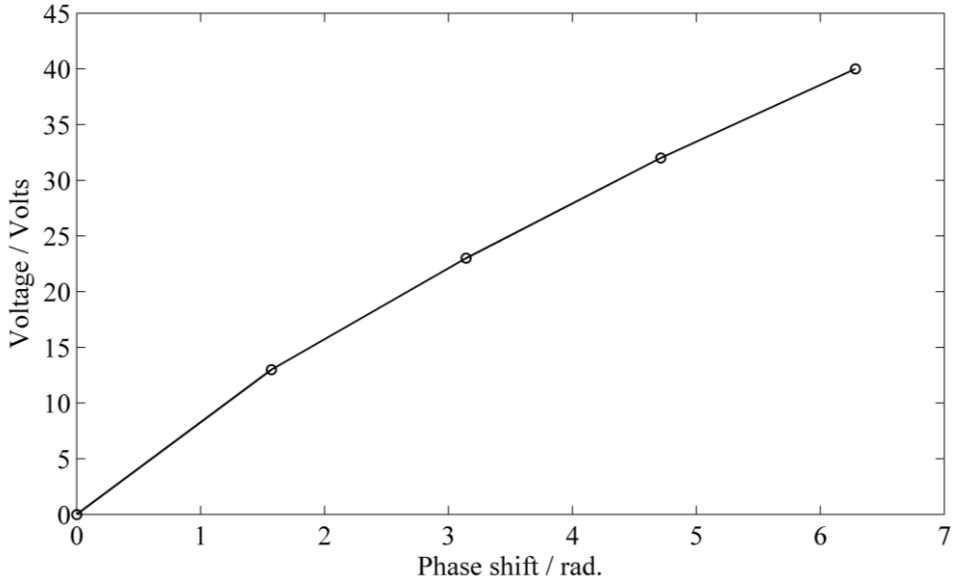

Figure 8.14: The voltage values required for phase shifts 0, $\frac{\pi}{2}$, π, $\frac{3\pi}{2}$ and 2π rad. were V_1=0, V_2= 13, V_3=23, V_4=32 and V_5=40 volts, respectively.

8.5 Measurement procedure

Figure 8.1 (a), (d), (g), and (j) depict the different cases for which the horizontal displacements were measured in *urushi* films as a result of substrate strain. The substrate was mounted with the *urushi* film lying on the xy plane as shown in Figure

8.8, presenting a field of view of 2.7 mm × 2.7 mm. The relative humidity and temperature during measurements was 55±1% and 18±2 °C, respectively.

1) First, the displacement field of a groove-free aged *urushi* film surface was measured as follows:

a) Four speckle interferograms of a reference state were recorded corresponding to phase shifts of 0, $\frac{\pi}{2}$, π and $\frac{3\pi}{2}$.

b) A certain deflection along the $z-$axis was introduced at the beam midspan by using the micrometre screw in the 3 point bending rig. This deflection was chosen to produce a strain level enough to introduce around two fringes across the measured field of view, which gives a good signal to noise ratio (phase measured vs. phase noise) and ensures that the aluminium beam remains in the elastic region.

c) Four speckle interferograms of the deformed state were recorded corresponding to phase shifts of 0, $\frac{\pi}{2}$, π and $\frac{3\pi}{2}$.

d) The wrapped phase change $\Delta\phi_w(x, y)$ was computed using Eq. (4.5).

e) The unwrapped phase $\Delta\phi\ (x, y)$ was evaluated, as described in Section 4.3, using a robust 2D phase-unwrapping algorithm (from Phase Vision Ltd., Loughborough, UK) convolved with 5 × 5 Kernel filter.

f) The horizontal component of the displacement field, $u(x, y)$, was obtained using Eq. (8.3).

g) The profile $< u > (x)$ was computed by averaging $u(x, y)$ along the y-axis (image columns), to obtain a horizontal component of the displacement estimator with low speckle noise content.

h) The profile $< u_1 > (x)$ was then taken as an average of two measurements of $< u > (x)$.

2) A 60 μm wide and ~6 μm deep vertical 'v' groove was introduced in the sample tested in step (1) as indicated in Section 8.3, and steps (a)-(g) were followed to obtain $< u_2 > (x)$ as an average of three $< u > (x)$ measured profiles. Note that the groove was initially aligned to the image columns.

3) The sample tested in step (2) was covered with a fresh layer of *urushi* and the excess was removed with a spatula, in order to just fill the groove. The fresh *urushi* in the groove cured as indicated in Section 8.3 and steps (a)-(g) were followed to obtain $< u_3 > (x)$ as an average of three $< u > (x)$ measured profiles.

4) The sample tested on step 3 was aged as indicated in Section 8.3 and steps (a)-(g) were followed to obtain $< u_4 > (x)$ as an average of three $< u > (x)$ measured profiles.

8.6 Results and discussion

Figure 8.15 and Figure 8.16 show the wrapped, $\Delta\phi_w(x, y)$, and the unwrapped, $\Delta\phi\ (x, y)$, phase difference maps obtained in steps 1-4 for the different cases described above for a deflection at midspan of the beam of 80 μm. Figure 8.17 shows the average displacements profiles $< u_i > (x)$, i=1,...4, obtained as indicated above. Just as expected, an anomaly in the displacement profile $< u_2 > (x)$ is visible around the groove exactly where the groove is. The amplitude of the anomaly relative to the linear slope is nearly 40 nm (see insert in Figure 8.17), not far from the speckle phase noise level of 8 nm *rms*, as shown in Table 8.1. The spatial extent of the anomaly is ~60 μm, corresponding to the groove's width.

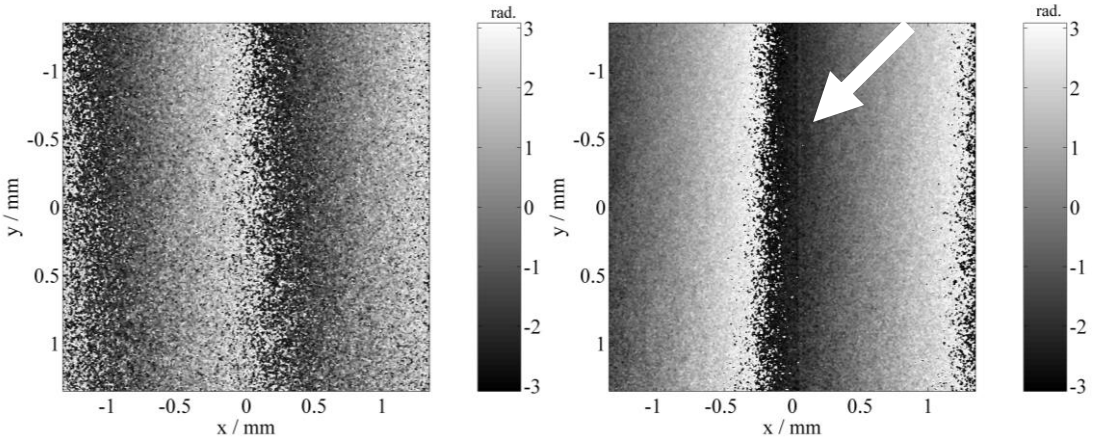

(a) (b)

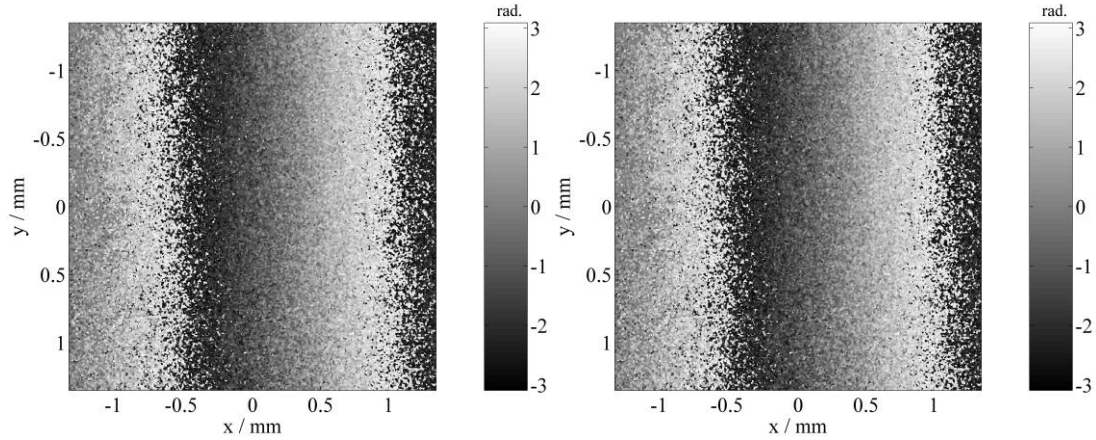

(c) (d)

Figure 8.15: Wrapped phase difference maps, $\Delta\phi_w(x, y)$, obtained for (a) groove-free aged *urushi* film; (b) aged *urushi* film with a 'v' groove (vertical line indicated by arrow); (c) non-aged cured *urushi* film on top of an aged film with a groove (consolidated crack) and (d) aged *urushi* film on top of an aged film with a groove (aged consolidated crack).

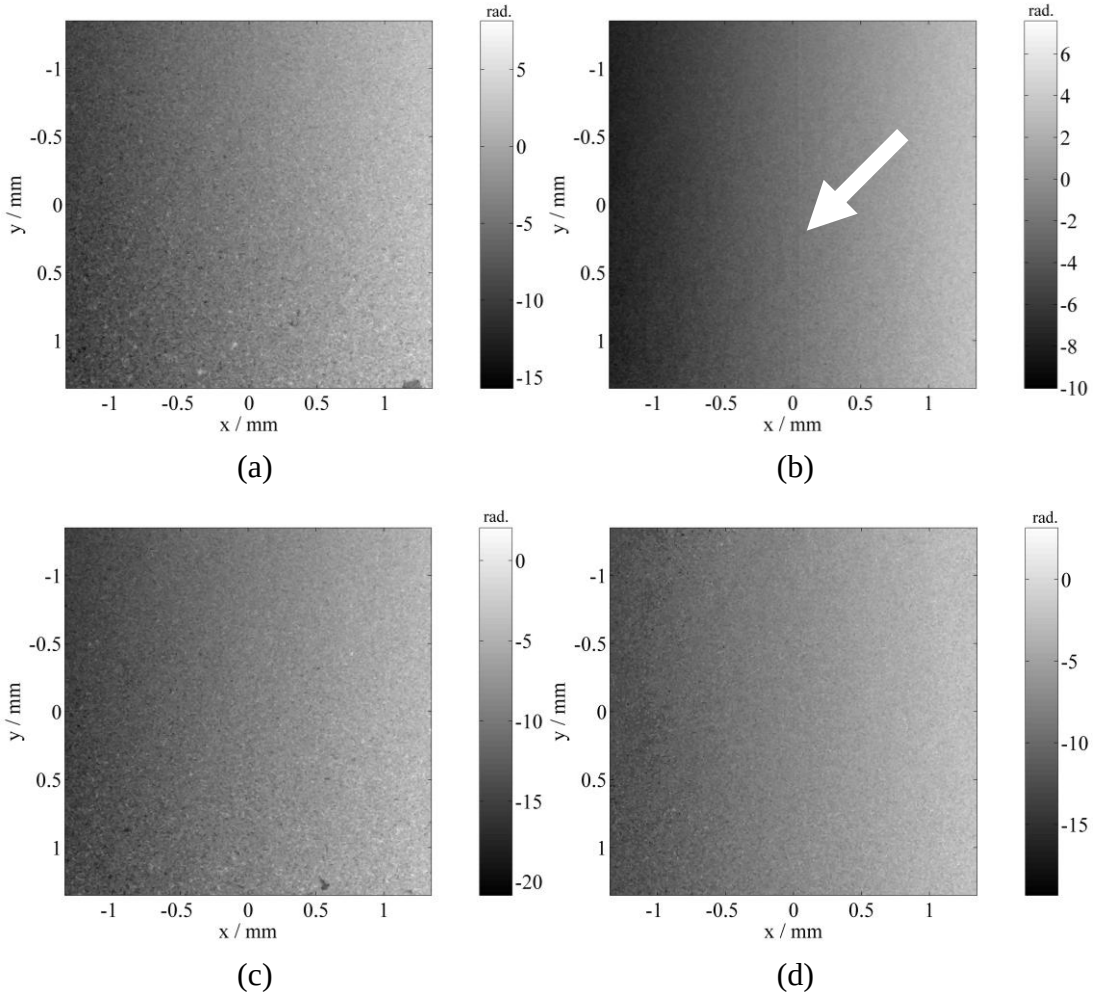

Figure 8.16: Unwrapped phase difference maps, $\Delta\phi(x, y)$, obtained for (a) groove-free aged *urushi* film; (b) aged *urushi* film with a 'v' groove (vertical line indicated by arrow); (c) non-aged cured *urushi* film on top of an aged film with a groove (consolidated crack) and (d) aged *urushi* film on top of an aged film with a groove (aged consolidated crack).

No anomaly is observed in any of the other cases where groove-free or consolidated films are studied. This seems to indicate that, if there is still a distortion in the surface displacement field above the consolidated groove, then its amplitude falls below the phase noise floor of the current setup and thus it is non detectable. The strain field seems to propagate undistorted from the film/substrate interface to the film surface.

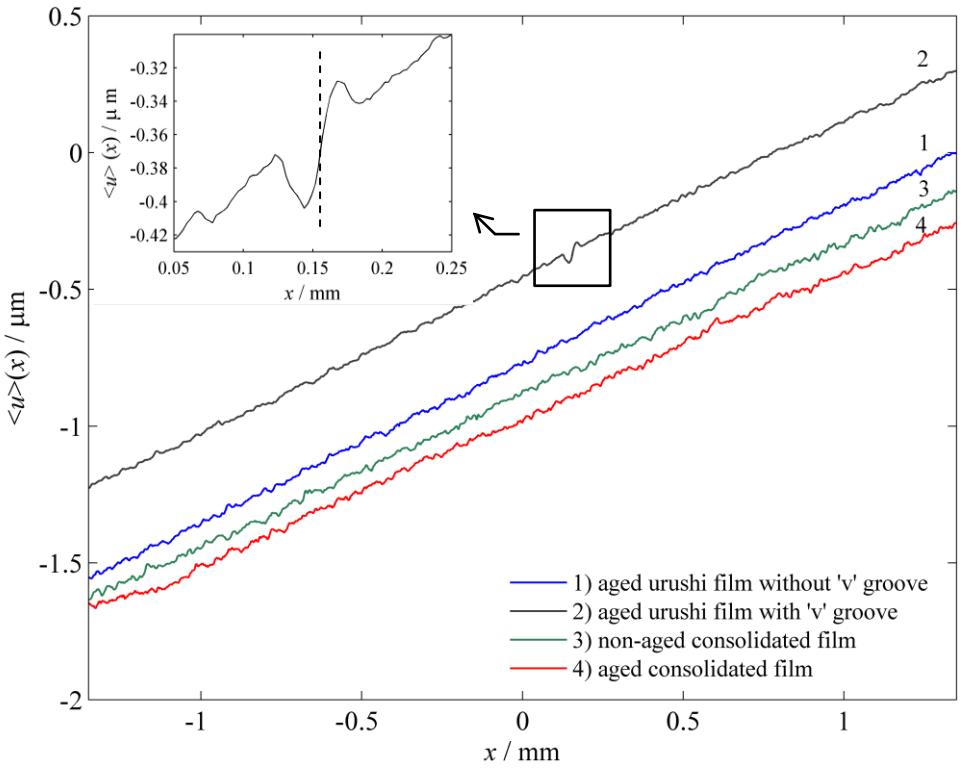

Figure 8.17: Average horizontal displacements $< u_i > (x)$, i=1,...4 measured across the groove for: (1) groove-free aged *urushi* film; (2) aged *urushi* film with a 'v' groove; (3) non-aged cured *urushi* film on top of an aged film with a groove (consolidated crack) and (4) aged *urushi* film on top of an aged film with a groove (aged consolidated crack). The dashed line indicates the position of the groove.

The average longitudinal strains $< \varepsilon_1 >$, $< \varepsilon_3 >$ and $< \varepsilon_4 >$, measured as the overall slope in the displacements profiles $< u_1 > (x)$, $< u_3 > (x)$ and $< u_4 > (x)$ in Figure 8.17, are presented in Table 8.1 for a deflection at midspan of 80 µm and different film conditions. The displacement profile root mean square (*rms*) errors are also tabulated, and indicate the noise level in the displacement measurements. The *rms* error increases with the level of ageing, which is consistent with the fact that aged *urushi* produces higher speckle phase fluctuations due to greater surface roughness.

Table 8.1: Substrate strain as measured with a strain gauge (second column); film average strain (third column); and film strain *rms* error (fourth column), at different stages in the experiment for a deflection at midspan of 80 μm.

Film	$< \varepsilon_{st.gauge} >$ (%)	$< \varepsilon >$ (%)	*rms* (μm)
aged *urushi* film without groove	0.051	0.058	0.008
non-aged consolidated *urushi*	0.054	0.055	0.01
aged consolidated *urushi*	0.055	0.053	0.012

Figure 8.18 shows the average displacement profiles around the groove for different levels of substrate strain. The amplitude of the displacement anomaly increases with substrate strain. The case for ε =0.047% corresponds to the one shown in Figure 8.17. In Figure 8.18, the displacement at the centre of the groove was subtracted to all the respective profiles, as this constant value is irrelevant in terms of strain evaluation. For this reason the curves cross each other at a zero displacement value.

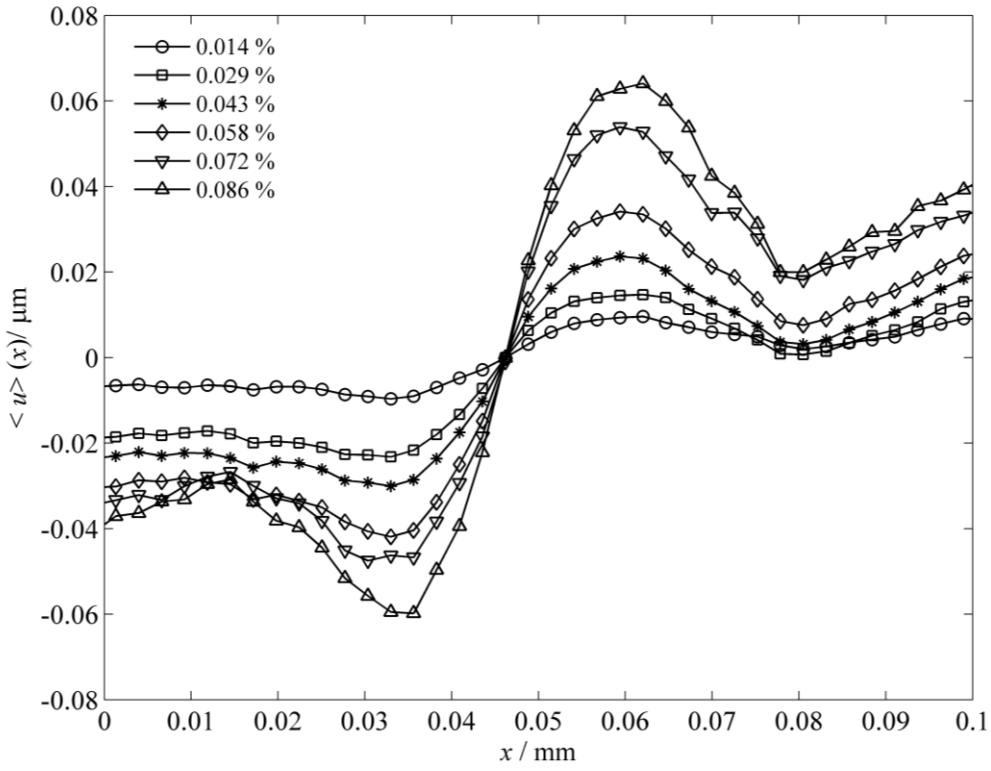

Figure 8.18: Average displacement profile around the 'v' groove for different levels of substrate strain.

The slope of the displacement profiles at the crossing point (around x=0.045 mm) depends on both the longitudinal strain and the shear strain in the film, as measurements of the displacement field in the groove region correspond to different depths into the film. This slope was evaluated by local least squares fitting of a straight line to the data, using a gauge length L =13 μm which corresponds to 5 samples/pixels. A comparison between the peak strain in aged *urushi* film with and without a 'v' groove is shown in Figure 8.19, as a function of substrate strain. A significant increase in the film strain, of nearly one order of magnitude, is observed on aged *urushi* with a 'v' groove as compared with the groove-free case.

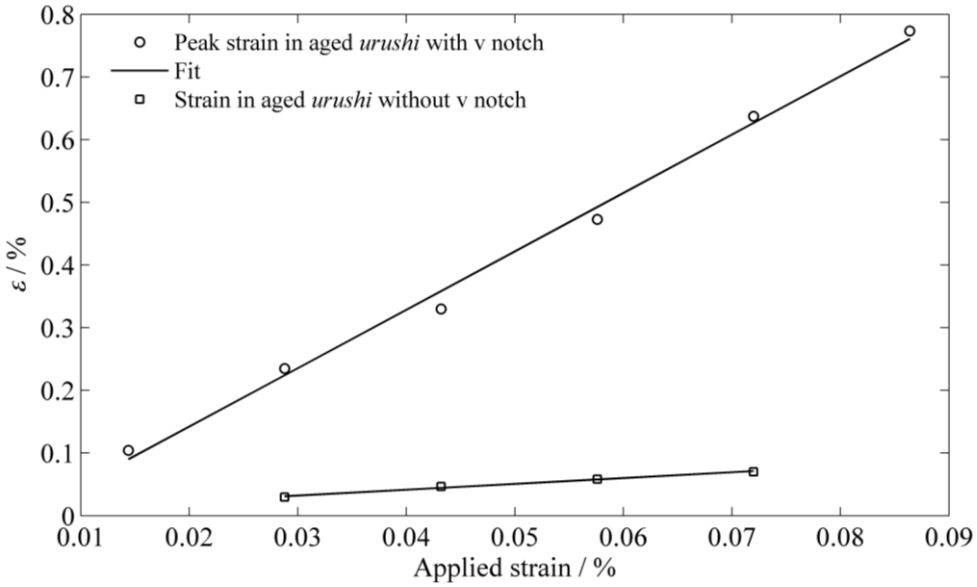

Figure 8.19: Peak strain measured in aged *urushi* versus applied substrate strain for films with and without a 'v' groove.

8.7 Conclusion

The sequence of events during film cracking is more or less as follows [127]: 1) tensile stress develops on the film due to substrate strain or film shrinkage; 2) as the tensile stress exceeds the strength of the film, it fractures; 3) the film stress is relaxed around the crack and perpendicular to it, and as a result the film deforms and retreats on both sides of the crack (the crack opens); 4) due to stress relaxation, the level of stress in the film decreases near the crack; 5) a material element which before the crack was under uniaxial stress, is after crack opening under shear stress, as there is a differential stress between the surface of the film and the film/substrate interface. As a consequence, a

bending moment appears which tends to peel off the film around the crack. In the words of Eric Paquette [127], a shearing force is introduced at the interface between the film and the substrate, pulling the film away from its original position; 6) finally, this leads to a loss of adhesion and in the worst case scenario, to film loss.

It is unknown whether the *urushi-gatame* consolidation procedure is effective in arresting crack propagation in aged *urushi* in the long term or whether it would accelerate damage mechanisms leading to propagation of pre-existing micro-cracks.

In this feasibility study, phase shifting DSPI was used for measuring in-plane displacements across a groove resembling a crack in aged *urushi* films before and after traditional Japanese consolidation. It was found that the displacement field presents an anomaly around the groove before consolidation, which indicates high levels of localized strain. This anomaly disappears below the sensitivity phase noise floor of the technique after the consolidation procedure and even after further ageing, which suggests a significant reduction in the level of localized in-plane strain.

It is worth noting here that in order to detect the small displacement anomaly we had to average along columns parallel to the groove, as indicated in point 1(g), Section 8.5. With the current method it is therefore not possible to measure strain fields around such small cracks as they propagate ‘on the plane’ of the film. This is the main reason for our second assumption in the Introduction of this Chapter and for our choice of a long groove.

Expansion and shrinkage of the wooden structural substrate of *urushi* due to RH and temperature changes is one of the main loading mechanisms that lead to deterioration and fracture of the *urushi* coating in the Mazarin chest. The experiment proposed in this Chapter isolated the effect of substrate strain from temperature and moisture induced stresses. It seems plausible that the same technique could be used on the Mazarin Chest or other art pieces to detect anomalies in the displacement field around treated cracks. The information retrieved, i.e. the in-plane displacements on the film surface, is however insufficient to estimate stress intensity factors through the thickness of the film, as displacements around the crack tip through the film cross section would be required for that.

As the fresh *urushi* crack filling is slightly more compliant than the aged underlying film ($E_{non\text{-}aged}$ = 1.9 GPa; E_{aged}= 2.13 GPa), it could be expected that a displacement anomaly should still be present, even though it would be of a much lesser amplitude than a non-treated crack.

We are currently developing an FEA model of the consolidation procedure, studying the displacement field under the same loading conditions as in the experiment described in this Chapter. It would be interesting to evaluate the response of the consolidated film to changes in relative humidity and temperature in terms of displacements across the groove and to check the FEA predictions with experimental measurements. One could imagine that displacement anomalies may arise due to differential water absorption and stiffness between the non-aged consolidating film and the cracked aged *urushi*. If the non-aged material expanded more than the aged underlying film, this could lead to stress concentration that would tend to open the cracks, promoting crack growth.

Chapter 9
Discussion

Lacquers generally serve two functions. They can be used as a means of protecting an object, attempting to insulate it from the effects of the environment or as a medium for decoration. In some objects, of course, the lacquer may serve both purposes and an exquisite example of this is the use of natural lacquers, also known as *urushi* in Japan, that have been used on Asian artefacts for centuries. A substantial collection of these artefacts held at the Victoria and Albert Museum (V&A) in London. Among the Asian artefacts objects, V&A has around 2,500 pieces of the Japanese lacquerware artefacts. They are classified as the most important collections outside Japan, dated from the Edo period (1615-1868).

A highlight from the collection of Japanese art at V&A is the Mazarin Chest, the most significant and valuable artefact of Japanese lacquerware in the world to have survived from the late 1630's. It was made in Kyoto in the European style and measures 59 cm high, 101.5 cm wide and 63.9 cm deep and adorned with pictorial scenes from

Japanese literature. Nearly every available space is filled with detailed intricate patterns, often human figures, and narrative imagery. Moreover, it is decorated with a wide range of traditional Japanese lacquer techniques such as *makie* (sprinkled picture), in which gold or silver powder and flakes are sprinkled over successive layers of *urushi* before it dries. These make the Mazarin Chest a very important artefact in cultural heritage and it is considered as a national treasure. This makes the research on the Mazarin Chest of great interest.

Unfortunately, however, environmental conditions and previous western restorations have taken their toll on the Mazarin Chest and conservators were faced with a number of questions regarding its repair. In the years since its manufacture, its condition has deteriorated as a result of storage and displaying in fluctuating environmental conditions, e.g. changing relative humidity, temperature and lighting. This deterioration including splits in the wood substrate, lifting gold and silver foil decoration, lifting mother-of-pearl decoration and degradation of the lacquer surface. Degradation of the lacquer surface resulted in discoloration and fading of the originally glossy lacquer surface as a result of the formation of micro-cracks on the surface. Therefore, the V&A, the Toshiba Foundation and the Getty Foundation have initiated a project, The Mazarin Chest project, to consider the most appropriate methodologies for conserving the Mazarin Chest and other similar objects. It was a major collaborative undertaking involving conservators, curator, scientists and engineering from the UK, Japan, Germany and Poland.

The traditional Japanese consolidation process (*urushi gatame*) used for conservation of natural lacquer objects is to apply another layer of diluted *urushi* to the damaged surface, in order to fill any micro-cracks on the lacquer surface. Unfortunately, although tradition holds that this is generally a successful route, conservators do not know for sure whether this is the most effective method, or indeed, whether such a choice can lead to a negative long term impact.

In order to be able to answer questions regarding the efficacy of conservation methods, we must first understand that the lacquer is a complex composite system that is affected by not only the environmental conditions, but by how it interacts with the object itself. The logical approach was firstly establishing the properties and response

of *urushi* in isolation, before then proceeding to consider the interaction between various components of the system as a whole: environment, lacquer layers and object.

To achieve this, we firstly developed a sample preparation procedure to produce consistent *urushi* samples. Our procedure involved different stages and using different techniques, in which we first started with an *urushi* filtration process using the traditional Japanese technique for this. The purified *urushi* were then mixed and cast onto a thin glass substrate using spin coater. Finally, the samples were kept in a curing chamber at 75% RH. The sample preparation procedure we developed enabled us to produce *urushi* films of different geometry and known thickness to be used in different stages of the experimental programme.

In this work, the dependence of film stress on environmental conditions and for aged and non-aged films was investigated. We presented a methodology to achieve this and started by measuring the film stress as a function of changes in relative humidity using the curvature method. The curvature method is the most popular technique for measuring thin film stress. It is based on measurements of the deflection of the substrate on which the film is deposited. Phase shifting interferometry (PSI), a well known powerful full-field optical technique for non-contact measurements of sub-micrometer deformations, was used to measure small deflections in a substrate coated with *urushi* thin films. The experimental deflection distribution was then fitted by a second order surface to quantify the quadratic coefficients, which reflect the curvature characteristics of the substrate, and convert it to polar coordinates. After representing the deflection distribution in polar coordinates, we were able to determine the deflection along two normal directions. Finally, the stresses along these directions were determined by using Atkinson's formula. The benefits of using this formula are that the stress measurements depend only on the dimensions of the film and the substrate and the elastic properties of the substrate. In this work, we compared the stress response in UV aged *urushi* films to that developed in non-aged *urushi* films when they subjected to 30%, 36% and 42% RH and when they subjected to 60%, 54% and 48% RH. The results showed a strong effect of the moisture contents on the stress response of non-aged and aged *urushi* films.

Gravimetric experiments were carried out to characterise the water diffusion process in non-aged and aged *urushi* films when they were subjected to step changes in RH. The experimental data were then fitted with the solution of the diffusion equation to extract the diffusion coefficient for *urushi* films, as a function of the moisture content and UV ageing. The knowledge of the response of *urushi* and the moisture contents were required for the development of a 1D model that capable of characterising and predicting *urushi* behaviour. It involved the employment of a three-element viscoelastic material model to describe the stress relaxation over time in *urushi* films. The model contains only three parameters where the hygroscopic expansion incorporates into these parameters. Moreover, the model has been extended to predict the stress response as a function of depth in non-aged *urushi* layer on the top of aged layer.

In order to fully characterise the rheological behaviour of *urushi* and its mechanical properties, a uniaxial tensile stress-strain and creep recovery tests were conducted for non-aged and aged *urushi* films. The tensile stress-strain tests were conducted under three different humidity levels (30%, 50% and 75% RH) and under each RH the samples were tested at three different stain rates (1.3×10^{-6} s^{-1}, 1.3×10^{-5} s^{-1} and 1.3×10^{-4} s^{-1}). The dependence of the elastic modulus, the tensile strength and the elongation at break, on the moisture contents and ageing were determined from the tensile stress-strain tests. In addition, the influence of the strain rates on the mechanical and the rheological behaviour of *urushi* were studied.

In order to achieve better understanding of the influence of relative humidity and UV ageing on viscoelastic behaviour of *urushi* materials, creep and recovery tests were carried out under three humidity levels (30%, 50% and 75% RH) where four different constant values of stress were used under each relative humidity. The experimental creep curves were employed to draw the isochronous creep curves for *urushi* samples and to calculate Burger's model parameters. The recovery behaviour was used to determine the amount of elastic recovery and its dependence on the RH and ageing for *urushi* films.

In order to assess the effectiveness of the traditional Japanese consolidation process (*urushi gatame*), we proposed a laboratory experimental scenario for simulating the

deterioration and consolidation stages as working on the real object, Mazarin Chest, is not possible. The proposed experiment involved applying a thin film of *urushi* onto aluminium substrate, ageing the film, cracking the film, consolidating the aged film using non aged *urushi* and finally ageing the both aged film and the consolidated film. Our sample preparation procedure was followed to produce 40 mm × 5 mm × 60 µm *urushi* films on 70 mm × 15 mm × 3 mm rectangular aluminium substrates. To simulate the ageing stage, the samples were exposed to UV radiation (340 nm) for 400 hrs and 0.7 $W.m^{-2}$ in a Q-Sun environmental test chamber. Micro-cracks simulation stage was achieved by creating a 'v' groove, 60 µm wide, across the *urushi* films using a sharp blade. *Urushi gatame* process was followed by applying a diluted layer of non-aged *urushi* on the 'v' groove to fill it and repeat the ageing treatment after curing the consolidated layer. The sample was mechanically loaded to simulate the environmental loading using three point bending device and the *urushi* surface displacement profile was measured during all the experimental stages.

The high displacement sensitivity, non-contact nature and high resolution make phase shifting digital speckle pattern Interferometry (DSPI) the best method to measure in-plane *urushi* surface displacement fields. The basic concepts of the speckle effect and the fundamental principles of DSPI were presented. The span of the displacement measurements covers construction and alignment of the interferometer, construction of three point bending device, construction and validation of the positioning stage with a PZT and gratings holder, phase shifting calibration and phase stepping/imaging synchronisation. Anomaly displacement profiles around the groove were obtained, but these anomaly profiles disappeared after consolidate the groove with non-aged and aged *urushi* layers.

Chapter 10
Recommendations for Future Works

Phase shifting interferometry technique constructed and developed in this work has been aimed at developing a feasible technique that is able to measure stresses in thin films under controllable environmental conditions (RH and temperature). The construction and validation of this technique not only made the experiments described in this thesis possible, but also provides a platform for work in the future. The stress measurements were carried out when cured transparent *urushi* thin films, aged and non-aged, exposed to three low and three high RHs where the temperature was kept constant. More stress experiments are needed to investigate the response of cured *urushi* films to changes in temperatures under constant RH and a combination of RH and temperature changes. This will result in a clear view about the stress developed in *urushi* as a result of RH and/or temperature changes.

It is known that stresses can develop within coating during film formation and curing (drying process) through temperature and RH changes. These internal stresses have an effect on coating degradation. They affect adhesion and/or cohesion and have effect on

delamination and cracking. These reasons make the measurements of internal stress during curing important where a correlation between the stress developed after curing and stress developed during curing can be established.

The stress measurements were carried out for fully cured *urushi* samples of single thickness value (~20 µm). The natural extension of this is to study the dependence of the stress on thickness of *urushi* films as it is a key parameter for the stress calculation.

In this work, we investigated the response of *urushi* in isolation but the response of a complete system, *urushi* and object, is in need in future work. This can be established by measuring the influence of changes in the environmental conditions on the response of a wooden substrate, similar to that used in the Mazarin Chest, covered with *urushi*.

The glass transition temperature (Tg) is a critical physical property which can dramatically influence the material chemical stability and its viscoelastic properties. As water acts as a plasticizer for *urushi*, further work is required to investigate the influence of the moisture content on the Tg of *urushi* and to correlate the Tg and the mechanical properties of *urushi*. Also, a set of spectroscopic investigations (FTIR) is required to evaluate the influence of the moisture contents and ageing on the chemical structure of *urushi* material.

Finally and as the lacquerware objects are covered with multiple layers of coloured *urushi*, the previous recommendations for future works can be repeated for multiple layers and coloured non-aged and aged *urushi* films.

In Chapter 8, the consolidation technique was assessed by measuring and comparing the displacement around a ‘v’ notch before and after consolidation. In this Chapter, aluminium substrate was covered with thin film of *urushi* and the substrate was mechanically loaded using three points bending device. Further FEA modelling of the consolidation procedure under the same loading conditions, as in the experiment described in this Chapter, is required. The work presented in this Chapter can be extended to evaluate the response of the consolidated film covered a wooden substrate under environmental loading (RH and temperature). It would be of interest to plan a set of experimental work to investigate the influence of the moisture content on the crack propagation through a multiple layers system of *urushi* covering a wood substrate.

Based on the results presented in this work, further modelling techniques need to be employed to predict long-term stress response as a function of changes in environmental conditions and long-term UV accelerated ageing treatments in order to simulate the circumstances in which lacquerwares artefacts are exposed to. In addition to stress response modelling, more extensive creep-recovery modelling is required to deepen the understanding of the effects of the environmental conditions and UV ageing on the viscoelastic behaviour of *urushi* during the creep-recovery processes.

References

[1] V&A: *The Mazarin Chest Project: History of the Mazarin Chest*. http://www.vam.ac.uk/res_cons/conservation/mazarin_chest/history/index.html: Accessed on 05/2009

[2] V&A: *Conservation of the Mazarin Chest, Further Investigation & Academic Partners*. http://www.vam.ac.uk/res_cons/conservation/mazarin_chest/Conservation/iInvestigation/index.html: Accessed on 05/2009

[3] Lu, R., Kamiya, Y., Wan, Y. Y., Honda, T., and Miyakoshi, T. *Synthesis of Rhus Succedanea Lacquer Film and Analysis by Pyrolysis-Gas Chromatography/Mass Spectrometry*, J. Anal. Appl. Pyrolysis **78** 117-124 (2007).

[4] Taguchi, K., Hirose, S., and Abe, Y. *Photo-Curing Composite Paint Containing Urushi (Oriental Lacquer), and Wrinkled Coating Caused by Phase Separation*, Prog. Org. Coat. **57** 290-295 (2007).

[5] Kumanotani, J. *Urushi (Oriental Lacquer) - a Natural Aesthetic Durable and Future-Promising Coating*, Prog. Org. Coat. **26** 163-195 (1995).

[6] Römich, H., Martin, G., and Lavedrine, B., V&A: *Lightcheck®: A New Tool in Preventive Conservation*. 2004 http://www.vam.ac.uk/res_cons/conservation/journal/number_47/lightcheck/index.html: Accessed on 5/2009

[7] Awazu, K., Yasui, H., Kasamori, M., Ichikawa, T., Funada, Y., and Iwaki, M. *Effect of H-Implantation Energy on the Optical Stability of Implanted Urushi Films under Photo-Irradiation*, Nucl. Instrum. Methods Phys. Res., Sect. B **148** 1121-1125 (1999).

[8] Lu, R. and Yoshida, T. *Structural and Molecular Weight of Asian Lacquer Polysaccharides*, Carbohydr. Polym. **54** 419-424 (2003).

[9] Ogawa, T., Arai, K., and Osawa, S. *Light Stability of Oriental Lacquer Films Irradiated by a Fluorescent Lamp*, J Environ Polym Degradation **6**(1) 59-65 (1998).

[10] Ogawa, T., Inoue, A., and Osawa, S. *Effect of Water on Viscoelastic Properties of Oriental Lacquer Film*, J. Appl. Polym. Sci. **69** 315-321 (1998).

[11] Kumanotani, J. *Enzyme Catalyzed Durable and Authentic Oriental Lacquer: A Natural Microgel-Printable Coating by Polyscaccharide-Glycoprotein-Phenolic Lipid Complexes*, Prog. Org. Coat. **34** 135-146 (1998).

[12] Agostinelli, E., Cervoni, L., Iartosio, A., and Morpurgot, L. *Stability of Japanese-Lacquer-Tree (Rhus Vernicifera) Laccase to Thermal and Chemical Denaturation: Comparison with Ascorbate Oxidase*, Open Biochem. J. **306** 697-702 (1995).

[13] Lu, R., Ishimura, T., Tsutida, K., Honda, T., and Miyakoshi, T. *Development of a Fast Drying Hybrid Lacquer in a Low Relative-Humidity Environment Based on Kurome Lacquer Sap*, J. Appl. Polym. Sci. **98** 105-1061 (2005).

[14] Nagas, K. *An Outline of the Japanese Lacquer*, J. Adhes. Soc. Jpn. **25**(2) 84-89 (1989).

[15] Niimura, N. and Miyakoshi, T. *Structural Study of Oriental Lacquer Films During the Hardening Process* Talanta **70** 146–152 (2006).

[16] Niimura, N., Miyakoshi, T., and Iijima, Y. *Characterization of Synthesized Lacquer Analogue Films by Two Stage Pyrolysis-Gas Chromatography/Mass Spectrometry and X-Ray Photoelectron Spectroscopy*, Anal. Sci. **17** 155-158 (2001).

[17] Kim, H. K., Park, M. Y., Yu, J. A., and Hong, J. W. *Surface and Curing Properties of Oriental Lacqur Modified by Acryl Monomer*, J. Ind. Eng. Chem. **12**(4) 444-448 (2001).

[18] Lu, R., Wan, Y. Y., Honda, T., Ishimura, T., Kamiya, Y., and Miyakoshi, T. *Design and Characterization of Modified Urethane Lacquer Coating* Prog. Org. Coat. **57** 215-222 (2006).

[19] Niimura, N. and Miyakoshi, T. *Characterization of Natural Resin Films and Identification of Ancient Coating*, J. Mass Spectrom. Soc. Jpn. **51**(4) 439-457 (2003).

[20] Obataya, E., Furuta, Y., Ohno, Y., Norimoto, M., and Tomita, B. *Effect of Aging and Moisture on the Dynamic Viscoelastic Properties of Oriental lacquer (Urushi) Film*, J. Appl. Polym. Sci. **83** 2288-2294 (2002).

[21] Vogl, O. *Oriental Lacquer, Poison Lvy, and Drying Oils*, J. Polym. Sci., Part A: Polym. Chem. **38** 4327-4335 (2000).

[22] Shiihara, I. *Studies on Confirming the Type of Dried Urushi Film and Its Formation Mechanism (Urushi Hardening Study Report Ii)*, Bulletin of the Chemical Society of JapanBull **75** 2061–2066 (2002).

[23] Bishop Museum, Art Conservation Handout: *Lacquer*. 1996 http://www.bishopmuseum.org/research/pdf/cnsv-lacquer.pdf: Accessed on 5/2009

[24] Webb, M. *Methods and Materials for Filling Losses on Lacquer Objects*, JAIC **37**(1) 117-133 (1998).

[25] Hong, J. W., Park, M. Y., Kim, H. K., and Choi, J. O. *Uv-Degradation Chemistry of Oriental Lacquer Coating Containing Hindered Amine Light Stabilizer*, Bull. Korean Chem. Soc. **21**(1) 61-64 (2000).

[26] Rivers, S. 2003 *On the Conservation of the Mazarin Chest*. In *27th International Symposium on the Conservation and Restoration of Cultural Property*, Tokyo National Research Institute for Cultural Property/Tokyo National Museum, Japan: 150-158.

[27] V&A: *History of the Mazarin Chest: Design Elements on the Mazarin Chest*. http://www.vam.ac.uk/res_cons/conservation/mazarin_chest/history/design_elements/index.html: Accessed on 05/2009

[28] Lu, R., Harigaya, S., Ishimura, H., Nagas, K., and Miyakoshi, T. *Development of a Fast Drying Lacquer Based on Raw Lacquer Sap*, Prog. Org. Coat. **51** 238-243 (2004).

[29] Toyoshima, K. *Study of Deterioration of Urushi Film with Ultraviolet Radiation*, Material Life Society **8**(1) 28-35 (1996).

[30] Yamashita, Y., '*On the Plan for the Conservation of the Mazarin Chest: The Role of Urushi in International Exchange*', Tokyo National Museum Report on the Restoration of Cultural Properties V 2004, Tokyo National Museum, Tokyo, 2005.

[31] Clyne, T. W. and Gill, S. C. *Residual Stresses in Thermal Spray Coatings and Their Effect on Interfacial Adhesion: A Review of Recent Work*, J. Therm. Spray Technol. **5** 1-18 (1996).

[32] Ogawa, T., Hamada, Y., and Kamel, T. *Analysis on Bonding Strength of Coated Film on Steel Ball*, J. Adhes. Soc. Jpn. **30** 536-541 (1994).

[33] Ogawa, T. and Kamel, T. *Fracture of Oriental Lacquer Film on the Ware with Water Absorption or Desorption*, J. Adhes. Soc. Jpn. **31** 347-353 (1995).

[34] Tsui, Y. C. and Clyne, T. W. *An Analytical Model for Predicting Residual Stresses in Progressively Deposited Coating - Part 1: Planar Geometry*, THIN SOLID FILMS **306** 23-33 (1997).

[35] Chou, K. S., Huang, K. C., and Lee, H. H. *Fabrication and Sintering Effect on the Morphologies and Conductivity of Nano-Ag Particle Films by the Spin Coating Method*, Nanotechnology **16** 779–784 (2005).

[36] Du, X. M., Origna, X., and Almeida, R. M. *Striation-Free, Spin-Coated Sol-Gel Optical Films*, J. Am. Ceram. Soc. **78**(8) (1995).

[37] Hwang, K. S. and Kim, B. H. *Preparation of Highly Oriented Lanio3 Thin Films by Spin-Coating Technique*, J. Sol-Gel Sci. Technol. **14** 203-207 (1999).

[38] Kontturi, E., Thüne, P. C., and Niemantsverdriet, J. W. *Novel Method for Preparing Cellulose Model Surfaces by Spin Coating*, Polymer Communications **44** 3621–3625 (2003).

[39] Natsume, Y. and Sakata, H. *Zinc Oxide Films Prepared by Sol-Gel Spin-Coating*, THIN SOLID FILMS **372** 30-36 (2000).

[40] Pethrick, R. A. and Rankin, K. E. *Criteria for Uniform Thin Film Formation for Polymeric Materials*, J. Mater. Sci. - Mater. Electron. **10** 141-144 (1999).

[41] Sathaye, S. D., Patil, K. R., Kulkarni, S. D., Bakre, P. P., Pradhan, S. D., Sarwade, B. D., and Shintre, S. N. *Modification of Spin Coating Method and Its Application to Grow Thin Films of Cobalt Ferrite*, J. Mater. Sci. - Mater. Electron. **38** 29-33 (2003).

[42] Kenjo, T. *Studies on Films of Japanese Lacquer. Iii. The Change in Infra Red Spectra of Japanese Lacquer Films in the Course of Their Hardening and Deterioration, and Discussion on Conservation of Japanese Lacquered Art Objects.*, J. Jpn. Soc. Color Material **46** 420-428 (1973).

[43] Kenjyo, T. and Toishi, K. *Deterioration of Coated Film of Japanese Lacquer*, J. Jpn. Soc. Color Material **40** 92-102 (1967).

[44] Francis, L. F., McCormick, A. V., Vaessen, D. M., and Payne, J. A. *Development and Measurement of Stress in Polymer Coatings*, J. Mater. Sci. **37** 4717-4731 (2002).

[45] Withers, P. J. and Bhadeshia, H. K. D. H. *Residual Stress. Part 1-Measurement Techniques*, Mater. Sci. Technol. **17** 355-365 (2001).

[46] Kandil, F. A., Lord, J. D., Fry, A. T., and Grant, P. V., '*A Review of Residual Stress Measurement Methods -a Guide to Technique Selection*', (A)04, National Physical Laboratory Report MATC, Teddington, UK, 2001.

[47] Lu, J. *Handbook of Measurement of Residual Stresses*, 1st edn, pp. 71-149. Lilburn The Fairmont Press, Inc, 1996.

[48] Cabié, M., Ponchet, A., Rocher, A., Paillard, V., and Vincent, L. *Transmission Electron Microscopy and Raman Measurements of the Misfit Stress in a Si Tensile Strained Layer*, Appl. Phys. Lett. **84**(6) 870-872 (2004).

[49] Kim, J. G. and Yu, J. *A Study on the Residual Stress Measurement Methods on Chemical Vapour Deposition Diamond Films*, J. Mater. Res. **13**(11) 3027-3033 (1998).

[50] Chen, J. and Wolf, I. D. *Study of Damage and Stress Induced by Backgrinding in Si Wafers*, Semicond. Sci. Technol. **18** 261-268 (2003).

[51] Klein, C. A. *How Accurate Are Stoney's Equation and Recent Modifications*, J. Appl. Phys. **88**(9) 5487-5489 (2000).

[52] Matejicek, J. and Sampath, S. *In Situ Measurement of Residual Stresses and Elastic Moduli in Thermal Sprayed Coatings: Part 1: Apparatus and Analysis*, Acta Mater. **51** 863-872 (2003).

[53] Schafer, J. D., Nafe, H., and Aldinger, F. *Macro-and Microstress Analysis in Sol-Gel Derived* $Pb(Zr_xTi_{1-X})O3$, J. Appl. Phys. **85**(12) 8023-8031 (1999).

[54] Chen, K. S., Chen, T. Y. F., Chuang, C. C., and Lin, I. K. *Full-Field Wafer Level Thin Film Stress Measurement by Phase-Stepping Shadow Moire*, IEEE Trans. Compon. Packag. Technol. (2004).

[55] Dorrio, B. V. and Fernández, J. L. *Phase-Evaluation Methods in Whole-Field Optical Measurement Techniques*, Meas. Sci. Technol. **10** R33–R55 (1999).

[56] Ovryn, B. and Andrews, J. H. *Measurement of Changes in Optical Path Length and Reflectivity with Phase-Shifting Laser Feedback Interferometry*, Appl. Opt. **38**(10) (1999).

[57] Patill, A., Langoju, R., and Rastogi, P. *Phase Shifting Interferometry Using a Robust Parameter Estimation Method*, Opt. Lasers Eng. **47** (2007).

[58] Patill, A. and Rastogi, P. *Approaches in Generalized Phase Shifting Interferometry*, Opt. Lasers Eng. **43** 475–490 (2005).

[59] Tien, C. L., Lee, C. C., and Jaing, C. C. *The Measurement of Thin Film Stress Using Phase Shifting Interferometry*, J. Mod. Opt. **47**(5) 839-849 (2000).

[60] Freund, L. B. *Substrate Curvature Due to Thin Film Mismatch Strain in the Nonlinear Deformation Range*, J. Mech. Phys. Solids **48** 1159-1174 (2000).

[61] Gunnars, J. and Wiklund, U. *Determination of Growth-Induced Strain and Thermo-Elastic Properties of Coatings by Curvature Measurements*, Mater. Sci. Eng., A **A336** 7-21 (2002).

[62] Zhang, Y. and Zhao, Y. P. *Applicability Range of Stoney's Formula and Modified Formulas for a Film/Substrate Bilayer*, J. Appl. Phys. **99** 1-7 (2006).

[63] Chen, K. S. and Ou, K. S. *Modification of Curvature-Based Thin-Film Residual Stress Measurement for MEMS Applications*, J. Micromech. Microeng. **12** 917-924 (2002).

[64] Huang, S. and Zhang, X. *Extension of the Stoney Formula for Film-Substrate Systems with Gradient Stress for MEMS Applications*, J. Micromech. Microeng. **16** 382-398 (2006).

[65] Huang, Y. and Rosakis, A. J. *Extension of Stoney's Formula to Non-Uniform Temperature Distributions in Thin Film/Substrate Systems. The Case of Radial Symmetry*, J. Mech. Phys. Solids **53** 2483–2500 (2005).

[66] Stoney, G. G. *The Tension of Metallic Films Deposited by Electrolysis*, Proc. R. Soc. London, Ser. A **82** 172-175 (1909).

[67] Cheng, Y. Y. and Wyant, J. C. *Phase Shifter Calibration in Phase-Shifting Interferometry*, Appl. Opt. **24**(18) 3049-3052 (1985).

[68] Huntley, J. M. 2001 Automated Analysis of Speckle Interferograms. In *Digital Speckle Pattern Interferometry and Related Techniques* (ed. P. K. Rastogi), pp. 59-139. Chichester: John Wiley & Sons Ltd.

[69] Wei, C., Chen, M., and Wang, Z. *General Phase-Stepping Algorithm with Automatic Calibration of Phase Steps*, Opt. Eng. **38**(8) 1357–1360 (1999).

[70] Huntley, J. M. *Noise-Immune Phase Unwrapping Algorithm* Appl. Opt. **28**(15) 3268-3270 (1989).

[71] Judge, T. R., Bryanston-Cross, P. J., and Bryanston-Cross, P. J. *A Review of Phase Unwrapping Techniques in Fringe Analysis*, Opt. Lasers Eng. **21** 199-239 (1994).

[72] Kerr, D., Kaufmann, G. H., and Galizzi, G. E. *Unwrapping of Interferometric Phase-Fringe Maps by the Discrete Cosine Transform*, Appl. Opt. **35**(5) 810-816 (1996).

[73] Ochoa, A. and Huntley, J. M. *Convenient Method for Calibrating Nonlinear Phase Modulators for Use in Phase-Shifting Interferometry*, Opt. Eng. **37**(9) 2501-2505 (1998).

[74] Saleem, Q., PhD thesis in *Wolfson School of Mechanical and Manufacturing Engineering, Loughborough University* (Loughborough, 2003).

[75] Ai, C. and Wyant, J. C. *Effect of Piezoelectric Transducer Nonlinearity on Phase Shift Interferometry*, Appl. Opt. **26**(6) 1112-1116 (1987).

[76] Langoju, R., Patil, A., and Rastogi, P. *A Novel Approach for Characterizing the Nonlinear Phase Steps of the Pzt in Interferometry*, Opt. Lasers Eng. **45** 258-264 (2007).

[77] Liu, M., Wu, P., Ding, Y., and Li, S. *Study on Diffusion Behavior of Water in Epoxy Resins Cured by Active Ester*, Phys. Chem. Phys. **5** 1848-1852 (2003).

[78] Nogueira, P., Ramirez, C., Torres, A., Abad, M. J., Cano, J., Lopez, J., Lopez-Bueno, I., and Barral, L. *Effect of Water Sorption on the Structure and Mechanical Properties of an Epoxy Resin System*, J. Appl. Polym. Sci. **80** 71-80 (2001).

[79] Crank, J. *The Mathematics of Diffusion* Oxford University Press, 1975.

[80] LaPlante, G. and Lee-Sullivan, P. *Moisture Effects on FM300 Structural Film Adhesive: Stress Relaxation, Fracture Toughness, and Dynamic Mechanical Analysis*, J. Appl. Polym. Sci. **95** 1285-1294 (2005).

[81] Shewmon, P. *Diffusion in Solids (Minerals, Metals & Materials Society, Pennsylvania,USA)*, 1990.

[82] Shirrell, C. D. *Diffusion of Water Vapor in Graphite/ Epoxy Composites*, Advanced Composite Materials-Environmental Effects, ASTM STP 658, Vinson, J. R., Ed., American Society for Testing and Materials 21-42 (1978).

[83] vanWesting, E. P. M., Ferrari, G. M., and deWrr, H. W. *The Determination of Coating Performance with Impedance Measurements-Ii. Water Uptaken of Coatings*, Corro. Sci. **36**(6) 957-977 (1994).

[84] Abdelkader, A. F. and White, J. R. *Water Absorption in Epoxy Resins: The Effects of the Crosslinking Agent and Curing Temperature*, J. Appl. Polym. Sci. **98** 2544-2549 (2005).

[85] Vanlandingham, M. R., Eduljee, R. F., and Gillespie, J. W. *Moisture Diffusion in Epoxy Systems*, J. Appl. Polym. Sci. **71** 787-798 (1999).

[86] Mouzakis, D. E. and Karger-Kocsis, J. *Effects of Gasoline Absorption on the Tensile Impact Response of Hdpe/Selar^{tm} Microlayer Composites*, J. Appl. Polym. Sci. **68** 561-569 (1998).

[87] Haddad, Y. M. *Viscoelasticity of Engineering Materials* Chapman & Hall, UK, 1995.

[88] Govaert, L., E., de Vries, P., J., Fennis, P., J., Nijenhuis, W., F., and Keustermans, J., P. *Influence of Strain Rate, Temperature and Humidity on the Tensile Yield Behaviour of Aliphatic Polyketone*, Polymer Communications **41** 1959–1962 (2000).

[89] He, S., Van Houtte, P., Van Bael, A., Mei, F., Sarban, A., and Boesman, P. *Strain Rate Effect in High-Speed Wire Drawing Process*, Modell. Simul. Mater. Sci. Eng. **10** 267–276 (2002).

[90] Krupĭcka, A., Johansson, M., Wänstrand, O., and Hult, A. *Mechanical Response of Ductile Polymer Coatings to Contact and Tensile Deformation*, Prog. Org. Coat. **48** 1–13 (2003).

[91] Mae, H., Omiya, M., and Kishimoto, K. *Effects of Strain Rate and Density on Tensile Behavior of Polypropylene Syntactic Foam with Polymer Microballoons*, Mater. Sci. Eng., A **477** 168-178 (2008).

[92] Abd-El Salam, F., Abd-El Salam, M., H., Mostafa, M., T., Nagy, M., R., and Mohamed, M., I. *Effect of Vulcanizing System on the Mechanical Properties of Butyl Rubber/Ethylene Propylene Diene Monomer-Carbon Black Blends*, J. Appl. Polym. Sci. **90** 1539-1544 (2002).

[93] Bae, J.-S., Oh, C.-S., Nam, J.-E., Lee, J.-K., and Lee, H.-J. *A Tensile Test Technique for the Freestanding Pmma Thin Films*, Curr. Appl Phys. **9** S107–S109 (2009).

[94] Farrokh, B. and Khan, A., S. *A Strain Rate Dependent Yield Criterion for Isotropic Polymers: Low to High Rates of Loading*, Eur. J. Mech. A. Solids **29** 274–282 (2010).

[95] Goble, D., L. and Wolff, E., G. *Strain-Rate Sensitivity Index of Thermoplastics*, J. Mater. Sci. **28** 5986-5994 (1993).

[96] Ha-Anh, T. and Vu-Khanh, T. *Prediction of Mechanical Properties of Polychloroprene During Thermo-Oxidative Aging*, Polym. Test. **24** 775-780 (2005).

[97] Larena, A., Jiménez de Ochoa, S., and Domínguez, F. *Dynamic-Mechanical Analysis of the Photo-Degradation of Long Glass Fibre Reinforced Polypropylene: Mechanical Properties' Changes*, Polym. Degrad. Stab. **91** 940-946 (2006).

[98] Qian, Z., Wang, J., Yang, J., and Liu, S. *Visco-Elastic-Plastic Properties and Constitutive Modeling of Underfills*, IEEE Trans. Compon. Packag. Technol. **22**(2) 152-157 (1999).

[99] Abd-El Salam, M., H. *Stress-Strain and Creep Characteristics of Haf Black-Loaded Nbr/Epdm Rubber Blends*, Egypt. J. Solids **30**(2) 175-187 (2007).

[100] Betten, J. *Creep Mechanics*, 2nd edn Springer, New York, 2005.

[101] Dolz, M., Hernández, M., J., and Delegido, J. *Creep and Recovery Experimental Investigation of Low Oil Content Food Emulsions*, Food Hydrocolloids **22** 421–427 (2008).

[102] Lafferty, S., V., Newton, J., M., and Podczeck, F. *Characterisation of the Mechanical Properties of Polymer Films Formed from Aqueous Polymer Dispersions by Creep Testing*, Int. J. Pharm. **239** 143–148 (2002).

[103] Yang, J., Zhang, Z., Schlarb, A., and Friedrich, K. *On the Characterization of Tensile Creep Resistance of Polyamide 66 Nanocomposites. Part I. Experimental Results and General Discussions* Polymer Communications **47** 2791–2801 (2006).

[104] Akinay, A., E. and Brostow, W. *Long-Term Service Performance of Polymeric Materials from Short-Term Tests: Prediction of the Stress Shift Factor from a Minimum of Data*, Polymer Communications **42** 4527-4532 (2001).

[105] Lai, J. and Bakker, A. *Analysis of the Non-Linear Creep of High Density Polyethylene*, Polymer Communications **36** 93-99 (1995).

[106] Nitta, K. and Maeda, H. *Creep Behavior of High Density Polyethylene under a Constant True Stress*, Polym. Test. **29** 60-65 (2010).

[107] Kovač, M., Gaberšček, M., and Pejovnik, S. *Influence of Humidity on Microstructure and Electrical Characteristics of (Peo–Plasticiser) Lial(So Cl) Polymer N 3 4 Electrolytes* Solid State Ionics **131** 323–327 (2000).

[108] Zheng, Y., Priestley, R., D., and Mckenna, G., B. *Physical Aging of an Epoxy Subsequent to Relative Humidity Jumps through the Glass Concentration*, J. Polym. Sci., Part B: Polym. Phys. **42** 2107–2121 (2004).

[109] O'Connel, P., A., Hutcheson, S., A., and MCKenna, G., B. *Creep Behavior of Ultra-Thin Polymer Films*, J. Polym. Sci., Part B: Polym. Phys. **46** 1952–1965 (2008).

[110] Scaffaro, R., Dintcheva, N., T., and La Mantia, F., P. *A New Equipment to Measure the Combined Effects of Humidity, Temperature, Mechanical Stress and U V Exposure on the Creep Behaviour of Polymers*, Polym. Test. **27** 49-54 (2008).

[111] Guo, Y., Xin, C., Song, M., and He, Y. *Study on Short- and Long-Term Creep Behavior of Plastics Geogrid*, Polym. Test. **24** 793–798 (2005).

[112] Majda, P. and Skrodzewicz , J. *A Modified Creep Model of Epoxy Adhesive at Ambient Temperature*, Int. J. Adhes. Adhes. **29** 396-404 (2009).

[113] Adams, R. D. and Harris, J. A. *The Influence of Local Geometry on the Strength of Adhesive Joints*, Int. J. Adhes. Adhes. **7** 69-80 (1987).

[114] McClintock, F. A. *Fracture of Soilids*. New York Wiley, 1963.

[115] Jones, R. and Wykes, C. *Holographic and Speckle Interferometry: A Discussion of the Theory, Practice and Application of the Techniques* Cambridge University Press, 1989.

[116] Leendertz, J. A. *Interferometric Displacement Measurement on Scattering Surfaces Utilizing Speckle Effect*, J. Phys. E: Sci. Instrum. **3** 214-218 (1970).

[117] Arai, Y. *In-Plane Displacement Measurement Using Electronic-Speckle-Pattern-Interferometry-Based on Spatial Fringe Analysis Method*, Opt. Eng. **43** 2168-2174 (2004).

[118] Huntley, J. M. *Automated Fringe Pattern Analysis in Experimental Mechanics: A Review*, J. Strain Anal. Eng. Des. **33** (1998).

[119] Petzing, J., N. and Tyrer, J., R. *Recent Developments and Applications in Electronic Speckle Pattern Interferometry*, J. Strain Anal. Eng. Des. **33** 153-169 (1998).

[120] Sun, P. *Evaluation of Two-Dimensional Displacement Components of Symmetrical Deformation by Phase-Shifting Electronic Speckle Pattern Interferometry*, Appl. Opt. **46** 2859-2862 (2007).

[121] Zhang, J. and Chong Chong, T. *Fiber Electronic Speckle Pattern Interferometry and Its Applications in Residual Stress Measurements*, Appl. Opt. **37** 6707-6715 (1998).

[122] Rastogi, P. K. 2001 Measurement of Static Surface Displacement,Derivatives of Displacements, and Three-Dimensional Surface Shapes-Examples of Applications to Non-Destructive Tesing. In *Digital Speckle Pattern Interferometry and Related Techniques* (ed. P. K. Rastogi), pp. 141-224. John Wiley & Sons Ltd.

[123] Leung, J., '*High Precision Positioning Stage for Optical Metrology*', Wolfson School of Mechanical & Manufacuring Engineering, Loughborough University, Loughborough, 2009.

[124] Creath, K. 1993 Temporal Phase Measurement Methods. In: Interferogram Analysis: Digital Fringe Pattern Measurement Techniques. (ed. D. W. Robinson and G. T. Reid), pp. Philadelphia, PA: Institute of Physics Publishing.

[125] Ruiz, P., D., Jumbo, F., Seaton, A., Huntley, J., M., Ashcroft, I., A., and Swallowe, G., M. *Numerical and Experimental Investigation of Three-Dimensional Strains in Adhesively Bonded Joints*, J. Strain Analysis **41** 583-596 (2006).

[126] Ruiz, P. D., Jumbo, F., Huntley, J. M., Ashcroft, I. A., and Swallowe, G. M. *Experimental and Numerical Investigation of Strain Distributions within the Adhesive Layer in Bonded Joints*, strain 1-17 (2009).

[127] Paquette, E. 2002 *The Simulation of Paint Cracking and Peeling*. In *Proceeding Graphics Interface 2002*, Alberta: 59-68. Canadian Human-Computer Communications Society and A K Peters Ltd.

Appendix A

Parameters in Burger's Model for Non-aged and Aged *Urushi* Films

A1: Parameters in Burger's model for non-aged urushi films.

RH (%)	σ (MPa)	E_1 (MPa)	E_2 (MPa)	η_1 (MPa.s)	η_2 (MPa.s)	η_1^r (MPa.s)
30	14	2368.86	16529.70	1.07E+9	6.55E+7	6.8E+9
	23	2304.60	8960.57	6.69E+8	8.03E+7	7.5E+8
	28	2124.43	6364.21	4.39E+8	3.62E+7	3.9E+8
	32	2226.86	6392.32	2.97E+8	3.43E+7	3.2E+8
50	10.5	2015.35	7659.76	5.67E+8	3.01E+7	7.9E+8
	17.5	2364.86	6598.79	4.88E+8	4.16E+7	4.2E+8
	21	2095.80	5148.06	2.57E+8	3.01E+7	2.5E+8
	24.5	2095.80	3895.07	2.1E+8	2.78E+7	2.0E+8
75	9	1829.26	6761.22	5.81E+8	3.13E+7	1.5E+8
	15	1809.40	3546.77	2.47E+8	2.61E+7	2.1E+8
	18	1574.80	2647.21	1.38E+8	1.97E+7	1.4E+8
	21	1680	4007.63	9.69E+7	1.16E+7	1.4E+8

A2: Parameters in a Burger's model for aged urushi films.

RH (%)	σ (MPa)	E_1 (MPa)	E_2 (MPa)	η_1 (MPa.s)	η_2 (MPa.s)	η_1^r (MPa.s)
30	9	2639.29	12788.3	6.91E+9	8.46E+7	1.7E+10
	14	2310.23	32198.71	7.24E+8	1.9E+8	3.7E+10
	17	2809.91	9941.05	1.38E+9	9.05E+7	7E+8
	20	2600.78	7978.29	4.68E+8	4.49E+7	3.5E+8
50	12	2424.24	13416.81	8.42E+8	4.06E+7	1.8E+9
	20	2125.39	6551.36	5.30E+8	3.68E+7	6E+8
	24	2086.95	5401.51	4.51E+8	3.87E+7	3.8E+8
	28	2259.88	3974.33	2.87E+8	2.87E+7	2.5E+8
75	9	1764.70	6065.34	9.34E+8	3.97E+7	5.3E+8
	14	1563.89	5872.48	5.79E+8	3.01E+7	4.1E+8
	17	1729.39	5463.42	1.95E+8	1.50E+7	2.5E+8
	20	1824.81	2492.52	2.96E+8	2.34E+7	1.8E+8

Appendix B

Publications

Journal and conference papers

Journal papers

1. Stress measurement in East Asian lacquer thin films owing to changes in relative humidity using phase shifting interferometry, *Pro. R. Soc. A,* Published online 24 November 2010.
   doi: 10.1098/rspa.2010.0414.

2. Experimental investigation and Material Modelling of fresh and UV aged Japanese lacquer (*Urushi*), Prog. Org. Coat. (2010).
   doi:10.1016/j.porgcoat.2010.09.020.

Conference papers

1. A methodology for modelling the mechanical response of urushi lacquer under varying environmental conditions (The conservation, Science and material Cultural of East Asian Lacquer, V&A London October 2009).

2. Stress measurement in East Asian lacquer thin films due to changes in relative humidity using phase shifting interferometry (The conservation, Science and material Cultural of East Asian Lacquer, V&A London October 2009).